Mesure et modélisation multiéchelle du comportement thermomécanique des alliages à mémoire de forme sous sollicitation mécanique multiaxiale

Xuyang Chang

Thèse de doctorat

NNT: NNT2020UPASN009

université PARIS-SACLAY

Full-field measurement and multi-scale modeling of thermomechanical behaviors of shape memory alloy under multi-axial loading

Thèse de doctorat de l'Université Paris-Saclay

École doctorale n° 579
Spécialité de doctorat: Solides, structure et matériaux
LMT Paris-Saclay
Science mécaniques et énergétiques, matériaux et géosciences

Thèse présentée et soutenue à Ecole Normale Supérieure de Paris-Saclay, le 04 février. 2020, par

M. Xuyang Chang

Composition du jury:

M. Sylvain CALLOCH Professor, ENSTA Bretagne	Président
M. Denis Favier Professor, Université Grenoble-Alpes	Rapportreur
M. Etienne Patoor Professor, GeogiaTech Lorraine	Rapporteur
Mme. Eva HERIPRE Ingénieure de Recherche, CentraleSupélec	Examinatrice
M. Yongjun He Professeur assistant, Ensta Paris-Tech	Examinateur
M. Oliver Hubert Professor, ENS Paris-Saclay	Directreur
Mme. Karine Lavernhe-Talliard Maîtresse de Conférences, ENS Paris-Saclay	Codirectrice

Remerciements

It is a long journey and a joyful adventure for previous three years and a half. During my PhD at LMT, I honestly appreciated the quality of exchanges with all the fellows, whom I've worked with.

First of all, I want to say a huge thanks to all the members in my jury for their great participation in my PhD defense. Particularly, to the President of the jury, Mr Sylvain Calloch, and also to the two reviewers, Mr Denis Favier and Mr Etienne Patoor. They have spent a part of their time during last Christmas, bringing both corrections and several interesting reflections over the possible ways to be explored. Their efforts and devotions helped me to elaborate even further the quality of this final version of document.

Then naturally, it's time to deliver my most sincere appreciations to my supervisors and mentors Olivier Hubert and Karine Lavernhe-Taillard, for their engagements and availability during the previous three years. Their remarks and various knowledges in multiple domains have greatly impressed me, helping me to form a global vision regarding the challenges concerning the Shape Memory Alloy, especially my beloved material NiTinol. Equally, I wish to say a great thank to the two engineers, Marc and Remi, who have been firmly supporting my PhD works, setting up the experimental campaigns.

Afterwards, personally I wish to express my great gratitude toward the two invisible mentors during my stay at LMT, Stéphane Roux and François Hild. Even though they are not officially my supervisors, their offices were always open to me. Along with the open discussions throughout all these years, they selflessly gave their opinions and suggestions, kindly helping me to conquer numerous challenges. Even until this day, I still miss the Eikology UTR meeting taking place every Thursday, where all PhD student present their research topics covering a great variety of domains. The pure beauty of science shining from my tutors and in their team contributes a lot to my motivation and devotion for my future scientific pursuit.

Of course, I cannot forget all other fellows at LMT. Hats off and a huge gratitude for my co-offices, Guillaume, Myriam and Gabriel, also Bhimal for their warmest company and their endless emotional supports. It is a great pleasure to work with all of you during the last three years with an extraordinary ambiance.

Last but not the least, I want to express my deep thanks to all my family members and my girlfriend for their remote emotional supports. Especially Zhen, who've endured my great anxiety at the very end, but my sweetheart, she is still relentlessly trying to comfort me before my PhD defense. Without her, I cannot imagine to deliver a document with such a quality.

Let me address this document as my best gift to my girlfriend.

Contents

List of Figures

List of Tables

Introduction

Since the discovery of the shape memory effect (**SME**) in the nickel-titanium (Ni-Ti) binary shape memory alloy (**SMA**), its unique properties have attracted the attention of many researchers, leading to often highly technical industrial applications in civil engineering, automotive, aerospace, mini-actuators and microelectromechanical systems (MEMS), robotics and biomedical fields. This trend, towards increasing industrial applications, requires a better understanding of the shape memory effect and a reliable prediction of its pseudoelastic hysteretic behavior especially in the context of multiaxial anisothermal loading.

SMA are famous first for their shape memory effect, meaning that these materials can remember their "high temperature" shape and thus find it back once again at high temperature despite any irreversible deformation of the material at a lower temperature (note that some SMA can memorize one shape at high temperature and another shape at low temperature). SMA are also known and used for their pseudoelastic (**PE**) behavior. Under mechanical loading, polycrystals can deform up to 8% and return to their original geometry after unloading. All of these behaviors are not reversible however. A mechanical loading/unloading is thus accompanied by a hysteresis cycle in the stress/strain space. SME and the PE behavior of SMA are the macroscopic results of the same phenomenon of crystalline phase transformation operating at a much lower scale. This solid to solid phase transformation is known as *martensitic transformation*.

The high temperature parent phase of SMA that exhibits the highest crystal symmetry is called austenite (**A**) and the low temperature phase is called martensite (**M**). Since the *martensitic transformation* of A toward M can be seen as a geometrical transformation of the crystal lattice, it is possible to form several variants whose number is directly related to the degree of symmetry of this phase. At the crystal scale, the abrupt structure change during martensitic transformation can induce reversible transformation strains of up to 10%. As a first-order phase change, the austenitic/martensitic transformation is always accompanied by heat emission or absorption associated with a variation of enthapy density. A strong thermo-

mechanical coupling therefore exists during the phase transformation of SMA. For some SMA (as Ni-Ti), depending on the chemical composition and the manufacturing process, an intermediate phase between A and M may also exist (**R**-phase for NiTi). R-phase defines, as for martensite, a geometric transformation, several variants, an enthalpy density variation, and associated thermomechanical effects.

Let us consider a SMA submitted to a low temperature. At the crystalline scale, under the effect of an applied stress, some martensitic variants better oriented than others (leading to a deformation in agreement with the loading) are selected during the transformation (this mechanism is referred as *detwinning*). The deformation of this twinned crystalline structure is generally maintained after complete unloading. Once placed at high temperature, the austenitic phase becomes more stable than the martensite phase, so that the backward transformation occurs. The crystalline structure returns to its original cubic symmetry which is identical whatever the M variant selected during the mechanical loading. The transformation strain disappears simultaneously, giving rise to the one-way shape memory effect. The pseudoelastic behavior is also explained by the combination of the phase transformation from A to M and a selection of the best-oriented variants. This mechanism may be partially or totally reversible during unloading (beyond the phenomena of germination / growth and associated thermal effects). The selection of certain variants to the detriment of others explains the observed macroscopic deformation. This transformation differs from the transformation under thermal loading alone. The latter leads indeed to an equiprobable distribution of variants without significant macroscopic deformation.

It should be noticed on the other hand that the martensitic transformation during a PE loading of a slender sample is generally concentrated inside one or more bands propagating along the specimen. This multiple localization of the deformation is the mark of intense mechanical softening associated with complex thermal phenomena (heat emission at the band / matrix interface and associated slowdown of transformations, conduction, convection). The nucleation point of a first band is often related to the existence of a local defect and associated stress concentrations. The number of bands generally changes with the strain rate at given heat exchange condition. Due to the above mentioned factors, stresses, deformations, thermal and phase fields are very heterogeneous in most cases.

Indeed, the major obstacle preventing the further use of SMA in industrial applications is that SMA devices, as other industrial devices, are frequently used in variable temperature environments and are subjected to complex loading configurations

(cyclic, multiaxial stress). This requirement demands to have a complete, reliable and robust prediction of SMA behaviors, which clearly remains above the capacity of most phenomenological models. Given the local origin of mechanisms now relatively well understood (see above), and given the increasing capabilities of calculating computers, a multiscale approach seems a relevant modeling choice, by describing the hysteretic nature of martensite phase transformation at variant/phase/grain scale. After a necessary step of parameters identification inherent to this model, it is also very important to have the permanent concern to compare the results of this model with experimental results obtained for various loading situations, thus ensuring a kind of validation.

To fulfill this purpose, the PhD thesis is divided into three axis:

- Develop a multiscale model, which permits to get a complete, robust and reliable prediction of the hysteretic response of SMA under complex thermomechanical loading configurations at different scales. This includes PE behavior and SME in multiaxial and anisothermal conditions.
- Identify the parameters of the model using a first set of experimental results.
- Compare the experimental SMA behavior (not used for identification) with numerical simulations under various uniaxial and multiaxial complex loading configurations.
- Compare directly the experimental/numerical phase field and strain field via a multiview multi-instrumented DIC-XRD combined setup.

According to this outline, the manuscript is made of four chapters

The first chapter addresses the most general aspects of SMA in order to give a general overview to readers. This overview begins with the introduction of the martensitic transformation at the microscopic scale: why M phase forms and how it gives rise to SME and PE. The localization phenomenon at macroscopic scale is presented next and the thermo-mechanical competition at the transformation front is discussed. The principal modeling tentatives available in the literature are then presented: both phenomenological macroscopic approaches and multiscale approaches are briefly reviewed. Their originalities and drawbacks are also listed. Finally the equiatomic NiTi SMA is chosen as the support of this thesis. Its thermo-mechanical properties and associated main physical parameters are also presented at the end of this chapter.

The second chapter presents an original stochastic multiscale model of a representative volume element (RVE) that considers the phase transformation at the single crystal scale. In the previous works of [Maynadier, 2012] and [Fall et al., 2016], a Boltzmann type distribution has been used to estimate the volume fraction of A and M variants. The main drawback of this approach was that the Boltzmann distribution only applies in a reversible thermodynamic framework: out-of equilibrium phenomena during phase transformation were not taken into consideration. This approach however was able to model multiaxial mechanical modeling in an appropriate way. In order to properly simulate the hysteretic response of SMA, the multiscale approach is reformulated going back to the stochastic origin of the Boltzmann equation and introducing the principle of energy barriers and characteristic times. Based on differential scanning calorimetry (DSC) experimental results, the out-of-equilibrium nature of phase transformation has been highlighted and repeatedly emphasized throughout the stochastic modeling. In this chapter, the whole approach is presented, including identification steps and validations by a point to point comparison with various experimental results from the literature.

The third chapter focuses on the measurement of the PE behavior of NiTi SMA subjected to uniaxial and multiaxial loading. A full-field global and continuous observation of the kinematic field by regularized DIC techniques has been carried out. This observation technique is made necessary since the phase transformation appears in highly strained localization bands for both 1D and 2D specimens. Averaged strains obtained from kinematic field are first compared to the numerical prediction of the stochastic multiscale model, highlighting a good agreement for 1D testing and unexpected discrepancies for 2D ones. A further analysis of biaxial experiments shows that it is not possible to obtain a RVE behavior with the specimen designed for the test. The measurement of spatial-temporal evolution of strain fields using a very high resolution allows a complete observation of the occurrence conditions and morphology of localization bands, and the competition between their propagation and the potential nucleation of other bands.

An in-situ multiview setup is proposed in the fourth and last chapter. It allows the concomitant evaluation of the phase field via XRD mapping and kinematic field via DIC. The question of co-existence of A, M and R phases during a 1D tensile loading at ambient temperature can for example be addressed. An accurate phase concentration identification procedure has been made possible too, using a novel reconstruction algorithm based on proper order decomposition (POD). Further enrichment of diffraction database allows some potential variant selections to be identified. Spatial undulations between the relative weights of some diffraction

planes indicate for example some specific variants selection across the border between the band region and the matrix.

Chapter 1

Shape memory alloys - state of the art

Contents

1.1 Introduction

This chapter gives an overview about the behavior of shape memory alloys (SMA). The martensitic phase transformation is first introduced. We then explain in a qualitative way how martensite transformation leads to the shape memory phenomenon. Behaviors such as pseudo-elasticity, band localization, thermo-mechanical coupling, under uniaxial or multiaxial mechanical loading are especially addressed. Classical models able to simulate SMA behaviors are reviewed next, complemented by a presentation of available experimental tests able to explore the nature of these behaviors. At the end of this chapter, some scientific challenges concerning SMA are listed. Some of them are addressed in the following chapters.

1.2 Martensitic transformation

1.2.1 General introduction about martensite transformation

The shape memory effect (SME) of shape memory alloys (SMA) is a particular manifestation of a displacive (diffusionless) crystalline phase transformation. This is a solid to solid phase (and mechanical) transformation where the lattice of crystal structure changes (deforms) abruptly at some temperature or stress level. The term of martensitic transformation is then generally employed to describe any transformation of this type, regardless of whether SMA is concerned or not. Generally, the stable phase at lower temperature is referred as Martensite (M) phase (or child phase) and the stable phase at higher temperature is denoted as Austenite (A) phase (or parent phase). Since this transformation is a first order thermodynamic transformation (involving a variation of enthalpy and entropy), it is accompanied by an heat emission or absorption depending on the transformation direction (M $\rightarrow$ A or A $\rightarrow$ M). The martensitic transformation of SMA is moreover usually considered as isochorus.

1.2.2 Transformation of the crystal lattice

First of all, it must be underlined that M phase can be obtained either by a one-step transformation (A $\rightarrow$ M), or a two-step transformation involving an intermediate phase noted as I (A $\rightarrow$ I $\rightarrow$ M). The transformation path of any SMA depends on the chemical composition of the material and on its thermomechanical history.

A $\rightarrow$ M one-step transformation

The A phase is stable at a higher temperature than the M phase. The martensitic transformation is moreover diffusionless, meaning that there is no rearrangement

of atoms. One final crystal can consequently be obtained from a 'deformation' of one initial crystal and vice-versa. Although the transformation parameters may be different from one alloy to another, it is always possible to create a M phase from A by the combination of elongation, shearing and contraction along certain directions. For most classical SMA (as Cu-Al-Ni and Ni-Ti), the austenitic crystal lattice has a higher symmetry than the Martensitic ones. The different martensitic crystal lattices can be obtained from a given reference lattice by a combination of rotations and symmetries. The different relative orientations are usually denoted as *correspondence variants of Martensite* or the *Martensite variants* in short. Depending on the chemistry of SMA, the number of total variants may also differ. For the case of a quasi-equiatomic NiTi SMA ($Ni_{50.2at\%}Ti$) mainly addressed in this thesis, A phase exhibits a B2 crystal structure and M phase a B19' crystal structure, leading to 12 possible martensite variants. Fe_7Pd_3 SMA exhibits only three different martensite variants as illustrated in Figure 1.1. [1].

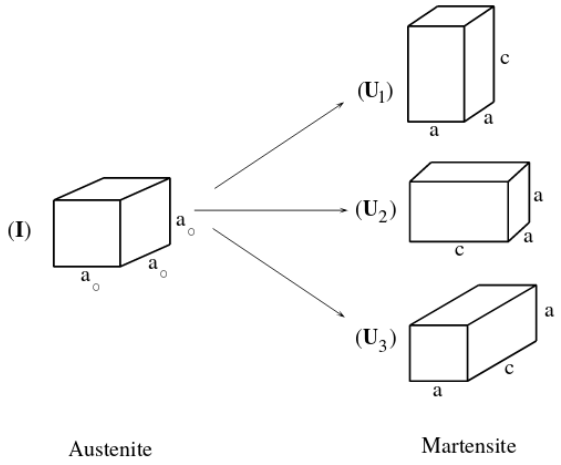

Figure 1.1: The three variants of martensite in a cubic to tetragonal transformation [Bhattacharya, 1999]

For martensitic transformation, nucleation and growth inside a crystal generates a high level of residual stress due to high strain incompatibilities. Two mechanisms allow a decrease of the elastic energy: twinning and slipping. Two variants may for example grow simultaneously much easier than a single variant once their averaged deformation is compatible [2]. They are called twinned martensite variants (twinning is a lattice invariant shearing). Inside the SMA crystal, martensite variants form disjoint domains separated by interfaces during the formation of the twinning structure. Complex microscopic structures such as wedge-like micro-structures can be obtained as illustrated in Figure 1.2b for CuAlNi SMA at the grain scale. This nucleation and

[1] This is the classical crystallographic definition for *Martensite variants*, a new statistic definition will be discussed in chapter 2.

[2] Forming interfaces without introduction of residual stress

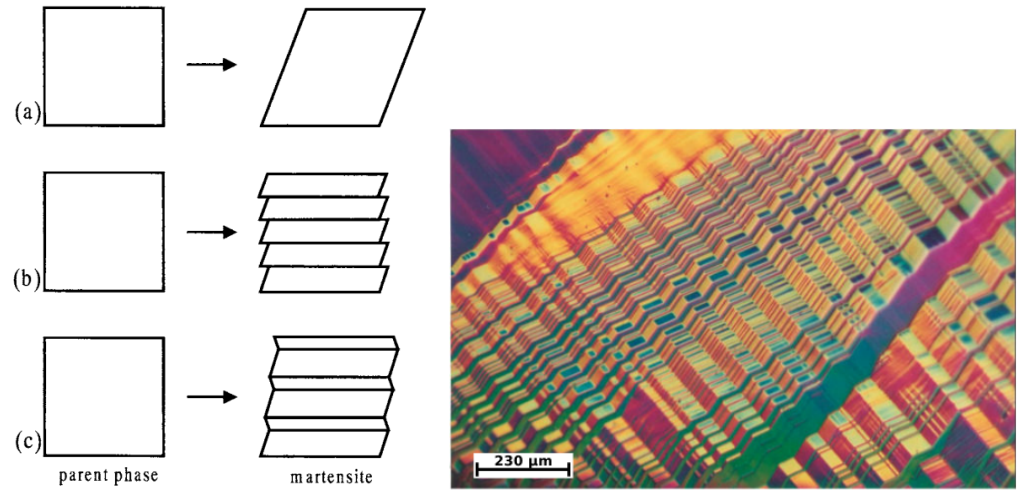

(a) a. Martensite transformation b. Slip c. Twinning [Otsuka and Wayman, 1999]

(b) Optical image: Wedge-like complex micro-structure pattern in CuAlNi [Chu and James, 1995]

Figure 1.2: Complex micro-structure of SMA material due to martensitic transformation

growth process, referred as martensite accommodation, is extremely common when the transformation is induced by cooling. When no compatible martensitic variants can be selected as neighbors, a natural local residual stress is created leading to a crystal distortion by classical plasticity and slip of dislocations.

A → I → M two-step transformation

A two-step transformation involves an intermediate phase that usually accommodates the deformation at the interface between A and M phase. This type of micro-structure, is only reported in Ni-Ti based and Au-Cu alloys.

For quasi-equiatomic NiTi alloy, A phase is a B2 crystal structure. The intermediate phase I is a rhombohedral crystal lattice (denoted as R phase). This structure can be seen as an intermediate structure between B2 and B19' structure of M phase.

As illustrated in Figure 1.3, R phase can be roughly viewed as a cubic B2 phase being elongated along one of the body diagonals $\langle 111 \rangle$. This elongation produces the Rhombohedral lattice. The lattice parameters of B2 phase, R-phase and B19' phase, and the lattice correspondences between B2 to R-phase and B2 to B19' transitions, have been established in [Otsuka and Wayman, 1999] [Schroeder and Wayman, 1977] and [Zhang and Sehitoglu, 2004]. It is worthy mentioning that 4 variants of R phase can be generated. Self-accommodation and twinning can consequently be observed for R phase as shown in Figure 1.4.

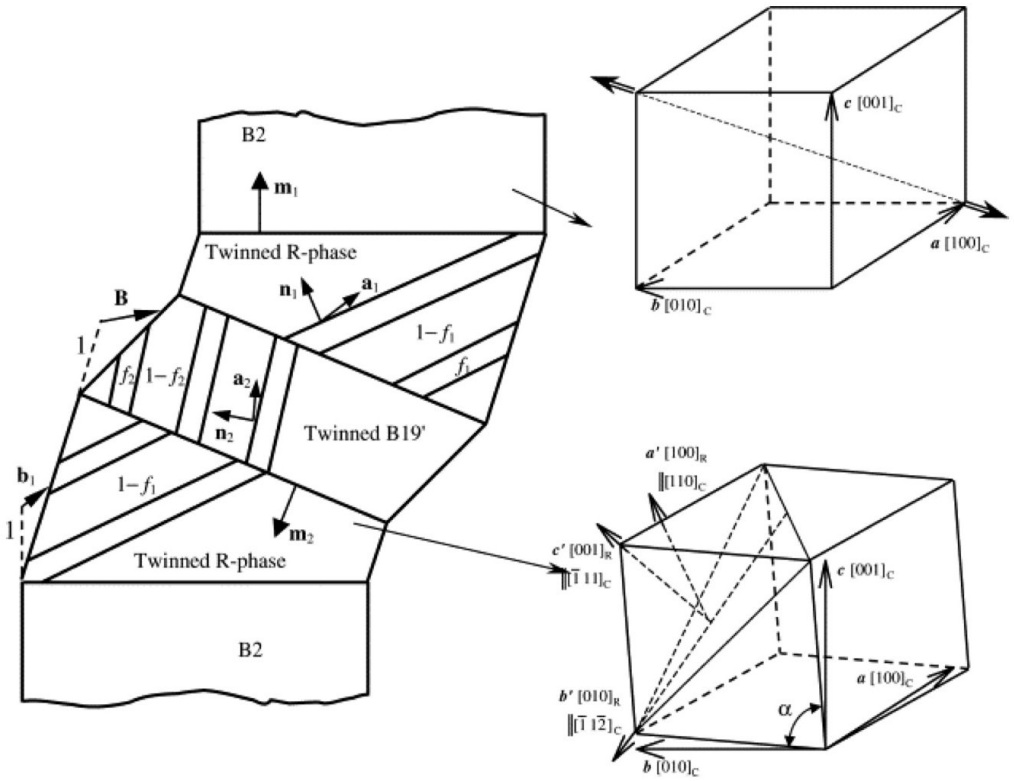

Figure 1.3: A schematic showing the transformation planes and directions associated with successive step transformation B2 → R and R → B19' in the unit A and R phases cells [Zhang and Sehitoglu, 2004].

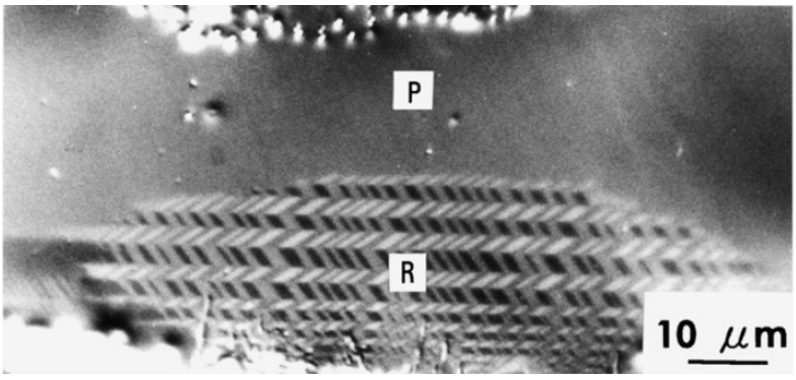

Figure 1.4: Optical microscope observation of A → R transformation for Ti-Ni-Fe alloy. P (parent A phase) and R (R phase) [Otsuka and Ren, 2005]

1.2.3 Transformation inside a single crystal

When a single crystal is subjected to a sufficient thermal (or mechanical) loading, martensitic phase propagates by nucleation and growth at nearly the velocity of sound. The mesoscopic domains (composed of several variants) form at the grain boundary first, where potential residual stress concentrations are mostly present.

From the grain boundary, multiple sets of twinning structures are formed to occupy the whole grain and thus seek to minimize the elastic energy of the system. For each neighbored distinguished mesoscopic subdomain containing different twinning structures, crystallographic orientations are by nature different, otherwise they do not define interfaces. These subdomains are mentioned as the first source of heterogeneity in SMA. A subdomain is illustrated in Figure 1.5.

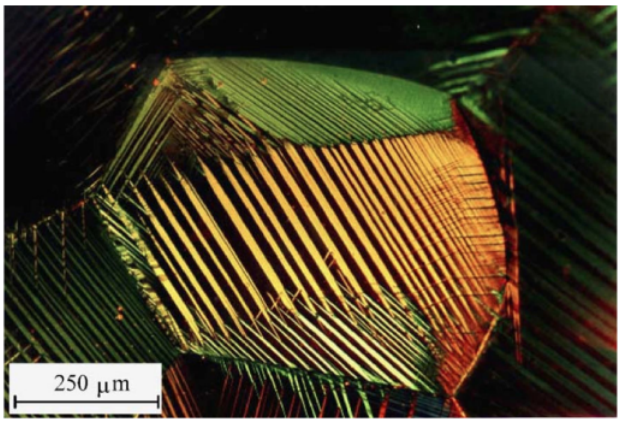

Figure 1.5: Subdomain and martensitic variants inside a grain [Patoor et al., 2006]

1.2.4 Transformation inside a polycrystal

SMA are usually polycrystalline. The crystallographic texture and grain size can differ greatly from one material to another at a given composition, depending on the forming process. For example, the grain size of CuAlBe can vary from 60 µm to 2 mm [Lexcellent et al., 2006] [Araya et al., 2008]. Large grain size is a characteristic of Copper based SMA. The grain size of Nickel based SMA is usually much smaller. For the previously mentioned equi-atomic NiTi SMA ($Ni_{50.2at\%}Ti$), the average grain size varies between 100 nm and 50 µm.

Inside a polycrystalline structure, each grain has its own orientation. Supposing a A $\rightarrow$ M transformation at low to medium macroscopic stress of after cooling, the twinning structures and subdomains are different from one grain to another. Each subdomain is thus stopped at the grain boundary. A stress higher than a critical value may force martensite subdomains to cross the grain boundaries. This point is illustrated in Figure 1.6. At higher scale, the macroscopic transformation bands are created from the accumulation of martensite subdomains.

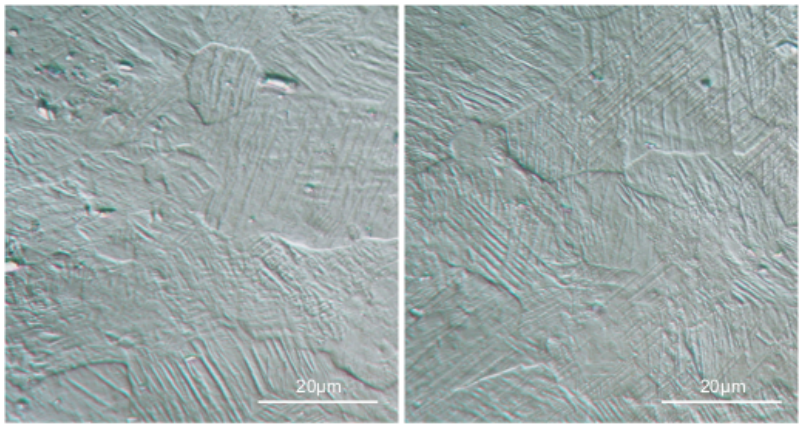

Figure 1.6: Optical image of a $Ni_{50.2at\%}Ti$ after uniaxial tensile test : (a) subdomains are limited by grain boundaries outside a macroscopic localization band; (b) subdomains are crossing the grain boundaries inside the band [Maynadier, 2012]

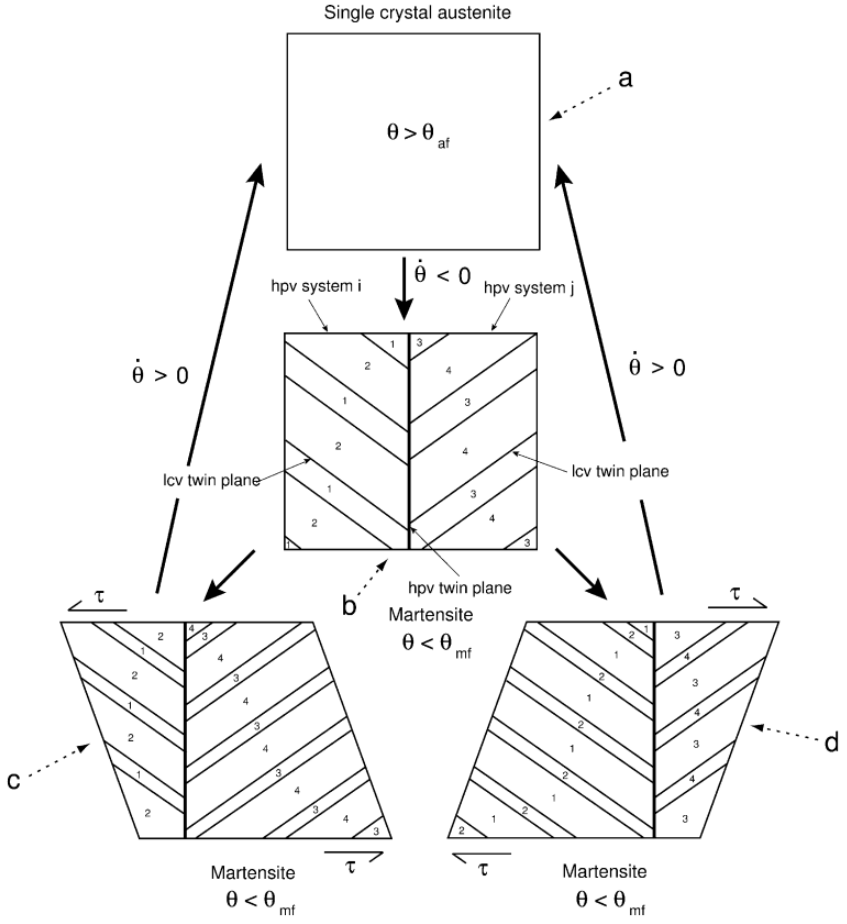

Figure 1.7: Schematic diagram: transformation of A single crystal into M variants, a → b; reorientation/detwinning of M (b → c/d); M to A transformation inside a single crystal (c/d → a).

1.2.5 Martensite reorientation

A more widespread use of SMA requires a better knowledge of their behavior under multiaxial loading and non proportional multiaxial loading especially. A better understanding of the martensitic reorientation is therefore necessary. In literature, it is universally admitted that martensite reorientation is due to the movement of the interfaces between two variants ([Thamburaja et al., 2005],[Yu et al., 2015]). Two situations can be encountered as illustrated in Figure 1.7:

1. At a temperature lower than the martensite finish temperature ($T \leq M_f$), martensite reorientation occurs when the applied stress reaches a critical value (under uniaxial or multiaxial loading conditions);

2. At a temperature higher than the austenite finish temperature ($T \geq A_f$), martensite reorientation only occurs when the material is submitted to a non-proportional mechanical loading.

1.3 Shape memory alloys

SME was firstly reported for $Au_{47.5at\%}Cd$ and in InTl alloys. SME began to draw the attention of a larger number of researchers when it has been observed in equiatomic NiTi alloy [Buehler et al., 1963] (also known as *nitinol*, name chosen as a combination of NiTi and *Naval Ordonance Laboratory*). NiTi alloy became quite popular because of its excellent mechanical properties, allowing a various set of industrial applications [Hautcoeur and Eberhardt, 1997] [Zider and Krumme, 1988] such as structures and composites [Furuya, 1996], automotive [Stoeckel, 1990] , aerospace [Humbeeck, 1999], mini actuators and micro-electromechanical systems (MEMS) [Sun et al., 2012] [Kohl, 2013], robotics [Sreekumar et al., 2007], and biomedical [Duerig et al., 1999] [Morgan, 2004]. Let us focus on two applications:

Civil engineering

Figure 1.8 (a) illustrates one particular application of SMA in the civil engineering domain. NiTi-Al composite is used to pre-stress the concrete in the walls of a building. In this case, two different SMA fibers, with two different A_f temperatures (one below, and one above the ambient temperature), are used to enhance the strength and the toughness of the concrete, and improve its damping.

Biomedical

Figure 1.8 (b) illustrates a particular but popular medical application of SMA: the

Simon filter allowing embolisms to be trapped is made of NiTi SMA. The device relies on thermal deployment. It is first collapsed and folded into a catheter in the martensitic state and flushed with chilled saline solution during the insertion in the body of patient to keep the M phase stable. When the deployment site is reached, the circulating saline solution is switched off, the filter is pushed out of the catheter and the body temperature causes it to open out with the M to A phase transformation.

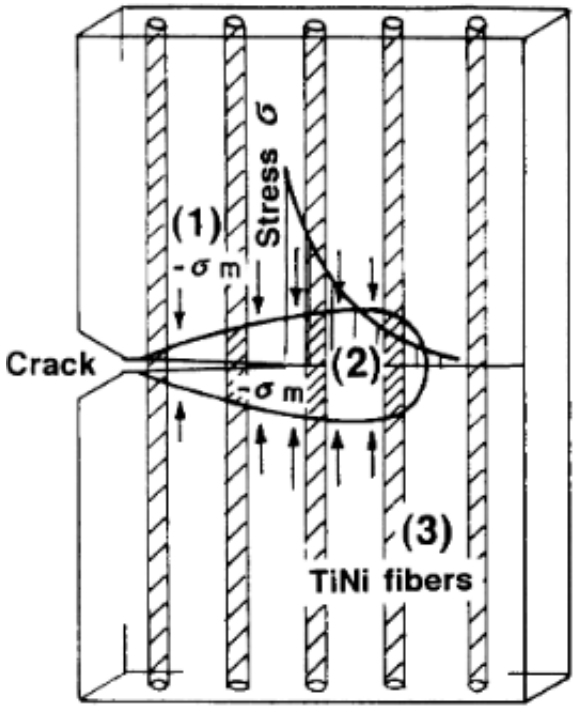

(a) Enhanced resistance to crack propagation of concrete by implementation of NiTi fibers [Furuya, 1996]

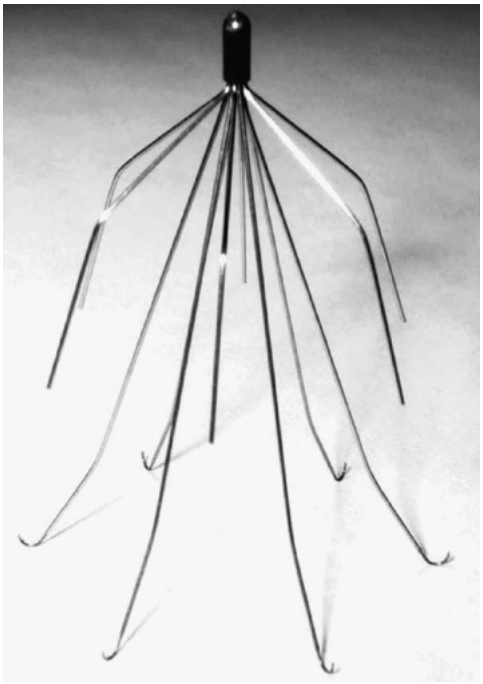

(b) Simon filter system made of NiTi SMA [Morgan, 2004]

Figure 1.8: Applications of SMA

1.3.1 Shape memory effect

Shape memory effect (SME) in a SMA results in a return to its original geometry (shape or size) after thermo-mechanical loading (see Figure 1.9). SME is obtained when the material is able to transform between two states corresponding to the two phases, involving a forward and reverse transformation. Shape change effects can be categorized into three groups:

1. One-way shape memory effect (OWSME);
2. Two-way shape memory effect (TWSME);
3. Pseudoelasticity;

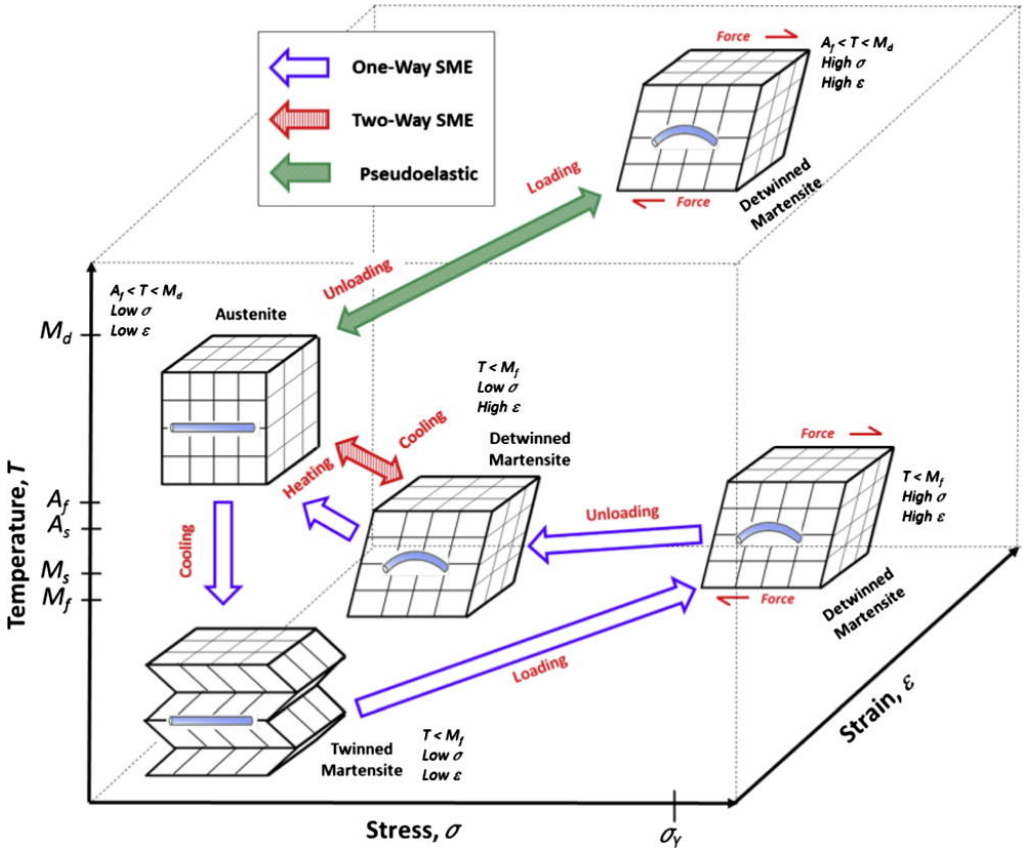

Figure 1.9: Shape memory effect and pseudoelasticity [Jani et al., 2014]

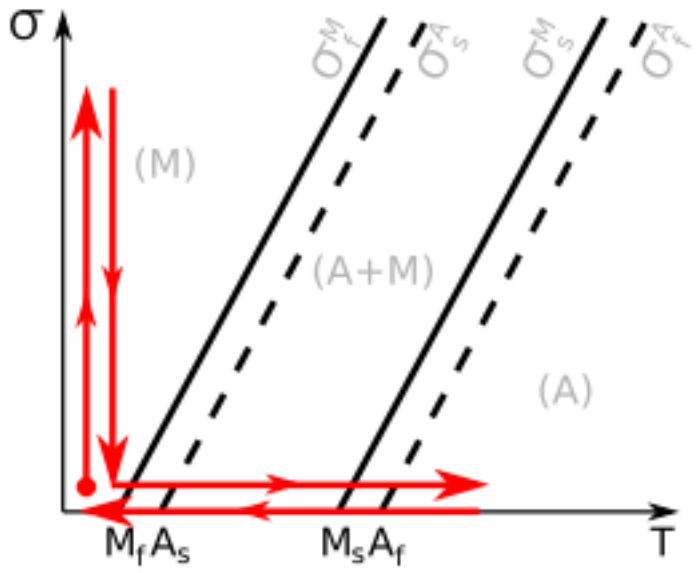

(a) Illustration of OWSME in the Clausius Clapeyron diagram

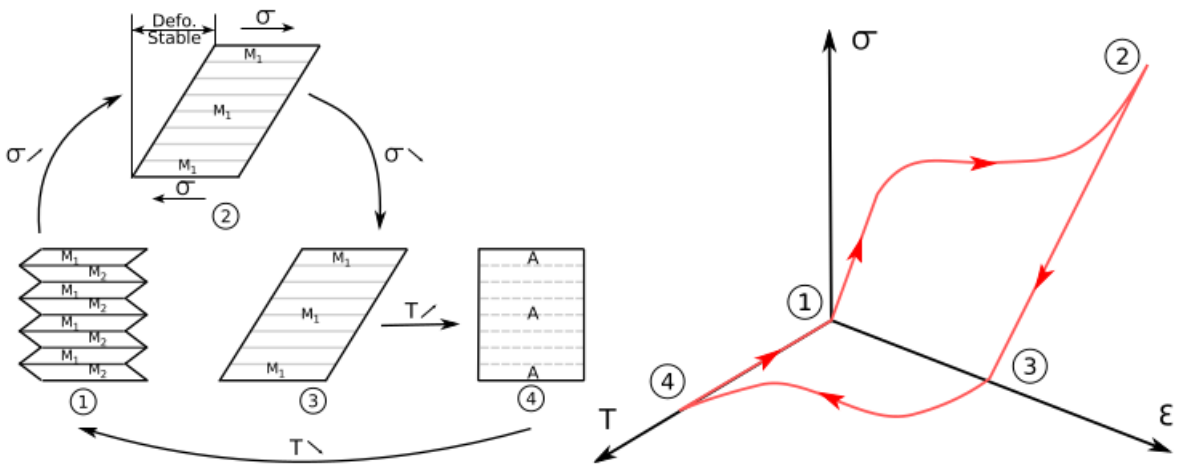

(b) OWSME

Figure 1.10: 3D schematic of OWSME [Maynadier, 2012]

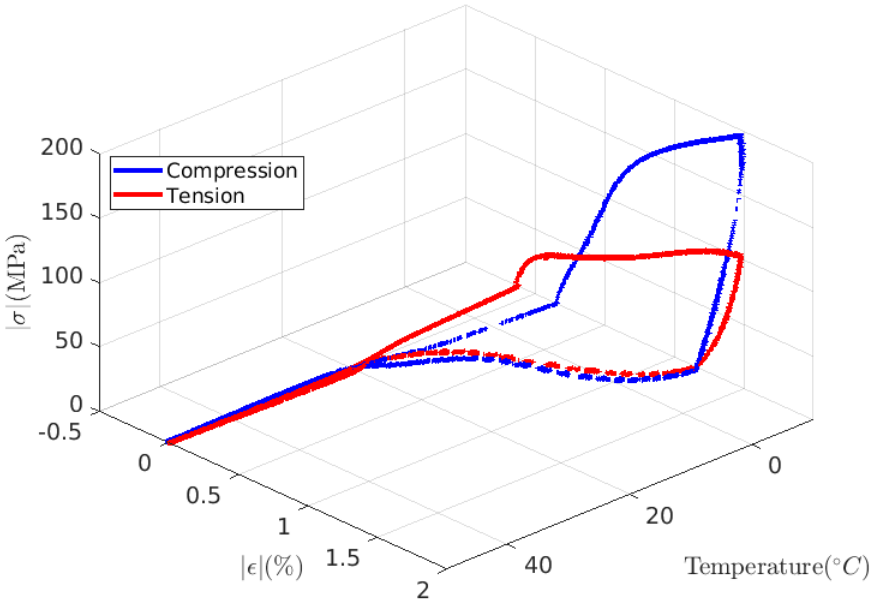

Figure 1.11: SME in NiTi: comparison between stress-strain-temperature response in tension and in compression [Lavernhe-Taillard et al., 2009]

One-way shape memory effect (OWSME):

One-way SME (OWSME) means that the SMA can retain a deformed state after the removal of an external force, and then can recover its original shape after a heating/cooling process. Qualitative illustrations of OWSME are presented in Figure 1.9 and Figure 1.10. Referring to Figure 1.10b, the following steps are highlighted:

$1 \rightarrow 2$: initially, the material is at low temperature, where martensite phase is stable (below martensite finish $T < M_f$). By applying a mechanical tensile loading[3] in a given direction, several pairs of Martensite twinned structures become more favorable than others. Due to these martensitic reorientation (or selective nucleation), a permanent deformation is generated.
$2 \rightarrow 3$: after removal of the applied stress, the SMA keeps its deformed shape (the thermomechanical equilibrium state is kept unchanged thanks to a large hysteresis).
$3 \rightarrow 4$: by applying a thermal heating, the SMA begins to transform from M to A phase ($M \rightarrow A$ denoted as backward transformation). The austenite start temperature A_s is the temperature where this backward transformation starts and the austenite finish temperature A_f is the temperature where this transformation is fully completed and the original geometry is recovered.
$4 \rightarrow 1$: after a return to low temperature where M phase is stable ($T \leq M_f$), austenite transforms towards martensite ($A \rightarrow M$ denoted as forward transformation) in an *accommodating* way without any introduction of macroscopic strain. The geometry is unchanged during this last step.
An asymmetrical behavior between tension and compression is usually observed for OWSME. Indeed, threshold for selective nucleation or twinning is much higher under compression than under tension, as illustrated in Figure 1.11.

Two-way shape memory effect (TWSME)

The one-way shape memory effect discussed in the previous section is characterized by a *memory* of alloy which is associated with the geometry of the parent phase (A phase) only. Two-way SME (TWSWE) indicates that the SMA can remember its shape at both high and low temperatures. More precisely, a material that exhibits a shape memory effect during both heating and cooling is defined as a two-way shape memory material.

It is generally admitted that a *training process* is required to produce a TWSME from an initially OWSME. Various training methods have been proposed in literature [Huang and Toh, 2000] [Schroeder and Wayman, 1977] [Ma et al., 2010] and [Ponikarova et al., 2017]. In general, two methods are most commonly em-

[3] Other loadings could be considered.

ployed: the spontaneous and the external stress-assisted (load-assisted) induction (illustrated in Figure 1.12a).

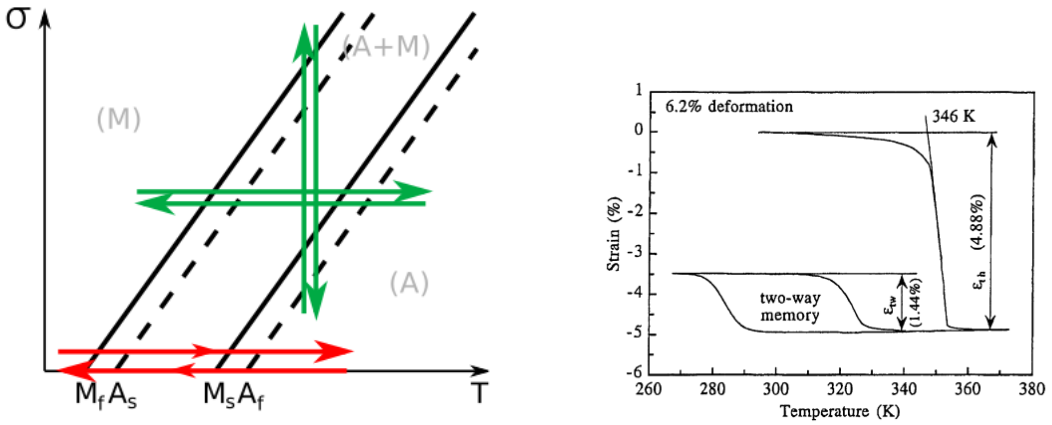

(a) Production of a TWSME material: green path indicates the spontaneous training process, and red path indicates external stress-assisted induction process.

(b) Two-way shape memory effect of $Ti_{50.0at\%}Ni$ alloy obtained after a deformation by 6.2% [Liu et al., 1998]

Figure 1.12: Two-way shape memory effect

TWSME Materials usually exhibit a lower recovery strain range than OWSME materials of the same chemical composition. This difference of recovery range strain is determined by the fact that the OWSME is due to a selective nucleation of some martensite variants, while the TWSME is due to the strong reversibility and unique lattice correspondence during reverse transformation [Otsuka and Wayman, 1999]. This is the main reason why industrial applications using TWSME are less developed than applications using OWSME.

1.3.2 Pseudoelasticity

The pseudoelasticity (PE) or super-elasticity (SE) is the ability for SMA to deform up to high levels (for example 10% in tension for NiTi single crystal) without any plasticity, and to recover its initial geometry after a complete unloading.
Generally, the martensitic transformation is a shear-like mechanism, where the stress assists the martensitic transformation. Thus, it is possible to stress-induce the M phase even at temperature $T \geq M_s$, (M_s martensite start is temperature at which A $\rightarrow$ M transformation begins during cooling). The stress-induced martensitic transformation can be analyzed by the Patel-Cohen theory [Patel and Cohen, 1953] (the work brought by an external stress equals the change of the free energy), and/or by the thermodynamic Clausius-Clapeyron relationship. The latter is a simple mathe-

matical form that summarizes the equivalence between stress and temperature effect:

$$\frac{d\sigma}{dT} = -\frac{\delta S}{\epsilon} = -\frac{\delta H}{\epsilon T} \tag{1.1}$$

Here δH and δS denote the enthalpy and entropy densities variations associated with the phase transformation. The above equation derives from an equilibrium relationship between the free energy of A and M phases (see subsection 2.2.2).

Figure 1.13 illustrates the pseudoelastic behavior inside the Clausius-Clapeyron diagram. The loading path is plotted in red, and is expected to cross a biphased domain (A+M). The global process can be synthesized as follows:

1. At initial stage, the specimen is purely austenitic until external stress reaches a critical stress transformation threshold $\sigma \geq \sigma_{M_s}$. Until this stage, the mechanical behavior is purely elastic.

2. When $\sigma_{M_f} \geq \sigma \geq \sigma_{M_s}$, the forward transformation (from A to M phase) begins. Consequently, a softening-like plateau is observed (apparent weakening of tangent modulus). This stage is commonly referred as 'transformation plateau'.

3. When the external stress is above the threshold of martensite finish $\sigma \geq \sigma_{M_f}$, the specimen is considered as purely martensitic. The mechanical behavior is purely elastic until it reaches the plastic yield stress of M phase.

During unloading, the transformation yield stresses are higher than the thresholds observed during loading. It results in a hysteretic behavior denoting an energy dissipation. Under isothermal condition, the hysteresis is related only to the germination process (germination of M inside A then germination of A inside M). A higher level of germination energy leads to a larger hysteresis.

In reality, the forward transformation ($A \rightarrow M$) is an exothermic process; the backward transformation ($M \rightarrow A$) is an endothermic process. Whatever the temperature regulation set-up (air convection or liquid cooling), environment and specimen are never at the same temperature during a pseudo-elastic cycle. Since the loading conditions are never isothermal, the transformation thresholds are modified. Finally, the pseudo-elastic stress-strain curve can be influenced by the nature of the material, the loading temperature, the loading rate, the thermal exchange conditions etc. The most significant characteristics of the pseudo-elastic behavior are detailed below.

Tension and compression asymmetry.

The PE behavior of SMA is usually asymmetric, meaning that the transformation thresholds in compression and tension are different (see the work of [Lexcellent et al., 2006] [Maynadier et al., 2012] [Plietsch and Ehrlich, 1997]). As illustrated

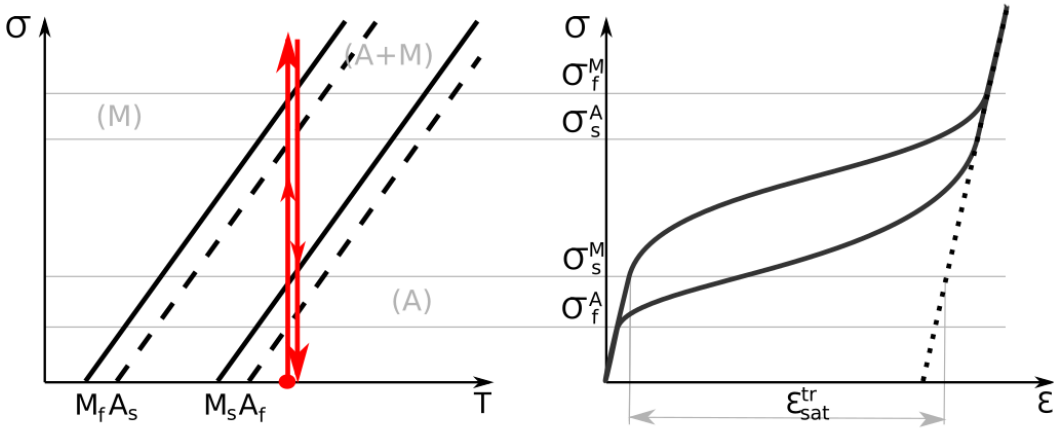

Figure 1.13: Pseudoelasticity: Clausius-Clapeyron phase diagram (left); associated stress-strain curve (right)[Maynadier, 2012]

in Figure 1.14a, the stress transformation threshold σ_{M_s} is higher in compression than in tension. The maximum strain reached when the forward transformation is complete is on the contrary lower in compression than in tension.
It must be noticed that the asymmetrical behavior is most significant when the temperature of the specimen is close to the ambient temperature, *i.e.* $T \simeq A_f$. Asymmetry decreases when the temperature of specimen is overwhelmingly lower than T_{M_f} as seen in Figure 1.14b (the M to R phase transformation is the source of asymmetry in this situation). When the temperature is extremely high, applied external stress can not trigger the forward transformation.
Of course, a pure A -phase NiTi SMA that does not transform into M phase (due to a too high ambient temperature for example) behaves similarly in tension and in compression, and the asymmetrical behavior disappears (this point is illustrated in Figure 1.14c).

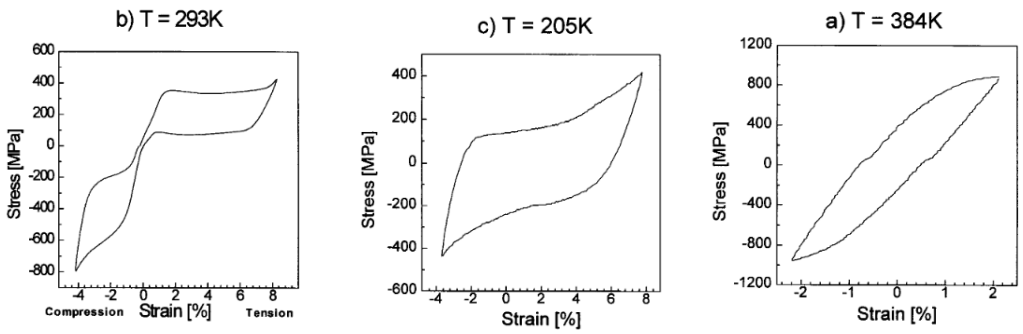

(a) Stress-strain curve $T = 293K$ (b) Stress-strain curve $T = 205K$ (c) Stress-strain curve $T = 384K$

Figure 1.14: Tension/compression hysteresis for a NiTi hourglass specimen at different temperatures [Plietsch and Ehrlich, 1997]

Temperature Influence.

As a consequence of the Clausius-Clapeyron relationship, a temperature change has a huge influence on the PE behavior. Many experimental tests have been reported in the literature (see [Lexcellent et al., 2006] for Cu-Al-Be alloy and [Shaw and Kyriakides, 1997] for a NiTi alloy) showing that the increase of temperature significantly increases the transformation yield stress σ_{M_s}. Figure 1.15 illustrates this point.

We observe moreover that the evolution of σ_{M_s} and σ_{A_s} are not completely linear as function of temperature inside the Clausius-Clapeyron diagram (Figure 1.15(b)). This potentially indicates the presence of R phase when the temperature is lower than $T \leq 20°C$. Below this temperature, the phase diagram should no longer be considered as bi-phased. This could explain the shape change of the stress-strain curve at low temperature in Figure 1.15(a) .

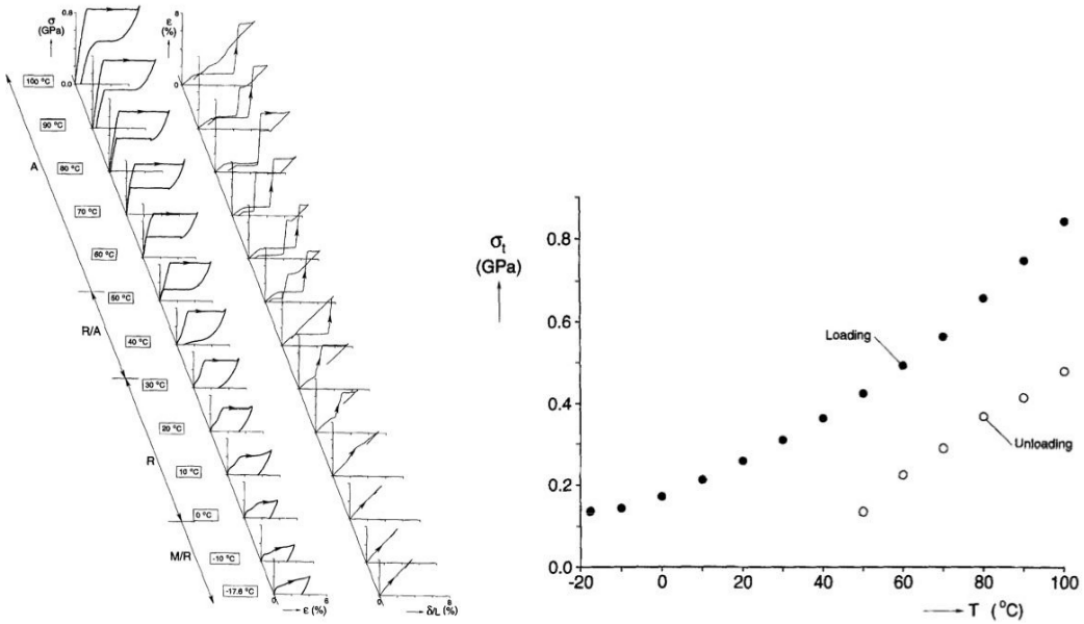

(a) (b)

Figure 1.15: (a) Stress-strain of NiTi SMA obtained at different temperatures; (b) Clausius-Clapeyron diagram with σ_{M_s} (black dots) and σ_{A_s} (white dots) [Shaw and Kyriakides, 1997]

Loading rate dependency.

In the literature, the reported trends for the rate-dependency of PE behavior are not always consistent: some authors reported an increase in the hysteresis size loop while others showed a decrease in hysteresis loop with increasing loading rate. More recent studies indicate that the rate dependency of the hysteresis size is non

monotonous at ambient temperature: it seems maximum at an intermediate strain rate. The work of [He and Sun, 2011] is presented in Figure 1.16: at low strain rate, the forward and backward transformation plateaus are both very well defined. When the strain rate increases, since the forward transformation (A→ M) is exothermic, an increasing loading rate induces a local temperature increasing at the transformation front. The mere consequence is a significant rise of transformation stress threshold σ_{M_s} (at given heat exchange conditions).

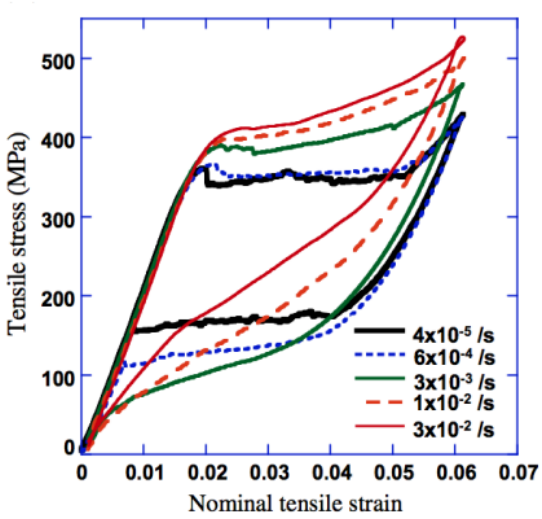

Figure 1.16: Loading rate dependency of PE behavior for NiTi alloy [He and Sun, 2011]

Cyclic loading.

When a SMA specimen is subjected to a cyclic loading, the macroscopic PE behavior is progressively modified as shown in Figure 1.17. The transformation stress threshold σ_{M_s} and the hysteresis loop progressively decrease. Indeed, defects are created during the cycles (dislocations and twinnings). These defects induce residual stresses, whose heterogeneous distribution at micro and meso scales may influence the macroscopic behavior. Around these defects, the backward transformation is not complete even after the full unloading. Consequently, retained heterogeneous martensite residuals gradually accumulate as function of the number of cycles [Saint-Sulpice et al., 2009].

Anisotropy.

The PE in most SMA materials is known to be significantly different in single crystals and in polycrystals. For single crystals, SME depends strongly the loading

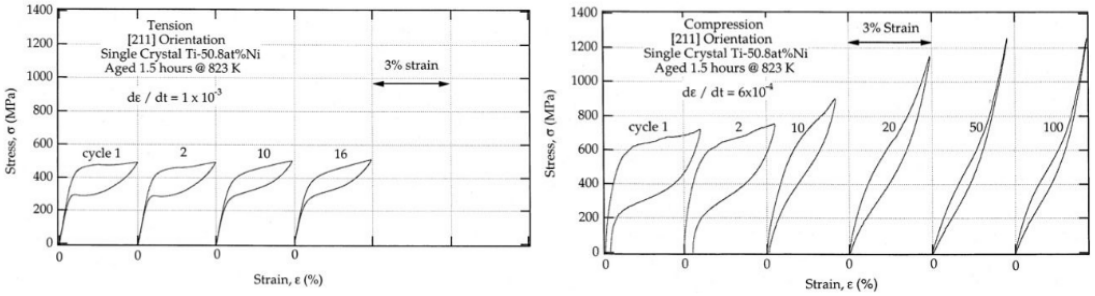

(a) Tensile cyclic of a NiTi single crystal

(b) Compressive Cyclic loading of a NiTi single crystal

Figure 1.17: Influence of a cyclic loading on the PE behavior of NiTi [Gall et al., 2001]

direction, leading to a strongly anisotropic PE behavior. A favorable orientation is defined as a direction for which a low stress is required to select a pair of martensite variants. An unfavorable orientation requires a higher stress level. Only few variants are selected during the loading of a single crystal. The stress applied to each grain of a polycrystal submitted to an uniaxial stress is usually multiaxial. This is due to a combination of the orientations of the grains and an anisotropic stiffness tensor for the material. A different set of variants is consequently created from one grain to another. The other consequences are:

1. Due to the variants selection, deformation becomes incompatible very fast from one grain to another, leading to an increasing amplitude of inter-granular stresses.

2. The obtained average deformation is therefore strongly dependent to the crystallographic texture of the polycrystal.

3. Obviously, the maximal strain reached by a single crystal loaded along an appropriate direction may be much higher than the strain of a the corresponding polycrystal loaded in the same condition (see Figure 1.18).

Moreover, after bypassing the transformation stress threshold, the softening plateau of a single crystal is nearly horizontal due to the limited number of selected variants. This is usually not observed for a polycrystal that experiences a multiple set of variants in each grain interacting with each other.

Multiaxiality and non-proportionnal loading.

The yield surface of a PE SMA can be defined as a surface in the stress space which determines the onset of stress-induced martensitic phase transformation. Some 2D yield surfaces have been experimentally measured. Figure 1.19 illustrates the partial yield surface of a NiTi alloy (experimental points have been obtained by

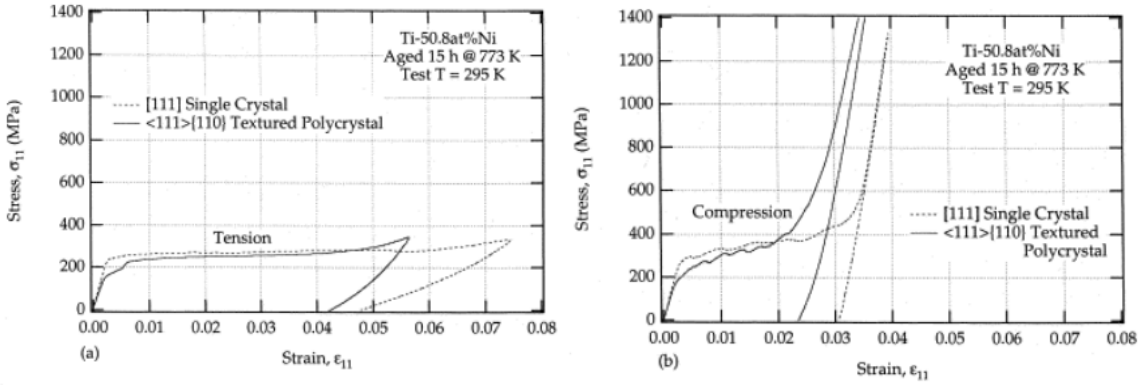

(a) Tensile loading (b) Compressive loading

Figure 1.18: Comparison of PE responses of a single crystal loaded along ⟨111⟩ direction and a textured polycrystal of the same material [Gall et al., 2001]

tension-torsion) [Lexcellent and Blanc, 2004] and the yield surface of a CuAlBe SMA polycrystal (experiments are carried out inside a biaxial compression machine) [Bouvet et al., 2004], both plotted in the principal stress frame. Results are compared to numerical criterion proposed by the authors. Yield surface shape is directly related to the number of M phase variants.

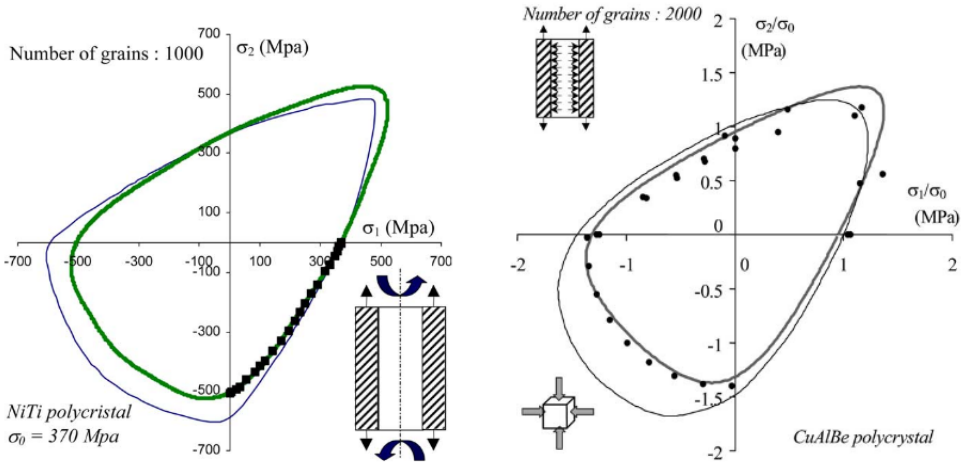

(a) Phase transformation surface of NiTi polycrystal in the space (σ_1, σ_2) - (b) Yield surface of CuAlBe polycrystal in the space (σ_1, σ_2)(austenite to untwinned martensite)

Figure 1.19: Multiaxiality of SMA - phase transformation yield surfaces (experimental data are plotted in black dots)

The yield surface is only one aspect of the multiaxiality of SMA. A more important challenge is to know the response of a PE SMA subjected to a multiaxial loading. The stress-induced martensite variants selection is both heavily influenced by the direction of external loads (tension, compression, torsion, ...) and the his-

tory of loading path (proportional or non-proportional loading). During a non-proportional loading, a SMA is frequently reported to experience a martensite (or R phase) reorientation, leading to the selection of a new set of variants. The only available non-proportional experiments reported in the literature are the tension-torsion tests carried out on Ni-Ti by [Lavernhe-Taillard, 2006]. The interpretation of the obtained results is made very complex due to the concomitant presence of three potential phases (A, M and R) and the unavoidable anisothermal conditions during the tests.

1.4 Strain localization

Many authors observed that a strain localization usually occurs during the tensile loading of PE SMA. This strain localization is associated with a localized phase transformation from A to M phase. This phenomenon constitutes another difficulty for further industrial applications of SMA.

1.4.1 Experimental observations

The localization results usually in the formation of bands : for sheet of film samples, two sets of symmetrical bands are usually formed to ensure stress equilibrium; helices are formed for tubular specimen.
Generally, during a uniaxial tensile loading, as soon as localization band initializes inside the SMA strip, the forward transformation continues to progress inside the bands until the local deformation reaches the maximum transformation strain (implying that forward transformation is complete inside the bands). Once the maximum transformation strain is obtained, a broadening of the principal band and a nucleation of other bands are observed. Once all localization bands joint together, the specimen is fully transformed into martensite.
Figure 1.20 and Figure 1.21 show the optical and thermal images of a localization phenomenon observed by [Shaw and Kyriakides, 1997] during a tensile test of a NiTi specimen using a loading rate $\dot{\epsilon} = 1 \times 10^{-4}\,\mathrm{s}^{-1}$. Bright regions are the martensitic transformed regions, dark regions are the non-transformed areas. The infra-red (IR) image shows that the forward transformation is accompanied by heat emission, leading to a local temperature rise at the front of the transformation.

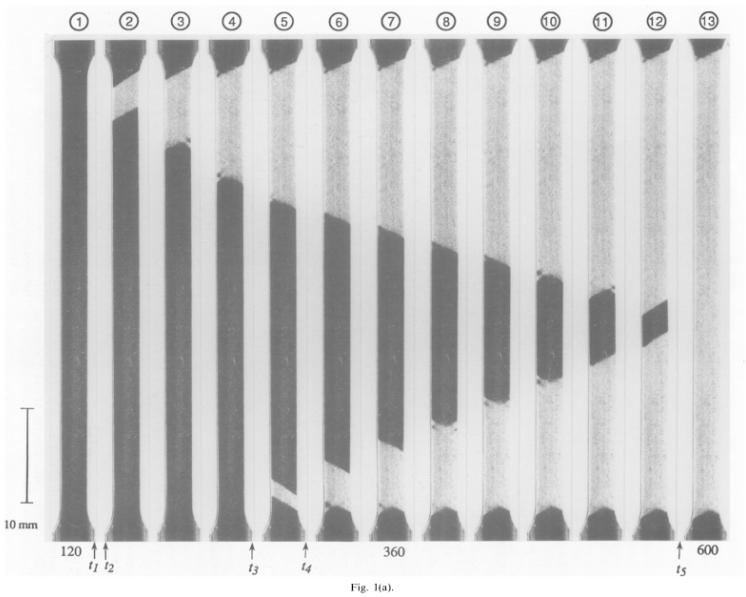

Figure 1.20: Optical imaging of localization bands observed by [Shaw and Kyriakides, 1997] during a tensile test over plate specimen of NiTi, with a loading rate $\dot{\epsilon} = 1 \times 10^{-4}\,\mathrm{s}^{-1}$

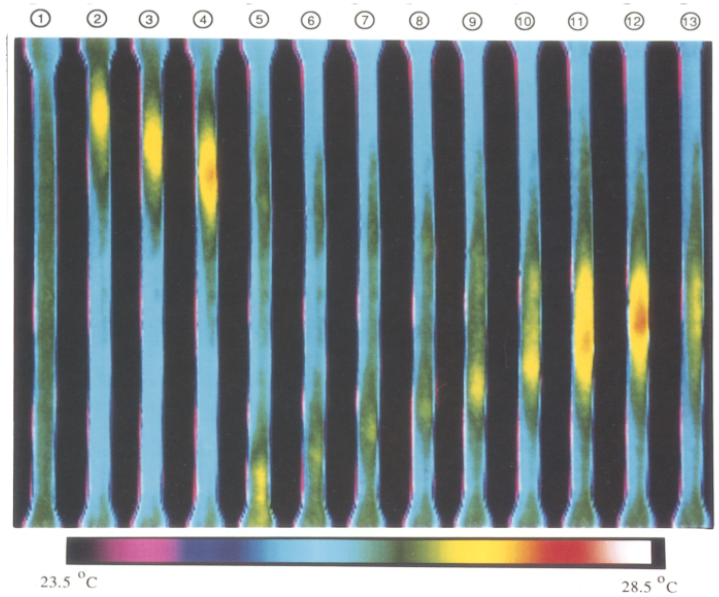

Figure 1.21: Infra-red imaging of localization bands observed by [Shaw and Kyriakides, 1997] during a tensile test over plate specimen of NiTi, with a loading rate $\dot{\epsilon} = 1 \times 10^{-4}\,\mathrm{s}^{-1}$

1.4.2 Nucleation and propagation stress

Under isothermal condition, it is generally admitted that the nucleation stress σ_N is relatively higher compared to the propagation stress σ_P during 1D tensile loading (as seen in Figure 1.22):

$$\sigma_N \geq \sigma_P \tag{1.2}$$

However, assuming that temperature field is constant across a 1D strip SMA specimen and that the same amount of energy is required to transform austenite into martensite, the nucleation and the propagation stress should be strictly identical according to the Patel-Cohen theory [Patel and Cohen, 1953]. The experimental observations reported in literature imply consequently that an additional stress concentration is present at the transformation front (the residual stress is potentially due to the nucleation of cohabit planes between austenite and martensite variants). The evidence of stress concentration at the neighborhood of localization region is illustrated in Figure 1.23, where a crack has been detected [Zheng et al., 2016].

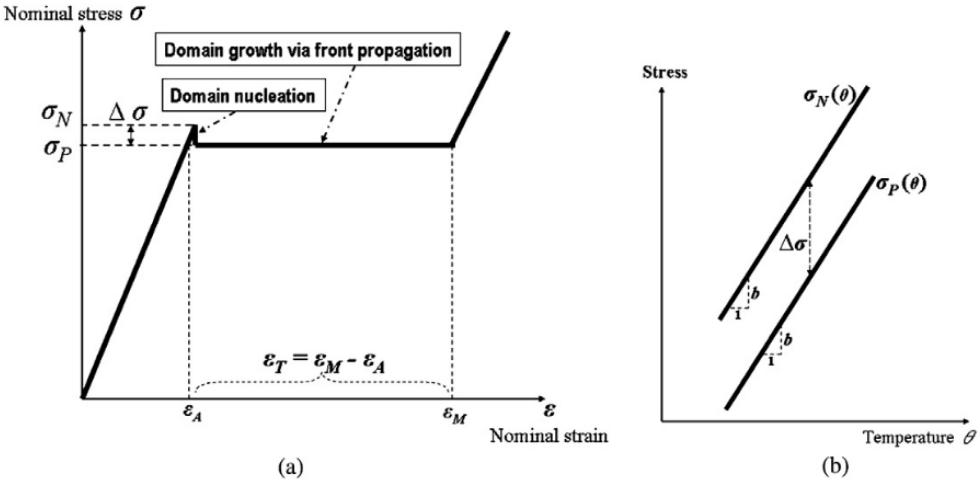

Figure 1.22: (a) Schematic isothermal stress/strain curve; (b) temperature dependency of domain-nucleation stress and front-propagation stress [He and Sun, 2010]

The localization mechanism has been observed in literature both for single and polycrystals. As illustrated in Figure 1.24, due to the limitation of boundary conditions for multiple grains, the band front inside the polycrystal is usually not straight [He and Sun, 2010]. On the contrary, the band front is very well defined in a single crystal, because only one cohabit plane is needed to define and separate the domain formed by twinned martensite variants and austenite.

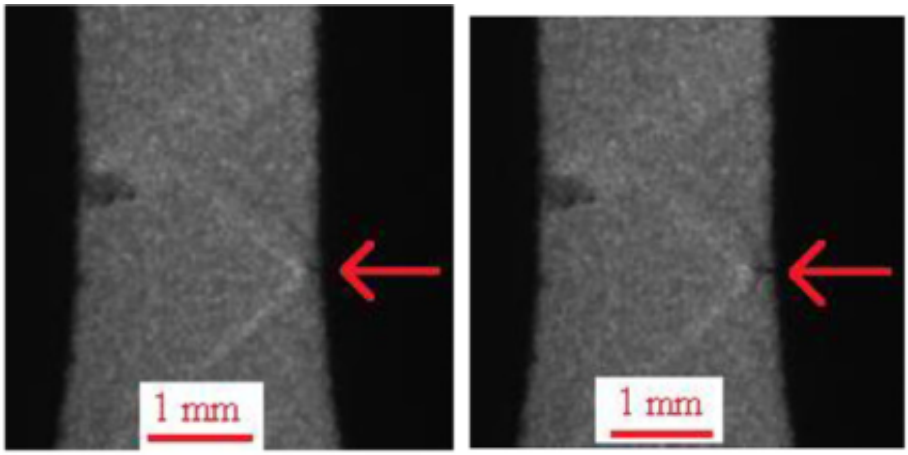

Magnified view of pattern 'e' crack length $d \approx 160\ \mu m$ (a)

Magnified view of pattern 'g' crack length $d \approx 260\ \mu m$ (b)

Figure 1.23: Detection of crack in the neighborhood of localization bands

1.4.3 Rate dependency - a thermo-mechanical competition

A temperature increase ranging up to about $\delta T \simeq 40$K (under adiabatic configuration) occurs at the band front concomitant with the phase transformation. As a major consequence, this heat emission tends to delay the forward transformation at the localization front. Meanwhile, because of the shear nature of the martensitic transformation, a stress concentration appears at the interface between the band and the matrix. This additional stress concentration accelerates the forward phase transformation at the front. The nucleation and the macroscopic broadening of the band results consequently from a competition between these two mechanisms.
[He and Sun, 2010] or [Shaw and Kyriakides, 1995] for instance have investigated the dependence of the localization phenomenon to the loading rate. As the transformation can be induced by temperature changes, the behavior is highly dependent on the competition between latent heat release and heat evacuation (by conduction and air convection). Indeed, if natural evacuation is too weak to compensate the released heat at the front of the band, the transformation is hampered. Thus a new localization band is nucleated at where the transformation is easier, for example, at the lowest temperature point of the sample [Shaw and Kyriakides, 1997]. Therefore, the number of bands is well linked to the thermal conditions and the loading rate. The following experimental law, established by [Zhang et al., 2010], associates the strain rate $\dot{\epsilon}$ with the maximum number of bands, denoted n_{max} :

$$n_{max} = C\dot{\epsilon}^m \tag{1.3}$$

$$C = \frac{1}{c\epsilon_{tr}^{max}} \tag{1.4}$$

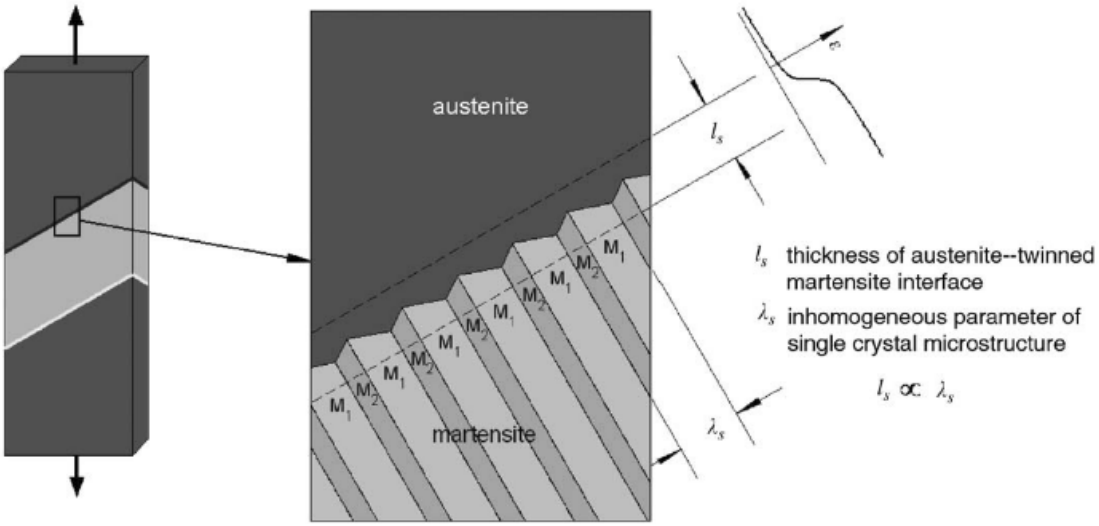

(a)

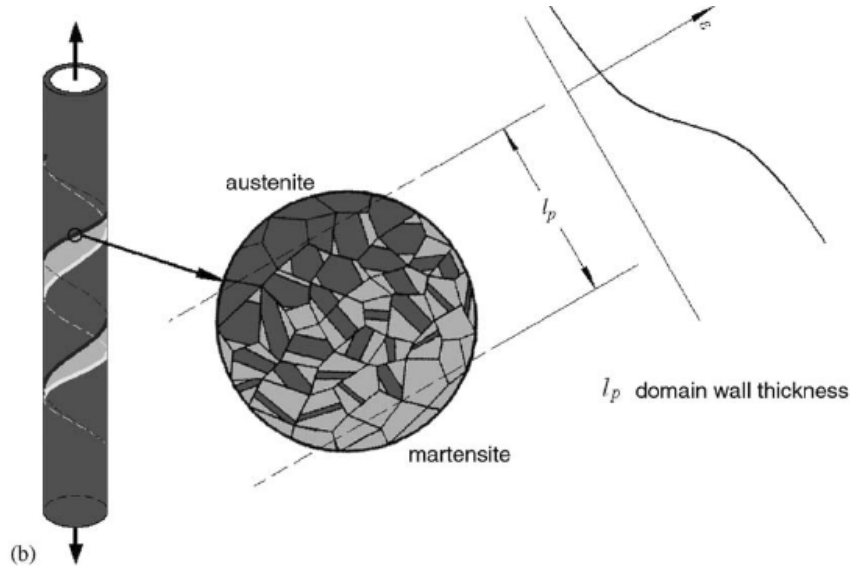

(b)

Figure 1.24: Schematic illustration of band front inside a single crystal (a) and a polycrystal (b).

where c is the velocity of the front propagation and ϵ_{tr}^{max} represents the maximum strain value observed inside the localization bands.
A numerical validation of this law has been proposed in [Depriester et al., 2014].

1.5 A short review of thermo-mechanical models of SMA

The specific behavior of SMA and potential industrial applications has drawn the attention of many researchers, leading to the intensive study of SMA behavior and modeling attempts in the last decades. Generally, three approaches are proposed to describe the thermomechanical phenomena in SMA.
First, macroscopic thermomechanical behavior can be obtained in the frame of the Generalized Standard Materials by using an average volume fraction of martensite and the associated mean transformation strain as internal variables [Boyd and Lagoudas, 1996],[Auricchio and Lubliner, 1997],[Liang and Rogers, 1997],[Lexcellent et al., 2002]. This approach addresses exclusively macroscopic scale but laws obtained are in general consistent with thermodynamics and experimental observations.
The second approach considers the phase transformation at the single crystal scale via an appropriate modeling and uses a scaling process to derive the macroscopic behavior by minimizing the associated energy. By performing this type of energy minimization, the local-scale modeling aims at establishing a direct link between the hysteretic response and the underlying events at different spatial-temporal scales. This approach supposes a more fundamental understanding concerning the nature of hysteresis phenomena such as meta-stability, micro-instability, material heterogeneity or grain-size induced hysteresis [Patoor et al., 2006] [Sun and He, 2008] [Maynadier et al., 2011].
The third approach is a mixture between the aforementioned two approaches, seeking to describe the hysteresis phenomena in SMA by adopting the concept of thermodynamic driving force, acting at the boundary between two phases or as an assembly of variants. The force must overcome (bypass) a level-set germination barrier to propagate. In this type of description, the width of an hysteresis loop is directly related to the magnitude of the germination barrier [Lagoudas et al., 2006] [Lagoudas et al., 2016].

1.5.1 Macroscopic approach

In the following, the works of [Lexcellent et al., 2002] and [Boyd and Lagoudas, 1996] are briefly introduced to give readers a general idea about these phenomenological models.

Phenomenological model proposed by [Lexcellent et al., 2006].

The model of [Lexcellent et al., 2006] is based on the experimental identification of the phase transformation surface. Within the framework of the thermodynamics of irreversible processes, two internal variables are chosen: the stress-induced martensite volume fraction z_σ and the self-accommodating martensite volume fraction z_T.
In this model, the martensite is partitioned into a self-accommodating martensite (MT) obtained by pure cooling and a stress-induced martensite (MS) obtained by pure mechanical loading. Let index the austenite thermomechanical properties as $\alpha = 1$, the self-accommodating martensite properties as $\alpha = 2$ and the stress-induced martensite properties as $\alpha = 3$. They correspond to three possible phases.
A representative volume element (RVE) composed of the three phases is considered. The equilibrium between these three phases that composes the RVE is described by the following variables:

- $\underline{\epsilon_\alpha}$ the total strain tensor of each partition ($\alpha = 1, 2, 3$);
- T the temperature;
- z_α volume fraction of each partitions;
- H_k a set of internal variables, representing the RVE internal pattern rearrangements at the micro-scale level.
- z_A, z_T and z_σ represent the volume fractions of each phase.

The total thermodynamic potential of RVE writes as:

$$\phi(\underline{\epsilon_\alpha}, T, z_\alpha, H_k) = z_A\phi_A + z_T\phi_T + z_\sigma\phi_\sigma + \nabla\phi \tag{1.5}$$

$$\nabla\phi = z_A(1 - z_A)\phi_{it}(T) + z_T z_\sigma \phi^m_{it}(T) \tag{1.6}$$

$$\phi_{it}(T) = u_0 - Ts_0 \tag{1.7}$$

$$\phi^m_{it}(T) = u^m_0 - Ts^m_0 \tag{1.8}$$

where ϕ_α is the specific Gibbs free energy potential after Legendre transformation (see subsection 2.2.2), The exact form of $\nabla\phi$ remains an open problem since it strongly depends on the incompatibilities between the martensite platelets and between M and A phases. ϕ_{it} and ϕ^m_{it} define the free energy density for A and M. u_0

and u_0^m define the internal energy at the reference temperature for A and M. s_0 and s_0^m define the entropy at the reference temperature for A and M.

Deriving from Clausius-Duhem inequality, the intrinsic dissipation can be expressed as follow:

$$D = \pi_\sigma^f \dot{z}_\sigma + \pi_T^f \dot{z}_T \geq 0 \tag{1.9}$$

where π_T^f and π_σ^f represent the thermodynamic forces associated with M nucleation and reorientation.

At this step, three important events should be investigated:

a pure thermal action $A - M_T$, $\dot{z}_\sigma = 0$, so $D = \pi_T^f \dot{z}_T \geq 0$

$$A \rightarrow M_T, \text{ if } \dot{z}_T \geq 0 \tag{1.10}$$

$$M_T \rightarrow A, \text{ if } \dot{z}_T \leq 0 \tag{1.11}$$

b pure stress action $A - M_\sigma$, $\dot{z}_T = 0$, so $D = \pi_\sigma^f \dot{z}_\sigma \geq 0$

$$A \rightarrow M_\sigma, \text{ if } \dot{z}_\sigma \geq 0 \tag{1.12}$$

$$M_\sigma \rightarrow A, \text{ if } \dot{z}_\sigma \leq 0 \tag{1.13}$$

c Pure reorientation of self-accommodating M platelets under a pure stress action. $M_T \rightarrow M_\sigma$:

$$\dot{z}_\sigma = -\dot{z}_T \text{ and } D = \pi_{T\sigma} \dot{z}_\sigma \geq 0 \tag{1.14}$$

where $\pi_{T\sigma}$ is the thermodynamic force associated with the reorientation

Herein, the model parameters defining the thermodynamical force during forward and backward transformation are identified experimentally. Required parameters are summarized as follows:

M_s and A_s : identify the forward and backward transformation start temperature at stress free state respectively;

σ_{M_s} and σ_{A_s} : concerning the pseudo-elastic behavior, the stress thresholds at which the forward and the reverse transformations are initiated at a given temperature T;

σ_{xx}, σ_{yy} : the stress states defining the initial reorientation threshold of M phase.

These experimental parameters permit to estimate the six modeling parameters: $\delta u_0, \delta s_o, u_0, s_0, \overline{u}_0^m, \overline{s}_0^m$

A consistent constitutive frame for the reverse phase transformation has been derived within the context of the generalized standard materials theory using non-associated approach. This phenomenological model takes into account the asymmetry between the tension and compression behaviors. Consequently, the numerical simulation of the anisothermal SMA behavior under multiaxial proportional loading is in good agreement with experimental results, at least for the forward transformation. However this model does not take into account of the thermomechanical coupling (*i.e.* the heat dissipation/absorption associated with phase transformation).

Phenomenological model proposed by [Boyd and Lagoudas, 1996].

The system is partitioned in three phase ($\alpha = 1, 2, 3$), where $\alpha = 1$ represents the self-accommodating martensite, $\alpha = 2$ the stress-induced martensite and $\alpha = 3$ the austenite, . This model adopts a similar description as in [Lexcellent et al., 2006], using generalized standard materials equations: it begins with the definition of the overall thermodynamic potential of the system, then the thermodynamic forces acting on the each volume fraction. Forces can be derived from the application of the second principle of thermodynamics. However, as the major drawback of most macroscopic models, numerous parameters are required to define each thermodynamic force. Most of them can be experimentally obtained from macroscopic measurements of stress, strain, temperature and resistivity. Simultaneous transformation and reorientation can be modeled by considering separated deformation rate tensors $\dot{\boldsymbol{\epsilon}}_t$ and $\dot{\boldsymbol{\epsilon}}_r$ in the dissipation inequality. The internal state variable for kinematic hardening is assumed to be the total irreversible strain, $\boldsymbol{\epsilon}^{irr}$.

Both macroscopic and phenomenological models proposed by [Boyd and Lagoudas, 1996] and [Lexcellent et al., 2006], can be relatively easily implemented inside Finite Element codes such as Cast3m or Abaqus. However, due to their ad-hoc and phenomenological nature, relationships between macroscopic response, fundamental material properties and evolution of microstructure during thermomechanical loading are not provided. Extension to thermomechanical-coupled multiaxial loading requires new parameters and a complex identification of the transformation thresholds.

1.5.2 Multiscale approaches

Multiscale approaches seek to describe phase transformation at local scale, and construct a macroscopic response through a progressive homogenization. The multiscale

models proposed by [Patoor et al., 1996] and [Siredey et al., 1999] are detailed in this subsection. By describing the internal residual stress across interface between A and M phases, this model grants a very realistic microscopic description of the martensitic transformation under an heterogeneous stress field condition.

Multiscale model proposed by [Patoor et al., 1996] and [Siredey et al., 1999].

In this model, a grain with volume V and boundary ∂V is considered as the RVE. Inside this RVE, several parts at position $\mathbf{r}$ undergo transformation strain $\boldsymbol{\epsilon}_t(\mathbf{r})$.

With the a-prior knowledge of an habit plane normal $\mathbf{n}'$, the displacement magnitude g, the displacement direction $\mathbf{m}$, the transformation strain can be given as:

$$\boldsymbol{\epsilon}_t = \frac{g}{2}(\mathbf{m} \otimes \mathbf{n}' + \mathbf{n}' \otimes \mathbf{m}) \tag{1.15}$$

The free energy densities in the RVE consist of the following contributions:

- The elastic strain energy density $w(\mathbf{r})$:

$$w(\mathbf{r}) = \frac{1}{2}\sigma_{ij}(\mathbf{r})\epsilon_{ij}(\mathbf{r}) = \frac{1}{2}\boldsymbol{\sigma}(\mathbf{r}) : \boldsymbol{\epsilon}_e(\mathbf{r}) \tag{1.16}$$

  where $\boldsymbol{\sigma}(\mathbf{r})$ represents the local stress field and $\boldsymbol{\epsilon}_e(\mathbf{r})$ is the elastic strain field;

- The chemical free energy density $\phi(\mathbf{r})$
- Interfacial energy dH: which is related with the austenite-martensite interfaces as well as the martensite-martensite ones.[4]

For a unit volume V inside the RVE, the total free energy density writes as :

$$\Phi = \frac{1}{V}\left[\int_v w(\mathbf{r})dv + \int_v \phi(\mathbf{r})dv\right] \tag{1.17}$$

In the vicinity of temperature equilibrium, the chemical potential is frequently linearized as:

$$\frac{1}{V}\int_v \phi(\mathbf{r})dv = -B(T - T_0)f_i \tag{1.18}$$

where f_i indicates the volume fraction of the martensite variant i (defining volume V), B is a material parameters and T_0 the reference temperature.
By decomposing the stress field into the macroscopic stress $\boldsymbol{\Sigma}$ and the internal stress $\boldsymbol{\tau}$, the total energy densities of the considered RVE can be written as:

$$\frac{1}{V}\int_v w(\mathbf{r})dv = \frac{1}{2}(\boldsymbol{\epsilon}_{ij} - \boldsymbol{\epsilon}^t_{ij}) : \mathbb{C}_{ijkl} : (\boldsymbol{\epsilon}_{kl} - \boldsymbol{\epsilon}^t_{kl}) - \frac{1}{2V}\int_V \boldsymbol{\tau}_{ij}(\mathbf{r})\boldsymbol{\epsilon}^t_{ij}(\mathbf{r})dv \tag{1.19}$$

[4] martensite-martensite interface component is usually neglected in the case of PE shape memory alloys

With the interaction energy W_{int} expressed as follows:

$$W_{int} = \frac{1}{2V}\int_V \boldsymbol{\tau}_{ij}(\mathbf{r})\boldsymbol{\epsilon}^t_{ij}(\mathbf{r})dv \tag{1.20}$$

By assuming that inside each A and M domains of RVE, variants are compatible, the mere source of internal stress is located at the interface, respecting the following equation:

$$[\boldsymbol{\sigma}] = -\mathbb{Q} : [\boldsymbol{\epsilon}] \tag{1.21}$$

where $[\boldsymbol{\sigma}], [\boldsymbol{\epsilon}]$ represent the stress and strain discontinuities along the normal direction of the interface, and $\mathbb{Q}$ is the interfacial operator proposed by [Hill, 1983]. Moreover, experimental observations showed that two principal variants have to grow up to form interface between domains. As a result, the internal energy can be reduced to the following simplified form (m and n indicate the number of the variant; f_m and f_n are their volume fraction):

$$W_{int} = -\sum_m \sum_n \frac{1}{2} f_m f_n H_{mn} \tag{1.22}$$

Using this formulation of total free energy potential for RVE, [Siredey et al., 1999] proposed to use the Kuhn-Tucker condition to derive the driving force F_i acting on each variants' volume fractions: L denotes the Lagrangian of the complementary free energy, aiming to minimize the total energy potential inside the RVE and respect physical constraints:

$$L(\boldsymbol{\Sigma}, T, \{f_i\}) = \sum_i \Phi_i f_i - \lambda_0(\sum_i f_i - 1) - \sum_i \lambda_i f_i \tag{1.23}$$

$$F_i = \frac{\partial L}{\partial f_i} \tag{1.24}$$

$$F_i = 0, \forall i \rightarrow f_i = \arg\min L \tag{1.25}$$

λ_0 and λ_i are Lagrange multipliers. They are defined by:

$$\lambda_0(\sum_i f_i - 1) = 0 \tag{1.26}$$

$$\lambda_i f_i = 0 \quad \forall i \tag{1.27}$$

If and only if one transformation force F_i reaches a critical value, the transformation may progress on variant i.

The model proposed by [Patoor et al., 1996] and [Siredey et al., 1999] is a multiscale and a multivariant model; based on the estimation of residual stress across the interface, the interaction matrix H_{mn} can be built. The transformation force F_i increases when the volume fraction f_i increases, causing a continuous strain hard-

ening effect. This multiscale model permits to describe the principal specificities of SMA's behavior: pseudoelasticity, temperature influence, asymmetrical tension-compression behavior. In terms of experimental validations, this multiscale model shows a good qualitative agreement with the experimental results carried out under uniaxial loading and allows an appropriate modeling of the initial multiaxial transformation threshold.

1.5.3 Comparison between several models

In general, no model permits to describe all aspects of SMA behavior especially regarding the hysteretic thermo-mechanical behavior. For macroscopic phenomenological model, the number of parameters to be identified is quite numerous, and the lack of description at lower scales is a strong limitation of these models. Multiscale models are probably more physical, their implementation involving a progressive homogenization of RVE inside any FE code to perform a structure calculation remains unreachable yet.
The second approach has been adopted during the work of [Maynadier, 2012] and [Fall, 2017], by using a uniform stress hypothesis and a Boltzmann type distribution to estimate the volume fraction of A phase and M variants under a complex thermomechanical loading configuration (this model will be recalled in chapter 2). The main drawback of this approach was that Boltzmann distribution applies in a reversible thermodynamic framework: out-of equilibrium phenomena during phase transformation were not taken into consideration. This approach however was able to model multiaxial loading effects in an appropriate way.

1.6 NiTi SMA

The SMA can be classed into overall three categories based on their chemical compositions:

- Iron based SMAs, e.g: Fe-Mn-Si;
- Copper based SMAs, e.g : Cu-Zn-Al and Cu-Al-Ni;
- NiTi-based SMAs, e.g: equiatomic NiTi ;

Iron-based and copper-based SMA, such as Fe-Mn-Si, Cu-Zn-Al and Cu-Al-Ni, are relatively low-cost and commercially available. However, due to their mechanical instability, brittleness [Cederstrom, 1995] [Hodgson et al., 1990] and poor thermo-mechanical performance [Huang, 2002], few industrial applications have been developed. NiTi-based SMA are more preferable for most applications despite their

higher cost.

Hence in this thesis, the motivation to focus our study on the equiatomic NiTi is twofold: firstly, as already presented, NiTi based alloys are the most used SMA for industrial applications; secondly, depending on their forming process and the fluctuation in their chemical composition, the NiTi alloy can exhibit or not the presence of an intermediate phase (so called R phase). Thus this alloy system will serve as an excellent test case to build a numerical model which can be generalized to all classical SMA.

All the experimental tools and numerical model achieved in this PhD thesis can be applied to all types of SMA with martensitic transformation. In this work, it is applied in the case of a quasi equiatomic Ni-50.2(at %)Ti alloy. 1D and 2D NiTi specimens (2mm thick sheets) have been provided by NiTi-France (http://www.nitifrance.com/v2/fr.html)

In the following sections, several details concerning the NiTi SMA as the support of this thesis to are given, including:

- Crystalline properties;
- Texture and morphology;
- Chemical and mechanical properties.

1.6.1 Crystal lattice, Bain matrix, transformation strain

Equiatomic Nickel-Titanium alloy undergoes a two-step phase transformation : B2 (cubic) to R (Rhombohedral) to B19' (Monoclinic) (see Figure 1.3). To illustrate the calculation of transformation matrix, the crystal lattice change between A and M (as illustrated in Figure 1.25) is chosen.
We select the lattice vectors of the A and M phase to be the edges of the tetragonal and monoclinic cells, respectively.

Hence, for austenite (lattice parameter a_0):

$$\begin{aligned} \mathbf{e}_1^a &= a_0(0,1,1)^T \\ \mathbf{e}_2^a &= a_0(0,-1,1)^T \\ \mathbf{e}_3^a &= a_0(1,0,0)^T \end{aligned} \tag{1.28}$$

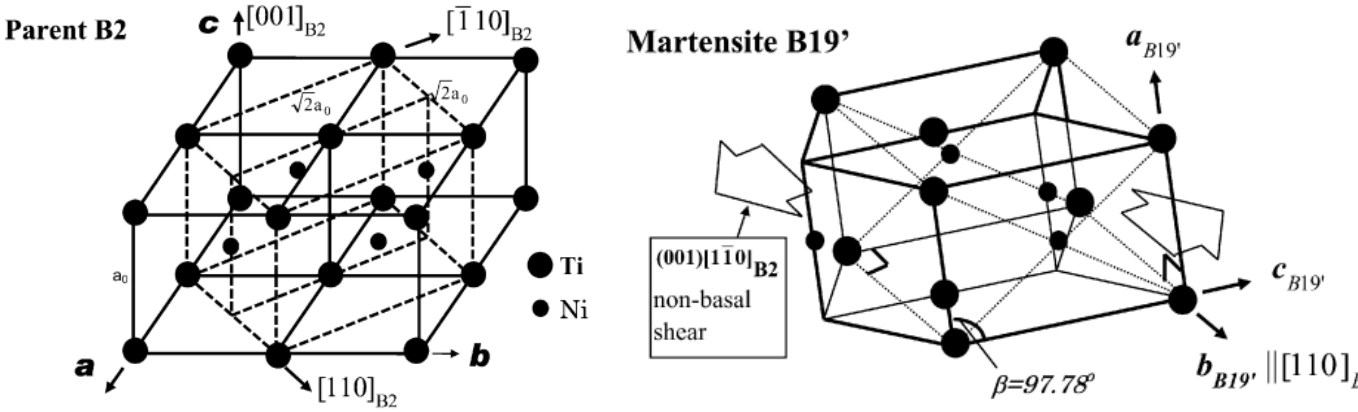

Figure 1.25: Structure relationship between parent phase B2 and monoclinic martensite B19' [Otsuka and Wayman, 1999]

and for martensite (lattice parameters a, b, c and β):

$$\begin{aligned}
\mathbf{e}_1^m &= \frac{c}{\sqrt{2}}(\sqrt{2}\cos\beta, \sin\beta, \sin\beta)^T \\
\mathbf{e}_2^m &= \frac{b}{\sqrt{2}}(0, -1, 1)^T \\
\mathbf{e}_3^m &= a(1, 0, 0)^T
\end{aligned} \tag{1.29}$$

The transformation matrix for variant 1, $\mathbf{T}_1$, allows the passage:

$$\mathbf{e}^m = \mathbf{T}^1 \mathbf{e}_j^a \tag{1.30}$$

This matrix is not symmetrical according to the definition of the transformation matrix (see the work of [Bhattacharya et al., 2003]). It can be decomposed into:

$$\mathbf{T_1} = \mathbf{Q_1}\mathbf{U_1} \tag{1.31}$$

where $\mathbf{Q}_1$ is a rotation matrix and $\mathbf{U}_1$ is denoted as the *Bain matrix* and describes the homogeneous transformation that takes the lattice from one phase towards another at microscopic scale. $\mathbf{U}_1$ is positive, defined and symmetrical.

Bain matrices of different NiTi SMA phases. Following this procedure for our example where $\mathbf{T}_1$ is defined by Equation 1.31, the axis of monoclinic symmetry in the martensite is along the edge axis marked in Figure 1.25 which comes from a $\langle 111 \rangle$ direction. With this convention, we can show that Bain matrix associated with B2→B19' can be expressed as follows:

$$\mathbf{U}_1 = \begin{bmatrix} \gamma & \epsilon & \epsilon \\ \epsilon & \alpha & \delta \\ \epsilon & \delta & \alpha \end{bmatrix} \tag{1.32}$$

where

$$\begin{aligned}
\gamma &= \frac{a(\sqrt{2}a + c\sin\beta)}{a_0\sqrt{2a^2 + c^2 + 2\sqrt{2}ac\sin\beta}} \\
\epsilon &= \frac{ac\cos\beta}{\sqrt{2}a_0\sqrt{2a^2 + c^2 + 2\sqrt{2}ac\sin\beta}} \\
\alpha &= \frac{1}{2\sqrt{2}a_0}\left(\frac{c(c + \sqrt{2}a\sin\beta)}{\sqrt{2a^2 + c^2 + 2\sqrt{2}ac\sin\beta}} + b\right) \\
\delta &= \frac{1}{2\sqrt{2}a_0}\left(\frac{c(c + \sqrt{2}a\sin\beta)}{\sqrt{2a^2 + c^2 + 2\sqrt{2}ac\sin\beta}} - b\right)
\end{aligned} \tag{1.33}$$

We list herafter three different transformations that are of great interest in the study of NiTi SMA.

Bain matrix for austenite.
Since austenite has the highest crystal symmetry and by convention, its Bain matrix is the identity matrix:

$$\mathbf{U}_A = \begin{bmatrix} 1 & 0 & 0 \\ 0 & 1 & 0 \\ 0 & 0 & 1 \end{bmatrix} \tag{1.34}$$

Bain matrix for martensite.
Table 1.1 describes the cubic (A phase) to Monoclinic (M phase) transformation for the 12 variants of NiTi SMA.

$U_1 = \begin{bmatrix} \gamma & \epsilon & \epsilon \\ \epsilon & \alpha & \delta \\ \epsilon & \delta & \alpha \end{bmatrix}$	$U_2 = \begin{bmatrix} \gamma & -\epsilon & -\epsilon \\ -\epsilon & \alpha & \delta \\ -\epsilon & \delta & \alpha \end{bmatrix}$	$U_3 = \begin{bmatrix} \gamma & -\epsilon & \epsilon \\ -\epsilon & \alpha & -\delta \\ \epsilon & -\delta & \alpha \end{bmatrix}$	$U_4 = \begin{bmatrix} \gamma & \epsilon & -\epsilon \\ \epsilon & \alpha & -\delta \\ -\epsilon & -\delta & \alpha \end{bmatrix}$
$U_5 = \begin{bmatrix} \alpha & \epsilon & \delta \\ \epsilon & \gamma & \epsilon \\ \delta & \epsilon & \alpha \end{bmatrix}$	$U_6 = \begin{bmatrix} \alpha & -\epsilon & \delta \\ -\epsilon & \gamma & -\epsilon \\ \delta & -\epsilon & \alpha \end{bmatrix}$	$U_7 = \begin{bmatrix} \alpha & -\epsilon & -\delta \\ -\epsilon & \gamma & \epsilon \\ -\delta & \epsilon & \alpha \end{bmatrix}$	$U_8 = \begin{bmatrix} \alpha & \epsilon & -\delta \\ \epsilon & \gamma & -\epsilon \\ -\delta & -\epsilon & \alpha \end{bmatrix}$
$U_9 = \begin{bmatrix} \alpha & \delta & \epsilon \\ \delta & \alpha & \epsilon \\ \epsilon & \epsilon & \gamma \end{bmatrix}$	$U_{10} = \begin{bmatrix} \alpha & \delta & -\epsilon \\ \delta & \alpha & -\epsilon \\ -\epsilon & -\epsilon & \gamma \end{bmatrix}$	$U_{11} = \begin{bmatrix} \alpha & -\delta & \epsilon \\ -\delta & \alpha & -\epsilon \\ \epsilon & -\epsilon & \gamma \end{bmatrix}$	$U_{12} = \begin{bmatrix} \alpha & -\delta & -\epsilon \\ -\delta & \alpha & \epsilon \\ -\epsilon & \epsilon & \gamma \end{bmatrix}$

Table 1.1: Bain matrices of the 12 martensite variants associated with B2 → B19' transformation.

Bain matrix for R phase.

There are four lattice correspondence variants in B2 → B19' transition according to the lattice relationship as shown in Figure 1.3. Assuming that the length of the sides of cubic and trigonal unit cells is same, the transition can be solely described by the rhombohedral angle β and the deformation matrices in B2 coordinates are listed in Table 1.2 which describes the cubic (A phase) to Rhombohedral (R phase) transformation for the 4 variants of NiTi SMA.

$U_{R_1} = \begin{bmatrix} \eta & \delta & \delta \\ \delta & \eta & \delta \\ \delta & \delta & \eta \end{bmatrix}$	$U_{R_2} = \begin{bmatrix} \eta & -\delta & -\delta \\ -\delta & \eta & \delta \\ -\delta & \delta & \eta \end{bmatrix}$	$U_{R_3} = \begin{bmatrix} \eta & \delta & -\delta \\ \delta & \eta & -\delta \\ -\delta & -\delta & \eta \end{bmatrix}$	$U_{R_4} = \begin{bmatrix} \eta & -\delta & \delta \\ -\delta & \eta & -\delta \\ \delta & -\delta & \eta \end{bmatrix}$

Table 1.2: Bain matrices of the four R phase variants; other examples of materials undergoing a B2→R transformation are available in [Zhang and Sehitoglu, 2004].

$$\text{where } \eta = (\sqrt{1+2\cos\beta}+2\sqrt{1-\cos\beta})/3 \text{ and } \delta = (\sqrt{1+2\cos(\beta)}-\sqrt{1-\cos\beta})/3$$

Crystal parameters of equiatomic NiTi SMA The crystal lattice values reported in Table 1.3 have been taken from literature. Austenite (a_0) and Martensite (a, b, c, M_β - M_β denotes angle β for martensite) values are taken from the work of [Bhattacharya et al., 2003] ($\alpha = 1.0243$, $\gamma = 0.9563$, $\delta = 0.058$, $\epsilon = -0.0427$); and

R phase parameters (R_β - it denotes Rhombohedral angle β) are taken from [Zhang and Sehitoglu, 2004], with $\eta = 0.998$ and $\delta = -0.0131$.

Crystal parameters	a_0 (Å)	a (Å)	b(Å)	c(Å)	M_β(deg)	R_β(deg)
	3.015	2.889	4.12	4.622	96.8	91.5

Table 1.3: Crystal parameter for A, M and R phase [Bhattacharya et al., 2003]

Transformation strain The transformation strain from austenite to austenite is obviously null. The transformation strain tensors for R and M phases can be obtained as the Green-Lagrange tensors attached to each transformation matrix:

$$\boldsymbol{\epsilon}_A^{tr} = 0 \tag{1.35}$$

$$\boldsymbol{\epsilon}_i^{tr} = \frac{1}{2}(\mathbf{U}_i^T\mathbf{U}_i - \mathbf{I}) \tag{1.36}$$

where i refers to a variant (either M or R phase) and $\mathbf{U}_i$ is the associated Bain matrix.

1.6.2 Texture and morphology

Crystallographic texture

Observations by Scanning Electron Microscope (**SEM**) and Electron Back-Scattered Diffraction (**EBSD**) analyses have been performed over the surface $S = 1\,\mathrm{mm}^2$ of a NiTi SMA sheet after diamond polishing and electro-polishing. The pole figure and inverse pole figure are reported in Figure 1.26 and Figure 1.27. They clearly illustrate an isotropic transverse texture with a $\langle 111 \rangle$ pole along the normal direction to the sheet. This texture may result in a quite isotropic behavior for stress-controlled experiments loaded in a direction belonging to the sheet plane.

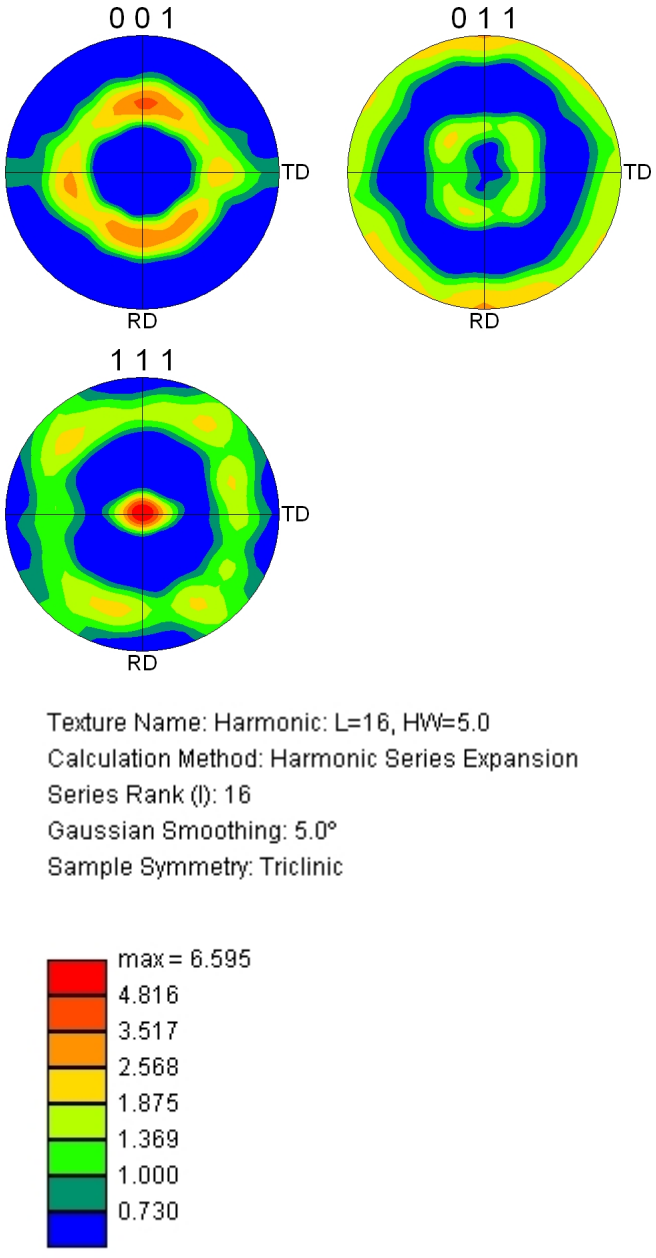

Figure 1.26: Pole figures obtained via EBSD and associated scale.

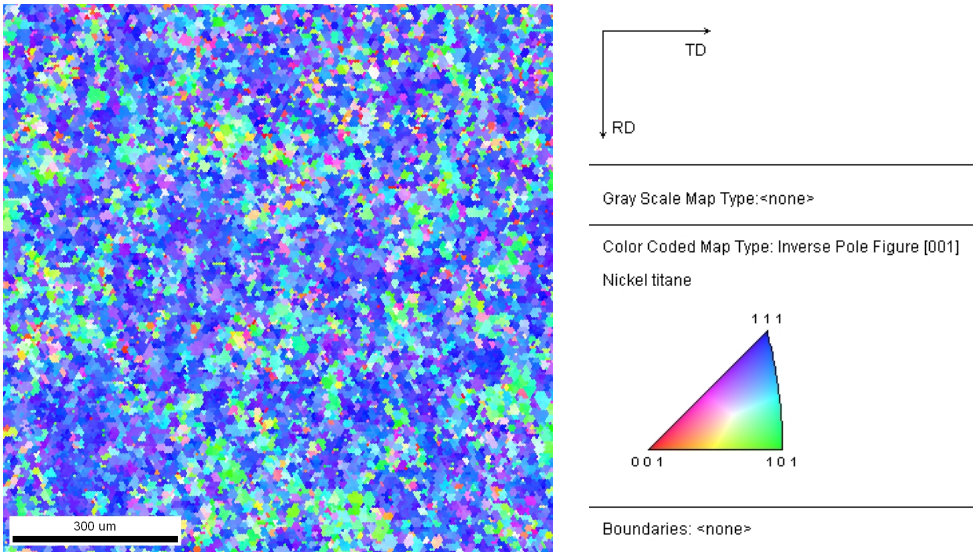

Figure 1.27: Inverse pole figure (representing orientations normal to the sheet plane) obtained via EBSD

Average Grain size

As seen in Figure 1.28, EBSD analysis also grants to measure the average surface of grains inside the investigated windows. Hence we observe that the overall distribution of grain varies between $8\,\mu m \leq d \leq 40\,\mu m$, with an average value of about $d \simeq 15\,\mu m$. Area defined in Figure 1.27 and associated EBSD data can therefore be considered as representative of the material. They will define the RVE of the multiscale model introduced in chapter 2.

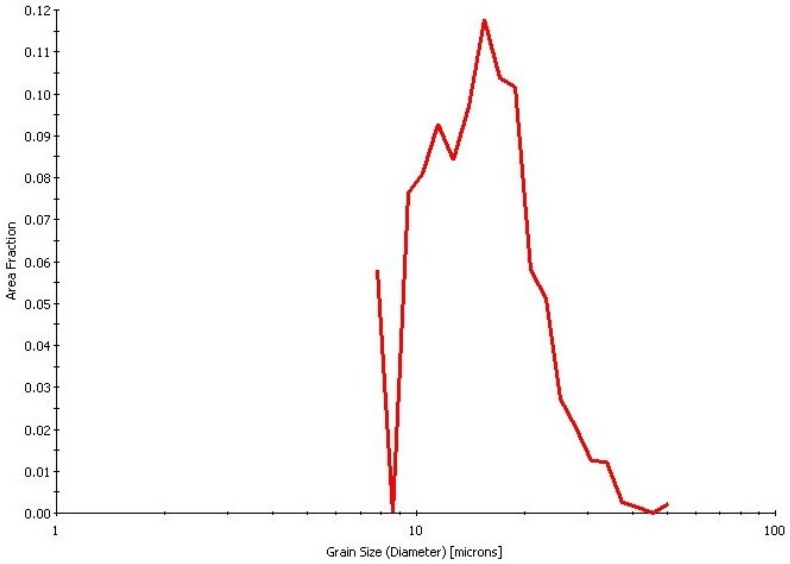

Figure 1.28: Grain size distribution

1.6.3 Thermochemical properties

The DSC (differential scanning calorimetry), consists in measuring the difference in heat flux between a specimen and a reference (often an empty crucible) at stress free state, and aims to determine the chemical properties of the material:

- Specific heat capacity c_p ;
- Phase transformation properties, including transition temperatures T_{tr}, associated latent heat ΔH and variations of entropy s and enthalpy h densities.

The DSC analysis is conducted over a small sample (8.4 mg) taken from a virgin specimen of NiTi SMA. A quasi-static thermal cycle is applied as illustrated in Figure 1.29 :

- Isothermal at $T = 373K$ for 10 min;
- Cooling from $T = 373K$ to $T = 193K$ with a temperature rate of $\dot{T} = 5\,\mathrm{K\,min^{-1}}$;
- Isothermal at $T = 193K$ for 10 min;
- Heating from $T = 193K$ to $T = 373K$ with a temperature rate of $\dot{T} = 10\,\mathrm{K\,min^{-1}}$;

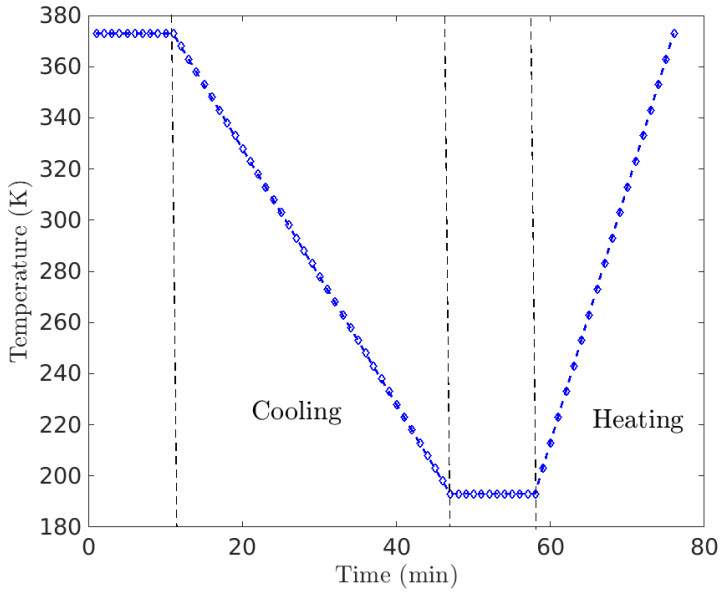

Figure 1.29: Applied quasi-static thermal cycle

Specific heat capacity.
Without phase transformation, the difference measured in heat flux between specimen and the reference can be interpreted as the heat required by the material to

maintain the temperature variations, which helps us to identify the specific heat capacity of the specimen:

$$\begin{aligned} p &= \dot{q} = \rho c_p \dot{T} \\ c_p &= \frac{p}{\rho \dot{T}} \end{aligned} \tag{1.37}$$

where p represents the heat flux difference without phase transformation and ρ is the mass density.

The specific heat capacity of A, R and M phases in NiTi SMA are nearly close. For simplicity reasons, we will assume for calculations that the three phases share the same specific heat capacity:

$$c_p^A = c_p^M = c_p^R = c_p \tag{1.38}$$

Thermal hysteresis and presence of A, R and M phase.
The results of the DSC analysis confirms the existence of A , R and M phases for different temperature ranges. As we can see in Figure 1.30, two significant heat flux peaks are observed during the cooling stage. They correspond to the A→R and R→M phase transformations. Only one significant heat flux peak is observed during the heating stage. It may be possible that the backward transformation M→A passes through the intermittent formation of the R phase.

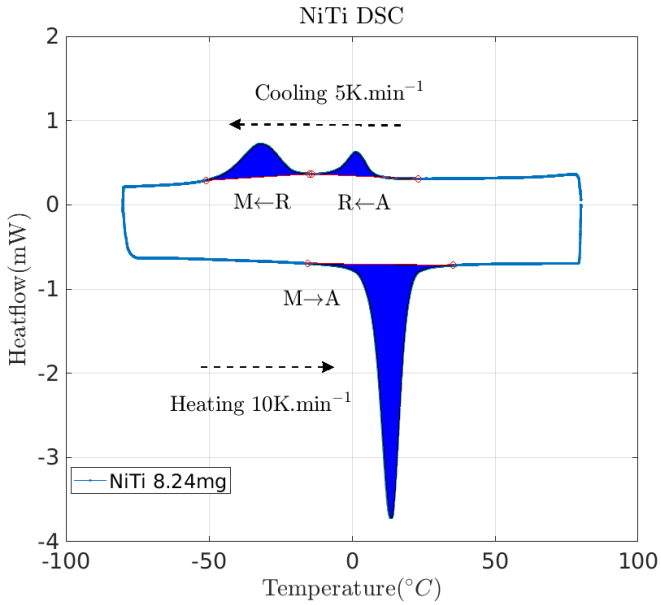

Figure 1.30: DSC: Heat flow as function of temperature

Latent heat.

Latent heat (or enthalpy of transition) is defined as an additional quantity of heat exchanged between external heat source and analyzed specimen to maintain the same reference command temperature during the phase transformation. Herein the raw curve[5] of heat flux as function of time during cooling is used to explain the protocol:

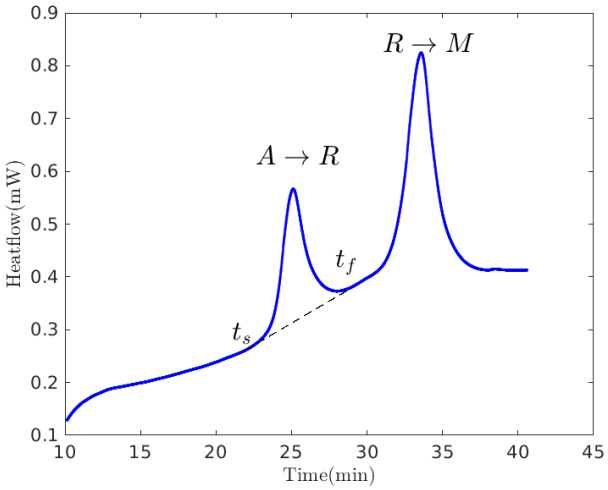

Figure 1.31: Determination of latent heat Δh: example of NiTi SMA during DSC (cooling).

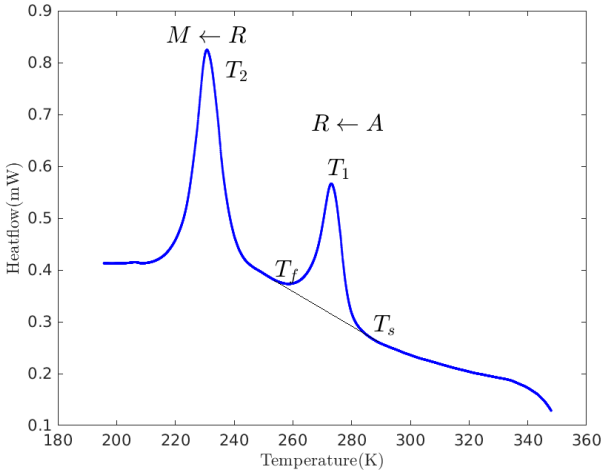

Figure 1.32: Transformation temperature and entropy variations: example of NiTi SMA during DSC (cooling).

[5]before baseline correction

As illustrated in Figure 1.31, by defining the transformation start and finish time (or temperature), the specific latent heat Δh can be calculated as follows:

$$\Delta h = \frac{1}{V} \int_{t_s}^{t_f} p(t) dt \tag{1.39}$$

where $p(t)$ represents the additional heat flux (mW) required by the specimen to ensure the phase transformation. V is the volume of material used for the DSC.

Transformation temperature and variation of entropy.
Usually, the transformation temperature is defined at the point where the additional heat flux reaches its maximum during the DSC measurement. As shown in Figure 1.32, T_1 represents the transformation temperature during the cooling from A $\rightarrow$ R and T_2 represents the transformation temperature during the cooling from R $\rightarrow$ M. Given the transformation temperatures, the variation in entropy density can be expressed as follows:

$$\Delta s = \frac{\Delta h}{T_{tr}} \tag{1.40}$$

Temperature of transition start.
The temperature of transformation start T_s illustrated in Figure 1.32 indicates the onset of phase transformation $A \rightarrow R$, implying that the R phase chemical potential is at least equal or lower than A phase chemical potential (otherwise, this type of phase transformation would not even occur). On the contrary, the transformation temperature where the maximum heat flux is measured can be related to the germination energy and some metastable kinetic effects as they will be introduced in chapter 2. Nonetheless, the transformation temperature is not discarded because it gives the definition of the entropy density's variation.

Parameters	Symbol	Value
Specific entropy of martensite	s_m	$0.24\,\mathrm{MJ\,m^{-3}}$
Specific entropy of R phase	s_r	$0.62\,\mathrm{MJ\,m^{-3}}$
Specific entropy of Austenite	s_a	$0.76\,\mathrm{MJ\,m^{-3}}$
Latent heat density $A \to R$	$\Delta h(A \to R)$	$40(9)\,\mathrm{MJ\,m^{-3}}$
Latent heat density $A \to M$	$\Delta h(A \to M)$	$138(12)\,\mathrm{MJ\,m^{-3}}$
Specific heat capacity	c_p	$460\,\mathrm{J\,kg^{-1}\,K^{-1}}$
Temperature of transformation start for $A \to R$	T_s^{A-R}	285 K
Temperature of transformation start for $R \to M$	T_s^{R-M}	260 K

Table 1.4: NiTi SMA chemical parameters identified by DSC

1.6.4 Elastic mechanical properties

Elastic mechanical properties have been identified via a tensile test performed on a 1D strip specimen of Ni-Ti alloy using digital image correlation (DIC) (see chapter 3). The central region used for DIC is a parallelepiped volume, *i.e.* $10 \times 3 \times 0.3\mathrm{mm}^3$. Longitudinal and transversal average deformations have been extracted at several stress levels (material remaining austenitic). The engineering stress expresses as follows:

$$\sigma_{xx} = \frac{F}{S_0} \tag{1.41}$$

where F is the axial force recorded by the force cell of the loading machine and S_0 is the initial section of NiTi strip (see Figure 3.4b).

The longitudinal and transverse averaged stress-strain curves are plotted in Figure 1.33. The basic elastic properties (Young modulus and Poisson ratio) can be easily calculated by considering the material as isotropic and homogeneous. Values are reported in Table 1.5. For simplicity reasons, elastic properties will be considered

identical for all phases.

$$E_Y = \frac{\sigma_{xx}}{\epsilon_{xx}}$$
$$\nu = -\frac{\epsilon_{yy}}{\epsilon_{xx}} \tag{1.42}$$

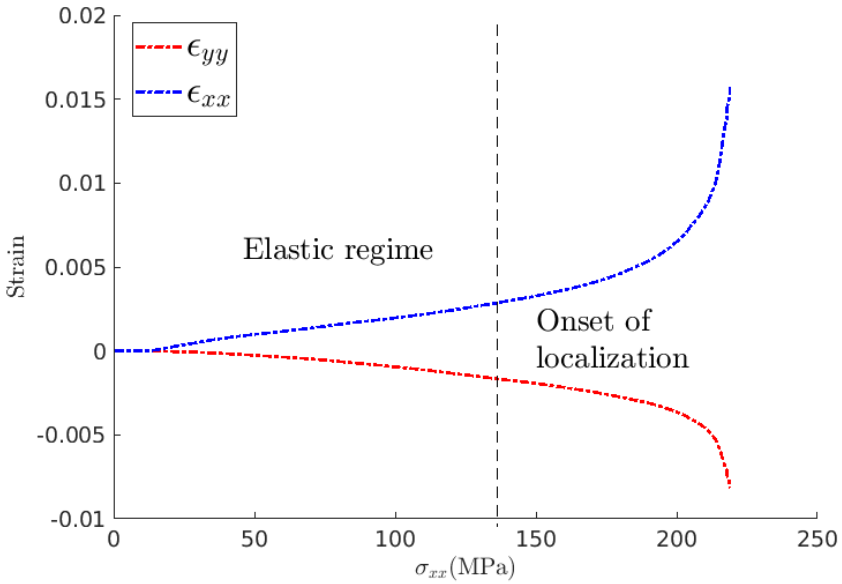

Figure 1.33: Longitudinal strain ϵ_{xx} and transversal strain ϵ_{yy} as function of engineering stress σ_{xx} for 1D NiTi SMA strip

Parameters	Symbol	Value
Young modulus	E_Y [GPa]	60 ± 9
Poisson ratio	ν	0.31 ± 0.02

Table 1.5: Elastic parameters identified by 1D tensile testing

1.7 Conclusion - challenges and outline of the PhD thesis

Overall challenges regarding SMA and NiTi SMA in particular can be divided into two aspects:

Challenges in numerical modeling.
The main features that make the modeling of SMA difficult are:

- Phase transformations are out-of equilibrium phenomena, as evidenced by the hysteretic character of the transitions.

- Latent heat of martensite transformation modifies the temperature in the neighborhood, and as a result, prevents the transformation to propagate. Associated with heat exchange as boundary conditions, localization can occur at different points leading to highly contrasted slender structures [Shaw and Kyriakides, 1997][Maynadier, 2012][Huang et al., 2017].

In addition to these difficulties, any model should be able to predict and simulate various key aspects of the SMA thermomechanical behavior:

- Hysteretic and thermomechanical coupling behavior (*i.e.* velocity effect, anisothermal conditions, etc) at the mesoscopic scale and below.

- Multiaxiality: proportional and non-proportional multiaxial loading in the context of reorientation and anisothermal condition.

- Structure model is required to predict any structural response of SMA specimen (*i.e.* strip, dogbone, etc) under simple or complex loading configurations.

Challenges in experimental validation.
Even for a 1D SMA strip specimen under uniaxial quasi-static loading, the localization phenomenon at the macroscopic scale is the consequence of a competition between thermomechanical coupling effects, temperature, and strain heterogeneity. Collecting the information over the spatial distribution of phases, temperature, and strain heterogeneity is crucial for the validation of any structural modeling of SMA. As a result, it is of considerable interest to have a spontaneously and continuous global full-field observation of phase, strain and temperature field during a mechanical uniaxial or multiaxial loading, in a either isothermal or anisothermal configuration.

This PhD study aims at addressing these above-mentioned challenges. Therefore we propose the following organization:

- In chapter 2, we aim to construct a multiscale hysteretic model at the grain and variant scale. This will be integrated in a homogenization procedure from the grain scale to the polycrystal scale to properly simulate the whole thermomechanical behavior of any SMA.

- In chapter 3, we aim to capture the spatial-temporal kinematic field evolution of NiTi SMA during uniaxial and multiaxial loading, under either isothermal or anisothermal configurations.

- In chapter 4, for the purpose of future structural modeling and validation, an in-situ, multiview, and multi-instrumented (X-ray diffraction and digital images correlation) setup has been developed to make a full-field observation of kinematic and phase field evolution of 1D/2D NiTi SMA specimen under uniaxial and multiaxial, proportional or non proportional loading. The protocol of phase field reconstruction by Proper Orthogonal Decomposition based on X-ray diffraction signals (POD-XRD) will be explained in detail.

Chapter 2

Multiscale stochastic modeling of SMA materials

Reproduced from

Contents

2.1 Introduction

This chapter is an out of equilibrium extension of the multiscale models initially proposed by [Maynadier, 2012] and [Fall, 2017]. It is organized as follows: in section 2.2, the different scales involved are first recalled. Gibbs free energy density is introduced as representative of the energy level of each variant i. An energetic stochastic formulation is introduced next: master equation and metastability are presented in order to describe the evolution of a metastable SMA system towards equilibrium. In section 2.3, the kinetic Monte-Carlo framework is proposed to give a robust response of the master equation under metastable situations and its extension is also presented to take account of a potential thermomechanical coupling at the RVE scale. In section 2.5, an implementation of the kinetic Monte Carlo framework is described. Protocols of identification of the germination energy and the intrinsic characteristic relaxation time via DSC are explained. Several virtual tests are simulated at the end of this chapter section 2.6. They are compared to various experimental results reported in the literature.

2.2 Boltzmann system and master equation at the grain scale

2.2.1 Multiscale approach

Based on the various features concerning martensite transformation at different spatial scales as presented in section 1.2, any pertinent multiscale model should be able to describe properly the mechanism of martensite transformation at variant scale, monocrystal and polycrystal scale. Hence the proposed scale passage implemented inside this model can be visualized as in Figure 2.1.

Microstate. The grand philosophy of the multiscale model can be summarized as follow: *Any considered system can be characterized by its microscopic states, defined at lower scale.*

Certainly, the choice of microstate is largely dependent to the choice of the considered system. For instance, we can consider a polycrystal to be an assembly of single crystals randomly oriented and consider a single crystal as an assembly of different phases and each phase can be seen as an assembly of variants. The only important principle is that, we need to be able to describe individually the evolution of each microstate.

Scale organization

The scale organization is illustrated in Figure 2.1, from the variant scale to RVE scale. The idea of the multiscale approach is to use the volume fraction of variant i at time t in a phase ϕ ($f_\phi(i,t)$) or a grain gr ($f_{gr}(i,t)$), to describe the physical quantities at different scales by some appropriate averaging operations. A multiscale approach supposes on the other hand an appropriate *localization* of the loading. This step is strongly simplified in the present section by using an hypothesis of homogeneous loading.

For the case of a SMA, a single crystal or grain gr is supposed to be composed of several phases ϕ (Austenite, Martensite, etc). Hereafter, i denotes a variant meaning that a phase ϕ may be composed of different variants i depending on the crystal symmetry. Variant i is the lowest scale. A single crystal may contain n different types of variants i in total (sum of all variants in all phases), $i = 1, 2, \cdots n$.

For simplicity consideration, a unified variant to grain (counting all variants for all phase) scale passage is then used :

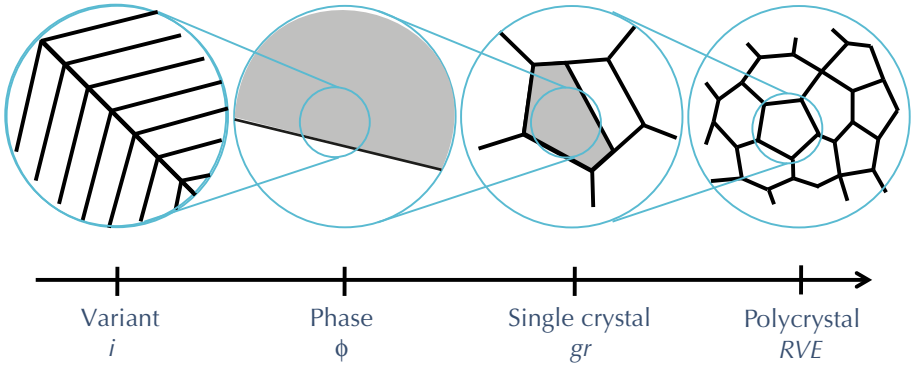

Figure 2.1: Scales involved in the multiscale modeling of SMA from variant to polycrystal scales.

Standard Unit, the microstate of SMA grain.

A Standard Unit (SU) is used to define the statistic volume (V_u) of microstate at the grain (phase) scale. Each SU is characterized by a unique crystal-lattice configuration i.

Due to the diffusionless nature of martensitic transformation, at time instant t, the total population of SU inside the grain is considered as fixed and noted as N. In the meantime, the total volume occupied by variant i can be described by a number $N_i(t)$ of unit volume V_u too. Indeed $N_i(t)$ is time dependent, due to the variant to variant or the phase to phase transition. As for grain, this volume may be occupied by a fraction of each variant i at time instant t, written simply as $f(i,t)$, leading to a discrete definition of the volume fraction of variant i at the grain scale::

$$N = \sum_{i=1}^{n} N_i(t) \tag{2.1}$$

$$f_{gr}(i,t) = \frac{N_i(t)}{N} \tag{2.2}$$

with respect to the physical admissibility

$$\sum_{i=1}^{n} f_{gr}(i,t) = 1 \tag{2.3}$$

Consequently, based on the definition of microstate as SU volume , the discrete volume fraction of each type of variant i, $f_{gr}(i,t)$ is a statistic description of the monocrystal, which helps us to define the current 'macroscopic' state of considered system .

It is assumed in the following that a SMA system always *seeks* to minimize its overall energy. Hence, an energetic approach is proposed to describe the dynamic

evolution of the variants' volume fraction as function of thermal and mechanical loading. The Gibbs free energy densities are used to quantify the energy of each variant i at variant scale.

2.2.2 Definition of the Gibbs free energy density at the variant scale

The first principle given at the local scale states that the total energy density composed of kinetic energy and internal energy densities [$\mathrm{J\,m^{-3}}$] can only be modified by the action of external work and heat flux. The internal energy density at the variant scale is written as $\mathfrak{u}$. At constant velocity, kinetic energy remains as a constant. There is a direct relationship between the variation of internal energy density and heat sources:

$$d\mathfrak{u}(i,s,\boldsymbol{\epsilon}) = dh(i) + T(i)ds(i) + \boldsymbol{\sigma}(i) : d\boldsymbol{\epsilon}(i) \tag{2.4}$$

This expression is composed of:

- $dh(i)$: chemical energy variation= bound energy variation inside a variant;
- $T(i)ds(i)$: heat quantity variation (thermal power), function of entropy variation ds (second law of thermodynamics) and local temperature T;
- $\boldsymbol{\sigma}(i) : d\boldsymbol{\epsilon}(i)$: mechanical energy variation (mechanical power), function of deformation variation $d\boldsymbol{\epsilon}$ and local stress $\boldsymbol{\sigma}$.

The free (Helmholtz) energy density $\psi(i)$ is the result of the Legendre transformation of the internal energy density by a heat quantity. It allows the energy variation to be defined as function of the temperature variation instead of the entropy variation:

$$\psi(i,T) = u(i,s) - T(i)s(i) \tag{2.5}$$

The Gibbs free energy (or free enthalpy) is the result of the Legendre transformation of Helmholtz energy density by a mechanical quantity. It allows finally the energy variation to be defined as function of the stress variation instead of the deformation variation.

$$\mathfrak{g}(i,T,\boldsymbol{\sigma}) = \psi(i,T) - \boldsymbol{\sigma}(i) : \boldsymbol{\epsilon}(i) \tag{2.6}$$

Variation of Gibbs free energy density is given by:

$$d\mathfrak{g}(i,T,\boldsymbol{\sigma}) = dh(i) - s(i)dT(i) - \boldsymbol{\epsilon}(i) : d\boldsymbol{\sigma}(i) \tag{2.7}$$

A second order Taylor expansion of entropy leads to derive $s(i)$ as function of temperature T, reference entropy s_0 at the reference temperature T_0, mass density ρ and specific heat capacity c_p:

$$s(i,T) = s_0(i,T_0) + \rho(i)c_p(i)\log(\frac{T_0(i)}{T(i)}) \tag{2.8}$$

On the other hand, in the framework of small perturbation hypothesis, we wish to consider the total deformation $\boldsymbol{\epsilon}(i)$ as a sum of elastic $\boldsymbol{\epsilon}_e(i)$, thermal $\boldsymbol{\epsilon}_{th}(i)$ and transformation $\boldsymbol{\epsilon}_{tr}(i)$ deformations associated with the phase transition. The total deformation at the variant scale i can be expressed as function of stress, temperature and $\boldsymbol{\epsilon}_{tr}(i)$ (considered as a *free* deformation) following:

$$\boldsymbol{\epsilon}(i,T,\boldsymbol{\sigma}) = \mathbb{C}^{-1}(i) : \boldsymbol{\sigma}(i) + \frac{\alpha_v(i)}{3}(T(i) - T_0(i))\boldsymbol{I} + \boldsymbol{\epsilon}_{tr}(i) \tag{2.9}$$

$\mathbb{C}(i)$ is the local stiffness tensor, $\alpha_v(i)$ is the local volumetric dilatation coefficient and $\boldsymbol{I}$ the second order identity tensor. The transformation strain $\boldsymbol{\epsilon}_{tr}$ is usually considered to be stress independent (and here is assumed to be so).
Gibbs free energy density is finally expressed after integration as a formal sum of thermal part $\mathfrak{g}_t(i,T)$, mechanical part $\mathfrak{g}_m(i,\boldsymbol{\sigma})$ and coupled thermomechanical part $\mathfrak{g}_{tm}(i,T,\boldsymbol{\sigma})$.

$$\mathfrak{g}(i,T,\boldsymbol{\sigma}) = \mathfrak{g}_t(i,T) + \mathfrak{g}_m(i,\boldsymbol{\sigma}) + \mathfrak{g}_{tm}(i,T,\boldsymbol{\sigma}) \tag{2.10}$$

with

$$\mathfrak{g}_t(i,T) = h(i) - s_0(i)T(i) - \rho(i)c_p(i)\left[T(i) - T_0(i) + T(i)ln\left(\frac{T(i)}{T_0(i)}\right)\right] \tag{2.11}$$

$$\mathfrak{g}_m(i,\boldsymbol{\sigma}) = -\frac{1}{2}\boldsymbol{\sigma}(i) : \mathbb{C}^{-1}(i) : \boldsymbol{\sigma}(i) - \boldsymbol{\sigma}(i) : \boldsymbol{\epsilon}_{tr}(i)$$

$$\mathfrak{g}_{tm}(i,T,\boldsymbol{\sigma}) = -\frac{\alpha_v(i)}{3}(T(i) - T_0(i))tr(\boldsymbol{\sigma}(i))$$

where $tr(\boldsymbol{\sigma})$ denotes the trace of the stress tensor.

The main simplifications that can be made at this step concern the ad-hoc loading. We will consider in the following that:

- stress is supposed as homogeneous over the RVE, leading to: $\boldsymbol{\sigma}(i) = \boldsymbol{\sigma}$;
- temperature is considered homogeneous over the RVE, leading to: $T(i) = T$;

- stiffness, mass density, specific heat capacity and dilatation coefficient are considered constant for all phases and variants: $\mathbb{C}(i) = \mathbb{C}$, $\rho(i) = \rho$, $c_p(i) = c_p$ and $\alpha_v(i) = \alpha_v$.

The Gibbs free energy density simplifies into:

$$\mathfrak{g}(i, T, \boldsymbol{\sigma}) = h(i) - s_0(i)T - \rho c_p \left[T - T_0 - T \ln\left(\frac{T}{T_0}\right)\right] - \frac{1}{2}\boldsymbol{\sigma} : \mathbb{C}^{-1} : \boldsymbol{\sigma} \\ -\boldsymbol{\sigma} : \boldsymbol{\epsilon}_{tr}(i) - \frac{\alpha_v}{3}(T - T_0)tr(\boldsymbol{\sigma}) \quad (2.12)$$

Assuming that stress and temperature are homogeneous inside the considered system, Boltzmann stochastic system is a pertinent candidate to describe the tendency of energy minimization through the evaluation of the Master equation.

2.2.3 Philosophy of the stochastic approach

Following a stochastic perspective, for any system, its history of evolution from any out-of-equilibrium state towards the state of equilibrium can be described by the probability functions in the space of volume fraction (the 'state' space). In order to do that, the first important requirement for a stochastic approach is to establish **the evolution law** towards the so-called 'equilibrium' for the system based on a-prior knowledge about probability functions. A secondary requirement is to evaluate **the intrinsic time** or the characteristic relaxation time. And the final requirement is to justify whether **the equilibrium can be achieved or not under certain conditions (metastability/germination barrier)**.

In order to have a response to all these questions, the first task to be fulfilled is to formulate properly probability function in the space of volume fraction. When the evolution of system is purely **Markovian**, indicating that for the state of system at time $t + dt$, it only depends on the probability distribution at time t. Under such circumstances, a simple probability equation, the so-called 'Master equation', can be used to study the dynamic evolution of the considered system.

2.2.4 Boltzmann system and master equation

In Boltzmann stochastic theory, a Boltzmann system is referred as a specific system consisting of N different independent units (N Standard units), where each unit has no interaction with others and the total population of units remains unchanged (diffusionless). The equilibrium state presenting the state of energy minimum, the evolution of Boltzmann system and its equilibrium can be achieved through the Master equation (see Equation 2.14).

Formulations For simplicity reasons, we first consider a system containing one standard unit $N = 1$. This simple system may contain n discrete Gibbs free energy levels at time instant t, $(\mathfrak{g}(i,t), i = 1, 2 \cdots n)$. Consequently the conservation of population in terms of standard unit can be expressed as:

$$\sum_{i=1}^{n} \frac{df(i,t)}{dt} = 0 \tag{2.13}$$

As a result, the temporal variation of variant i's volume fraction at time t, $\frac{df(i,t)}{dt}$, can be calculated via the Master equation, which is defined by the following system of equations:

$$\begin{aligned}
&\frac{df(i,t)}{dt} = -f_{\mathrm{d}}(i,t) + f_{\mathrm{b}}(i,t) \\
&\frac{df(i,t)}{dt} = -\sum_{j=1,j\neq i}^{n} \mathrm{Tr}(i,j) f(i,t) + \sum_{j=1,j\neq i}^{n} \mathrm{Tr}(j,i) f(j,t) && (2.14) \\
&f_{\mathrm{b}}(i,t) = \sum_{j=1,j\neq i}^{n} \mathrm{Tr}(j,i) f(j,t) && (2.15) \\
&f_{\mathrm{d}}(i,t) = \sum_{j=1,j\neq i}^{n} \mathrm{Tr}(i,j) f(i,t) && (2.16) \\
&\mathrm{Tr}(i,j) = \min(1, c_{ij} \exp(-\beta_s(\mathfrak{g}(j,t) - \mathfrak{g}(i,t)))) \\
&\beta_s = \frac{V_u}{k_b T} && (2.17)
\end{aligned}$$

$\frac{df(i,t)}{dt}$ indicates the temporal increment of variant i's volume fraction, which is determined by the difference between birth amount $f_{\mathrm{b}}(i,t)$ and death amount $f_{\mathrm{d}}(i,t)$;

$f_{\mathrm{b}}(i,t)$ and $f_{\mathrm{d}}(i,t)$ are the birth and death amount of variant i's volume fraction. These two amounts are both determined by the transition probability function $\mathrm{Tr}(i,j)$ and the current volume fraction of the system $f(i,t)$ (Equation 2.15 and Equation 2.16);

$\mathrm{Tr}(i,j)$ is the transition probability, defining the probability for variant i to transform towards variant j;

β_s is a parameter that defines the severity of transformation (Equation 2.16). It is calculated from the unit volume V_u, current temperature T and Boltzmann constant k_b;

c_{ij} is the transformation rate of variant i towards variant j.

Markov Convention In order to simplify the Master equation, we decide to adopt the Markov convention. The Markov transition matrix $M(i,j)$ is thus introduced, verifying:

$$\begin{aligned} M(i,j) &= \mathrm{Tr}(i,j), \forall (i,j), i \neq j \\ M(i,i) &= -\sum_{j=1}^{n} \mathrm{Tr}(j,i) \end{aligned} \tag{2.18}$$

It is introduced in Equation 2.14 allowing to get the following expression:

$$\frac{df(i,t)}{dt} = \sum_{j=1}^{n} M(j,i) f(j,t) \tag{2.19}$$

Through the description of the temporal variation of volume fraction, the Master equation is the main tool to estimate the dynamic evolution of any system. This relationship applies at the unit volume scale as well as at the grain scale. Without the presence of heterogeneous residual stresses, the grain can be considered as a typical Boltzmann stochastic system. This point is addressed in subsection 2.2.5 and subsection 2.2.7.

2.2.5 Previous modeling

In the modeling proposed by [Maynadier, 2012] and [Fall et al., 2016], β_s is considered to be a constant (temperature independent). Moreover, it is assumed that the Boltzmann system is always at the thermodynamic equilibrium so that we get at the grain scale:

$$\frac{df_{\mathrm{gr}}(i,t)}{dt} = 0, \ \forall i = 1, \cdots, n \tag{2.20}$$

When the Boltzmann system is at equilibrium, it is by nature extensive, meaning that N standard units possess the exact same variant volume fractions as 1 standard unit (Equation 2.21 and Equation 2.22). At the equilibrium state, for the system containing 1 standard unit, the volume fraction of each variant $f(i,t)$ equals the probability of presence for variant i, (prob(i,t)), whereas the Boltzmann distribution is the unique and converged solution of (Equation 2.23).

$$f_{gr}(i,t) = f_{N=1}(i,t), \ \forall i = 1, \cdots, n \tag{2.21}$$

$$\frac{df_{gr}(i,t)}{dt} = \frac{df_{N=1}(i,t)}{dt} = 0, \ \forall i = 1, \cdots, n \tag{2.22}$$

$$f_{N=1}(i,t) = \mathrm{prob}(i,t) = \frac{\exp(-\beta_s \mathfrak{g}(i,t))}{\sum_{i=1}^{n} \exp(-\beta_s \mathfrak{g}(i,t))} \tag{2.23}$$

Despite these strong hypotheses, a pretty good prediction of transformation threshold of Ni-Ti SMA alloy under multiaxial stress condition was obtained, as a good qualitative estimation of phase composition under thermal loading. However, due to the thermodynamic equilibrium assumption, the thermomechanical behavior is reversible. An artificial germination energy barrier had to be introduced to produce only major hysteresis loops. Master equation provides a more natural modeling of hysteresis since the SMA system is considered as out of equilibrium.

2.2.6 Out-of-equilibrium phase transformation

Herein, we focus on the Boltzmann system containing 1 standard unit ($N = 1$). A generalization towards Boltzmann system at the grain scale consisting of N standard units would be addressed in subsection 2.2.7. Hysteresis phenomena are the macroscopic outcomes of time evolution for out-of-equilibrium microscopic systems, indicating that :

$$\frac{df(i,t)}{dt} \neq 0, \ \forall i \in [1, \cdots, n] \tag{2.24}$$

c_{ij} constants are consequently bounded (that determines indirectly the relaxation time):

$$0 \leq c_{ij} \leq \infty, \ \forall (i,j) \ i \neq j \tag{2.25}$$

In order to highlight the source of hysteresis when the system is out of equilibrium, the classic notion of meta-stability and associated transition probability are firstly reviewed.

Meta-stability and Transition probability

We seek to compare the Gibbs free energy density of three chosen variants i, j and k. Their Gibbs free energy is supposed given by the function plotted in Figure 2.2: variant i exhibits the lowest energy that corresponds to a 'stable' state; variant k has the highest Gibbs free energy that corresponds to an 'unstable' state; The intermediate variant j exhibits an intermediate energy level in a local minimum that corresponds to a 'metastable' state.

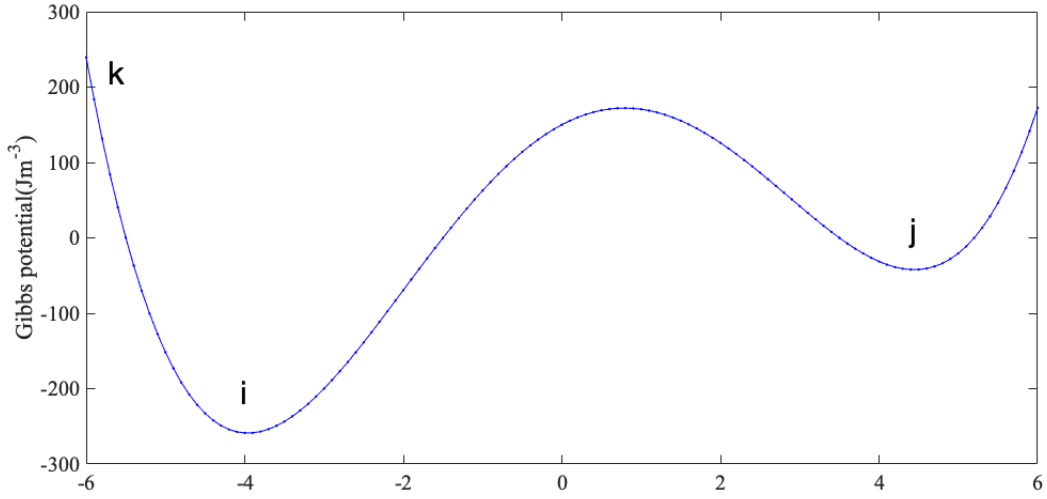

Figure 2.2: Schematic evolution of Gibbs free energy density in variant space (seen as a continuous function): illustration of unstable(k), stable(i) and metastable(j) variants.

The transition probability matrix $\mathrm{Tr}(i,j)$ helps us to define these different states in a stochastic way. Indeed, we get:

$$\mathrm{Tr}(i,j) = \mathrm{Tr}(i,k) = 0 \tag{2.26}$$

$$\mathrm{Tr}(k,i) = 1 \tag{2.27}$$

$$\mathrm{Tr}(j,i) = c_{ji} \exp(-\beta_s(\mathfrak{g}(i,t) - \mathfrak{g}(j,t)) \tag{2.28}$$

Equation 2.26 indicates that the transition probability for variant i to transform towards another variant is strictly 0. This state corresponds to the stable state and applies to variant i in Figure 2.2. On the contrary, when the variant k is unstable, the transition probability for variant k to transform towards stable variant i is strictly 1. Equation 2.27 illustrates this situation. Equation 2.28 applies for the metastable situation. Indeed, variant j *may* transform to variant i: the transition probability for variant j to transform towards stable variant i is consequently a constant between $[0,1]$.

Meta-stability and Germination energy density

For the case of martensite transformation, we propose to present meta-stability in a stochastic way:

a Unstable $\rightarrow$ stable : An unstable variant k transforms towards a stable variant i nearly immediately (see Equation 2.29).

$$\mathfrak{g}(k,t) \geq \mathfrak{g}(i,t) + d\mathfrak{g}(k,i,dt=0) \rightarrow \mathrm{Tr}(k,i) = 1 \rightarrow dt \ll t_r \tag{2.29}$$

b Meta-stable → stable : A meta-stable variant j can transform towards a stable variant i at time $t' = t + dt$ once it affords an additional energy $d\mathfrak{g}(j, i, dt)$ to ensure that the transition probability equals to one. However, when a variant i has a slight lower Gibbs free energy than a variant j, but the difference in Gibbs free energy can not be justified as a significant energy advantage, the system itself has to wait until a characteristic relaxation time $dt \geq t_r$, to make sure the accumulated transformation probability reaches 1 (see Equation 2.30).

$$\mathfrak{g}(i,t) + d\mathfrak{g}(j,i,t=0) \geq \mathfrak{g}(j,t) \geq \mathfrak{g}(i,t) \rightarrow dt \geq t_r, \text{ when } p_{acc}(dt) = 1 \quad (2.30)$$

where τ represents the first transformation time and t_r represents the typical relaxation time.
This additional germination energy term $dg(j, i, dt)$ can be divided into two parts (see Equation 2.31). We can identify these two parts using several simple DSC scans :

a $d\mathfrak{g}^c(dt)$: this term is the meta stable germination energy density, it decreases as function of time dt (see as Equation 2.32 and Equation 2.33)

b $d\mathfrak{g}^a(j, i)$: this term is the mechanical incompatibility related to the germination energy density between variant i and j (a same kind of germination energy associated with mechanical incompatibility has been proposed in [Siredey et al., 1999] and [Patoor et al., 2006])

$$d\mathfrak{g}(j,i,dt) = d\mathfrak{g}^c(dt) + d\mathfrak{g}^a(j,i) \quad (2.31)$$

$$d\mathfrak{g}^c(dt=0) = -\frac{\log(c_{ji})}{\beta_s} \quad (2.32)$$

$$d\mathfrak{g}^c(dt=\infty) = 0 \quad (2.33)$$

Saturation of hysteresis loop and temporal relaxation of germination energy

In the stochastic theory, when the variation of the Gibbs free energy density from variant j to variant i is overwhelmingly higher than the corresponding germination energy density, the transformation takes place immediately without any temporal delay. This transformation generates an incompressible energy loss associated with the predefined difference of Gibbs free energy between the two variants. In other words, for this type of configuration, the hysteresis loop is always saturated and remains constant (see Equation 2.32), ignoring any possible dynamic effect.

Otherwise, when the variation of the Gibbs free energy density from variant j to variant i is not high enough to achieve the immediate transformation, the

accumulation of transition probability with an increasing differential time interval $p_{acc}(j \to i, t' = t + dt)$, allows the transition to eventually occur. A time delay is consequently necessary to achieve the transformation. The associated energy loss is on the other hand lower in accordance with a lower Gibbs free energy difference, which is only related to the mechanical incompatibility between variants (see Equation 2.34 and Equation 2.35).

When an infinite time is considered and mechanical incompatibilities are neglected $d\mathfrak{g}^a(i,j) = 0, \forall(i,j)$, the system does not have theoretically to compensate any germination energy $d\mathfrak{g}(j,i)$ in order to achieve the transformation (see Equation 2.35).
Consequently the Boltzmann system can reach its equilibrium state leading to a reversible behavior (see Equation 2.36 and Equation 2.35). This point has been already addressed in subsection 2.2.5.

$$p_{acc}(j \to i, t' = t + dt) = \int_t^{t+dt} \mathrm{Tr}(j,i)dt \tag{2.34}$$

$$d\mathfrak{g}(j,i,dt = \infty) = 0 + d\mathfrak{g}^a(j,i) = 0 \tag{2.35}$$

$$p_{acc}(j \to i, t' = \infty) = \int_t^{\infty} \mathrm{Tr}(j,i)dt = 1 \tag{2.36}$$

Modified master equation

In order to take account of these above-mentioned metastable factors, the Master equation is being modified as follows to properly describe the evolution of the phase transformation at the grain scale:

$$\begin{aligned}
\widehat{\mathrm{Tr}}(i,j) &= \min(1, c_{ij}\exp(-\beta_s(\mathfrak{g}(j,t) - \mathfrak{g}(i,t) + d\mathfrak{g}^c(i,j)))) \\
M(i,i) &= -\sum_{j=1}^{n} \widehat{\mathrm{Tr}}(j,i) \\
M(i,j) &= \widehat{\mathrm{Tr}}(i,j), \forall(i,j), i \neq j \\
\frac{df(i,t)}{dt} &= \sum_{j=1}^{n} M(j,i)f(j,t)
\end{aligned} \tag{2.37}$$

where c_{ij} is the transformation rate and $d\mathfrak{g}^c(i,j)$ the germination energy density.

2.2.7 Numerical issues

When the system contains only 1 or a few standard units, the temporal evolution of the volume fraction of each variant can be analytically calculated from the implemented germination energy barrier via Equation 2.37.

However, it should be emphasized that when the system is out-of-equilibrium

and the germination energy is required to induce any phase transformation, the considered system is no longer stochastically extensive, in other word, the response of one SU can not represent the average response of the system. More precisely, at grain scale, when the system (grain) consists of N standard units, it is associated with n^N different levels of Gibbs free energy. To give a short example, for the grain at configuration ξ, which consists of N standard units (SU), and N_i is the sub-population of standard unit described by each variant i, the associated energy level can be expressed as :

$$\xi = [N_1, N_2, \cdots N_n], \text{ with } \sum_{i=1}^{n} N_i = N = \sum_{i=1} \xi(i) \tag{2.38}$$

$$\mathfrak{g}_{gr}(\xi, t) = \frac{1}{N} \sum_{i=1}^{n} N_{_i}(t) \mathfrak{g}_i(t) \tag{2.39}$$

The average Gibbs free energy density associated with configuration ξ, can be seen as probabilistic quantity where all linear combinations (n^N combination in total) should be tested to extract the *grand* probability function (i.e. the highest probability at infinite time instant $f_{grain}(i, t = \infty)$ corresponding to the combination where the average Gibbs energy density at the grain scale is minimized).
The master equation and volume fraction for variant i at grain scale can be written, considering two different possible configurations $\{\xi, \xi^*\}$:

$$\frac{d\hat{f}(\xi, t)}{dt} = \sum_{\xi^*=1}^{n^N} M(\xi, \xi^*)\, \hat{f}(\xi^*, t) \tag{2.40}$$

$$f_{gr}(i, t) = \sum_{1}^{n^N} \hat{f}(\xi, t) \frac{\xi(i)}{N} \tag{2.41}$$

where $\hat{f}(\xi, t)$ is the volume fraction of configuration ξ at time instant t.
The computation cost of the Master equation may grow very fast when a high number of SU are required to get a stochastic result. Classical procedures are consequently not relevant to solve the problem analytically. An alternative way can be therefore proposed, it is detailed in the next section.

2.3 Kinetic Monte-Carlo framework at grain scale

The use of Kinetic Monte-Carlo algorithm can be traced back to the early work of [Bortz et al., 1975] and [Daniel, 1976]. This algorithm is essentially a re-organization of former stochastic algorithms. By deploying the density of

transformation probability function, it accounts for the previous distribution of volume fractions and the state of Markov Transition Matrix (both at time instant t), to get the volume fractions at the next investigated time instant t'. Doing this way, we aim to evaluate the current state of the master equation at the given time t instead of solving analytically the Master equation itself. Based on these indirect observations, the temporal volume fraction variation is generated through the Kinetic Monte-Carlo framework in a stochastic way. After a sufficient number of repeated independent samplings, the stochastic average should converge towards the analytical response of the Master equation at the grain scale.

2.3.1 Transformation quantities and transformation weight

We first consider the initial time $t = t_0$. $f(i, t_0)$ is the initial volume fraction of variant i, inside a grain. Equation 2.14 gives the raw increase and decrease of the volume fraction of variant i:

$$\begin{aligned} \frac{df(i,t)}{dt} &= \sum_{j=1}^{n} M(j,i) f(j, t = t_0) \\ \frac{df(i,t)}{dt} &= \frac{df_b(i,t)}{dt} + \frac{df_d(i,t)}{dt} \end{aligned} \tag{2.42}$$

The raw transformation birth quantities $\zeta(t = t_0)$ are given by:

$$\zeta(t = t_0) = N \sum_{i=1}^{n} \frac{df_b(i,t)}{dt} \tag{2.43}$$

ζ evaluates the total number of variant transformed inside the Boltzmann system at instant $t = t_0$.
We seek next to obtain the weight of each transformation type inside ζ. Therefore $\gamma(j, i, t = t_0)$ in Equation 2.44 indicates the weight of transformation from $j \to i$ inside the total transformed quantities ζ at instant $t = t_0$.

$$\gamma(j, i, t = t_0) = N \frac{M(j,i) f(j, t = t_0)}{\zeta(t = t_0)} \tag{2.44}$$

$\zeta(t = t_0)$ and $\gamma(j, i, t = t_0)$ describe the global tendency of the master equation at instant $t = t_0$. These quantities indirectly indicate when the next transformation triggers and which variant is chosen to transform towards another in the Boltzmann system. These parameters can be denoted as the 'indirect observers' of the Boltzmann system. To describe directly the evolution of the volume fraction, two new concepts must be introduced: the first transformation time τ and the first transformation type μ.

2.3.2 First transformation time and first transformation type

First transformation time and *first transformation type* are two variables defining the stochastic Monte-Carlo step (τ, μ).

- τ is the first transformation time. It corresponds to the time delay needed for at least one SU inside the system transform from one variant to another for the time instant $t = t_0$.

- $\mu : j \to i$ is the first transformation type. It is evaluated when at least one SU is transformed. A μ type transformation is corresponding to a specific transformation of variant j towards variant i (since $i \neq j$, there are $n^2 - n$ possible transformation types).

Parameters (τ, μ) describe exactly the time delay for the first transformation and the associated transformation type.

Given the indirect observers of the Boltzmann system (ζ, γ), the transition probability to have a (τ, μ) transformation can be written as follows (mathematical demonstration available in [Daniel, 1976]):

$$p(\tau, \mu)d\tau = \gamma(\mu, t)\exp(-\zeta(t)\tau) \tag{2.45}$$

$$\gamma(\mu, t) = \gamma(j, i, t), \forall(i, j), i \neq j \tag{2.46}$$

where $p(\tau, \mu)d\tau$ indicates the probability at time t that a SU transforms in the time interval $[t + \tau, t + \tau + d\tau]$ inside a Boltzmann system consisting of N SU, and that this transformation is a μ type transformation.
For the seek of simplicity, Equation 2.46 is introduced and used throughout this section [1].

2.3.3 Procedure for random generation of (τ, μ)

As we mentioned in previous section, (τ, μ) are the two direct stochastic descriptors for the hysteretic behavior at the grain scale. The classical approach to generate the pair of variables based on probability function is referred as 'conditioning': $p(\tau, \mu)$ can be built through the product of two independent one-variable density of probability functions $p_1(\tau)$ and $p_2(\mu|\tau)$, where $p_1(\tau)$ and $p_2(\mu|\tau)$ indicate the probabilities of two cause-related events:

1. $p_1(\tau)$ measures whether or not at least one variant inside the system transforms into a different variant type in the differential time interval $[t, t + \tau]$.

[1] We reshape a matrix towards a vector by this numerical operation.

2. $p_2(\mu|\tau)$ is the conditional probability measuring when at least one variant inside the system transforms into a different variant type in the differential time interval $[t, t+\tau]$ following a μ type transformation.

These conditional probability functions can be estimated using the current transformation quantity $\zeta(t)$ and the associated transformation weight $\gamma(\mu, t)$ following:

$$p(\tau, \mu) = \gamma(\mu, t) \exp(-\zeta(t)\tau) = p_1(\tau)p_2(\mu|\tau) \tag{2.47}$$

$$p_1(\tau) = \sum_{\mu} p(\tau, \mu) = \exp(-\zeta(t)\tau)\zeta(t) \tag{2.48}$$

$$p_2(\mu|\tau) = \frac{\gamma(\mu, t)}{\zeta(t)} \tag{2.49}$$

In the work of [Daniel, 1976], it is demonstrated that the generation of τ and μ can be done separately based on $p_1(\tau)$ and $p_2(\mu|\tau)$ (see Equation 2.48 and Equation 2.49). The numerical implementation of random number generations (RNG) to produce (τ, μ) by using Inverse Monte Carlo technique is discussed in section A.1.

2.3.4 Kinetic Monte-Carlo framework

The basic idea of this computation procedure is to deploy the two-variables density of probability function $p(\tau, \mu)$ using a Monte-Carlo technique to generate the two stochastic descriptors (τ, μ) of the system at current time t. To begin with, we simplify the problem by neglecting the heat source (absorption or emission) impact due to phase transformation. With this simplification, the Kinetic Monte-Carlo algorithm at the grain scale is straightforward and can be summarized as follows (the corresponding KMC algorithm flowchart for a grain is shown in section 2.4):

Step 0: Set the time variable t at t_0. Define the total variant population N inside the grain system and initialize the volume fraction for each variant $f(i, t_0), i = 1, \cdots n$; Specify c_{ji} according to each type of transformation $\mu \to (j, i)$; Specify a series of *sampling time* and a stopping time: $t = t_1 < t_2 \cdots < t_n < \cdots t_{stop}$ with a time interval dt between each sampling time step; Reposition t in differential time interval $[t_{n-1}, t_n]$; Load the crystal texture then interpolate the Gibbs free energy density $g(i, t), i = 1, \cdots n$ for each variant at current time t in each grain;

Step 1: Using Equation 2.14, calculate $\zeta(t)$ and $\gamma(\mu, t)$ which collectively determine the density of transformation probability function $p(\tau, \mu)$ in Equation 2.45. Select a proper inverse Monte Carlo technique to generate one random pair (τ, μ) based

on the joint density probability function $p(\tau, \mu)$ pre-calculated at the previous step. An explicit random variable generation technique is used for this step. It is detailed in Appendix section A.1.

Step 2: Deploy the two random variables (τ, μ) obtained at the previous step, increment the current time t by τ, update the variant population involved in transformation $\mu : j \rightarrow i$.

$$\begin{aligned} t' &= t + \tau \text{ and } dt = \tau \\ df(\mu, t) &= M(j, i) f(j, t) \tau \\ f(i, t') &= f(i, t) + df(\mu, t) \\ f(j, t') &= f(j, t) - df(\mu, t) \\ t &= t' \end{aligned} \tag{2.50}$$

.

Step 3: If τ is higher than the sampling time interval $[t_m, t_{m+1}]$, increment t towards t_{m+1} keeping the volume fractions unchanged. If $t > t_{stop}$, return to Step 0 , otherwise return to Step 1.

Step 4: Perform N_s independent Kinetic Monte-Carlo repeated sampling; Obtain the stochastic average response for grain gr.

Concerning the last point, indeed, when a complex thermomechanical loading is applied, several variants may have the same level of Gibbs free energy at current time t, meaning that the activation of these transformation types are equiprobable. The KMC procedure will randomly choose a specific transformation type and move forward depending on the probability functions, leading to a final result that may have been different if another transformation type had been chosen. The solution is to multiply the KMC estimations $f_d(i, t)$ and process to a stochastic average $f_{st}(i, t)$ as defined in Equation 2.51. The result converges to the macroscopic solution $f_{sol}(i, t)$ when enough independent KMC samplings are performed.

$$f_{st}(i, t) = \lim_{N_s \rightarrow \infty} \frac{1}{N_s} \sum_{d=1}^{N_s} f_d(i, t) = f_{sol}(i, t) \tag{2.51}$$

An exact convergence criterium of the Monte-Carlo process cannot however be properly estimated (mentioned as stochastic fluctuation). The most discriminant situation is probably the simulation of a pure thermal loading (DSC scan for example), because all variants are equiprobable at the transformation temperature.

The simulation requires several independent samplings before reaching suitable the convergence (see Figure A.1).

2.3.5 Kinetic Monte-Carlo framework with additional heat source due to phase transformation

Heat emission or absorption are not considered in the previous sections. It is however possible to evaluate their effects by solving the heat equation and by using some admissible boundary conditions to mimic the anisothermal macroscopic behavior.
The heat equation in the framework of a stochastic approach can be derived as follows. We consider first a simple two phases (1,2) problem so that their volume fraction verifies $f_1 = 1 - \psi$,$f_2 = \psi$ and are consequently only given by the ψ parameter. As a result, volume fractions verify the physical admissibility:

$$f_1 + f_2 = 1 \tag{2.52}$$

The equilibrium is supposed to be changed by stress $\boldsymbol{\sigma}$ or temperature T as homogeneous quantities over the volume. Some complementary assumptions are used:

- homogeneous mass density ρ
- homogeneous stiffness $\mathbb{C}$
- homogeneous heat capacity c_p
- homogeneous thermal conductivity κ

The Gibbs free energy density of both phases is given by:

$$\begin{aligned} \mathfrak{g}_1 &= h_1 - Ts_1 - \frac{1}{2}\boldsymbol{\sigma} : \mathbb{C} : \boldsymbol{\sigma} - \boldsymbol{\epsilon}_1^{tr} : \boldsymbol{\sigma} \\ \mathfrak{g}_2 &= h_2 - Ts_2 - \frac{1}{2}\boldsymbol{\sigma} : \mathbb{C} : \boldsymbol{\sigma} - \boldsymbol{\epsilon}_2^{tr} : \boldsymbol{\sigma} \end{aligned} \tag{2.53}$$

The average Gibbs free energy density is simply given by:

$$\mathfrak{g} = f_1\mathfrak{g}_1 + f_2\mathfrak{g}_2 = \psi(\mathfrak{g}_2 - \mathfrak{g}_1) + \mathfrak{g}_1 \tag{2.54}$$

leading to:

$$\mathfrak{g} = \psi(\Delta h - T\Delta s - \Delta\boldsymbol{\epsilon}^{tr} : \boldsymbol{\sigma}) + h_1 - Ts_1 - \frac{1}{2}\boldsymbol{\sigma} : \mathbb{C} : \boldsymbol{\sigma} - \boldsymbol{\epsilon}_1^{tr} : \boldsymbol{\sigma} \tag{2.55}$$

where $\Delta h = h_2 - h_1$, $\Delta s = s_2 - s_1$ and $\Delta\boldsymbol{\epsilon}^{tr} = \boldsymbol{\epsilon}_2^{tr} - \boldsymbol{\epsilon}_1^{tr}$ are the enthalpy density variation, entropy density variation and transformation strain variation respectively. ψ is considered as an internal variable of the macroscopic problem. so that $\mathfrak{g} = \mathfrak{g}(\psi, \boldsymbol{\sigma}, T)$.
The total deformation $\boldsymbol{\epsilon}$, total entropy density s and thermodynamic force X associated with the volume fraction ψ are obtained thanks to:

$$\boldsymbol{\epsilon} = -\frac{d\mathfrak{g}}{d\boldsymbol{\sigma}} = \mathbb{C} : \boldsymbol{\sigma} + \psi\Delta\boldsymbol{\epsilon}^{tr} + \boldsymbol{\epsilon}_1^{tr} = f_1\boldsymbol{\epsilon}_1 + f_2\boldsymbol{\epsilon}_2 \tag{2.56}$$

$$s = -\frac{d\mathfrak{g}}{dT} = \psi\Delta s + s_1 = \psi s_2 + (1-\psi)s_1 = f_1 s_1 + f_2 s_2 \tag{2.57}$$

$$X = -\frac{d\mathfrak{g}}{d\psi} = -\Delta h + T\Delta s + \Delta\boldsymbol{\epsilon}^{tr} : \boldsymbol{\sigma} = \mathfrak{g}_1 - \mathfrak{g}_2 \tag{2.58}$$

Indeed, if $X > 0$, the Gibbs free energy density of phase 2 is lower than the Gibbs free energy density for phase 1. The transformation which is favored leads to an increase of the phase 2 .
This result is formally given by the application of the second principle leading to the following intrinsic inequality:

$$-X\dot{\psi} \geq 0 \tag{2.59}$$

The heat equation (without internal convection) related to this two phases system comes from the application of energy conservation:

$$\frac{d\mathfrak{g}}{dt} = \boldsymbol{\sigma} : \dot{\boldsymbol{\epsilon}} + q_v - \mathrm{div}(\vec{q}_s) \tag{2.60}$$

where q_v represents the "other" heat sources (that can be considered as zero here since all heat sources are derived from the other terms) and $\vec{q}_s$ is the heat flux vector. The introduction of the decomposition given by Equation 2.61 with associated variables and the Fourier law (Equation 2.62) in the energy conservation relationship leads to the heat equation after few calculations (see Equation 2.63 in the work of [Lemaitre et al., 1985] and [Depriester et al., 2014]).

$$\mathfrak{g} = \mathfrak{g} + Ts + \boldsymbol{\sigma} : \boldsymbol{\epsilon} \tag{2.61}$$

$$\vec{q}_s = -\kappa\vec{\nabla}(T) \tag{2.62}$$

$$\rho c_p\dot{T} = -T\frac{d\boldsymbol{\epsilon}}{dT} : \dot{\boldsymbol{\sigma}} + (X - T\frac{dX}{dT})\dot{\psi} + \kappa\Delta_L T \tag{2.63}$$

Δ_L indicates a Laplacian operator.

$-T\frac{d\boldsymbol{\epsilon}}{dT} : \dot{\boldsymbol{\sigma}}$ is the so-called *thermoelasticity* heat source term. This term is usually neglected in the phase transformation problems leads to a few millikelvin temperature increase even in adiabatic conditions (to be compared to dozens of Kelvin given by the second term). It will not be considered in the modeling. Quantity $(X - T\frac{dX}{dT})$ is the so-called *latent heat* denoted as L. It is interesting to observe that this term is composed of the enthalpy density variation and a mechanical energy associated with the transformation strain variation between the two phases:

$$L = X - T\frac{dX}{dT} = h_1 - h_2 - \boldsymbol{\sigma} : (\boldsymbol{\epsilon}_1^{tr} - \boldsymbol{\epsilon}_2^{tr}) \tag{2.64}$$

In the framework of the stochastic theory developed in the paper, the transformation $\mu : i \to j$ at time step τ is considered. This transition involves two variants (parent and child variants that can belong or not to the same phase) making this situation very close to the two phases situation illustrated above. A specific latent heat L_{ij} can be derived allowing the thermal effect of all possible $i \to j$ transitions to be estimated. Equation 2.65 gives this latent heat introduced in the new heat equation valuable at time instant τ for the considered $\mu : i \to j$ transition.

$$L_{ij} = h_i - h_j - \boldsymbol{\sigma} : (\boldsymbol{\epsilon}_i^{tr} - \boldsymbol{\epsilon}_i^{tr}) \tag{2.65}$$

The temperature increment associated with time step $\tau = t_n - t_{n-1}$ is simply given by:

$$dT(\tau, \mu) = \frac{1}{\rho c_p} L_{ij} df(\tau, \mu) + \frac{\tau}{\rho c_p} \kappa \Delta_L T \tag{2.66}$$

Using Equation 2.66, an adiabatic situation can easily be modeled by neglecting the thermal diffusion. Of course any spatial derivation has no direct physical signification for a model at the RVE scale. An anisothermal situation, intermediate between adiabatic and isothermal extreme situations can only be modeled by transforming the Laplacian by an equivalent convection effect, supposing that the RVE is embedded in a coolant. Heat conduction term in Equation 2.66 is then replaced by:

$$\kappa \Delta_L(T) \to k(T_{sys} - T_{amb}) \tag{2.67}$$

where T_{amb} is the ambient temperature, T_{sys} is the temperature of system and k an equivalent convection coefficient. We can consider the following situations:

- $k = 0$: the system is adiabatic, without heat exchange with environment;
- $k = \infty$ (ideal convection): the temperature is fully controlled by the ambient

temperature, leading to the isothermal situation;

- $\infty \geq k \geq 0$: intermediate anisothermal situations

By solving Equation 2.66, we can calculate the temperature variation $dT(\tau, \mu)$ at each time step.

$$\begin{aligned} t' &= t + \tau \\ T(t') &= T(t) + dT(\tau, \mu) \\ t &= t' \end{aligned} \tag{2.68}$$

In the present paper, no real convergence between KMC and heat equation has been looked for to avoid too long computation time. The retained strategy is to update the temperature at each time step and consider it for the next calculation. A converged result is not guaranteed but the chosen time interval $[t_n, t_{n+1}]$ is sufficiently small to describe the evolution of temperature with a good accuracy and observe some relevant anisothermal effects.

2.3.6 Homogenization and localization

The procedure has been detailed for a grain gr in the previous sections but it can apply the same way for all grains of RVE (polycrystal defined by the Orientation Data Function - ODF obtained via EBSD measurement). Once $f(i,t)$ is defined, the calculation of the average transformation strain $\boldsymbol{\epsilon}_{tr}(gr)$ and the entropy density $s(gr)$ (as associated variables to stress and temperature loading) over the grains is easily obtained:

$$\boldsymbol{\epsilon}_{tr}(gr) = \sum_{i=1}^{n} f(i)\boldsymbol{\epsilon}_{tr}(i) \tag{2.69}$$

$$s(gr) = \sum_{i=1}^{n} f(i)s(i) \tag{2.70}$$

The same quantities can be calculated at the RVE scale by an average over the grains. It must be noticed that no strain localization is required since homogeneous stress assumption [Fall et al., 2016] is retained for all calculations.

$$\boldsymbol{\epsilon}_{tr} = \frac{1}{N_{gr}} \sum_{gr=1}^{N_{gr}} \boldsymbol{\epsilon}(gr)_{tr} \tag{2.71}$$

$$s = \frac{1}{N_{gr}} \sum_{gr=1}^{N_{gr}} s(gr) \tag{2.72}$$

Total deformation (sum of elastic, thermal and transformation) can be built by a simple summation of quantities whatever the scale.
An application of localization procedures is possible from RVE to grain scales. This localization is for example required if a real single crystal stiffness tensor (usually anisotropic) is considered for the polycrystalline calculation. Different localization procedures can however be applied. The most relevant is probably the self-consistent that allows the stress at the grain scale $\boldsymbol{\sigma}_{gr}$ to be defined as function of the applied macroscopic stress $\boldsymbol{\sigma}$, the transformation deformation matrix at the grain and macro scales, the accommodation stiffness tensor $\mathbb{C}^{acc}$ and the stress concentration tensor $\mathbb{B}$ (see more details concerning this procedure in [Daniel et al., 2008]).

$$\boldsymbol{\sigma}(gr) = \mathbb{B}(gr) : \boldsymbol{\sigma} + \mathbb{C}^{acc}(gr) : (\boldsymbol{\epsilon}_{tr} - \boldsymbol{\epsilon}_{tr}(gr)) \tag{2.73}$$

Once the full knowledge of the transformation strain for each grain is given, the macroscopic response $\boldsymbol{\epsilon}_{tr}$ of the material is obtained, through an averaging operation involving a strain localization:

$$\boldsymbol{\epsilon}_{\mathrm{tr}} = \frac{1}{N_{\mathrm{gr}}} \sum_{\mathrm{gr}=1}^{N_{\mathrm{gr}}} {}^{t}\mathbb{B}(\mathrm{gr}) : \boldsymbol{\epsilon}_{\mathrm{tr}}(\mathrm{gr}) \tag{2.74}$$

The following flowchart summarizes the entire numerical procedure :

2.4 Kinetic Monte-Carlo algorithm flowchart

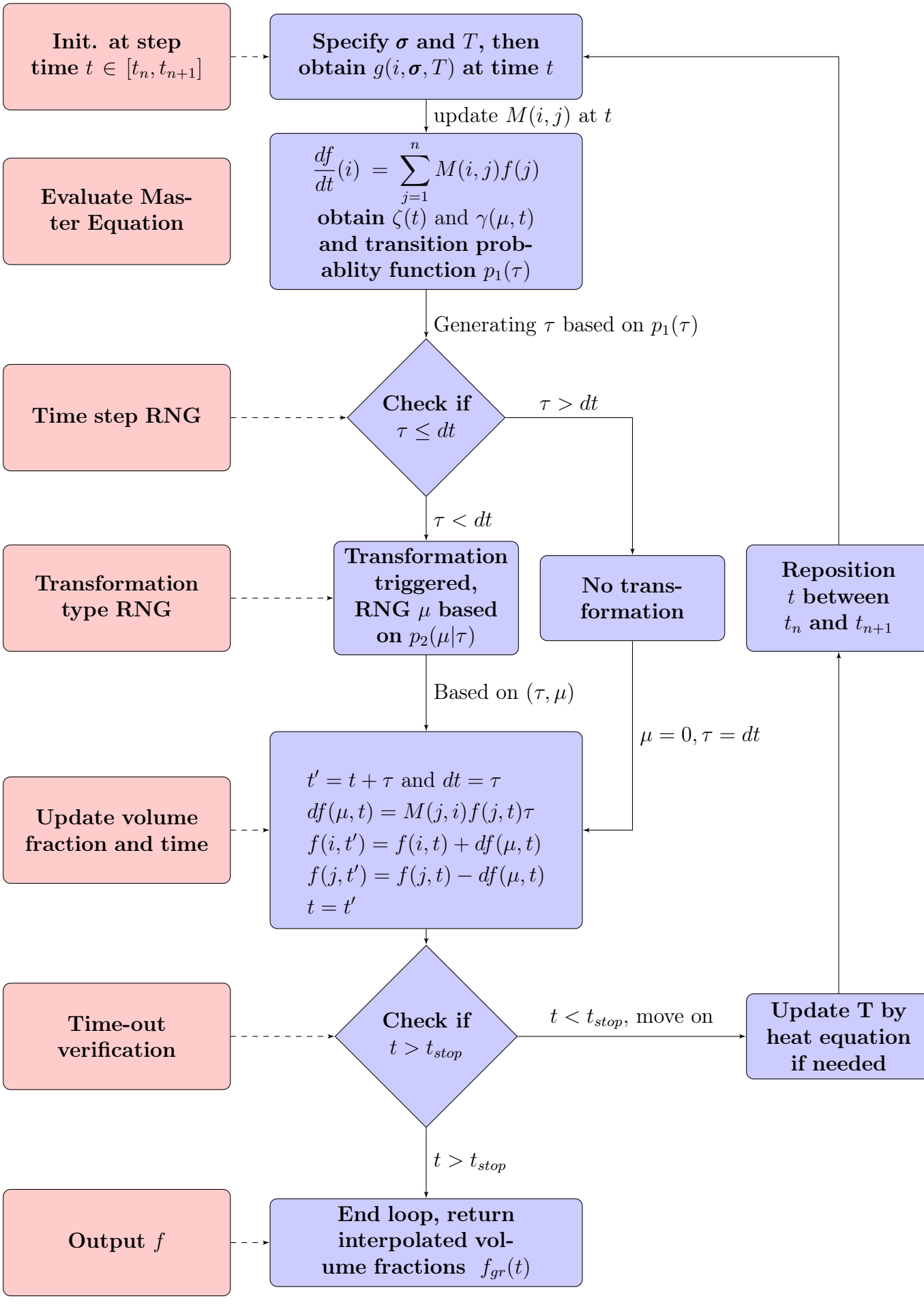

2.5 Implementation of the Kinetic Monte-Carlo framework

In this section, an example of numerical implementation of the KMC framework under homogeneous stress and temperature conditions is presented. The $Ni-50.2Ti$ SMA presented in the previous chapter has been used to illustrate the identification procedure and for some experimental vs modeling comparisons. The list of all necessary thermodynamic parameters used in the model and their identification methods are given in Table 2.1. Upon these parameters, the identification of instant germination energy $dg(\mu, t=0)$ must be specially addressed.

Parameters	Symbol	Identification test
Bain Matrix	$\mathbb{U}_i$	XRD
Transformation strain tensors	$\boldsymbol{\epsilon}_i^{tr}$	XRD
Latent heat densities	δh	DSC
Entropy densities	s	DSC
Enthalpy densities	h	DSC
Specific calorific capacity	c_p	DSC
Transition temperatures	T_{tr}	DSC
Instant germination energy	$dg(\mu, t=0)$	DSC
Crystal orientation	(Φ_1, Ψ, Φ_2)	EBSD
Young modulus	E_Y	1D Tensile test
Poisson ratio	ν	1D Tensile test
Dilatation coefficient	α_v	Dilatometry

Table 2.1: List of parameters experimentally identified

Basic mechanical properties and thermodynamic parameters are given in section 1.6. A representative orientation data function (ODF) made of 414 discrete orientations has been extracted from the EBSD measurements. Associated discrete

$\langle 100 \rangle$ and $\langle 111 \rangle$ pole figures are plotted in Figure 2.3.

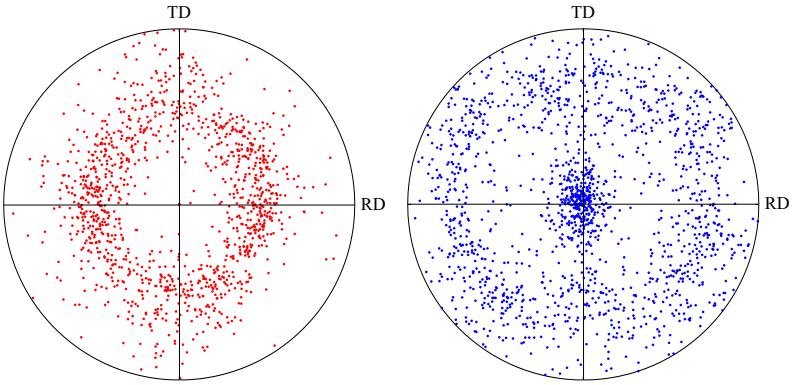

(a) Pole figure $\langle 100 \rangle$ (b) Pole figure $\langle 111 \rangle$

Figure 2.3: Pole figures associated with the 414 orientations representative of the NiTi specimen (RD: rolling direction; TD: transverse direction).

It must be noticed that dilatation effects have not been considered in the modeling (α_v set at $0\,\mathrm{K}^{-1}$) since associated deformations are negligible compared to elastic or transformation strains for the temperature range addressed in this work. Consequently, the remaining sets of parameters remains to identify are: the stochastic parameters (β_s, N, c_μ) and the incompressible germination energy dg^a.

2.5.1 Calibration of stochastic parameters

Reversible model and convex Gibbs free energy densities mapping

DSC scans, shown in Figure 1.30 are reused for the purpose of identification. To give an initial guess, the transition temperature of NiTi SMA is taken as follows:

$$T_{tr} = \frac{T_s^h + T_s^c}{2} \tag{2.75}$$

Herein, the transition temperature is taken as the average temperature between the transformation start upon cooling and heating. Based on Equation 2.75, the Gibbs free energy density of different phases are plotted in Figure 2.4.
It has been shown in [Fall et al., 2016] that β_s, seen as temperature independent in the framework of reversible modeling, is related to the maximal heat flux $q_m(\mathrm{W.m}^{-3})$ of a DSC peak emission (using A to R phase or R to M emission peak), the variation of enthalpy and entropy densities (Δh and Δs) and the temperature rate $\dot{T}$ used during the experiment (Equation 2.76).

$$\beta_s = -\frac{4q_m}{\dot{T}\Delta s \Delta h} \tag{2.76}$$

By assuming that SMA are under thermodynamic equilibrium and no germination energy is required to induce any transformation. The thermal response of NiTi SMA is completely symmetrical as illustrated in Figure 2.4b.

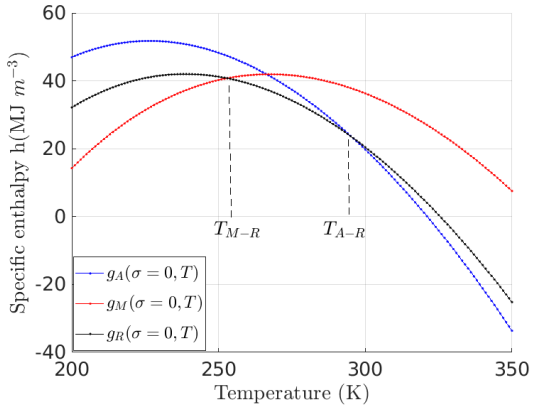

(a) Initial energy mapping

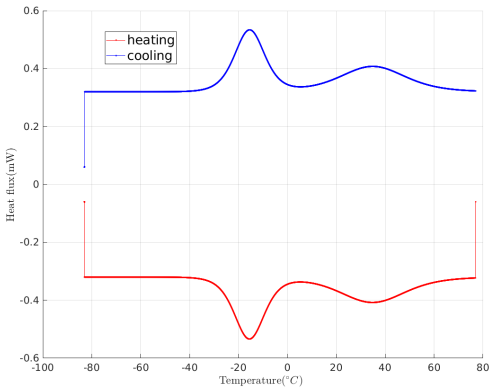

(b) Simulation with reversible Boltzmann model and β_s defined as a constant

Figure 2.4: Reversible modeling

In the stochastic theory, stochastic constant β_s has its own physical interpretation:

$$\beta_s = \frac{V_{SU}}{k_b T} \tag{2.77}$$

where T represents current temperature and k_b is the Boltzmann constant, meanwhile V_u represent the volume of a standard unit, inside which all loading parameters $(\sigma, T$, etc) can be considered as homogeneous .
Based on the pre-defined Gibbs free energy density mapping and the initial value of β_s, a first Boltzmann reversible based DSC simulation is produced (result is shown in Figure 2.4b). β_s is then used to define the appropriate unit volume V_u at the transformation temperature.

Effect of germination energy barrier

In order to illustrate the role of an in-compressible germination energy barrier, a simple qualitative explanation is given here taking the phase transformation $R - M$ during thermal heating/cooling as an example. The Gibbs free energy density mapping between each phase is firstly built.
To explore the thermal hysteresis of DSC observed in Figure 1.30, we will assume initally that the same amount of additional energy density $d\mathfrak{g}^a_{R-M}$ is required to induce the phase transformation from both $R \to M$ and $M \to R$. This additional energetic term can be seen as the energy required to nucleate any new interface between two phases (or two variants) inside a pure phase matrix.

The nucleation energy renders the energy as a non-convex function of the volume fraction. For example, upon cooling, during the phase transformation from R phase to M, the free energy densities of M variants during cooling are higher than their reference level:

$$\mathfrak{g}^*_M(\sigma = 0, T) = \mathfrak{g}_M(\sigma = 0, T) + d\mathfrak{g}^a_{R-M} \tag{2.78}$$

In this context, the transition temperature (the intersection point $T^c_{M_s}$ between $\mathfrak{g}*_M$ and $\mathfrak{g}_R$) during Cooling ($R \to M$) is lower than T_{M_s} (as shown in Figure 2.5).

$$T^c_{M_s} \leq T_{M_s} \tag{2.79}$$

where $T^c_{M_s}$ represents the temperature of M start during cooling.
Vice versa, upon heating, the transition from Martensite to R phase is also delayed due to this additional nucleation energy:

$$\mathfrak{g}^*_R(\sigma = 0, T) = \mathfrak{g}_R(\sigma = 0, T) + d\mathfrak{g}^a_{R-M} \tag{2.80}$$

$$T^h_{R_s} \leq T_{R_s} \tag{2.81}$$

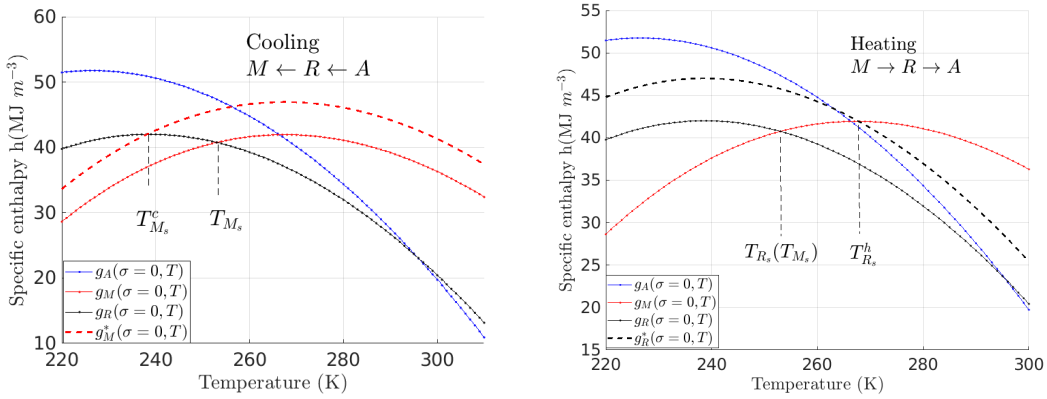

(a) Relative energy level upon cooling (b) Relative energy level upon heating

Figure 2.5: Relative energy level and effect of germination energy

Identification of germination energy barrier

The identification of the germination energy barrier can be achieved as follows : in order to initialize, we assume that all transformation types $\mu \to (j \to i)$ share the same germination barrier $d\mathfrak{g}^c$ related to the delay between forward and reverse DSC

peaks. The germination barrier $d\mathfrak{g}(j,i,dt=0)$ for all transformation types verifies:

$$d\mathfrak{g}^c(i,j,t=0) = d\mathfrak{g}^c(dt=0),\ \forall (i,j), i \neq j \tag{2.82}$$

$$d\mathfrak{g}^c(i,i,dt=0) = \infty,\ \forall i \tag{2.83}$$

The strong penalty used in the second relation is introduced to forbid any self transformation. After several tries, the uniform germination barrier $d\mathfrak{g}^c$ can be estimated (Figure 2.6a). Optimized values for NiTi used in the experiments are[2]:

$$N = 2 \times 10^4; \tag{2.84}$$

$$c_\mu = 1 \times 10^{-7}\,\mathrm{s}^{-1} \tag{2.85}$$

$$d\mathfrak{g}^c(dt=0) = \frac{-\log(c_\mu)}{\beta_s} = 15.2 \times 10^6\,\mathrm{J\,m}^{-3} \tag{2.86}$$

We need to consider in the next step the optimization of the non-compressible germination term $d\mathfrak{g}^a$ for the transformation from A and R phase into M ($d\mathfrak{g}^a_{A-M}$ and $d\mathfrak{g}^a_{R-M}$). It must be consistent with the DSC scan showing that the hysteresis for A-R transformation is lower than the M-R hysteresis.
After certain trials, the optimum values are proposed:

$$d\mathfrak{g}^a_{A-M} = 6.0 \times 10^6\,\mathrm{J\,m}^{-3} \tag{2.87}$$

$$d\mathfrak{g}^a_{R-M} = 5.0 \times 10^6\,\mathrm{J\,m}^{-3} \tag{2.88}$$

$$d\mathfrak{g}^a_{A-R} = 1.0 \times 10^6\,\mathrm{J\,m}^{-3} \tag{2.89}$$

- $(j,i) \rightarrow$ Transformation A/M $\qquad d\mathfrak{g}^a(j,i) = d\mathfrak{g}^a_{A-M}$
- $(j,i) \rightarrow$ Transformation R/M $\qquad d\mathfrak{g}^a(j,i) = d\mathfrak{g}^a_{R-M}$
- $(j,i) \rightarrow$ Otherwise $\qquad d\mathfrak{g}^a(j,i) = d\mathfrak{g}^a_{A-R}$

The meta-stable germination barrier is finally given by:

$$d\mathfrak{g}(j,i,dt) = \mathfrak{g}^c(dt) + d\mathfrak{g}^a(j,i) \tag{2.90}$$

With the ad-hoc correction, the numerical simulation of DSC process converges towards the experimental observation as illustrated in Figure 2.6b.
However the main drawback that we could observe from Figure 2.6b is that the simulated transformation peak from R phase towards M is 'sharper' than the experimental one. Phase transformation during M toward R phase involves a

[2]We would give a justification about these optimized values in subsection 2.5.2

nucleation of Martensite inside R phase matrix and the formation of a M twinning pattern. Indeed, by taking the homogeneous stress hypothesis, the residual stress between any variant to form cohabit plane is neglected. Taking account of the additional cost for forming the twinning structure may be the solution to smooth the simulated transformation peak.

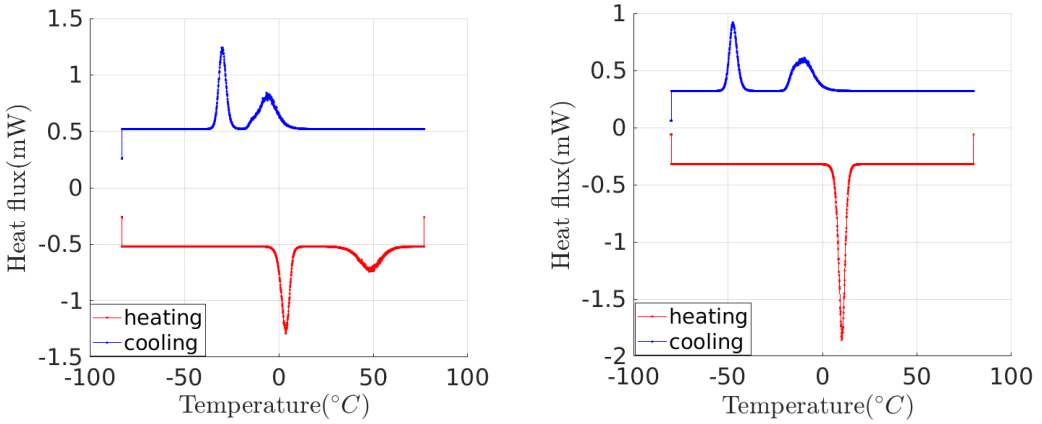

(a) Simulation with uniform germination barrier $d\mathfrak{g}^a = 1.5 \times 10^6\,\mathrm{J\,m^{-3}}$

(b) Simulation with $d\mathfrak{g}^a_{A-M} = 6.0 \times 10^6\,\mathrm{J\,m^{-3}}, d\mathfrak{g}^a_{R-M} = 5.0 \times 10^6\,\mathrm{J\,m^{-3}}, d\mathfrak{g}^a_{A-R} = 1.0 \times 10^6\,\mathrm{J\,m^{-3}}$

Figure 2.6: Germination barrier calibration based on DSC scan, $\dot{T}$=5 K min^{-1}

2.5.2 Relaxation time during thermal creep test via DSC scan

From previous section, we identify partially the mechanical compatible related germination matrix dg^a and the simulated DSC response is in good accordance with experimental DSC scan for Ni-Ti SMA. However, until now, the temporal delay associated with meta-stability is still missing.

To identify this relaxation time, we should consider a situation when the martensitic transformation has already initialized but is not completed ; then hold the external loading as constant and observe the characteristic relaxation time τ required for the system to be "stabilized" . Since at equilibrium state, the temporal variation of volume fraction equal to zero, the heat flow should be time independent as a constant. By plotting how much time it takes for the heat flow to stabilize at the isothermal configuration, the relaxation time can be estimated. The meta-stable germination energy dg^c and transformation rate of the standard

unit c_μ can be then deduced by combining the following equations:

$$N = \frac{V_{sys}}{V_{SU}} \tag{2.91}$$

$$\beta_s = \frac{V_{SU}}{k_b T} \tag{2.92}$$

$$c_\mu \simeq \frac{1}{N t_r} \tag{2.93}$$

$$d\mathfrak{g}^c(dt = 0) = -\frac{\log(c_\mu)}{\beta_s} \tag{2.94}$$

where N defines the population of standard units inside the system.

Remark (1) *Since the meta-stability barrier $d\mathfrak{g}^c(dt)$ decreases as function of time t, in the KMC framework, the transformation rate c_μ is directly calculated based on the identified characteristic relaxation time τ.*

Remark (2) *A initial estimation of both (N, V_{SU}) is made possible by using an admissible value for β_s (a similar value is also used in the work of [Maynadier, 2012] and [Fall et al., 2016]).*

Identification protocol To properly identify the characteristic relaxation time, an ad-hoc thermal loading is conducted to a Ni-Ti specimen:

1. Austenitization at $T = 373\,\mathrm{K}$.
2. Cooling is applied with a fixed rate, $\dot{T}$=5 K min^{-1}, from $T = 373\,\mathrm{K}$ to $T = 193\,\mathrm{K}$
3. Isothermal for 5 min at $T = 193\,\mathrm{K}$;
4. Heating is applied with a fixed rate, $\dot{T}$=5 K min^{-1}, from $T = 193\,\mathrm{K}$ to $T = 278\,\mathrm{K}$
5. Isothermal for 10 min(from A to B)
6. Heating is applied with a fixed rate, $\dot{T}$=5 K min^{-1}, from $T = 278\,\mathrm{K}$ to $T = 373\,\mathrm{K}$

Figure 2.8 shows the evolution of the heat flow measured by DSC as function of time. Between points A and B, when the temperature of specimen is held as constant $T = 278K$, a gradual but not immediate decreasing of the heat flow is observed with a relaxation time that can be estimated at $t_{relax} \simeq 5\,\mathrm{min}$. This delay is symptomatic of a transformation that still goes on illustrating the so-called *relaxation* phenomenon discussed . This indicates clearly that the thermodynamic

equilibrium has not yet been reached at point A but is close to be reached at point B (the non null heat flow at point B is set-up dependent but has no physical sense). Figure 2.9 shows a comparison between experimental and modeling results after optimisation of the relaxation term. The result, although unperfect since germination barrier has not yet been perfectly achieved, allows the delay to be addressed. A DSC simulation has also been conducted and compared with the experimental data (see Figure 2.9).

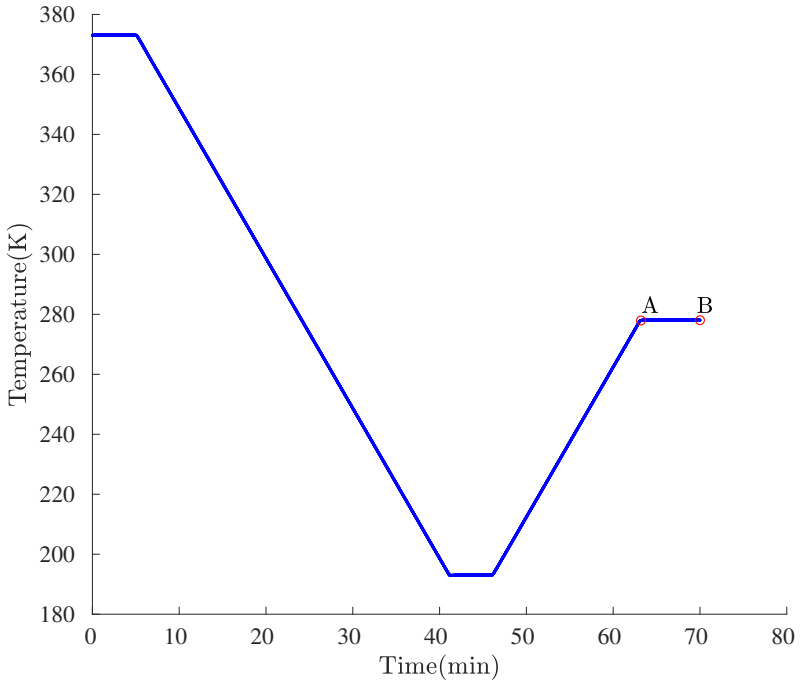

Figure 2.7: Ad-hoc thermal loading used for the relaxation time identification

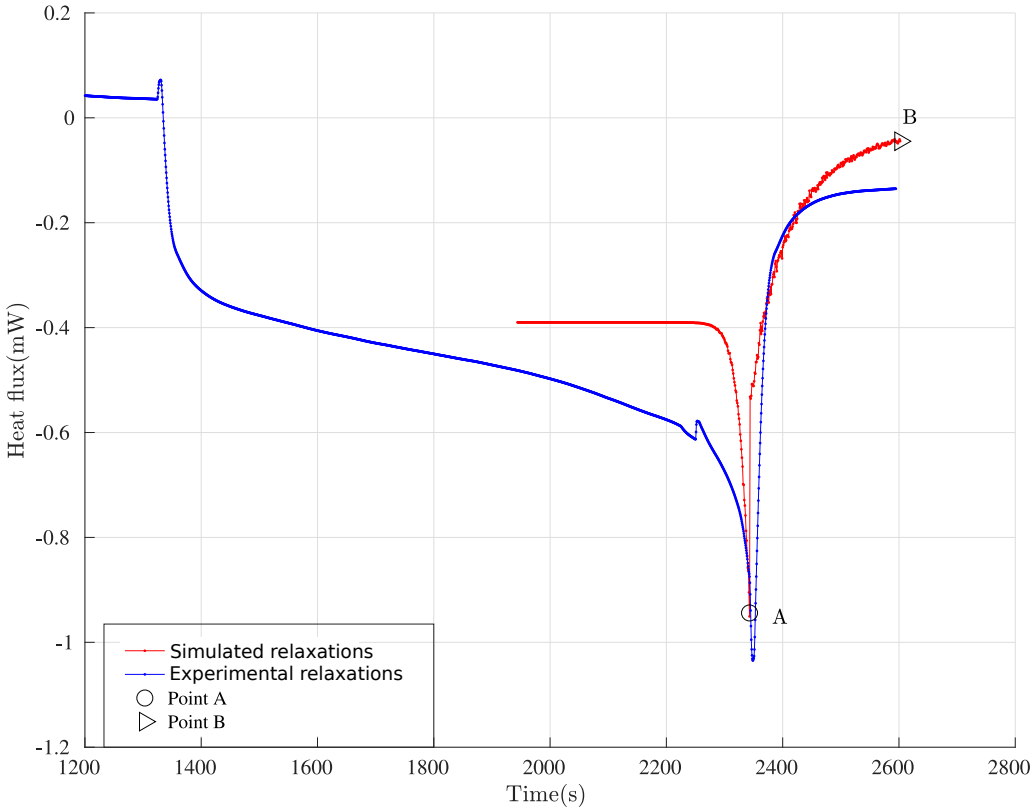

Figure 2.8: Heat flow as function of time between A and B : comparison of experimental and simulated relaxations.

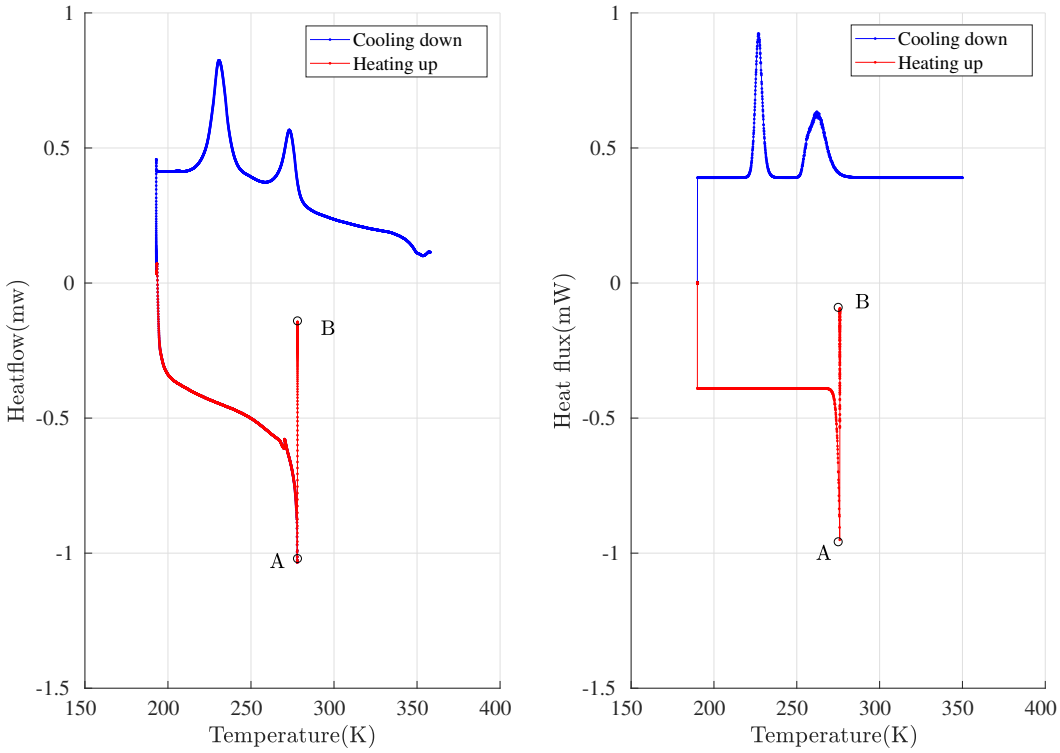

Figure 2.9: Heat flow as function of temperature between A and B : (left) experimental DSC scan ; (right) simulated DSC scan

2.6 Several examples of virtual tests

In this section, a series of virtual loadings of the Ni-Ti polycrystal (RVE constituted of 414 grains) is proposed. This series allows an illustration about the performance of the energy based stochastic model to be presented. Among those, we choose to present simulations, from the most classical to the most challenging cases: pseudo-elasticity under tension and compression, one-way shape memory effect under tension and compression, two ways shape memory effect and 2D plane-stress loading (the phase transformation threshold, non proportional loading). The Gibbs free energy density matrix defined at each time-step $g(i,t)$ is the main input of the KMC model, that returns the volume fraction of each variant in each grain as the principal output. To simplify the numerical simulation, the heat emission (or absorption) due to phase transformation was neglected in most simulations presented in this section ($k = \infty$). Anisothermal situations are illustrated only for the 1D tensile loading at the end of this section. Gibbs free energy density of variants are plotted vs. time for a single crystal considering a tensile axis along the $< 111 >$ axis of the austenite parent phase $(\Phi_1 = -\pi/2, \Psi = -acos(1/\sqrt{3}), \Phi_2 = \pi/4)$. Average phase volume fractions are given for the entire RVE.

2.6.1 Simulation of 1D isothermal tensile loading

A quasi-static stress-controlled tensile loading and unloading is simulated at two different temperature $T = 293K$ and $T = 303K$, the loading protocol is synthesized as follows:

- 1D Load at $T = 303K$: Apply stress-controlled load and unload with a speed $v = 1\,\mathrm{MPa\,s^{-1}}$ at $T = 303K$, with a maximum amplitude of $\sigma_{max} = 500\,\mathrm{MPa}$
- 1D Load at $T = 293K$: Apply stress-controlled load and unload with a speed $v = 1\,\mathrm{MPa\,s^{-1}}$ at $T = 293K$, with a minimum amplitude of $\sigma_{max} = 500\,\mathrm{MPa}$

Figure 2.10 shows respectively: the associated temporal evolution of phases volume fractions, the Gibbs free energy density evolution of each variant in the selected grain, the numerical and experimental [Shaw and Kyriakides, 1995] stress-strain response of the material at different temperatures. The general comments that can be given are:

a General trends for Ni-Ti pseudo-elastic behavior are observed, in accordance with experiments (without any optimization of parameters); The mechanical hysteresis is remarkably modeled;

b The RVE is fully transformed at the maximum stress leading to an axial transformation strain of about 11%. This deformation level may appear too high. This is a common defect when a homogeneous stress assumption is used [Fall et al., 2016]. Value reached is however in accordance with parameters of the Bain matrices.

c At the $T = 303$K, martensite transformation is fully accomplished at a higher maximum stress level compared to $T = 293K$.

d The phase transformation threshold increases following a temperature sensitivity of about $\Delta\sigma/\Delta T \simeq 6.4\,\mathrm{MPa\,K^{-1}}$.

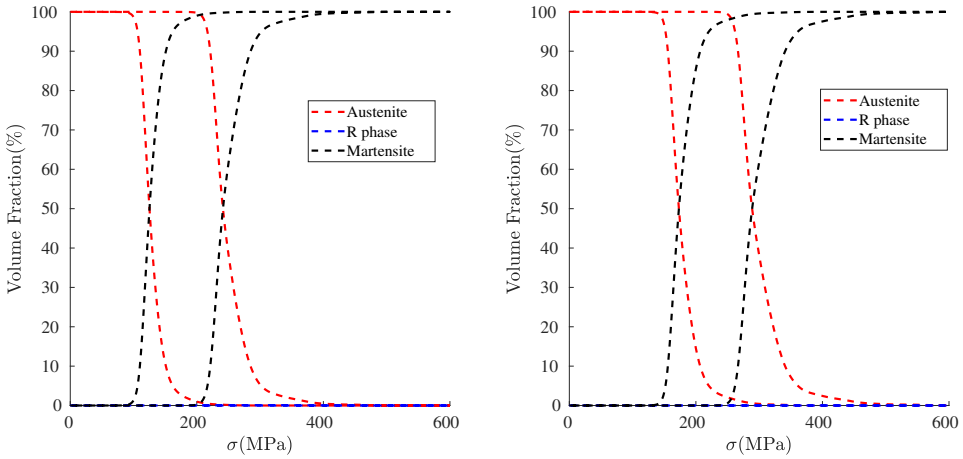

(a) Phases volume fraction as function of stress: (Left)$T = 293\,\mathrm{K}$ (Right) $T = 303\,\mathrm{K}$

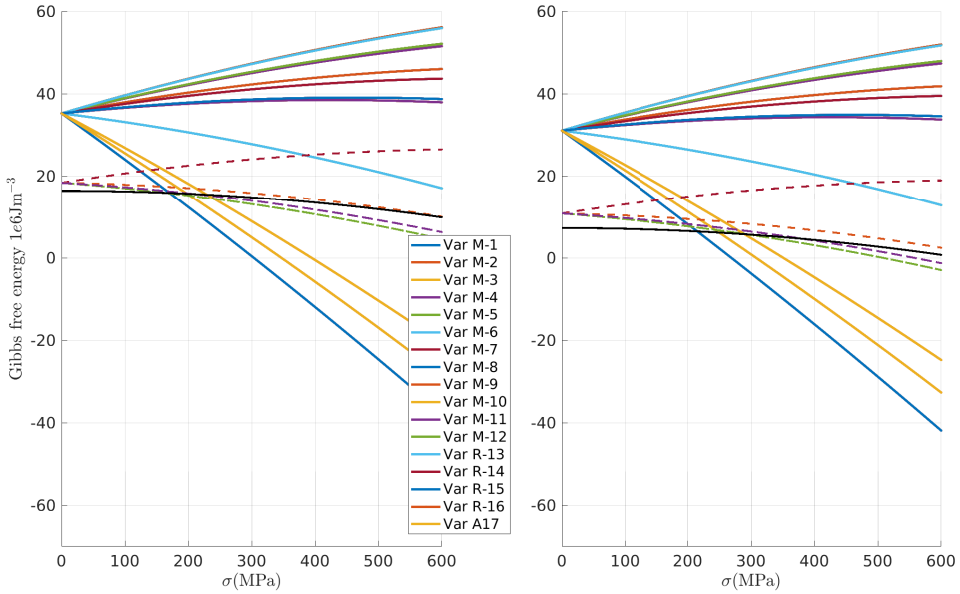

(b) Gibbs free energy density evolution of each variant: (left) $T = 293\,\mathrm{K}$; (right) $T = 303\,\mathrm{K}$.

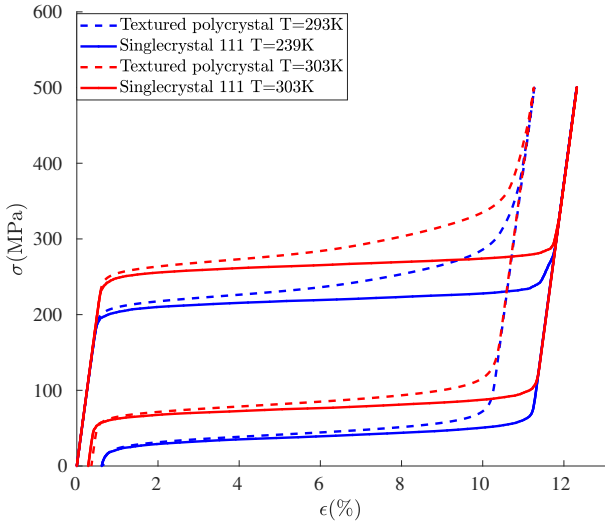

(a) Numerical stress/strain response at the two different temperatures for single and polycrystal

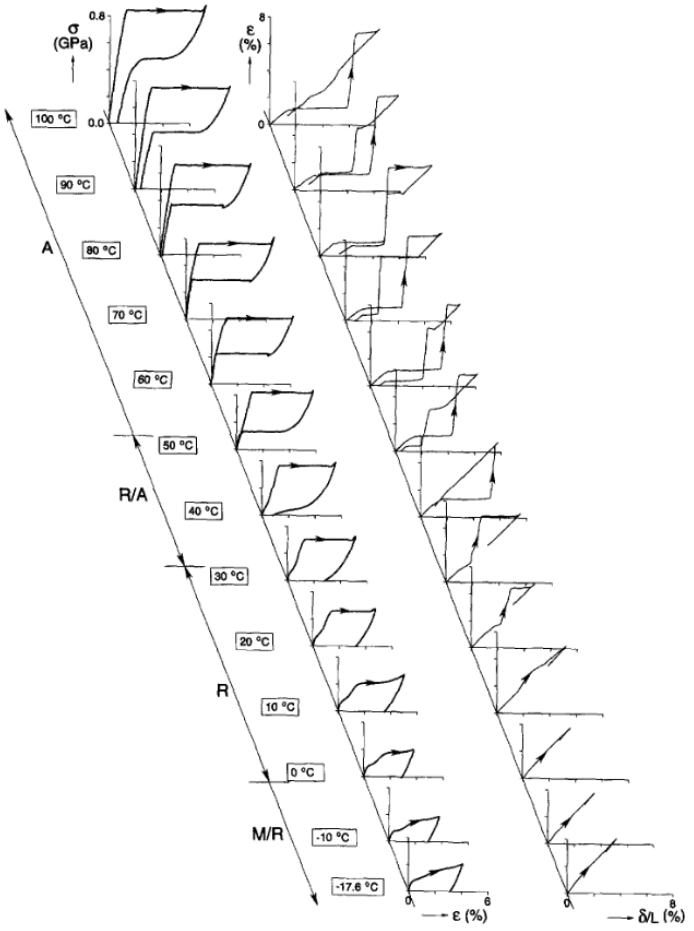

(b) Experimental stress-strain response at different temperatures of nearly equiatomic NiTi [Shaw and Kyriakides, 1995]

Figure 2.10: 1D tensile loading/unloading at different temperatures

2.6.2 Simulation of 1D tension-compression loading

In literature, for nearly equiatomic NiTi SMA at room temperature, the stress threshold in compression is slightly higher than in tension ([Maynadier, 2012]). A virtual loading is applied in order to simulate this asymmetry. The loading protocol can be summarized in:

- 1D tensile load: apply stress-controlled tensile load and unload with a speed $v = 1\,\mathrm{MPa\,s^{-1}}$ at $T = 293K$, with a maximum amplitude of $\sigma_{max} = 500\,\mathrm{MPa}$
- 1D compression load: apply stress-controlled tensile load and unload with a speed $v = 1\,\mathrm{MPa\,s^{-1}}$ at $T = 293K$, with a maximum amplitude of $\sigma_{min} = -500\,\mathrm{MPa}$

Figure 2.11 shows respectively: the Gibbs free energy density evolution of each variant in the selected grain, numerical stress/strain response for the polycrystal and the single crystal strained along $< 111 >$ direction, the associated temporal evolution of phases volume fractions, and an experimental tension-compression stress-strain response of single-crystal and textured polycrystal [Gall et al., 2001]. The general comments that can be given are:

- General expected trends are observed;
- In Figure 2.11a, the first time period $0 \leq t \leq 1000s$ belongs to the evolution of the Gibbs free energy density during tensile load and unload; the second time period $t \geq 1000s$ belongs to compression load and unload. We clearly observe that martensite variants activated during tension are different from martensite variants activated during compression;
- This selection leads to the asymmetry observed for the tension vs. compression stress-strain response (Figure 2.11b), and is consistent with experimental observations [Gall et al., 2001];
- Under compression, the presence of R-phase is observed during both loading and unloading stages before the austenite transformation starts. As seen in Figure 2.11a for single crystal loaded along $< 111 >$ direction, the R phase variant (R14) has the lowest Gibbs potential at $\sigma_{min} = -500\,\mathrm{MPa}$. Consequently a large volume fraction of R phase is expected after full loading and unloading, as seen in Figure 2.11c, which induces a significant residual strain of about $\epsilon_{res} = 2\%$. On the contrary, under tension, several martensite variants are more stable than R phase variants at higher stress level. As a result, the volume fraction of R phase as predicted by the simulation is low. The presence/non-presence of R phase is potentially the principal factor inducing the asymmetrical behavior between tension and compression.

- Differences of absolute strain and stress levels between modeling and experiments are related to different material compositions and transformations strain at the variant scale (not identified).

- Texture of materials are on the other hand different. Indeed $< uvw > \{111\}$ texture used for the modeling of polycrystal leads to a tensile behavior close to a testing along a direction between $< 110 >$ and $< 111 >$ directions of the corresponding single crystal.

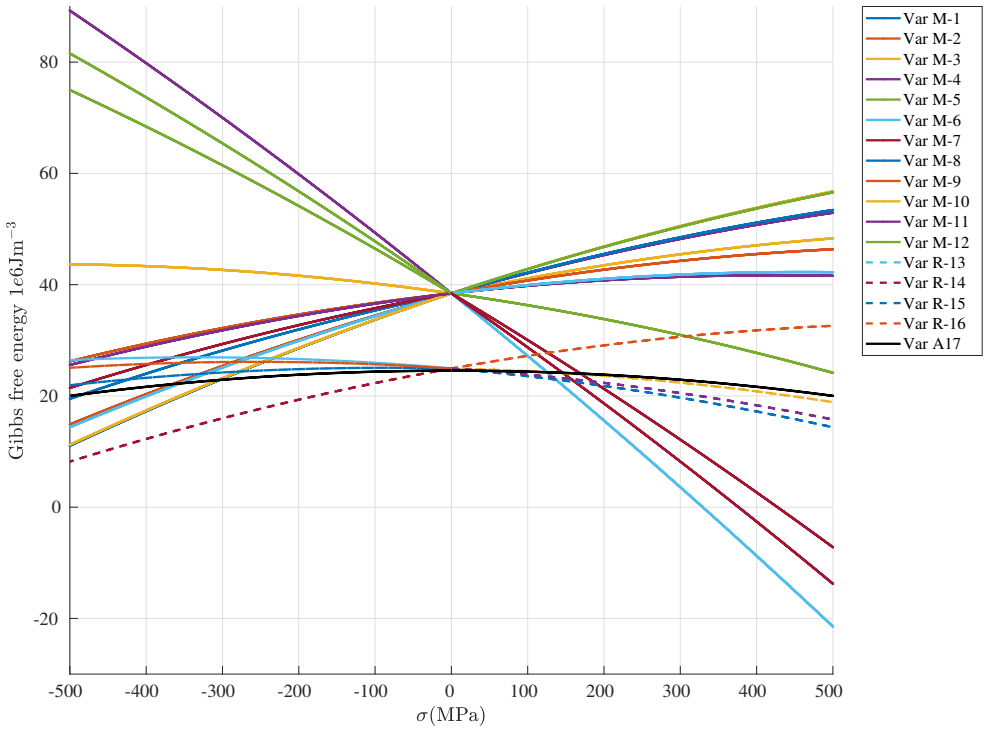

(a) Gibbs free energy density evolution of each variant for singlecrytal 111

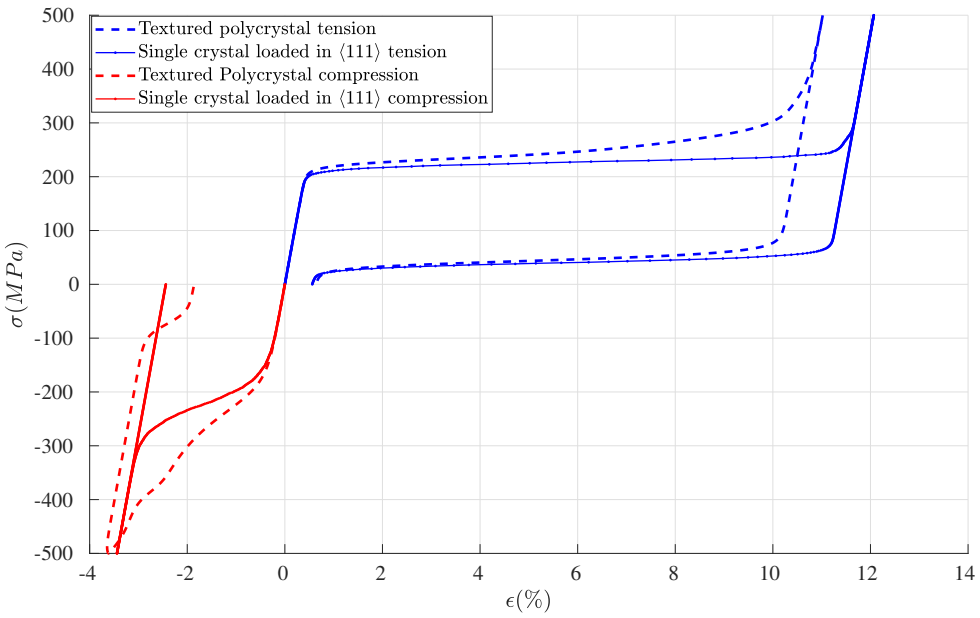

(b) Axial stress/strain response

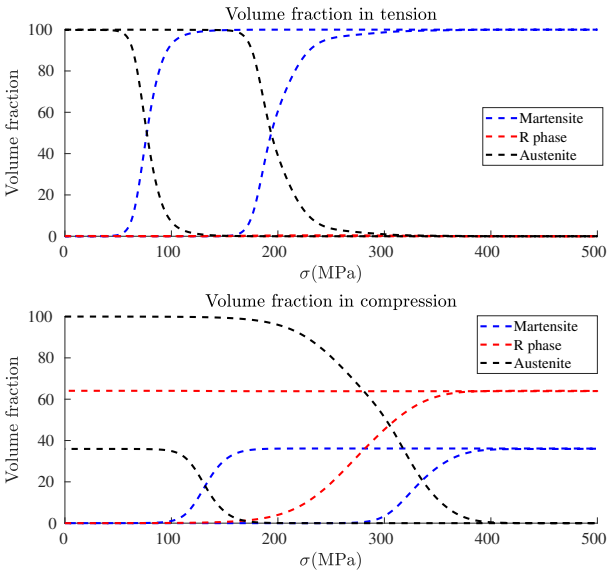

(c) Phases volume fraction as function of stress for tension(up) and compression(down) for single crystal 111

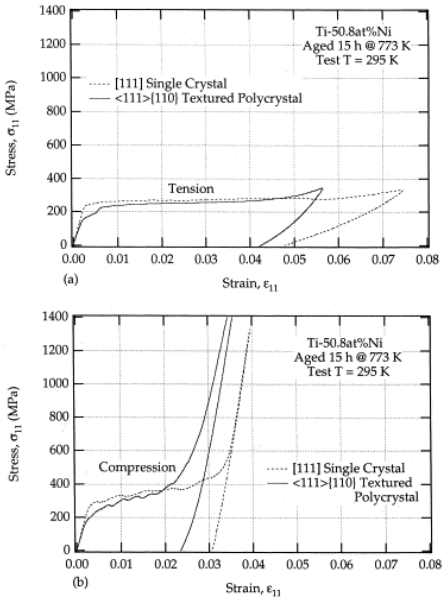

(d) Tensile and compressive response of a NiTi SMA single crystal [Gall et al., 2001]

Figure 2.11: 1D tension/compression loading at room temperature (T=293K)

2.6.3 Pseudoelasticity, partial load and velocity effects

In this subsection, some partial tensile loading/unloading tests have been simulated, we are looking for a situation where the stress level reached is insufficient to fully transform the austenite into martensite. This simulation especially allows the effect of temporal relaxation associated with the germination barrier to be illustrated. The following loadings are considered:

- Full Tensile Load: Apply stress-controlled tensile load and unload with a speed $v = 1\,\mathrm{MPa\,s^{-1}}$ at $T = 293K$, with a maximum amplitude of $\sigma_{max} = 500\,\mathrm{MPa}$
- Partial Tensile Load 1: Apply stress-controlled tensile load and unload with a speed $v = 1\,\mathrm{MPa\,s^{-1}}$ at $T = 293K$, with a maximum amplitude of $\sigma_{max} = 190\,\mathrm{MPa}$
- Partial Tensile Load 2: Apply stress-controlled tensile load and unload with a speed $v = 1\,\mathrm{MPa\,s^{-1}}$ at $T = 293K$, with a maximum amplitude of $\sigma_{max} = 190\,\mathrm{MPa}$. Stress is kept constant for 200s at the maximum stress amplitude level before unloading.

The comments that can be given are:

- As we can see in Figure 2.12a and Figure 2.12b, the partial load 1 illustrates the germination barrier delays for the two transformation directions ($A \rightarrow M$ and

$M \rightarrow A$). For partial load 1, when stress unload begins, the RVE is still far away from an equilibrium state, thus the stress/strain curve does not immediately go back to the elastic regime. A narrow non linear region is needed to overcome the germination barrier for $M \rightarrow A$ transformation initiation.

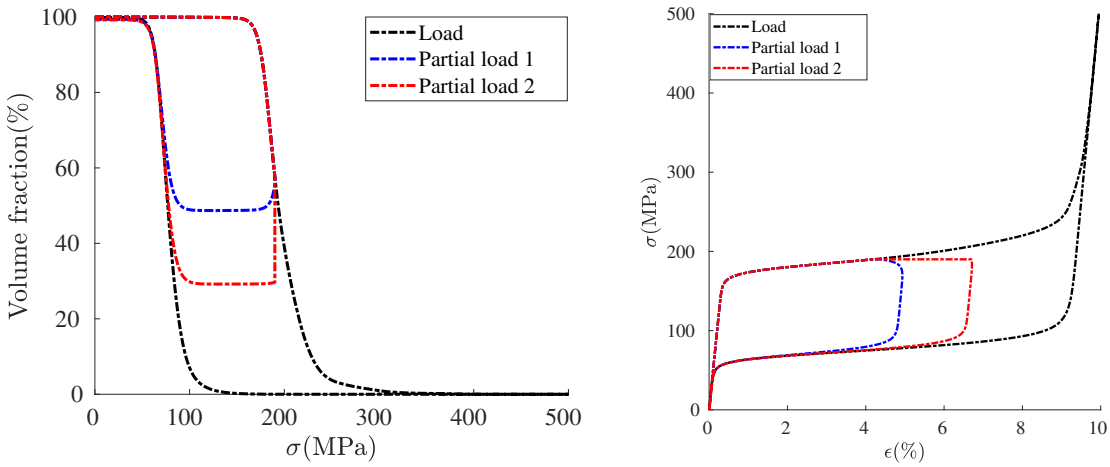

(a) Austenite volume fraction as function of stress (b) Stress/strain simulation

Figure 2.12: 1D tension/compression partial loadings at room temperature (T=293K)

- However, if we hold the stress level as constant for a long time instead of immediately unload the sample (case of partial load 2), transformation from $A \rightarrow M$ and deformation still increases until a certain martensite volume fraction is reached. This is a direct example of an effect of temporal relaxation associated with the germination barrier (discussed in section 2.2.6). When the Gibbs free energy density between variants is not enough to bypass the germination barrier, it takes a longer time to converge towards the equilibrium state (see Equation 2.36).

- For the case of partial load 2, the unload begins after the NiTi SMA reaches its equilibrium state (see Figure 2.12a). At that time, the polycrystal needs to bypass a germination barrier before any $M \rightarrow A$ transformation initializes, leading to an elastic unloading part.

- This point illustrates that an extremely low strain rate would be required to reach the 'true' static behavior, due to the time constant associated with the stochastic process. Stress threshold and hysteresis loop are sensitive to this process, superimposed to the classical thermal effects (not accounted for in this simulation).

Velocity effects over pseudoelasticity (remaining in an isothermal situation) of NiTi SMA can be more clearly illustrated by considering a 1D tensile load at three different stress-controlled loading rates ($\dot{\sigma} = 0.1, 1, 5, 20 \mathrm{MPa\,s^{-1}}$). Numerical tests are performed at $T = 293K$, with a maximum amplitude of $\sigma_{max} = 500\,\mathrm{MPa}$. Numerical results are reported in Figure 2.13. We observe that both stress threshold and hysteresis area increase at increasing loading rate. As briefly stated above, this trend has a stochastic explanation. At isothermal configuration, with a quasi-static loading rate (the associated mechanical dissipation is nearly zero), we observe that hysteresis is saturated and this hysteresis is the energy cost to maintain the temperature as constant.
By assuming that the low stress rate simulation ($\dot{\sigma} = 0.1\mathrm{MPa.s^{-1}}$) can be considered as quasi-static load ($dt = \infty$) and considering on the other hand a full transformation during both loading and unloading (along this direction, few R phase is created during tensile loading), only the double of energy gap dg^a_{A-M} should contribute to the hysteresis surface. The theoretical hysteresis surface S^{theory}_{hys} gives:

$$dg^c(dt = \infty) = 0 \rightarrow S^{theory}_{hys} = 2dg^a_{A-M} = 13.0 \times 10^6\,\mathrm{J\,m^{-3}} \tag{2.95}$$

to be compared to the simulated hysteresis S^{simu}_{hys}:

$$S^{simu}_{hys} = \int \sigma : d\epsilon \simeq = 13.6 \times 10^6\,\mathrm{J\,m^{-3}} \tag{2.96}$$

Theoretical and simulated values are in very good agreement. The hysteresis area is consequently saturated and insensitive to the loading rate. Otherwise, when loading rate could no longer be considered as static, the germination barrier is rate dependent:

$$\forall(\delta t_1, \delta t_2), 0 \leq \delta t_1 \leq \delta t_2 \leq \infty \tag{2.97}$$

$$dg^c(i, j, 0) \geq dg^c(i, j, \delta t_1) \geq dg^c(i, j, \delta t_2) \geq 0, \forall(i, j) \tag{2.98}$$

Consequently, the rate-dependency of hysteresis area and stress threshold is observed for the non quasi-static loading configurations.

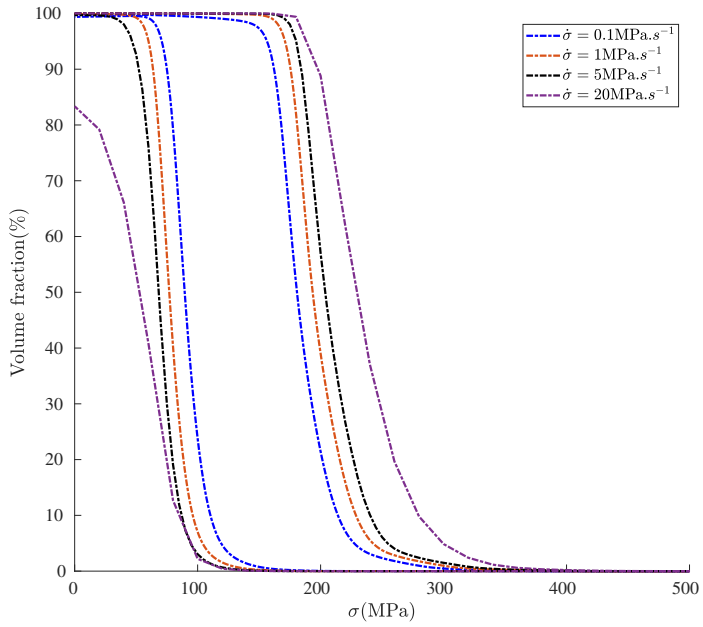

(a) Phases volume fraction as function of stress

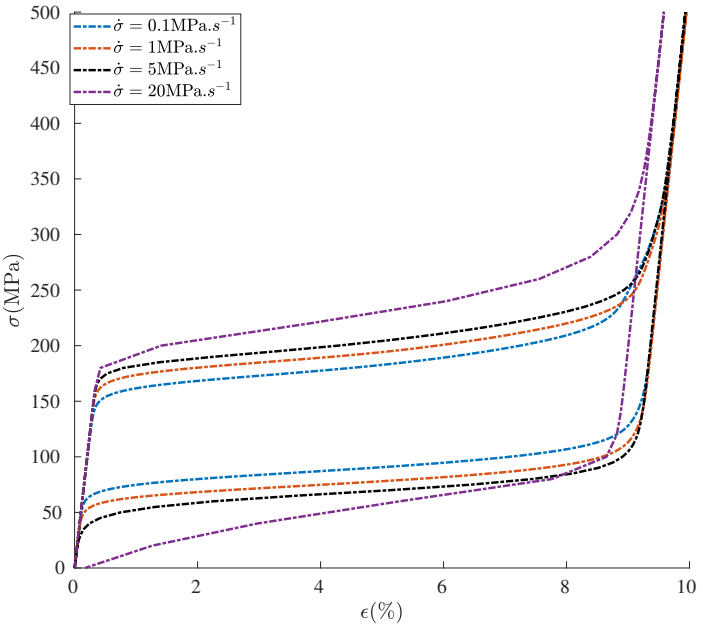

(b) Rate dependency of stress strain curve

Figure 2.13: Calculated stress-rate dependency of hysteresis area for NiTi SMA - isothermal condition

2.6.4 Simulation of one-way shape memory effect(OWSME)

The one way shape memory effect of SMA appears when the alloy is in its cold state (below austenite start temperature $T \leq A_s$, mainly indicating a martensite state). The alloy can be stretched and still hold the permanent deformation after unloading, until it is heated above the $M \rightarrow A$ transition temperature [Otsuka and Wayman, 1999] when the deformation is recovered. We propose hereafter to simulate a one way shape memory effect for both tension and compression of NiTi polycrystal, and to compare the numerical simulations to the experimental results available in literature [Lavernhe-Taillard et al., 2009] (Figure 2.14). Let consider the following steps illustrated by letters (A to K) in Figure 2.14:

- From A to F:
  - A $\rightarrow$ B: NiTi polycrystal is cooled at $T = 263\,\mathrm{K}$;
  - B $\rightarrow$ C $\rightarrow$ D: a tensile loading up to a maximum stress $\sigma_{max} = 160\,\mathrm{MPa}$ is applied. The material is then unloaded to zero;
  - D $\rightarrow$ E $\rightarrow$ F: the material is heated up to $T = 373\,\mathrm{K}$ (above the $M \rightarrow A$ transformation temperature) and then cooled to $T = 263\,\mathrm{K}$.
- From F to J: the same steps are applied under compression.

Figure 2.14 allows modeling and experimental results to be compared considering the macroscopic quantities. Figure 2.15a and Figure 2.15b plot the associated variation of the Gibbs free energy density and the variants' volume fractions respectively in the reference single crystal.
The comments that can be given are:

a Initial cooling shifts points in Figure 2.14 from A to B (or E to F for compression). At point B and F, it must be first observed that R phase is dominant. R phase variants are equiprobable (equivalent in volume fraction) as illustrated in Figure 2.15b. By applying the stress loading, R phase variants whose transformation strain is mainly oriented along the loading direction are favored in tension. The same variants are unfavored under compression leading to an asymmetric selection of variant types and numbers (in accordance with their Gibbs free energy density as illustrated in Figure 2.15a). The selected variants remain stable during the unloading between C and D (or G and H under compression), leading to a permanent strain even when the stress is completely removed. The associated maximum eigenvalue of transformation matrix for R phase is around $\epsilon_{max} \simeq 2\%$, which explains the maximum value for permanent strain observed in the experimental data and simulation. Despite

some few differences of stress threshold observed between experimental data and simulation, results are in very good agreement.
The following thermal heating makes the R phase variants transform towards Austenite (D to E or H to J). The polycrystal returns to self consistent R phase structure during the final cooling without straining (or a very small dilatation observed in experiments - not modeled) between point E and F (or I and J).

b Asymmetry of OWSME between tension and compression is clearly illustrated in relation with the asymmetric selection of variant types and numbers in grains, although the reorientation mechanism between tension and compression has nearly the same stress threshold according to the definition of the germination energy. Indeed, It is possible following the proposition of some authors [Patoor et al., 2006] to make a more complete identification of the germination matrix $\mathbf{dg}(\mathbf{i},\mathbf{j})$ that could lead to an improvement of the modeling results.

c Despite this improvable definition of the germination energy, the numerical results prove to be in good consistency with the experimental response, unlike most models available in literature.

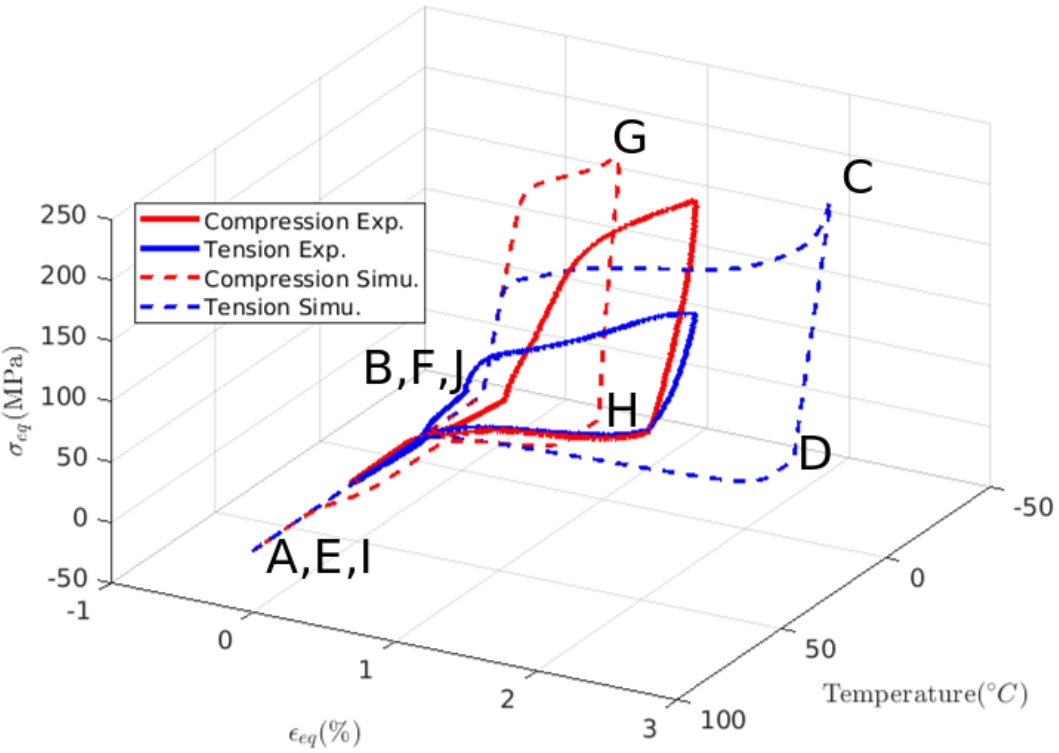

Figure 2.14: Comparisons between simulation and experimental test of OWSME in tension and compression

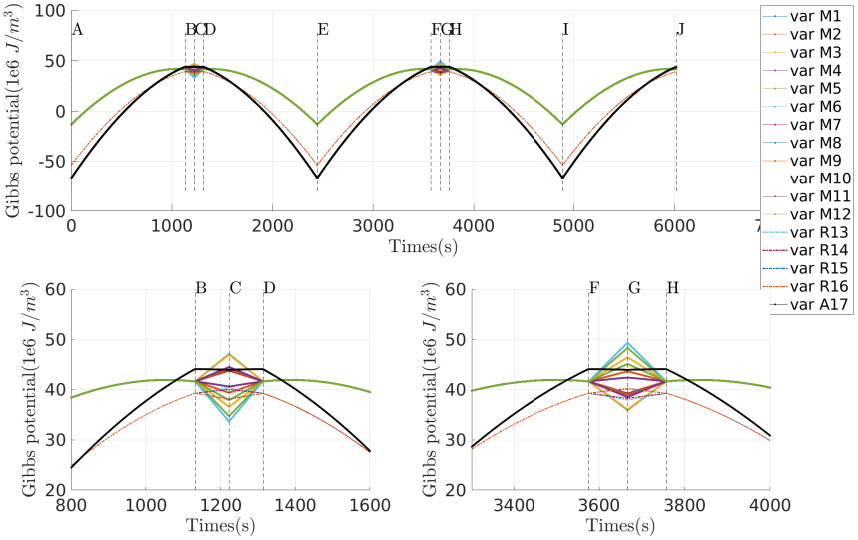

(a) Gibbs free energy density of variants

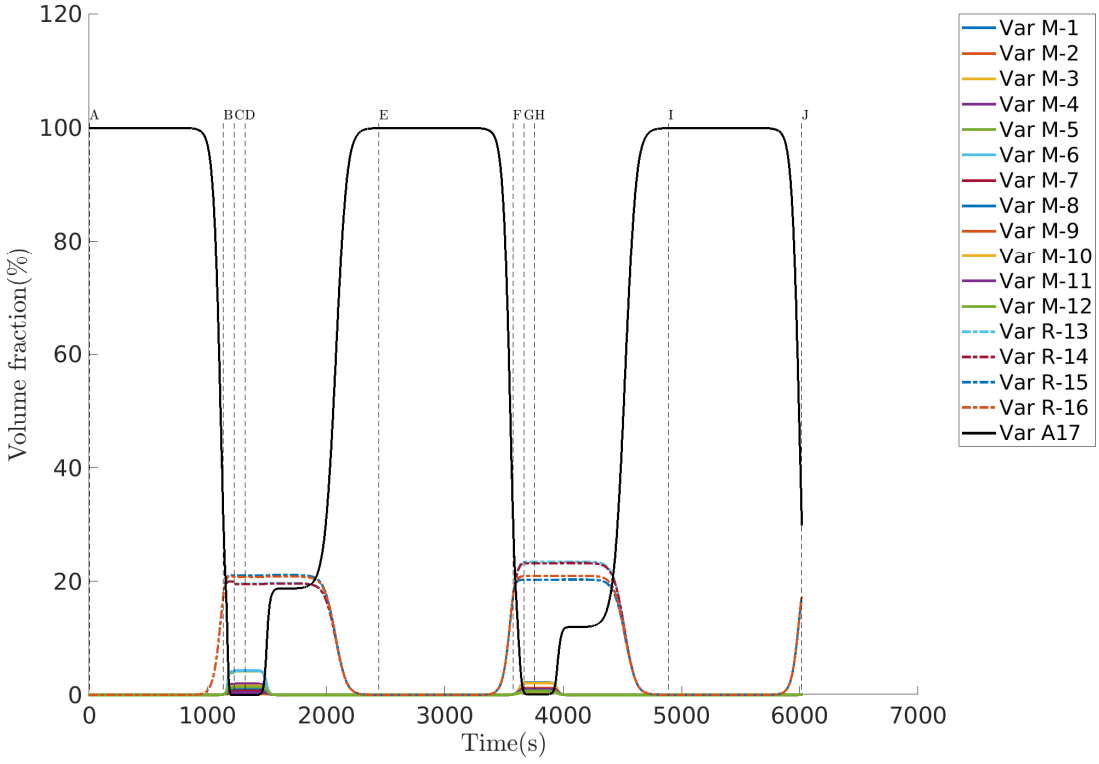

(b) Variants volume fraction evolution

Figure 2.15

2.6.5 Simulation of stress-assisted two-way shape memory effect (SA-TWSME)

Stress-assisted two-way shape memory effect refers to the fact that a SMA may remember two different shapes: one at high temperature and the other at low temperature. A material that exhibits a shape memory effect during both heating and cooling is a two-way shape memory effect material. The loading path that helps to produce the two-way shape memory effect of NiTi polycrystal (reference points are illustrated in Figure 2.16a) is the following:

- A-B-C-D: 1D tensile loading is applied to NiTi SMA. The stress is held as constant at $\sigma = 250\,\text{MPa}$, and a thermal cycle consisting of a constant rate heating and cooling is applied with a maximum amplitude $T_{max} = 373\,\text{K}$.
- D-E-F-G: From the end point of previous cycle, the applied stress is raised up and held as constant at $\sigma = 300\,\text{MPa}$, and a second thermal cycle consisting of a constant rate heating and cooling is applied with a maximum amplitude $T_{max} = 373\,\text{K}$.

Figure 2.16a illustrates the associated stress-strain behavior. The simulation plotted in Figure 2.16b illustrates how the thermal loading at two different stress levels ($\sigma = 250,\ 300$ MPa) can change the volume fraction of the different phases. For the two cycles investigated, the NiTi polycrystal always returns to its shape at the end of the thermal loading as illustrated in Figure 2.16a) in accordance with the experimental results reported in literature (Figure 2.16d). At higher stress level start ($\sigma = 300$ MPa), the thermal hysteresis area is higher because of a higher amount of martensite phase involved in the transformation (Figure 2.16b). The higher temperature threshold at high stress level for SA-TWSME can be explained by the fact that martensite variants are more stable. A higher temperature is required to destabilize this phase. Again, to the best knowledge of authors, very few models are able to simulate such kind of complex behavior, for single or polycrystals.

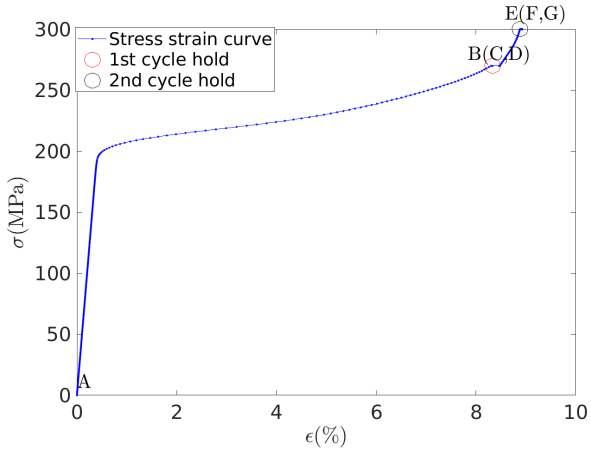

(a) Applied 1D tensile load and two thermal cycles

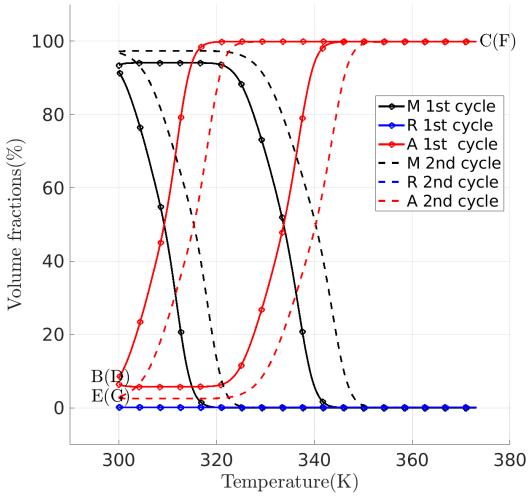

(b) Average volume fractions of A, M and R phases as function of temperature

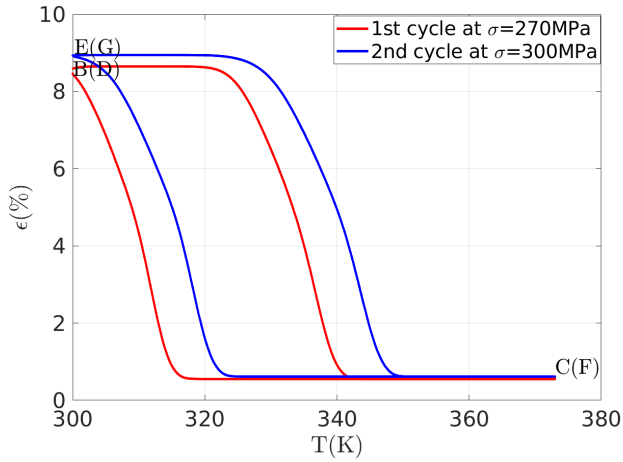

(c) Numerical strain-temperature response for NiTi polycrystal

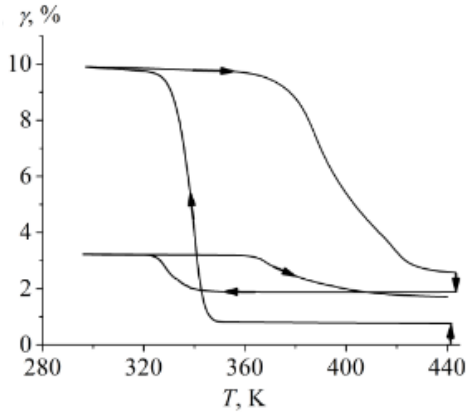

(d) Experimental strain-temperature response for NiTi polycrystal curve [Ponikarova et al., 2017]

Figure 2.16: Stress-assisted two ways shape memory effect

2.6.6 Proportional / non proportional biaxial loading - 2D phase mapping

The stochastic multiscale model (SMSM) for SMA can of course simulate the effect of multiaxial loading. Its intrinsic hysteresis makes the loading path crucial for the model's response. Situations that can be tested are then innumerable. We decided to focus on a simple biaxial loading since some biaxial experiments are available in literature allowing a model/experiment comparison. A proportional

stress-controlled loading is first applied on the polycrystal given by :

$$\boldsymbol{\sigma} = \sigma(t) \begin{pmatrix} \cos\theta & 0 & 0 \\ 0 & \sin\theta & 0 \\ 0 & 0 & 0 \end{pmatrix} \tag{2.99}$$

$$\sigma(t) = [0:1:1000\ 1000:-1:0]\text{MPa} \tag{2.100}$$

$$\theta = [0:5:355]\ \text{degree} \tag{2.101}$$

The forward transformation is defined for the proportional load $\sigma(t) = [0:1:1000]$MPa and the backward transformation is defined for the corresponding unload $\sigma(t) = [1000:-1:0]$MPa. Each simulation is performed at constant angle θ for a constant temperature $T = 303\,\text{K}$. The simulation is repeated for each angle, allowing a discrete mapping of the stress plane. Many figures can of course be drawn. We decided to illustrate this loading by plotting the volume fraction of A, R and M phases during loading and unloading (see respectively Figure 2.17a to Figure 2.18d). These figures illustrate clearly the global shape of the transformation threshold in the stress plane.

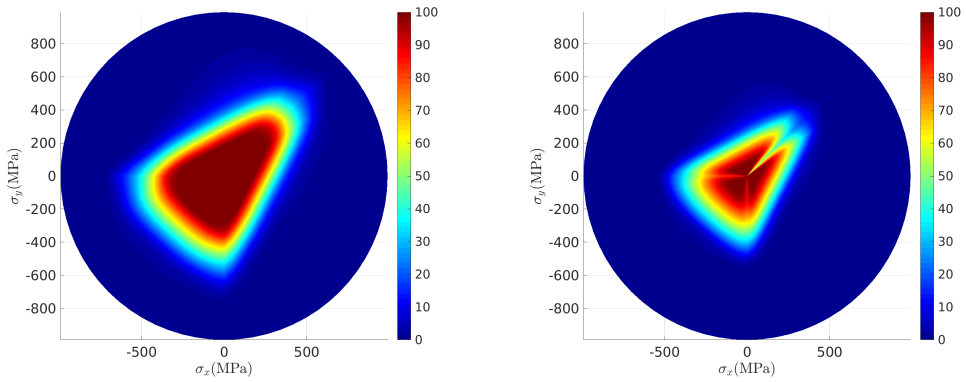

(a) Loading (b) Unloading

Figure 2.17: Austenite phase mapping under proportional stress condition.

As expected, the forward transformation leads to a larger stress threshold compared to the backward transformation, and the hysteresis between loading and unloading is consistent. However, there exists an unexpected area (narrow cone) where R phase concentration remains high along $\sigma_1 = \sigma_2$ axis ($\sigma > 0$). Indeed, depending on their orientation, a significant amount of grains does not transform from R to M phase under equibiaxial loading. Some validation of such result would require for example in-situ XRD measurement as proposed in [Chang et al., 2018]. Transformation thresholds under biaxial loading are available in literature [Lexcellent and Blanc, 2004][Lavernhe-Taillard et al., 2009]. They are always defined using a deformation criterion. Figure 2.19a illustrates the transformation

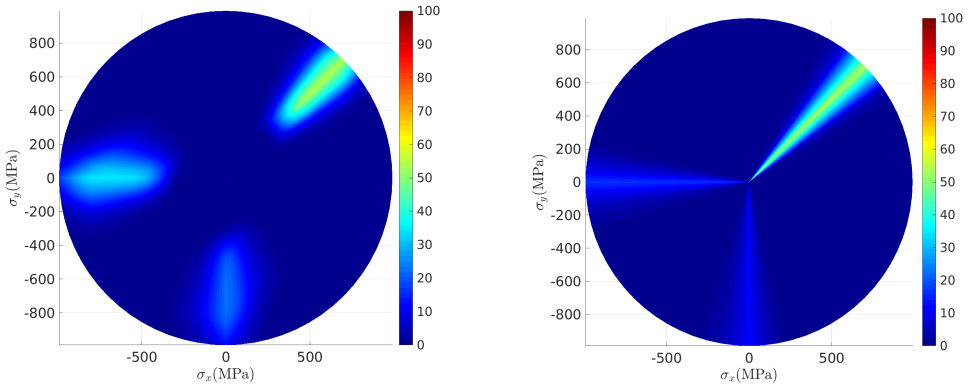

(a) R-phase - Loading

(b) R-phase - Unloading

(c) Martensite - Loading

(d) Martensite - Unloading

Figure 2.18: R phase and M phase mapping under proportional stress condition.

threshold predicted by the SMSM for an equivalent transformation strain of 0.6% (a Levy-Mises equivalent strain (Equation 2.102) has been chosen to define the deformation criterion). This result is in very good accordance with experimental results and phenomenological modeling of [Lexcellent and Blanc, 2004](see Figure 2.19). Of course, it could be interesting to use the SMSM as a virtual testing machine to verify the accuracy of some macroscopic models in other loading conditions.

$$\epsilon_{eq}^{tr} = \sqrt{\frac{2}{3}\boldsymbol{\epsilon}^{tr} : \boldsymbol{\epsilon}^{tr}} \tag{2.102}$$

The SMSM is an hysteretic modeling. Non proportional loading and sensitivity to stress path can consequently be tested. These points are highlighted in the next figures where the following paths have been used in $(\sigma_{xx}, \sigma_{yy})$ plane:

- Path 1: a quasi static stress-controlled uniaxial loading is first applied along $\vec{x}$ until $\sigma_{xx} = 600$MPa is reached. This stress is hold and a second stress loading is gradually applied along $\vec{y}$ direction until $\sigma_{yy} = 600$MPa, reaching the equibiaxial point $(\sigma_{xx}, \sigma_{yy}) = (600, 600)$MPa.

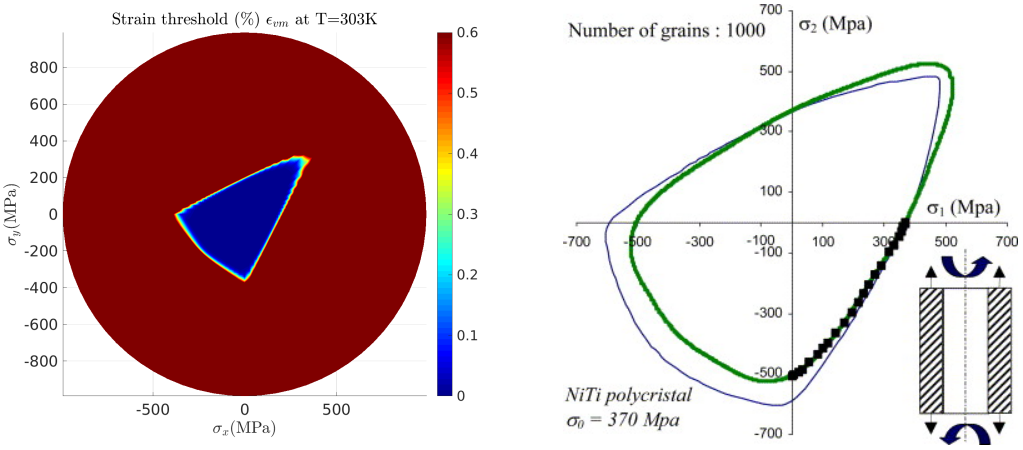

(a) Transformation threshold defined by Levy-Mises equivalent transformation strain at 0.6%

(b) Phase transformation surface of Ni-Ti polycrystal in the space (σ_1, σ_2) [Lexcellent and Blanc, 2004]

Figure 2.19: Comparisons of phase transformation surface between SMSM and experimental test/phenomenological model of Ni-Ti polycrystal.

- Path 2: $\vec{x}$ and $\vec{y}$ axes have been inverted comparing to path 1. The final stress point is exactly the same.

As we can see in Figure 2.20, the strain (total strain) response of the NiTi polycrystal for paths 1 and 2 is nearly symmetrical regarding to $\epsilon_{xx} = \epsilon_{yy}$ axis (ϵ_{zz} component exists but has not been plotted), in accordance with the transverse isotropic texture of the material, but the strain levels at the final point are strongly different highlighting the strong non-linear and hysteretic character of the material behavior. Some comparisons with experiments should be necessary too to validate the modeling.

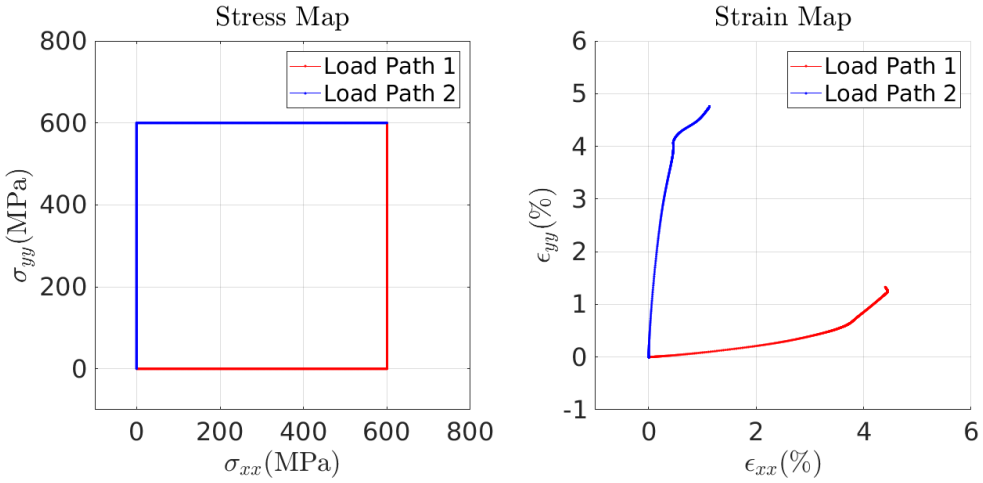

Figure 2.20: Illustration of the material behavior in case of non proportional loading and sensitivity to the stress path: stress and corresponding total strain paths

2.6.7 Pseudoelasticity and heat dissipation

All numerical simulations presented in this section until now have been obtained using isothermal condition ($k = \infty$). This choice has been made for an easier interpretation of results and because anisothermal conditions only make sense in the framework of a structure calculation with controlled thermal boundary conditions. The influence of heat dissipation and exchange of NiTi polycrystal can however be illustrated for all previous cases. It must be kept in mind that the validity of the results remains questionable considering the fact that a RVE is not a structure. A simple test case is proposed as an illustration: it is a 1D tensile stress controlled loading and unloading, using a stress rate $\dot{\sigma} = 1\,\mathrm{MPas}^{-1}$ and a maximum stress $\sigma_{max} = 600\,\mathrm{MPa}$ at $T = 293K$ (initial and ambient temperature). Three different heat dissipation conditions are applied:

- Adiabatic: $k = 0$ J.m^{-3}.K^{-1}
- Isothermal: $k = \infty$ (see subsection 2.6.1)
- moderate heat exchange: k =0.05 J.m^{-3}.K^{-1}

Results are plotted in Figure 2.21. The following comments can be proposed:

- The anisothermal situation has already been discussed. It corresponds to a perfect convection (or conduction) situation describing a quasi-static transformation;
- As we can see in Figure 2.21b, the emission of latent heat due to $A \rightarrow M$ phase transformation leads to a very high temperature increase reaching up to T=355 K for the adiabatic situation. This temperature increase is accompanied by a concommitant phase transformation threshold increase (see Figure 2.21c). Of course, the initial temperature of NiTi polycrystal ($T = 293K$) is almost fully recovered during unloading due to the heat absorption associated with the backward phase transformation ($M \rightarrow A$);
- In case of moderate heat exchange, the latent heat due to $A \rightarrow M$ phase transformation acts as heat source that brings to a temperature increase up to $T = 305K$ during loading. Indeed a part of the power source is transmitted to the (virtual) surrounding medium. The temperature of NiTi polycrystal decreases next to $T = 282K$ during the unloading reaching a temperature below the ambient temperature. These small temperature variations result in a moderate stress threshold increase during loading and a moderate stress threshold decrease during unloading. This phenomenon leads to a significant increase of hysteresis area, comparing to the isothermal situation (see Figure 2.21c).

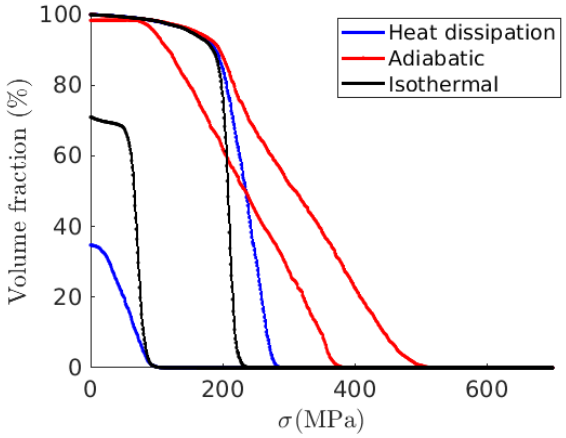

(a) Evolution of variants volume fractions as function of stress for the selected grain

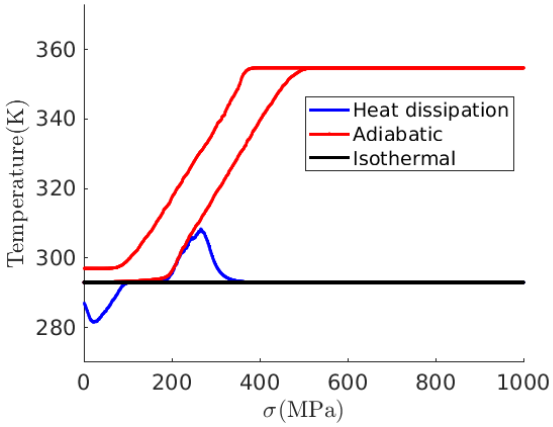

(b) Temperature evolution as function of stress

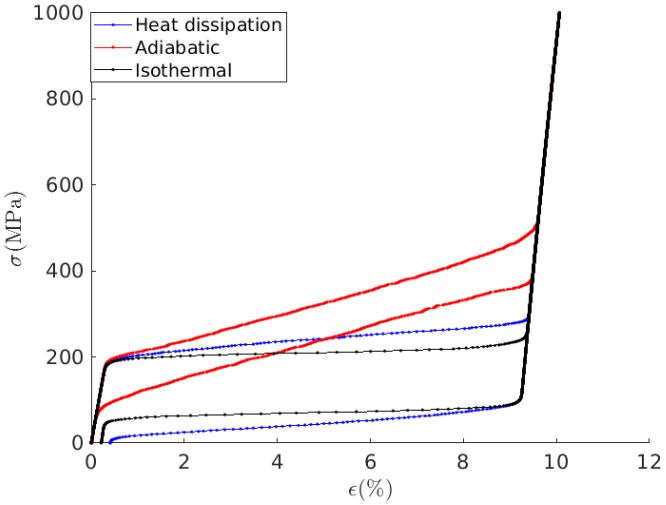

(c) stress-strain curves

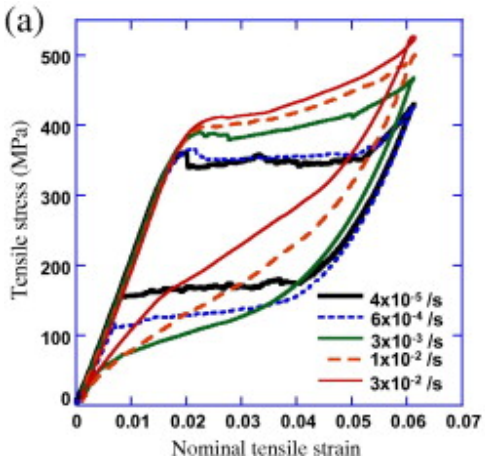

(d) Experimental observations [He and Sun, 2011] of the rate dependency of the stress/strain curves

Figure 2.21: Illustration of pseudoelastic behavior from SMSM depending on thermal conditions and comparison to NiTi SMA experimental data.

- These results are in accordance with results reported in Figure 2.21d where stress/strain cycles are performed at different strain rates, corresponding to different apparent convection conditions [He and Sun, 2011].

2.7 Conclusion

Objectives

This chapter focused on simulating the hysteretic behavior of a Ni-Ti SMA at the scale of polycrystal and below.

Stochastic multiscale model

A stochastic multiscale thermomechanical modeling of shape memory alloys (SMSM) has been presented. The stochastic description of the volume fraction of phase variants is ensured by a kinetic Monte-Carlo algorithm, using the local Gibbs free energy density as a main input. This model includes an instantaneous description of the germination process from variant to variant. It leads to simulate hysteretic and non-linear mechanical behavior of SMA materials and the phase volume fraction kinetic includes the nucleation of so-called R-phase usually omitted in former models. Only few parameters are required to describe the hysteretic behavior at the grain and RVE scales by successive homogenization: most of them can be obtained via a simple DSC scan. The model developed can be extended to simulate any SMA and MSMA material.

Qualitative comparison

Comparisons between simulated results and experimental observations were also summarized and were found to be in good agreement with each other: DSC scan; pseudo-elasticity under tension and compression; hysteresis loops for partial transformation; one way shape memory effect and stress-assisted two ways shape memory effect; tension-compression asymmetry and non-proportional loading effects.

Advantages and drawbacks

To the best knowledge of authors, no phenomenological model has demonstrated such capabilities to describe so completely a so wide diversity of behaviors. The model demonstrated its strength especially when phase transformation induced by multi-axial thermomechanical load was not fully finished and unloading begins. [Lagoudas et al., 2016] and [Patoor et al., 2006] has presented a summary of most classical existing models in recent twenty years. A brief comparison between several most classical models including SMSM is proposed in Table 2.2, underlining the relatively universal character of the present modeling. Moreover, the robustness and simplicity of presented stochastic modeling must be underlined: for example, the computation time to obtain a 2D transformation stress threshold (3.6×10^6 stress points) takes 8 hours for the investigated NiTi polycrystalline containing 413 grains (about 8 ms per point) with a processing power of 20 parallel

$\times$2.2 GHz computers.
Improvements are however possible. It has been for example shown that the R-phase to martensite peak emission during a DSC scan is not properly modeled (insufficient width). One possible explanation is that the mechanical incompatibility is not taken into account at the scale of variant. Indeed the presence of any M variant inside the grain would induce several variant-types prohibition at its neighborhood. The spatial heterogeneity of germination and associated variants' prohibition (see the work of [Soejima et al., 2016]) would slow down the process of phase transformation. The definition of a specific interaction matrix is a possible solution to take these phenomenon into account in a modeling, as proposed in the work of [Siredey et al., 1999] and [Patoor et al., 2006]). The numerical difficulty is the main obstacle to implement this interaction into the stochastic model.

More importantly, implementation of current model as constitutive behavior of RVE to a structural model is required to compute accurately the thermomechanical field.
For that purpose, a better understanding of the localization phenomena during the mechanical loading of SMA is required. A global full-filed measurement of the kinematic fields of a Ni-Ti specimen under uniaxial and multiaxial loading is proposed in the next chapter.

Model	Anisoth.	Non-prop.	Internal Variables	Partial load	OWSME	SA-TWSME	Asym.	Phase	Velocity	Cyclic Loading
[Lexcellent et al., 2006]	×		z_σ, π_f				×	A/M		
[Patoor et al., 2006]	×		H^{mn}			×		A/R/M		
[Chemisky et al., 2014]	×		$K(T), Q(t), Y_{vp}(t)$			×		A/M	×	×
[Lagoudas et al., 2016]	×	×	ξ^f, ξ^r, p^{re}				×	A/M	×	
[Helbert et al., 2018]	×		$\mu_M, \mu_R, \sigma_M^*, \sigma_R^*$					A/R/M	×	×
KMC	×	×	$f(i,t)$	×	×	×	×	A/R/M	×	×

Table 2.2: Comparison of some thermodynamic models for SMA.

Chapter 3

Kinematic full-field measurement via DIC

Contents

3.1 Introduction

In this chapter, we mainly focus on the measurement of the PE behavior of a NiTi SMA subjected to uniaxial and several multiaxial loading. Since the phase transformation appears in localization bands for both 1D and 2D specimens (as it will be shown), a measurement of the kinematic fields by digital image correlation (DIC) is necessary during the mechanical tests.
The regularized DIC has been used to grant a higher spatial resolution and reduce the uncertainties of the kinematic field. The principles of this technique, the associated numerical implementation and its main characteristics are presented. The experimental set-up (so called *MiniAstree*), 1D and 2D specimen geometries are presented next. A series of experimental results showing the PE behavior of NiTi SMA under uniaxial loading, multiaxial loading, proportional and non proportional loading are presented and compared with the numerical results from the SMSM at the end of this chapter.

3.2 Full-field measurement

The full-field technique allows the kinematic fields over a large area to be obtained. It provides a quantitative description of 2D displacement and 2D deformation fields in the region of interest (ROI) of the specimen. It is also worthy mentioning that since an optical imaging technique without contact is used, full field measurement tools are non intrusive by nature. A combination with other physical measurement is consequently allowed (X-ray diffraction mapping as addressed in the next chapter, or infrared imaging). The *PGD-RT3* DIC code developed by LMT has been used for the study. We begin this section by a presentation of the main principles of this method. For more details, lecturers are invited to look at the work of [Berny et al., 2018].

3.2.1 DIC - principles

Gray-level conservation. It is assumed that the gray level is conserved between the reference image $f(\mathbf{x})$ at initial configuration and an current image $g(\mathbf{x})$ at a deformed configuration, and that variations between images f and g is only due to the displacement $\mathbf{u}(\mathbf{x}, t)$:

$$f(\mathbf{x}) \simeq g(\mathbf{x} + \mathbf{u}(\mathbf{x}, t)) \tag{3.1}$$

where $\mathbf{u}(\mathbf{x}, t)$ is the displacement field in the deformed configuration. The sought displacement field minimizes the correlation residuals functions Φ_c^2 over the chosen

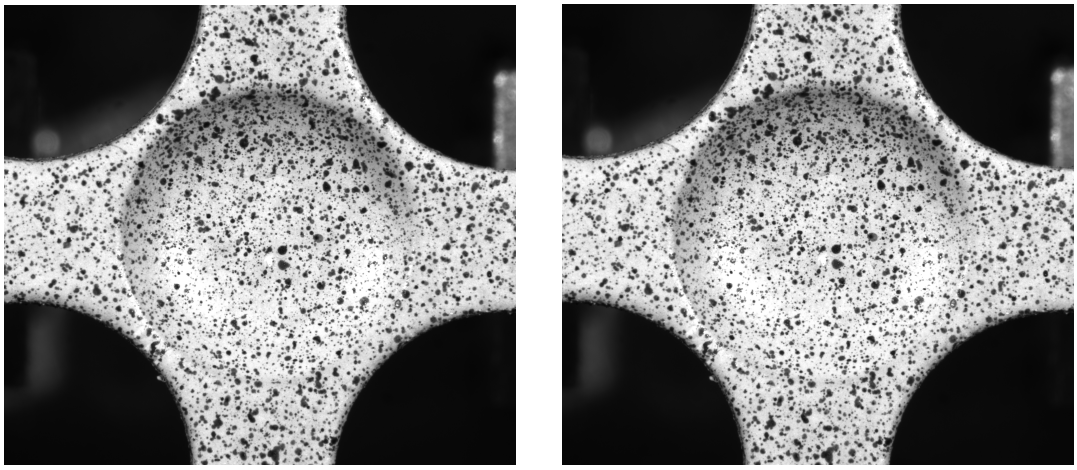

Figure 3.1: (a) Reference image at reference configuration; (b) current image at deformed configuration

region of interest (ROI):

$$\mathbf{u}(\mathbf{x}) = \arg\min(\Phi_c^2) \tag{3.2}$$

with

$$\Phi_c^2 = \int_{\text{ROI}} \phi_c^2(\mathbf{x}) d\mathbf{x} \tag{3.3}$$

where $\phi_c(\mathbf{x})$ defines the field of correlation residuals:

$$\phi_c(\mathbf{x}) = |g(\mathbf{x} + \mathbf{u}(\mathbf{x})) - f(\mathbf{x})| \tag{3.4}$$

A global approach is used here to circumvent the Gaussian noise distributed in the optical imaging.

Global approach with a Finite Element formulation. By adopting a global linear formulation, the residual field is integrated inside the ROI Ω.

$$\mathbf{u}(\mathbf{x}) = \arg\min \iint_{\Omega} |f(\mathbf{x}) - g(\mathbf{x}) - \nabla g(\mathbf{x}) \cdot \mathbf{du^i}|^2 d\Omega \tag{3.5}$$

where superscript i denotes the iteration index of the Newton procedure, and $\mathbf{u}(\mathbf{x})$ is spatially discretized as follows:

$$\mathbf{u}(\mathbf{x}) = \sum_n a_n \varphi_n(x) \tag{3.6}$$

where a_n is the associated d.o.f and $\varphi_n(x)$ is a n-th polynomial spatial shape function.

The resolution of the kinematic field $\mathbf{u}(\mathbf{x})$ is achieved by solving successively the linear system at each iteration:

$$[\mathbf{M}]\{\mathbf{du}\} = \{\mathbf{b}\} \qquad \text{or} \qquad b_i = M_{ij} du_j \tag{3.7}$$

where the components of $[\mathbf{M}]$ can be expressed as:

$$M_{ij} = \iint_{\Omega} (\varphi_i(\mathbf{x}) \cdot \nabla^t f(\mathbf{x}))(\varphi_j(\mathbf{x}) \cdot \nabla f(\mathbf{x}))d\mathbf{x} \tag{3.8}$$

$\mathbf{b}$ is a vector that vanishes when a perfect fit is obtained for each pixel. It verifies:

$$b_i = \iint_{\Omega} (\varphi_i(\mathbf{x}) \cdot \nabla^t f(\mathbf{x}))(f(\mathbf{x}) - g(\mathbf{x} + \mathbf{u^i}(\mathbf{x})))d\mathbf{x} \tag{3.9}$$

The displacement field is updated as follows:

$$\mathbf{u^{i+1}}(\mathbf{x}) = \mathbf{u^i}(\mathbf{x}) + \mathbf{du^i}(\mathbf{x}) \tag{3.10}$$

Challenges. One of the limitations of DIC comes from its ill-posedness (second minima trapping). The limited available information (generally two gray-level stored images) impedes the measurement of fast fluctuations of the displacement field, and hence constitutes a potential barrier to very small scale displacement resolution. Consequently, a compromise has to be found between the uncertainty in kinematic field and the desired spatial resolution.

Mechanical regularization. A mechanics-based regularization has been proposed by [Tomicevic et al., 2013]. This regularization acts as a low-pass filtering and assumes that high frequency components of the kinematic field are most likely due to the ill-posed nature of DIC and its resolution. It is based on the mechanical admissibility of the problem, expressed in the sense of Finite Elements (FE) interpolations. The notion of *equilibrium gap* has to be introduced. Indeed, if we enforce the isotropic elastic model for example, the equilibrium equation reads as

$$[\mathbf{K}]\{\mathbf{u}\} = \{\mathbf{f}\} \tag{3.11}$$

When the stiffness matrix $[\mathbf{K}]$ is given but the displacement vector $\mathbf{u}(\mathbf{x}, t)$ is not appropriate, the calculated generalized forces will differ from the true forces. Consequently the components of the residual force vectors f_r that is defined as the difference between true and calculated forces (**Equilibrium gap**), will be high. The mechanical regularization (equilibrium gap method) consists in the minimization of these mechanical residuals:

$$\Phi_m^2 = \{\mathbf{u}\}^\mathbf{t}[\mathbf{K}][\mathbf{K}]^\mathbf{t}\{\mathbf{u}\} \tag{3.12}$$

Φ_m^2 is the equilibrium gap of the ROI, which represents the sum of squared sum of all the equilibrium gaps at the interior nodes only. Moreover, any displacement field prescribed at the boundary nodes gives rise to a displacement field for which $\Phi_m = 0$. The method requires an additional regularization. The purpose of this regularization is to penalize the short wavelength displacement fluctuations of the boundary nodes. We introduce the function Φ_b^2 that measures the **boundary fluctuations** of the **ROI**:

$$\Phi_b^2 = \{\mathbf{u}\}^\mathbf{t}[\mathbf{L}][\mathbf{L}]^\mathbf{t}\{\mathbf{u}\} \tag{3.13}$$

$[\mathbf{L}]$ is an operator acting only at the boundary nodes. Its construction is detailed in [Tomicevic et al., 2013]. This operator has a relatively simple mechanical interpretation. A third aspect of the Regularized DIC is that it removes the rigid body motion.

In order to minimize the three terms (Correlation Residuals Φ_c^2, Equilibrium Gap Φ_m^2 and Boundary Fluctuations Φ_b^2), a new residual function Φ_t has to be introduced:

$$(1 + w_m + w_b)\Phi_t^2 = \tilde{\Phi}_c^2 + w_m\tilde{\Phi}_m^2 + w_b\tilde{\Phi}_b^2 \tag{3.14}$$

w_m and w_b are the weights that define the length scales associated with $\tilde{\Phi}_m^2$ and $\tilde{\Phi}_b^2$ (symbol ˜ denotes a normalization operation). To perform the procedure of normalization, we use a displacement field in the form of a plane wave $\mathbf{v}(\mathbf{x}) = \mathbf{v_0}\exp(i\mathbf{k}\cdot\mathbf{x})$ where $\mathbf{v_0}$ is the amplitude of the wave and $\mathbf{k}$ is the wave vector. The normalized residuals become:

$$\tilde{\Phi}_c^2 = \frac{\Phi_c^2}{\{\mathbf{v}\}^\mathbf{t}[\mathbf{M}]\{\mathbf{v}\}}, \tilde{\Phi}_m^2 = \frac{\Phi_m^2}{\{\mathbf{v}\}^\mathbf{t}[\mathbf{K}][\mathbf{K}]^\mathbf{t}\{\mathbf{v}\}}, \tilde{\Phi}_b^2 = \frac{\Phi_b^2}{\{\mathbf{v}\}^\mathbf{t}[\mathbf{L}][\mathbf{L}]^\mathbf{t}\{\mathbf{v}\}} \tag{3.15}$$

And the weight w_m and w_b are chosen as

$$w_m = (2\pi|\mathbf{k}|l_m)^4\,,\; w_b = (2\pi|\mathbf{k}|l_b)^4 \tag{3.16}$$

where l_m and l_b denote the regularization length for Φ_m^2 and Φ_b^2

When the material parameters are known (this is the case for NiTi specimens), the minimization of Φ_t^2 with respect to the unknown degrees of freedom can be performed even at the pixel scale. In the following, the element mesh is considered to be a 3-nodes triangle ($T3$) associated with a cubic displacement interpolation.

Representation of data. The localization phenomenon of SMA is associated with an isochoric strain that comes out through the formation of shear bands. Consequently, some displacement discontinuity may appear toward the normal of bands (leading to significant strain gradient). All components of in plane deformation ($\epsilon_{xx}, \epsilon_{yy}, \epsilon_{xy}$) include information on the kinematic fields over the

specimen surface.

$$\boldsymbol{\epsilon}(\mathbf{x},t) = \frac{\nabla u(\mathbf{x},t) + \nabla^t u(\mathbf{x},t)}{2} \tag{3.17}$$

Using Levy-Mises equivalent strain as a norm is finally a good way to represent the strain gradients in one single representation. The Levy-Mises equivalent strain expresses as follows:

$$\epsilon_{eq} = \sqrt{\frac{2}{3}(\mathbf{d}:\mathbf{d})} \tag{3.18}$$

with $\mathbf{d}$ the strain deviator verifying:

$$\mathbf{d} = \boldsymbol{\epsilon} - \frac{1}{3}\mathrm{tr}(\boldsymbol{\epsilon})\mathbf{1} \tag{3.19}$$

Incompressibility hypothesis is used (that supposes to neglect the elastic part of strain), leading to:

$$\mathrm{tr}(\boldsymbol{\epsilon}) \simeq 0 \rightarrow \epsilon_{zz} \simeq -\epsilon_{xx} - \epsilon_{yy} \tag{3.20}$$

and

$$\epsilon_{eq} \simeq \sqrt{\frac{4}{3}\left[\epsilon_{xx}^2 + \epsilon_{yy}^2 + \epsilon_{xx}\epsilon_{yy} + \epsilon_{xy}^2\right]} \tag{3.21}$$

The associated equivalent strain rate field can also be deduced:

$$\dot{\epsilon}_{eq}(\mathbf{x},t) = \frac{\epsilon_{eq}(\mathbf{x},t^{n+1}) - \epsilon_{eq}(\mathbf{x},t^n)}{t^{n+1} - t^n} \tag{3.22}$$

A strain rate representation allows an observation of transformation front evolution either in time or in space.
Moreover, using the equivalent strain brings significant simplification when the SMA specimen is subjected to a multiaxial loading. Representations using axial strain are however useful when a comparison to an experimental axial response from the literature is looked for.

3.2.2 Numerical implementation of the mechanical regularization

In most cases, the correlation residuals are non linear functions depending on the degrees of freedom in the ROI. A Newton iterative procedure is used to handle with the non-linear aspect of the minimization problem. By adopting small increment of $\mathbf{du^i}(\mathbf{x})$ of the solution from Equation 3.10, $\frac{\partial \Phi_t^2}{\partial u^j} = \{0\}$ is recast in a matrix-vector product as

$$([\mathbf{M}] + [\mathbf{N}])\{du\} = \{b\}^j - [\mathbf{N}]\{u\}^j \tag{3.23}$$

with

$$[\mathbf{N}] = w_m \frac{\{\mathbf{v}\}^{\mathbf{t}} [\mathbf{M}] \{\mathbf{v}\}}{\{\mathbf{v}\}^{\mathbf{t}} [\mathbf{K}] [\mathbf{K}]^{\mathbf{t}} \{\mathbf{v}\}} [\mathbf{K}]^t [\mathbf{K}] + w_b \frac{\{\mathbf{v}\}^{\mathbf{t}} [\mathbf{M}] \{\mathbf{v}\}}{\{\mathbf{v}\}^{\mathbf{t}} [\mathbf{L}] [\mathbf{L}]^{\mathbf{t}} \{\mathbf{v}\}} [\mathbf{L}]^t [\mathbf{L}] \tag{3.24}$$

For each iteration j, the picture in the deformed configuration is corrected by using the current estimates of the displacement $\{u^j\}$. Then the vector $\{b^j\}$ is accordingly updated. However, matrices $[\mathbf{M}]$ and $[\mathbf{N}]$ are computed once for all iterations. Iterations stop when the displacements correction $\{du\}$ is smaller than the convergence criteria chosen by the user.

In general, the regularization procedure is introduced to mend the trapping problem of the second minimum, which is usually related to the choice of a very fine mesh. This regularization procedure is based on the assumption that the displacement field is in accordance with an elastic continuous medium. Thus, in the practical analyze of numerical resolution, a specific approach called as 'Relaxation' is used: the problem is first solved by using very large regularization lengths l_m and l_b. These lengths are progressively decreased keeping the previous displacement as an initial set for a second iteration.

3.3 Experimental setup for the study of NiTi SMA

3.3.1 Experimental protocol and setup

The uniaxial loading test is conducted by a multiaxial (biaxial) loading machine *Mini Astree*[1](see Figure 3.2). This machine can reach a maximal force $F_{max} = 2.3\,\text{kN}$ per axis. This specially designed machine, piloted by a MTS program, makes it feasible to conduct multiaxial tension or compression loading tests and can be also positioned inside the XRD chamber at LMT or inside a Scanning Electron Microscope (SEM).

Mechanical loading command The machine can apply prescribed displacements or forces as function of time along two orthogonal directions $\mathbf{e}_x$ and $\mathbf{e}_y$ using opposite actuators. Actuators can be controlled in a symmetrical way so that to keep the geometrical center of the specimen motionless [Chevalier et al., 2005] [Bertin, 2016].

Throughout this PhD thesis, a displacement-controlled loading has been used to investigate the macroscopic behavior of SMA. We define u_x and u_y the differences

[1]This name refers to the famous triaxial machine ASTREE available in LMT for macroscopic samples - 100kN along two orthogonal horizontal axes and 250KN along the vertical axis.

in axial displacements applied by actuators along $\mathbf{e}_x$ and $\mathbf{e}_y$, so that:

$$u_x(t) = (U_2(t) - U_4(t)) \tag{3.25}$$
$$u_y(t) = (U_3(t) - U_1(t)) \tag{3.26}$$
$$U_2(t) = -U_4(t) \text{ and } U_3(t) = -U_1(t)$$

where $U_\alpha(t), \alpha = 1 \cdots 4$ indicate the displacement applied by each actuator, as depicted in Figure 3.2.
The axial forces are recorded by cells positioned between actuators and clamps, hence the axial force can be expressed as:

$$F_x(t) = \frac{F_2(t) + F_4(t)}{2}$$
$$F_y(t) = \frac{F_3(t) + F_1(t)}{2} \tag{3.27}$$

The forces indicated two by two are theoretically equal. Any discrepancy means that an asymmetry has occurred, which may invalidate the results since the test conditions are no longer nominal.

Optical Imaging A digital optical camera EDGE-PCO is positioned in front of the surface of specimen with a telecentric lens. It allows a spatial resolution of about 7.5 µm per pixel. Two cold LED lights generate quasi-constant lightning conditions for the observation of the specimen surface. The surface is covered with black/white speckle paints (see Figure 3.1) to provide an sufficient gray level contrast. The reference image is taken at the onset of the test. The image sampling frequency is fixed at $1\,\mathrm{s}^{-1}$ for all tests except for the 1D high strain rate test ($10\,\mathrm{s}^{-1}$). As explained in chapter 1, the PE behavior is highly influenced by the room/ambient temperature. A temperature regulation setup (see Figure 3.3) has been designed to conduct the mechanical tests at fixed temperature. A thermo-electric Peltier module provides an external heat source. The cooled/warmed air is blown by a fan toward the biaxial testing machine. This experimental setup permits to vary the initial temperature of the specimen ranging from $10\,^\circ\mathrm{C} \leq T \leq 50\,^\circ\mathrm{C}$.
Of course, a mechanical induced phase transformation is accompanied by a heat emission or absorption that leads to local temperature fluctuations despite the temperature regulation setup. The thermal field of the specimen can not be considered as isothermal. The temperature regulation setup only allows having specimens at different initial temperatures corresponding to different ambient temperatures.

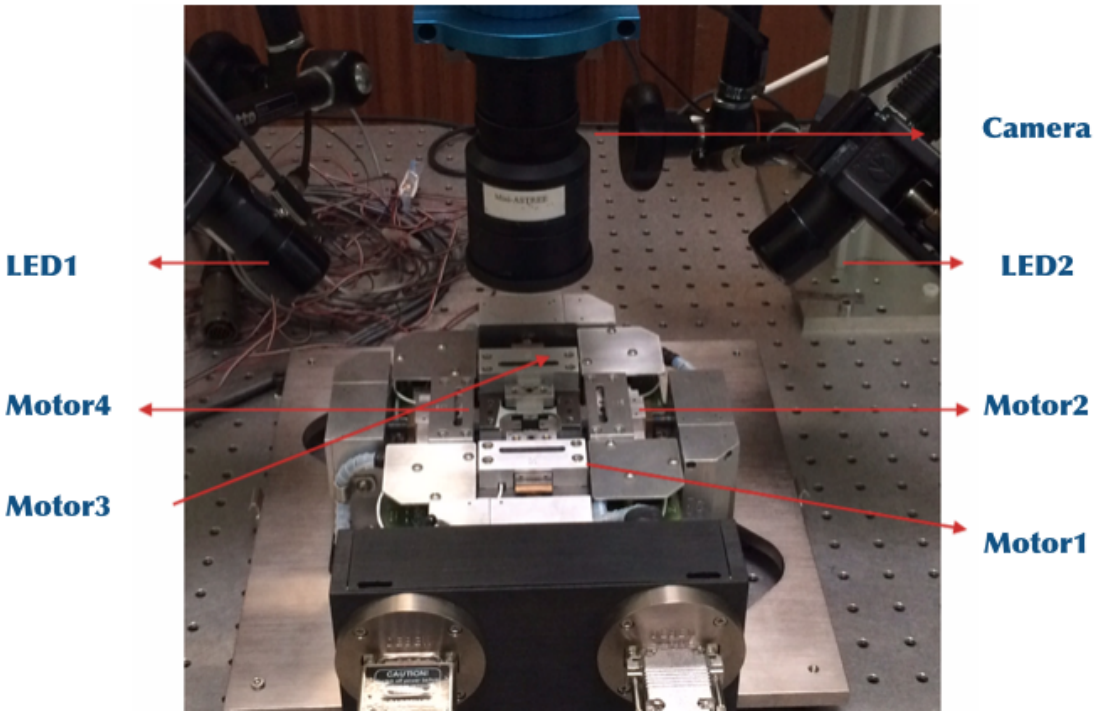

Figure 3.2: Experimental setup of uniaxial loading test

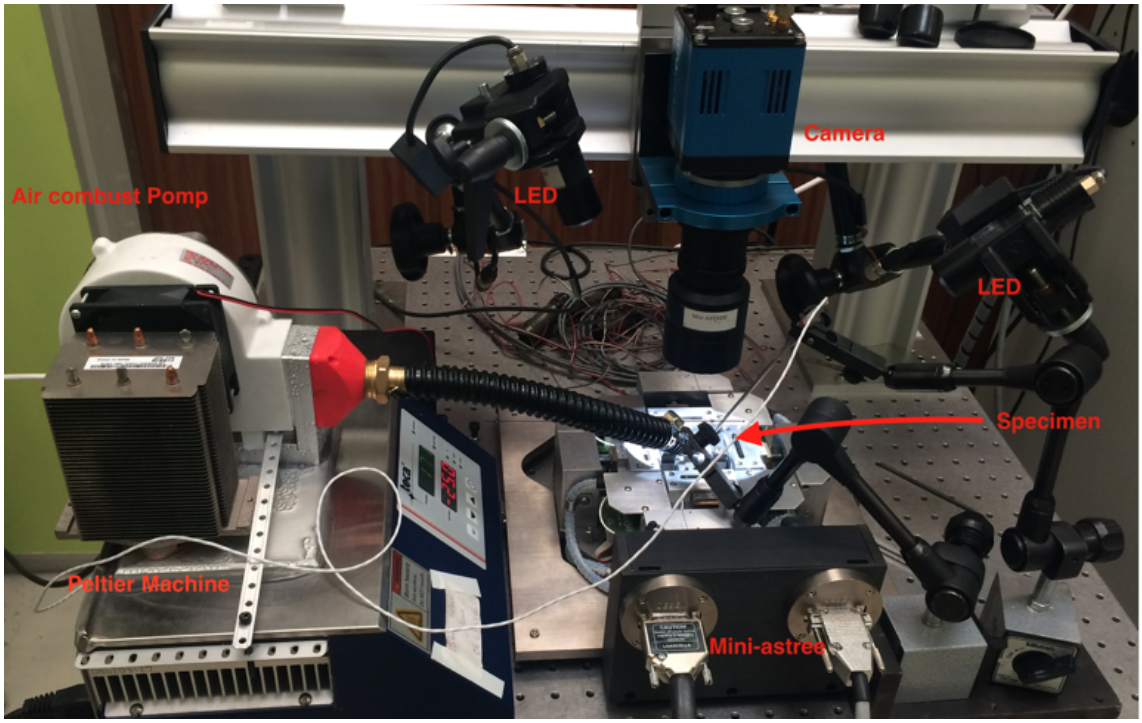

Figure 3.3: Air-convection cooling system

3.3.2 Geometry of the specimens

The geometry of the 1D specimen is illustrated in Figure 3.4a, its central region is a parallepipedic rectangle :

$$V = 10 \times 3 \times 0.3\,\mathrm{mm}^3 \tag{3.28}$$

This design has been chosen first to reach a stress higher than 600 MPa at an intermediate force level and avoids secondly the specimen to accumulate heat during the martensite transformation by improving the heat convection with the ambient environment.
The 2D specimen is illustrated in Figure 3.6 and Figure 3.7. This design has been developed during the work of [Fall, 2017]. The region of interest is a central disk with a thickness $h = 0.3\,\mathrm{mm}$ and a radius of $r = 1.5\,\mathrm{mm}$. The thickness of the specimen grants to have a stress concentration enough to reach a biaxial stress level of 600 MPa, and a good heat convection rate.
Both the 1D and 2D specimen are obtained initially by cold rolling, then followed by diamond tool cutting for the region of interest and heat treated to obtain the **PE** effect.

As proposed in [Fall, 2017], a finite element calculation via Abaqus has been conducted. Using the assumption that specimen remains purely elastic during the loading, this modeling allows an estimation of the average stress level in the central region of the 2D specimen. This assumption becomes less acceptable after the onset of the phase transformation, when the deformation significantly increases. The finite element calculation gives also a direct indication of an acceptable radius r_{max} to position a virtual gauge. r_{max} is chosen to get a homogeneous stress distribution and a shear strain that remains close to zero.

$$|\epsilon_{xy}(r \leq r_{max})| < 1\%\,\max[\,{}_{\mathrm{Sup}}(|\epsilon_{xx}|, |\epsilon_{yy}|)] \tag{3.29}$$

As illustrated in Figure 3.7, the specimen is painted with black and white speckle patterns. The red rectangle drawn in the figure indicates the chosen ROI for DIC analysis. The blue circle indicates the area of the virtual gauge used to calculate the average strain field. The same area is chosen to calculate the passage matrix $\mathbf{P}$ which permits to convert the experimental measured forces applied along each axis (F_x, F_y) toward the stress components $(\sigma_{xx}, \sigma_{yy})$ of the average stress tensor using the Abaqus modeling (see Equation 3.31 - values are given in MPa/N).

$$\{\boldsymbol{\sigma}\} = \mathbf{P}\{\mathbf{F}\} \tag{3.30}$$

or

$$\begin{Bmatrix} \sigma_{xx} \\ \sigma_{yy} \end{Bmatrix} = \begin{Bmatrix} 0.311 & -0.092 \\ -0.092 & 0.311 \end{Bmatrix} \begin{Bmatrix} F_x \\ F_y \end{Bmatrix} \tag{3.31}$$

Figure 3.8 shows the Abaqus calculation and the applied boundary conditions. For each actuators, the displacements realized are :

$$U_2 = 0.03\,\text{mm} \quad \text{and } U_4 = -0.03\,\text{mm} \tag{3.32}$$

$$U_3 = 0.03\,\text{mm} \quad \text{and } U_1 = -0.03\,\text{mm} \tag{3.33}$$

Figure 3.9 plots the amplitude of the Von Mises equivalent stress (given by Equation 3.34 considering plane stress condition) for an equibiaxial stress ($F_x = F_y = 1400$ N).

$$\sigma_{eq} = \sqrt{\frac{1}{2}\left[\sigma_{xx}^2 + \sigma_{yy}^2 + (\sigma_{xx} - \sigma_{yy})^2 + 6\sigma_{xy}^2\right]} \tag{3.34}$$

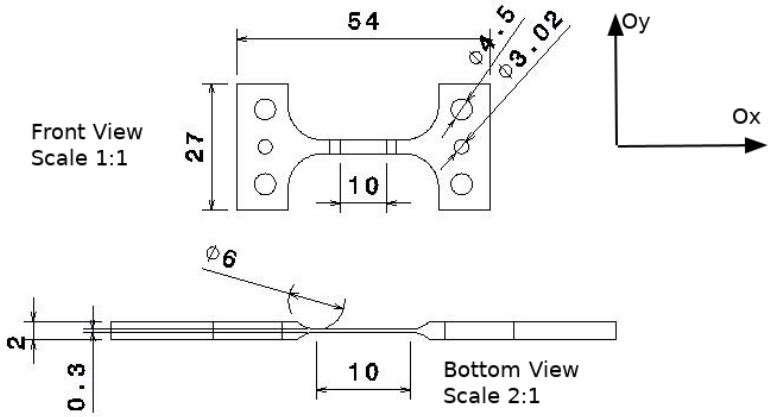

(a)

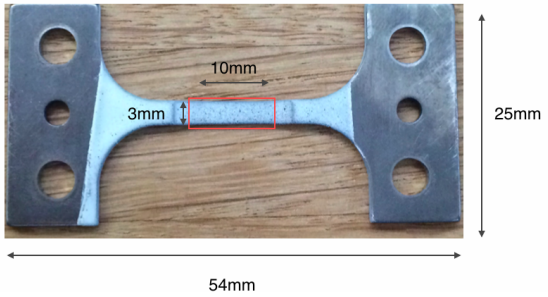

(b)

Figure 3.4: (a) Geometry of the 1D specimen; (b) 1D strip specimen with black and white speckle paints.

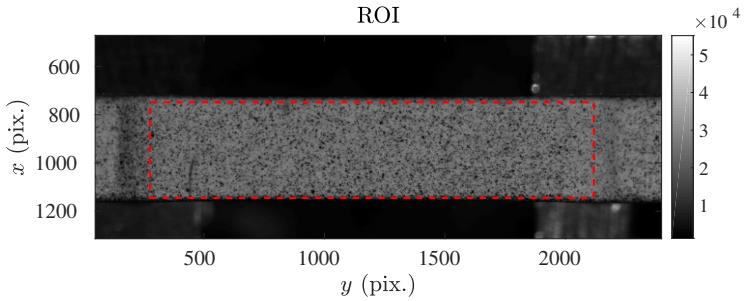

Figure 3.5: Black and white speckle patterns covering the central region. The ROI is plotted in red.

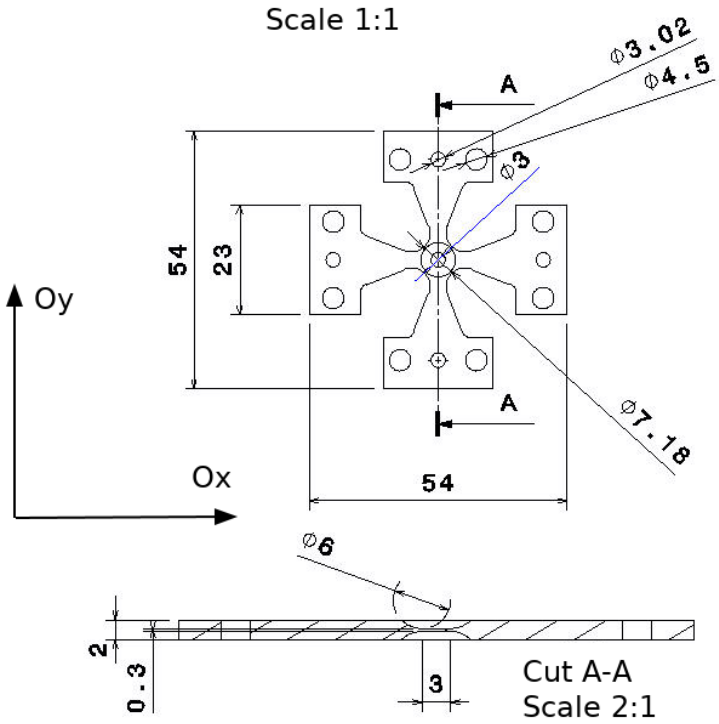

Figure 3.6: 2D specimen used for multiaxial loading

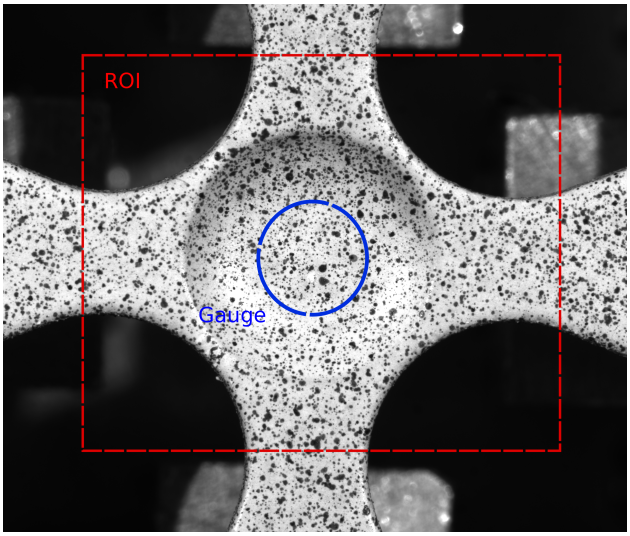

Figure 3.7: 2D specimen: (the red rectangle represents the ROI chosen for DIC and the blue circle indicates the virtual gauge.)

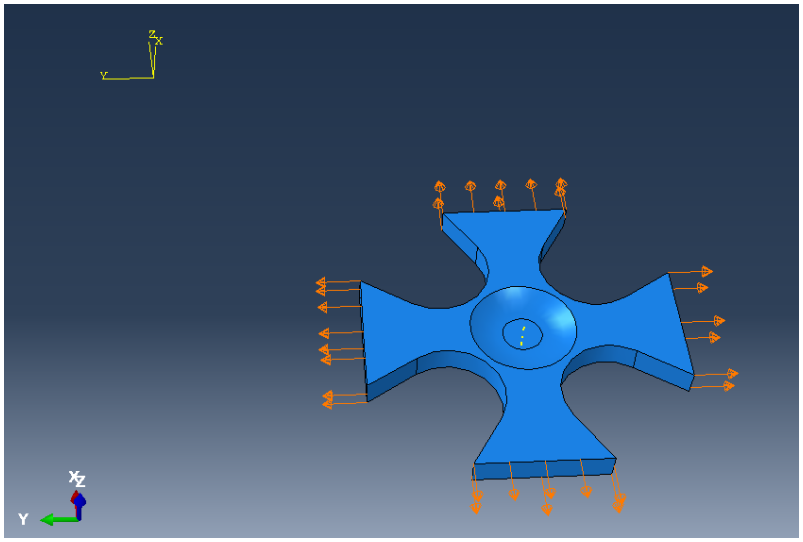

Figure 3.8: Abaqus design and boundary conditions.

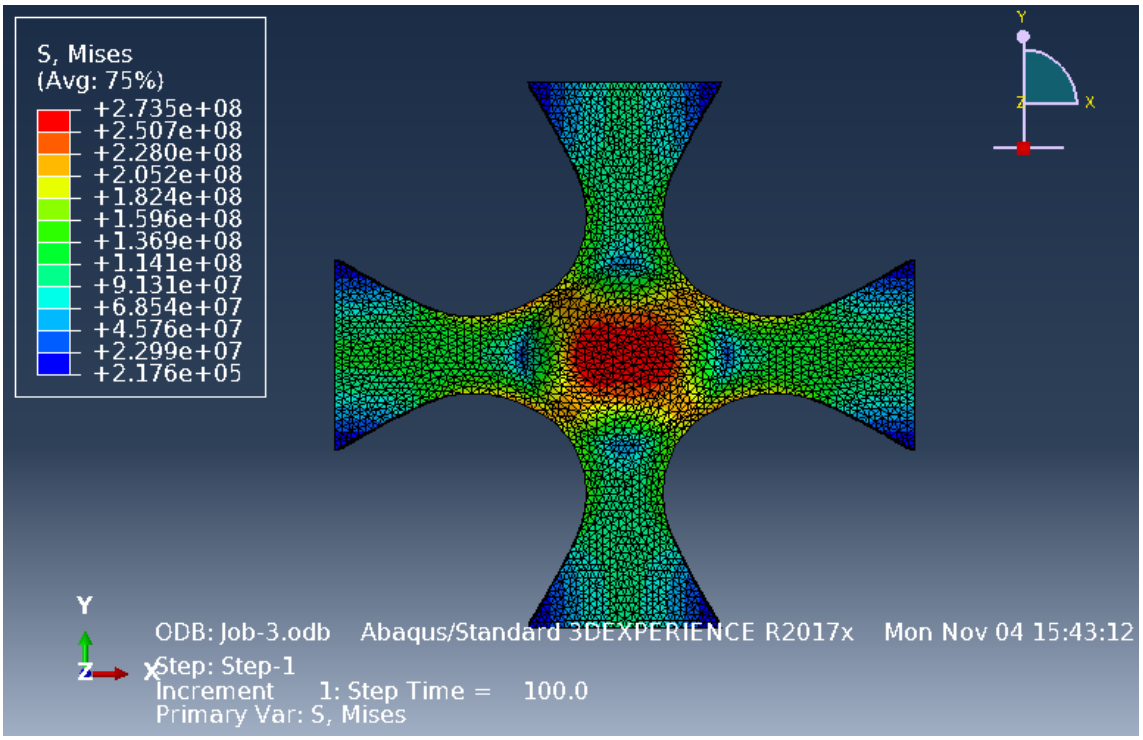

Figure 3.9: Von Mises stress from FE calculation.

3.3.3 Choice of finite element mesh size for regularized DIC

Theoretically, a large mesh size allows the displacement uncertainty estimated by DIC to be decreased. A good spatial resolution of the localization phenomena requires on the contrary a very small mesh size. A compromise has therefore to be chosen.

In order to illustrate the performance of the mechanical regularization, we choose the kinematic displacement field obtained during the tensile loading[2] of a NiTi strip at room temperature ($T = 300\,\mathrm{K}$).

A first uncertainty study is conducted over a static image sequence (20 images in total without external stress load). Since no external load is applied and assuming no significant fluctuation of the lightning conditions, the expected spatial-temporal displacement field should be strictly zero. The calculated displacement field is giving consequently the uncertainty associated with the texture of black and white speckle paints and with the chosen element size. Several T3 meshs with a characteristic {4,8,16,32,64,128} pixels have been chosen. The corresponding uncertainty in displacement field δU is plotted in Figure 3.11. Decreasing the mesh size leads to an exponential increase of the uncertainty. In this situation, a characteristic size of 16 pixels for the mesh leads to a good compromise between accuracy of spatial description and a relatively low uncertainty level.

[2]The velocity used is $\dot{u}_x = 1 \times 10^{-3}\,\mathrm{mm\,s^{-1}}$

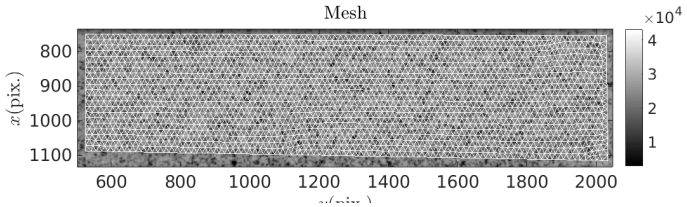

(a) FE Mesh with an element size of 16 pix.

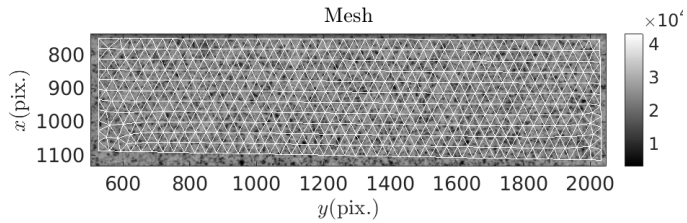

(b) FE Mesh with an element size of 32 pix.

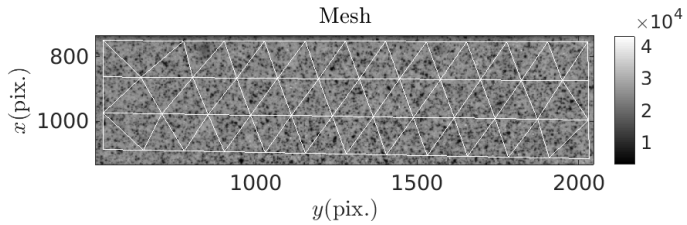

(c) FE Mesh with an element size of 128 pix.

Figure 3.10: Visualization of several FE mesh with different element sizes

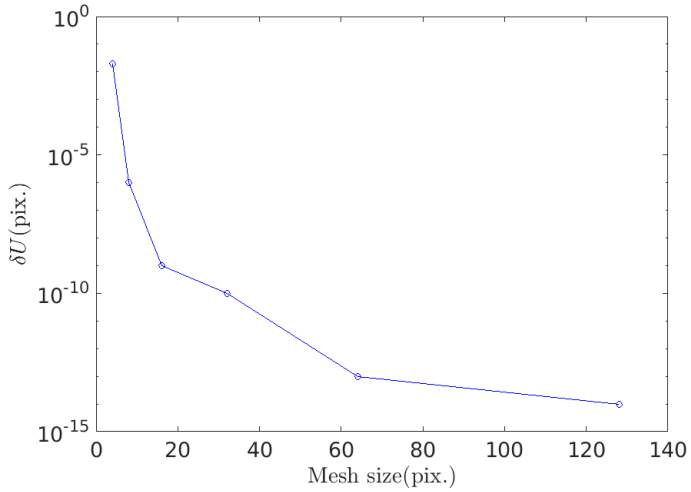

Figure 3.11: Uncertainty in the displacement field's determination for the same speckle with different characteristic sizes of elements

3.3.4 Performance of the mechanical regularization

The choice of a mesh size of 16 pixels($\simeq 0.1\,\mathrm{mm}$) leads however to a relative high uncertainty compared to a larger mesh size (e.g. 128 pixels). Uncertainties may be

too high to properly describe the phenomena of localization bands, especially in a zone with strong strain gradients.

One possible solution is to add a part of mechanical admissibility to estimate the kinematic field. This is the purpose of mechanical regularization. Assuming that the material is purely elastic, the objective of this regularization is to remove some (supposed to be) non-physical high frequency components of the displacement field. These high frequency components are more likely due to artifacts in B/W pattern. To give an illustration of the performance of the implemented mechanical regularization, the kinematic strain field during the uniaxial loading test of NiTi is used as an example (quasi-static average strain rate $\dot{\epsilon} = 1 \times 10^{-4}\,\mathrm{s}^{-1}$ at the room temperature $T = 300\,\mathrm{K}$).

The region of interest has been meshed with a triangular element size of 16 pixels. Without mechanical regularization, the classical DIC method and other commercial codes are not able to properly estimate the highly heterogeneous strain field. As we can see in Figure 3.12, without mechanical regularization, the kinematic field calculation does not converge (as reflected in the axial displacement and associated residual field) , leading to a non-physical equivalent strain $\epsilon_{eq} \simeq 8$. The relaxation approach is then used (see Equation 3.15 and Equation 3.15): we first solve the problem by using a very large regularization length (l_m=$2l_b$=1000 pixels in Figure 3.13). Next, we progressively decrease these lengths l_m and $2l_b$ ($500 \rightarrow 250 \rightarrow 125$ pixels), by using the previous solution of kinematic field as initial solution for the next minimization.

A T3 mesh with $L_{mesh} = 16$pixels and the above mentioned relaxation steps have been used for all experiments reported in the manuscript. The uncertainty level is estimated to be around $\delta\epsilon \simeq 0.1\%$ for the reported deformation fields.

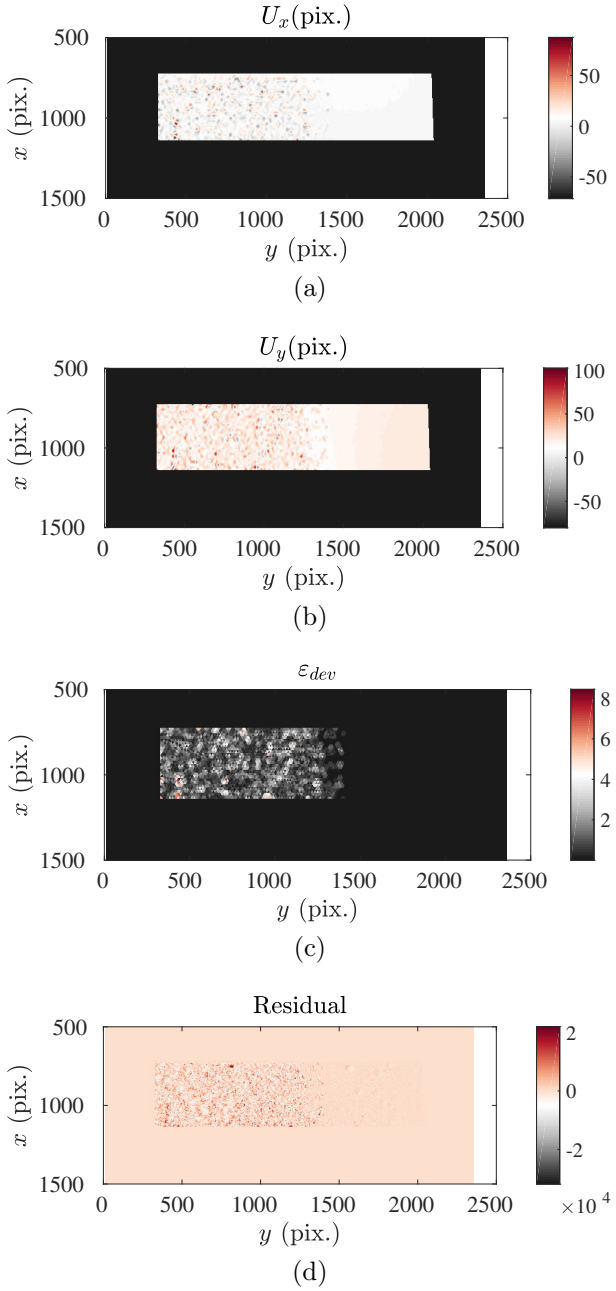

Figure 3.12: Obtained results without mechanical regularization : (Upper left) axial displacement field u_x; (Upper right) axial displacement field u_y; (Down left) equivalent strain field ϵ_{eq}; (Upper right) residual field ρ with a residual level of 11%.

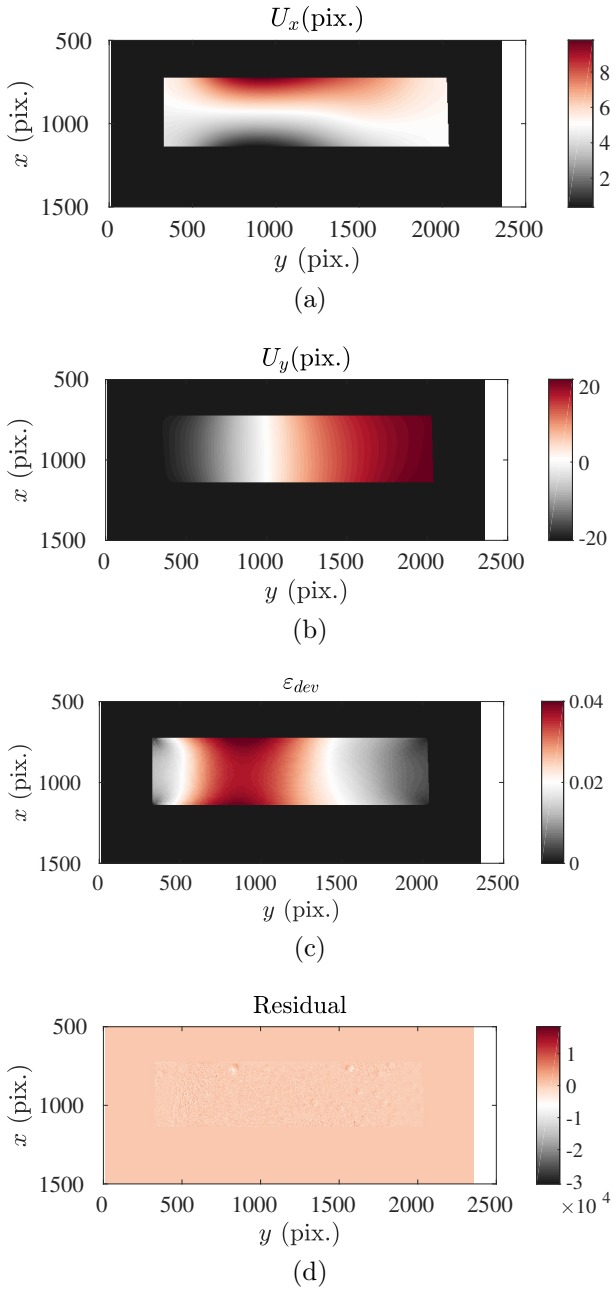

Figure 3.13: Obtained results with mechanical regularization l_{reg} = 1000pixels : (Upper left) axial displacement field u_x; (Upper right) axial displacement field u_y; (Down left) equivalent strain field ϵ_{eq}; (Upper right) residual field ρ with a residual level of 1.5%.

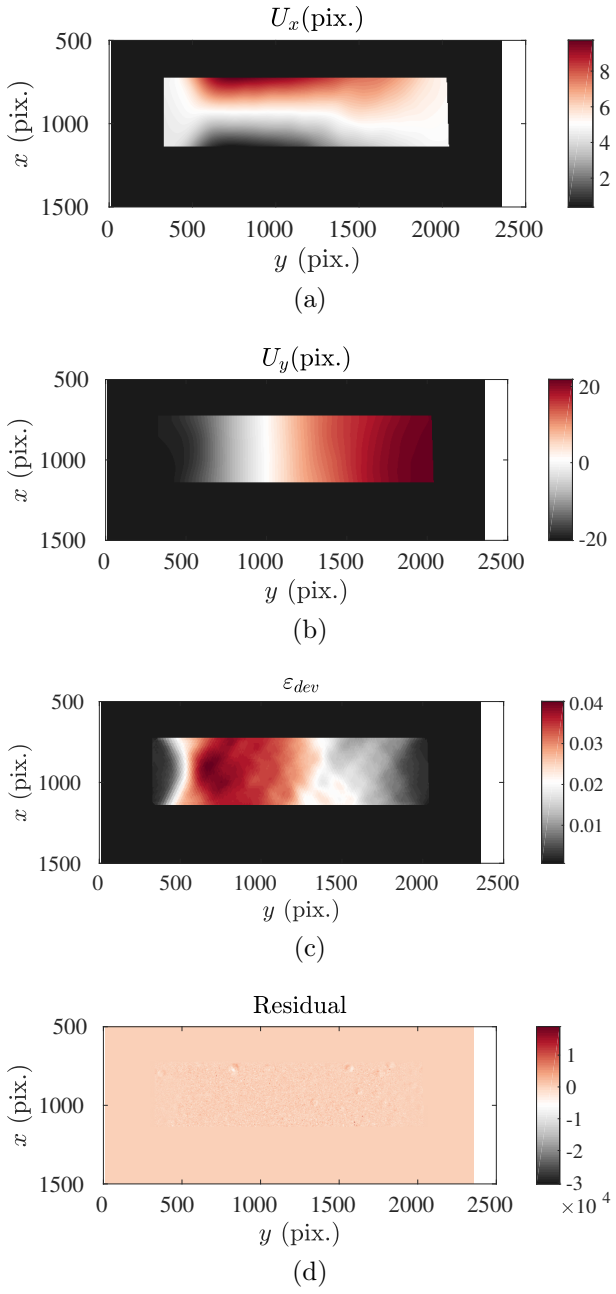

Figure 3.14: Obtained results with mechanical regularization l_{reg} = 250pixels : (Upper left) axial displacement field u_x; (Upper right) axial displacement field u_y; (Down left) equivalent strain field ϵ_{eq}; (Upper right) residual field ρ with a residual level of 1.4%.

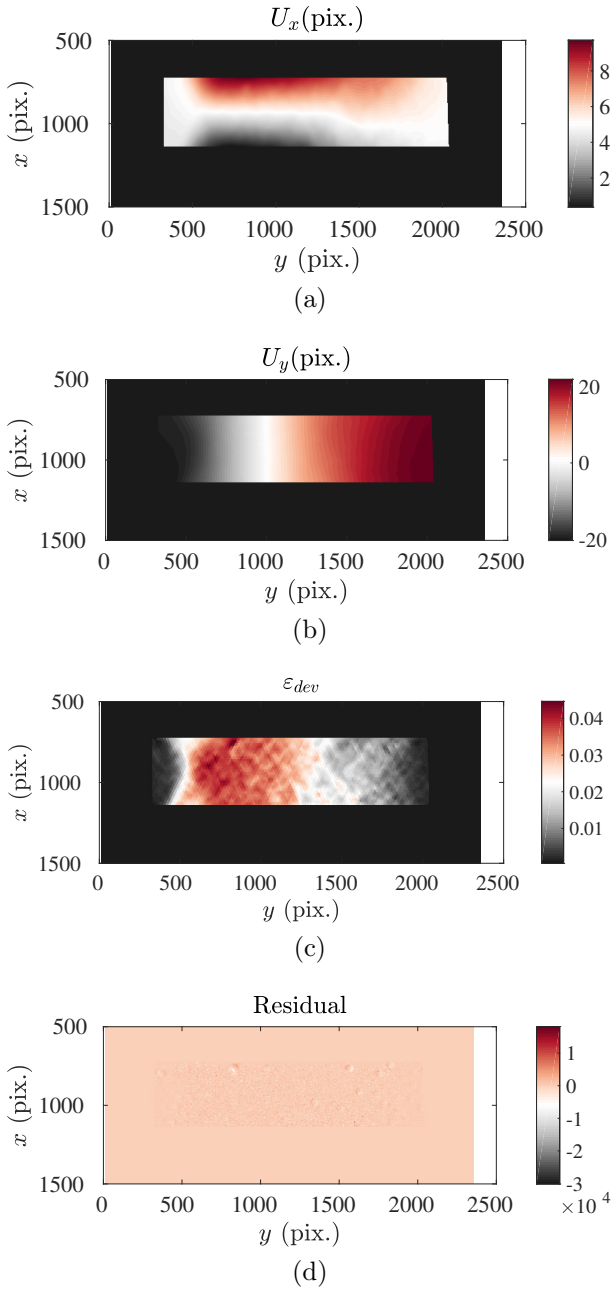

Figure 3.15: Obtained results with mechanical regularization l_{reg} = 125pixels : (Upper left) axial displacement field U_x; (Upper right) axial displacement field U_y; (Down left) equivalent strain field ϵ_{eq}; (Upper right) residual field ρ with a residual level of 1.4%;

3.4 PE behavior of NiTi SMA - uniaxial tensile loading

3.4.1 Uniaxial tensile loading - T=300 K

The ambient temperature corresponds to a temperature close to 300 K.
For this first set of tests, a displacement controlled quasi static uniaxial loading is applied on the investigated NiTi SMA ($\dot{u}_x = 1 \times 10^{-3}\,\mathrm{mm\,s^{-1}}$).
The applied loading protocol can be synthesized into:

$$u_x(t) = \frac{0.5t}{500} \quad , \quad t \leq 500\,\mathrm{s} \rightarrow \text{Loading} \tag{3.35}$$

$$u_x(t) = \frac{0.5(1000-t)}{500} \quad , \quad 500 \leq t \leq 1000\,\mathrm{s} \rightarrow \text{Unloading} \tag{3.36}$$

where u_x describes the axial tensile displacement applied as function of time (already defined in Equation 3.25)

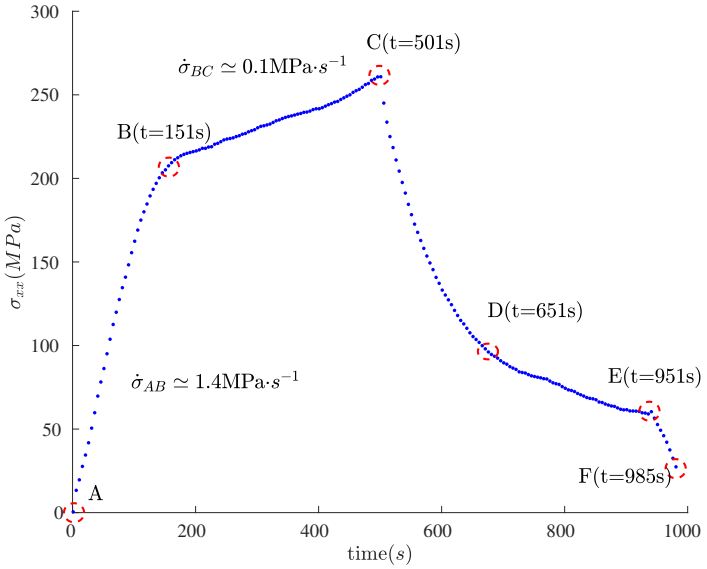

Figure 3.16: Engineering stress as a function of time t

Equivalent strain and strain rate Figure 3.17 shows the engineering strain vs. engineering stress obtained at 300 K. The markers reported all along the curve correspond to different DIC steps reported in Figure 3.18 and Figure 3.19).
The equivalent strain fields obtained at different time steps are plotted in Figure 3.18. Results can be synthesized as follows:

- we notice that the distribution of transformation is heterogeneous (scatter transformation) even before reaching the stress threshold, implying the potential

existence of R/M phase transformation (see from $t = 51\,\mathrm{s}$ to $t = 151\,\mathrm{s}$ in Figure 3.18). Before the onset of localization bands, this scatter transformation reflects some structural defects associated with potential stress concentrations;

- once the equivalent stress reaches the stress threshold at $\sigma = 220\,\mathrm{MPa}$ at $t = 151s$ (see in Figure 3.18), a band initializes at the upper region of the strain field $\epsilon(\mathbf{x}, t)$ and the strain rate field $\dot{\epsilon}(\mathbf{x}, t)$;
- after $t = 201\,\mathrm{s}$, the first localization band is created. It forms an angle $\theta_1 \simeq 53.5°$ with the loading direction, consistent with the classical localization theory;
- after $t = 251\,\mathrm{s}$, a symmetrical set of bands nucleates, forming an angle $\theta_2 \simeq -53.5°$ with the loading direction.
- a broadening of bands is observed when the loading increases. We can observe that the transformation fronts (for example at $t = 351\,\mathrm{s}$) propagate in a non-continuous way. This implies strong and evolving competition between the probable temperature heterogeneity (already reported in [Maynadier, 2012]) due to phase transformation and stress concentration related to mechanical incompatibility (or phase field heterogeneity);
- after the whole ROI is transformed into martensite ($t = 501\,\mathrm{s}$), the elastic strain inside band begins to increase (stiffness of martensite). This deformation remains however heterogeneous, concentrated more in the regions that were deformed first; (these regions correspond to where we already notice the non-uniform scatter transformation before the onset of localization).
- the unloading begins by a global elastic unloading that looks nearly homogeneous from $t = 501\,\mathrm{s}$ and $t = 601\,\mathrm{s}$;
- no major transformation front is observed in the strain field (see Figure 3.18 and Figure 3.19)
- from $t = 601\,\mathrm{s}$ to $t = 701\,\mathrm{s}$ (when the stress-strain curve reaches the reverse transformation plateau), a tightening of the bands is observed. Several isolated bands can be observed (see at $t = 751\,\mathrm{s}$ and $t = 801\,\mathrm{s}$), probably indicating a temperature heterogeneity;
- when the stress-strain curve leaves the backward transformation plateau at $t = 951\,\mathrm{s}$, localization bands disappear and the strain field becomes again homogeneous;
- it is still worthy mentioning that the initialization and ending region of localization phenomena is almost the same, indicating a probable presence of structural defects at the upper-right zone of the tested specimen.

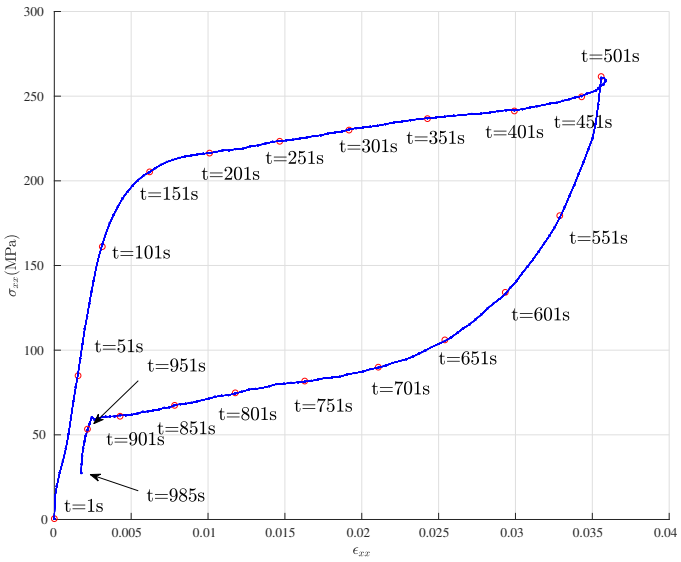

Figure 3.17: Axial stress/strain curve $\sigma_{xx}(\epsilon_{xx})$ at 300K (red markers correspond to different time frames in Figure 3.18 and Figure 3.19)

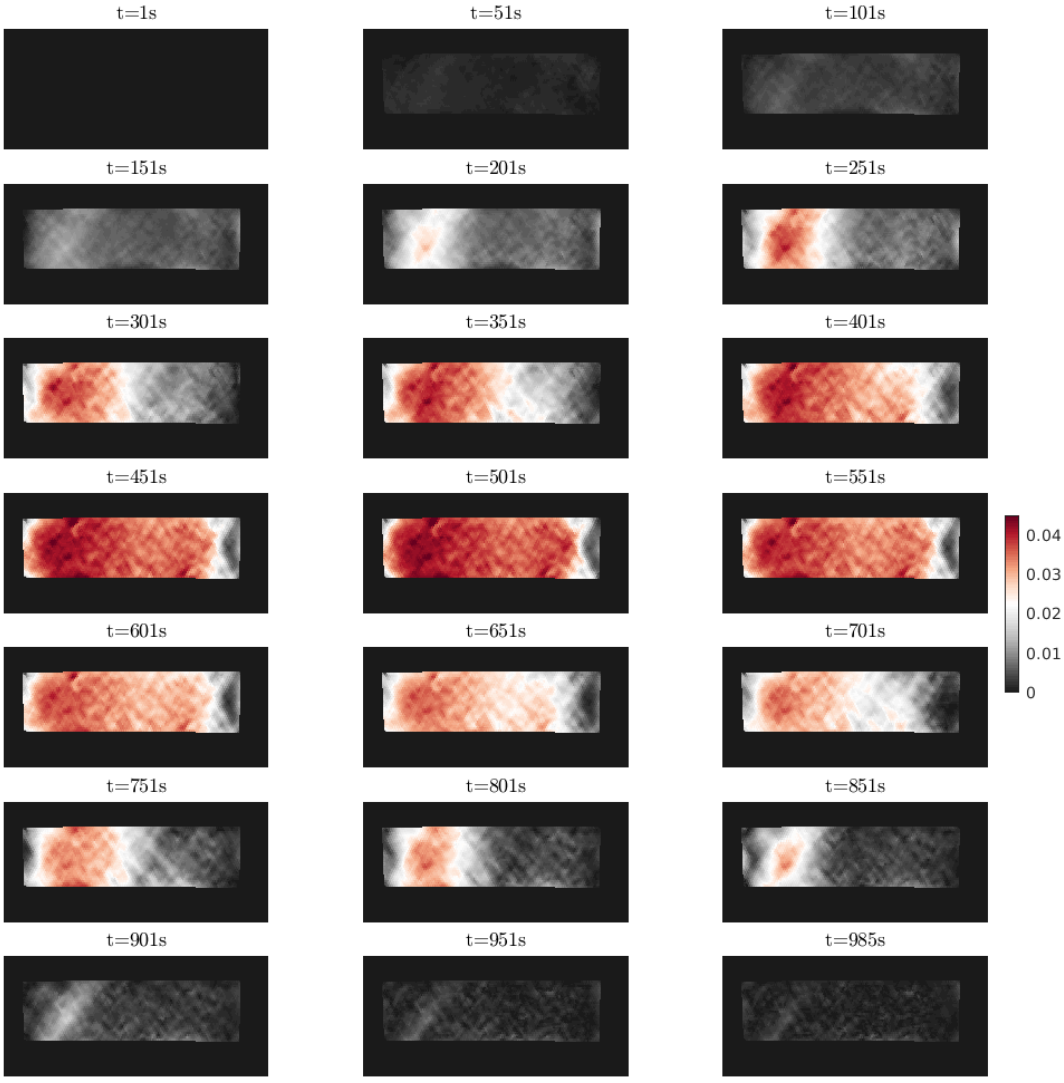

Figure 3.18: Equivalent strain field evolution $\epsilon_{eq}(\mathbf{x}, t)$ as function of time

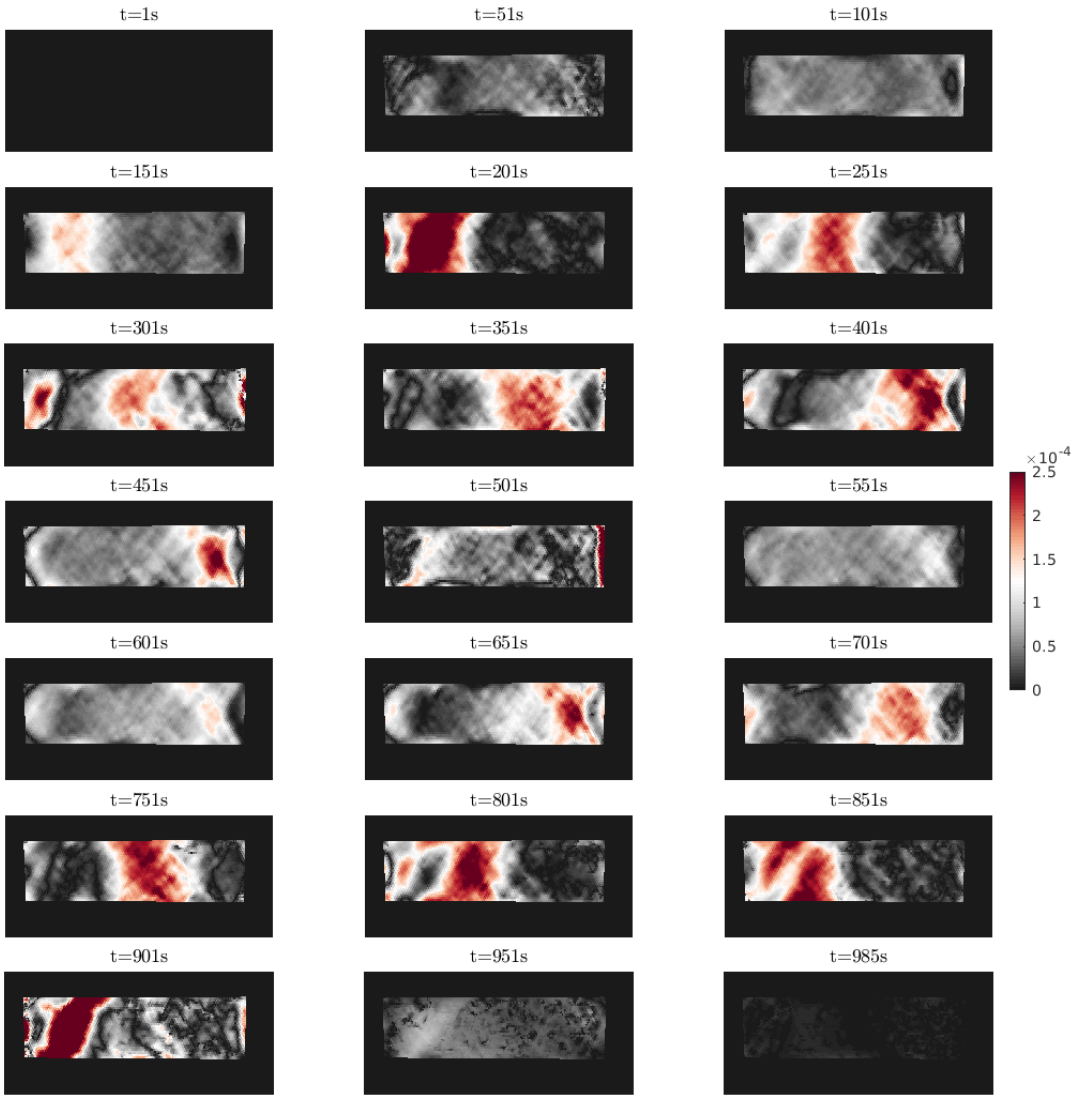

Figure 3.19: Equivalent strain rate field evolution $\dot{\epsilon}_{eq}(\mathbf{x}, t)$ as function of time

Virtual gauge

Other analyses of these results are possible. We can for example build a *virtual strain gauge* to extract an averaged axial strain over a chosen area S of the image (as the blue rectangle in Figure 3.20a see Equation 3.37).

$$\bar{\epsilon}_{xx} = \frac{1}{S} \iint_S \epsilon_{xx}(x, y)\, dxdy \tag{3.37}$$

As illustrated in Figure 3.20a, three different virtual gauges have been defined (with the same surface $S = 1.5 \times 1.5\,\text{mm}^2$ chosen at different axial positions separated by a distance of about $d_{AB} = 2.7\,\text{mm}$ and $d_{BC} = 3.1\,\text{mm}$ between *zone A*, *zone B* and *zone C*). Results of averaged deformation as function of time are plotted in Figure 3.20b. Several conclusions can be drawn:

- *zone A*: the forward phase transformation begins in this zone (around $t \simeq 100\,\text{s}$). The deformation saturates very quickly at the maximum equivalent transformation strain level ($\epsilon^A_{max} \simeq 3.5\%$ is reached in less than $10\,\text{s}$). This zone is the last region to see the backward transformation during the unloading (at $t \simeq 960\,\text{s}$);

- *zone B*: in this zone, the forward martensitic transformation occurs after the forward phase transformation in the zone A. The deformation reaches its maximum value at $t = 225\,\text{s}$. The forward transformation begins in zone C when it ends in zone B (at $t = 400\,\text{s}$);

- *zone C*: this zone is the last to initialize the forward transformation upon loading and the first where the backward transformation occurs.

Figure 3.21 gives a spatial-temporal representation of the same results. Equivalent strain is now calculated as an average value over a Q4 mesh with a characteristic length of 20 pixels for points located along a line parallel to the loading direction(the symmetry axis of the sample). Values are represented at each time-step. They form a surface where localization and propagation of bands are clearly highlighted.

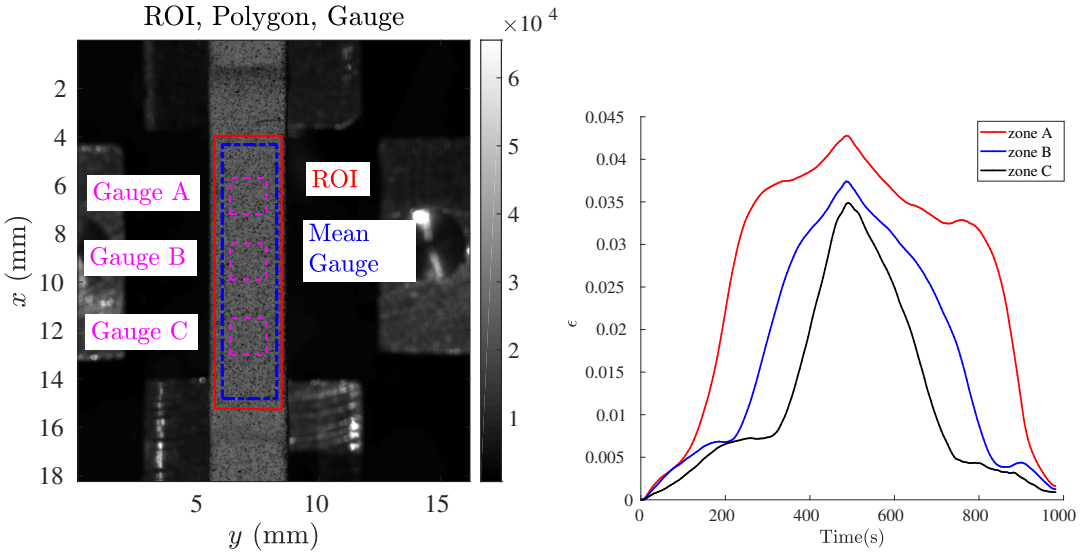

(a) Position of each virtual strain gauges(ROI plotted in red, Mean gauge plotted in blue and three small gauges plotted in magenta)

(b) The mean axial strain $\bar{\epsilon}_{xx}$ evolution as function of time

Figure 3.20: Virtual strain gauge

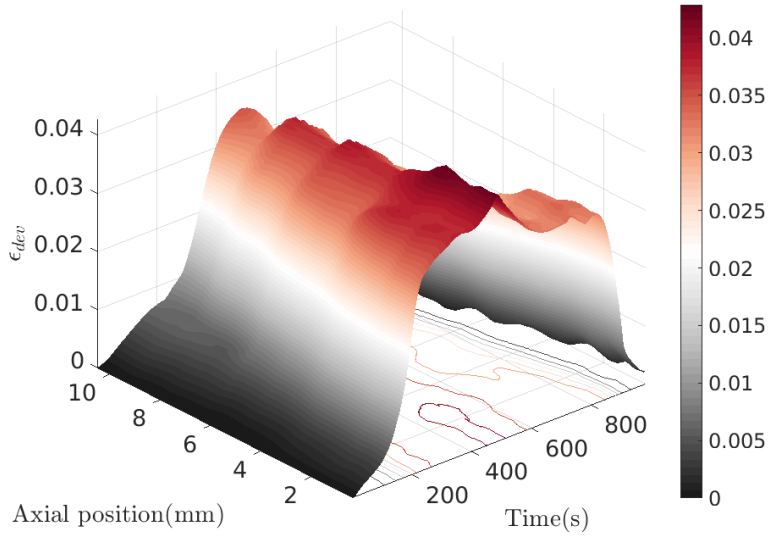

Figure 3.21: Spatial-temporal evolution of axial strain at points along the strip axis.

Attempt of comparison with the multiscale stochastic model

Figure 3.22 allows the comparison of the experimental axial stress-strain curve with the model results. In this situation, the experimental strain is taken as the average value of ϵ_{xx} calculated over the blue rectangle in Figure 3.20. The simulation conditions are the same than the conditions employed for simulations reported in chapter 2 (polycrystalline NiTi SMA with 413 grains). This RVE is subjected to the same experimental engineering stress as measured during the 1D tensile test. The reference temperature is $T = 300\,\mathrm{K}$ and a moderate convection rate k=0.05 J.m^{-3}.K^{-1} has been used. Several observations can be drawn:

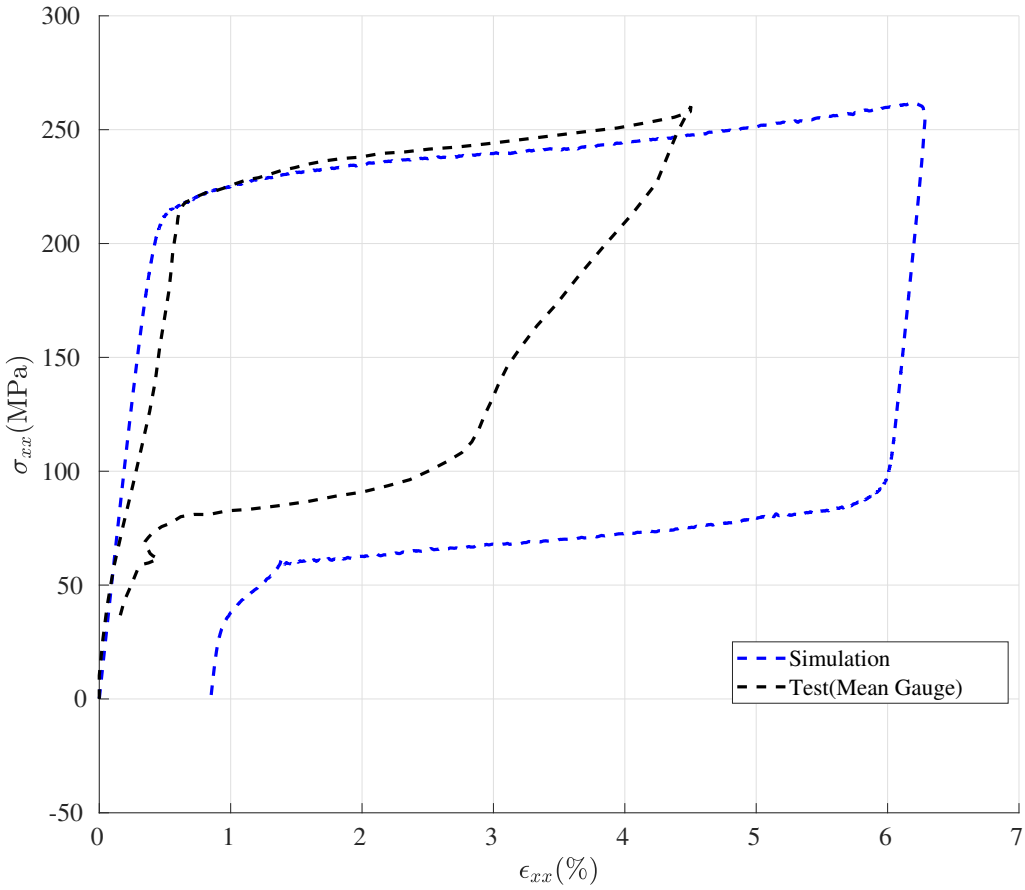

Figure 3.22: Comparison of experimental and modeled axial stress/strain curves: (the experimental curves plotted in dot and the numerical prediction plotted in blue)

- The multiscale model leads to a good prediction of the yield stress;
- Even if a simplified heat exchange condition has been used, the numerical results are consistent with the experimental curve in terms of hardening rate during the transformation plateau;
- The main observed drawback is that the numerical prediction gives a higher estimation of the maximum axial strain compared to the experimental results.

- During unloading, the backward transformation is properly modeled: thresholds are respectively $\sigma^e_{M\to A} \simeq 85\,\text{MPa}$ for the experiment, and $\sigma^s_{M\to A} \simeq 75\,\text{MPa}$ for the simulation.

The over-estimation of the maximum axial strain was already observed in the work of [Maynadier, 2012] and [Fall et al., 2016]. It was attributed to the chosen homogenization strategy of the current stochastic model. Indeed stress is supposed uniformly distributed over the polycrystal. Self consistent scheme gives a better evaluation of deformation but is associated with a higher hardening rate during the transformation plateau. It seems actually insufficient to look for an explanation only turned towards the scheme of homogenization.
The RVE model obviously has its limitations and the best agreement is obtained for transition points and at the beginning of the transformation. The strain localization mechanism and associated thermal field heterogeneity are of course not captured. This may have significant consequences on the dynamic of phase and variant selection, and finally on the measured axial deformation. The appendix B presents a first attempt of a structure model taking into account the incompatibilities between variants. One of the consequences is a significant reduction in the amplitude of the axial deformation.

3.4.2 Uniaxial tensile loading - T=287 K

The same displacement-controlled quasi-static uniaxial loading test has been carried out at $T = 287\,\text{K}$. Results presented have been obtained using the same strip than the strip used for the test presented in the previous section. The austenitization procedure is applied between two tests [3].

Figure 3.23 shows that martensite transformation initialize at $\sigma_{M_s} = 130\,\text{MPa}$ with an associated axial strain $\epsilon^{yield}_{xx} \simeq 0.6\%$.
The space-time evolution of equivalent strain and equivalent strain rate fields are presented in Figure 3.24 and in Figure 3.25.

- Figure 3.23 and Figure 3.24 illustrate a slight larger maximum average axial strain $\epsilon^{max}_{eq} \simeq 4\%$ at frame $t = 500\,\text{s}$ than at T=300 K;

- During the loading, the onset of localization initializes at the right part of 1D strip. The broadening of strain localization has been observed afterward. With experimental air cooling condition and near quasi-static tensile load, no major nucleation band has been observed inside the Austenite matrix.

- Two sets of symmetrical bands are observed, with a localization angle of $\theta \simeq 54°$ between the normal vector of bands and transverse direction of external loading.

[3] The austenitization procedure is applied to remove any potential retained martensite.

- The transformation front is smoother compared to results obtained for the previous test performed at $T = 300\,\mathrm{K}$. This could be an unexpected effect of the cooling system. Indeed the cold air is pulsed on the surface of the specimen. Its improves the heat exchange and the evacuation of heat produced by the phase transformation.

- During the unloading, we nearly do not observe any tightening of the localization bands. Indeed, strain rate field is nearly homogeneous from $t = 551$ to $t = 801$ in Figure 3.25. There is no propagation front associated with the phase transformation. This result is in accordance with the stress-strain curve (Figure 3.23), where no significant backward transformation plateau is observed[4].

- A large residual strain with retained martensite persists at the end of the test, especially where the localized transformation began.

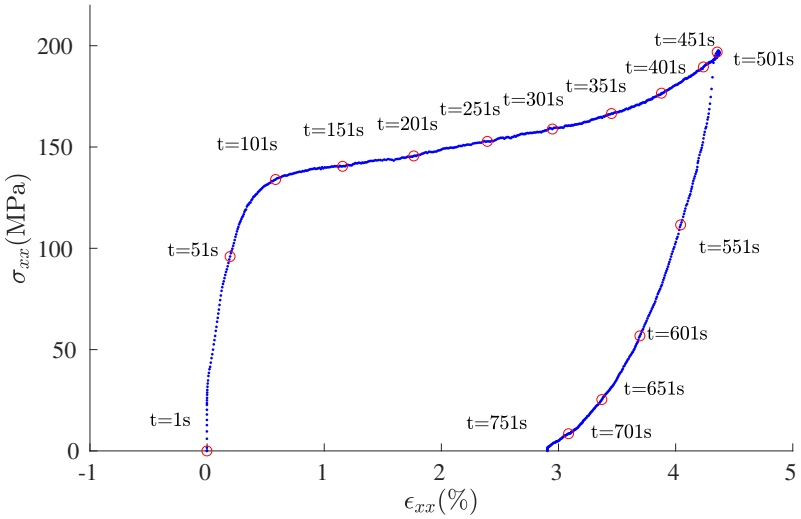

Figure 3.23: Axial stress/strain curve at $T = 287\,\mathrm{K}$ (red dots correspond to frames in Figure 3.24 and Figure 3.25)

The same procedure as introduced in section 3.4.1 has been used to follow an averaging deformation at three different points (surface $S = 1.5 \times 1.5\,\mathrm{mm}^2$ chosen at different axial positions separated by a distance of about 3.6 mm), defining three virtual gauges. The average equivalent strain in each area as a function of time is plotted in Figure 3.26a:

- Zone C is the first to see a strain localization. The onset of strain localization of this gauge initialize at $\sigma_{xx} \simeq 140\,\mathrm{MPa}$

- Zone A is the last to transform at a low stress level (at $\sigma_{xx} \simeq 170\,\mathrm{MPa}$).

[4] at $t = 701\,\mathrm{s}$, a potential backward transformation may be initialized.

- The unloading mainly corresponds to martensite elastic unloading for all these three zones, associated with a slight decrease of the strain intensity inside the bands.

Figure 3.27 compares between the axial stress/strain curve at these two different temperatures. As expected, a lower temperature leads to a smaller transformation threshold.

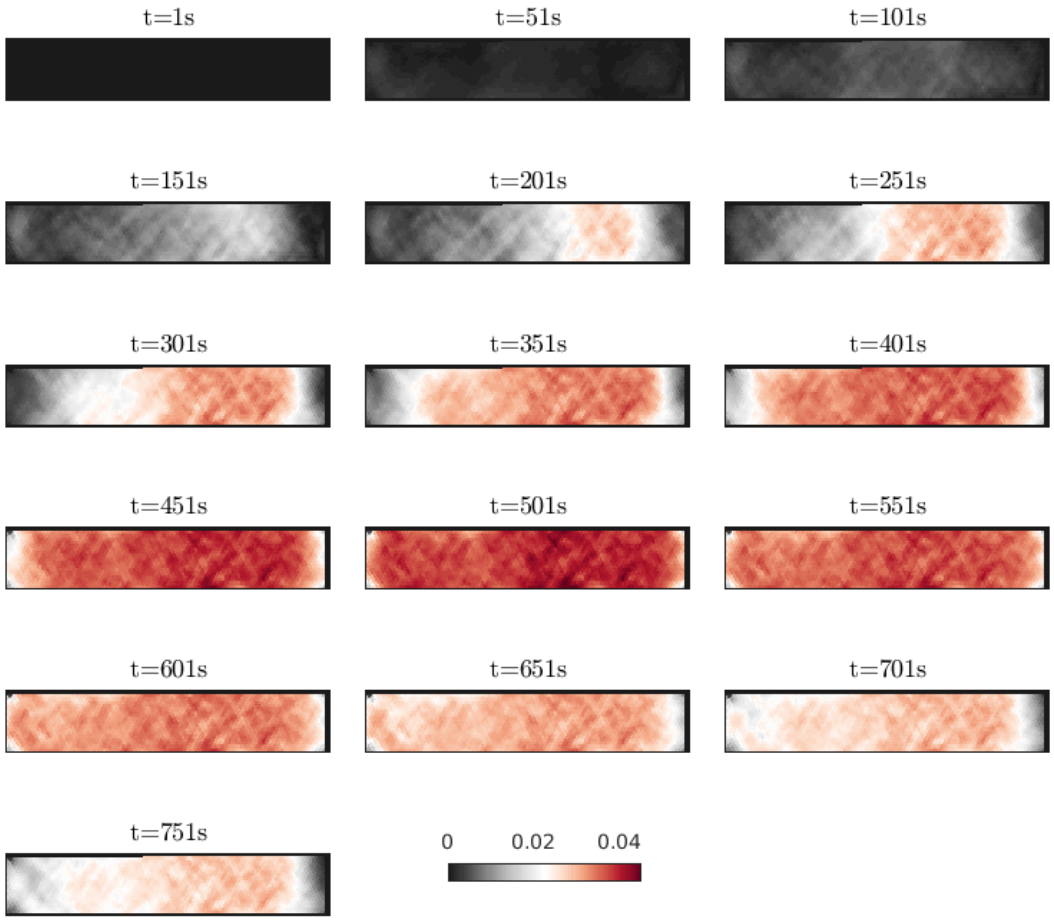

Figure 3.24: Equivalent strain field evolution as function of time ($T = 287K$)

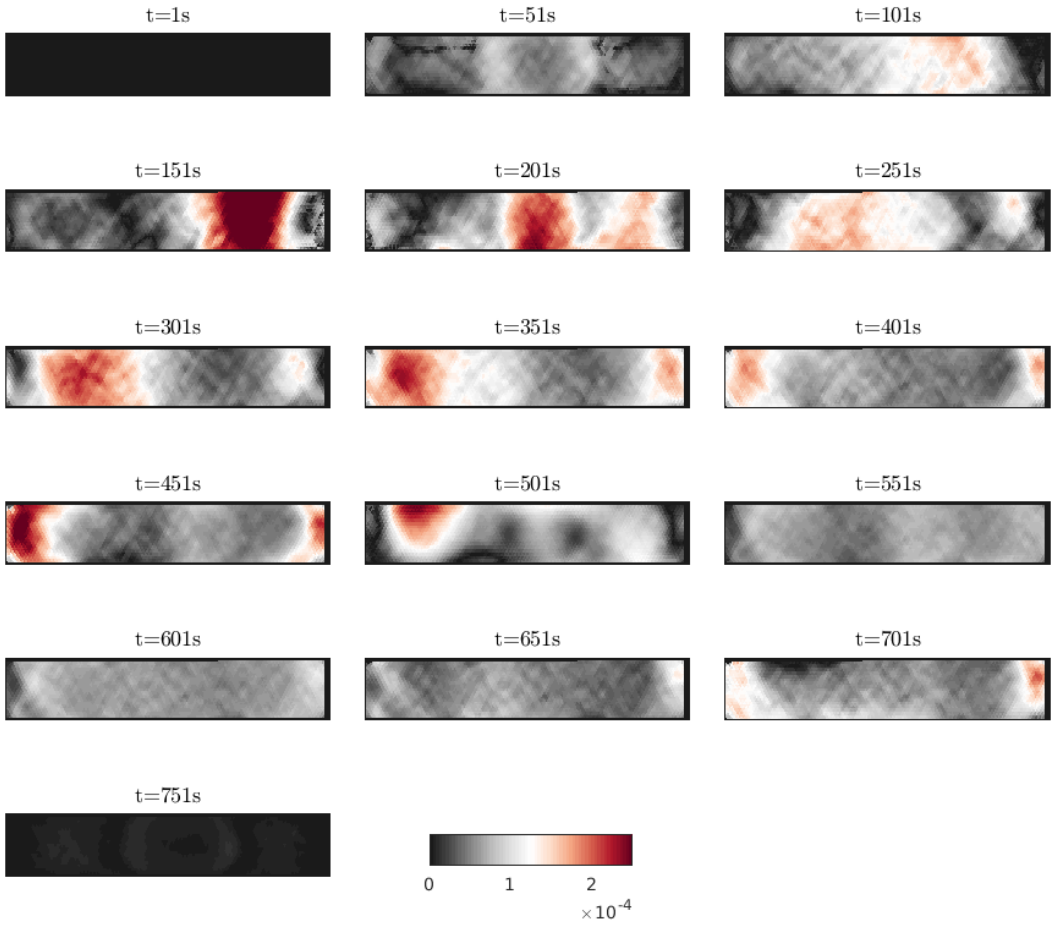

Figure 3.25: Equivalent strain rate field evolution as function of time ($T = 287K$)

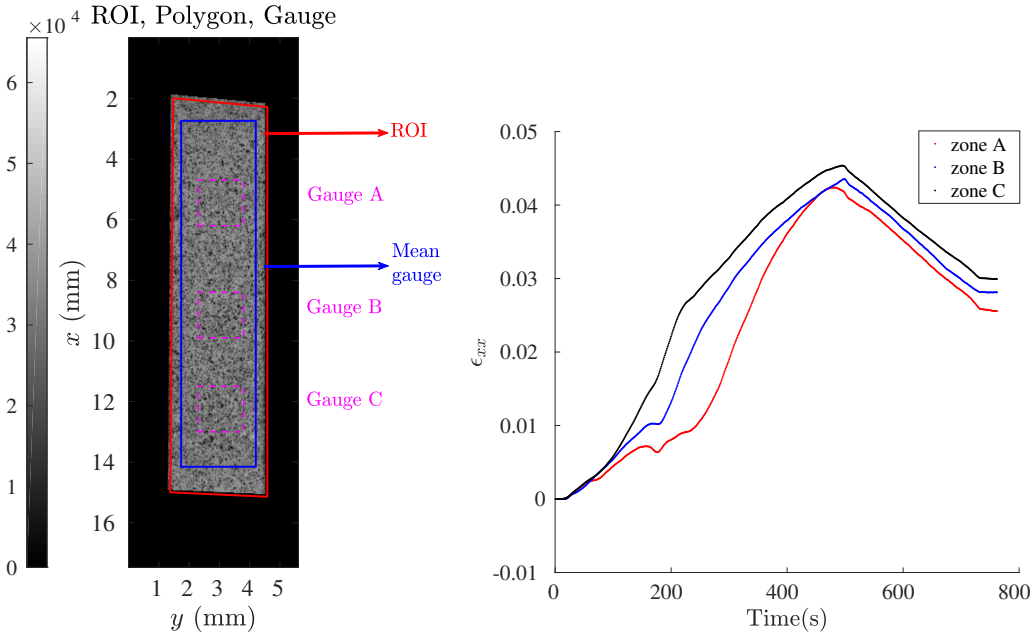

(a) Chosen virtual gauge over the surface of NiTi 1D strip (Red polygon indicates the Region of Interest; Blue rectangle represent the gauge to obtain the mean axial strain; and the three small rectangles are the three local virtual gauges)

(b) Average strain evolution as a function of time

Figure 3.26: Three virtual gauges

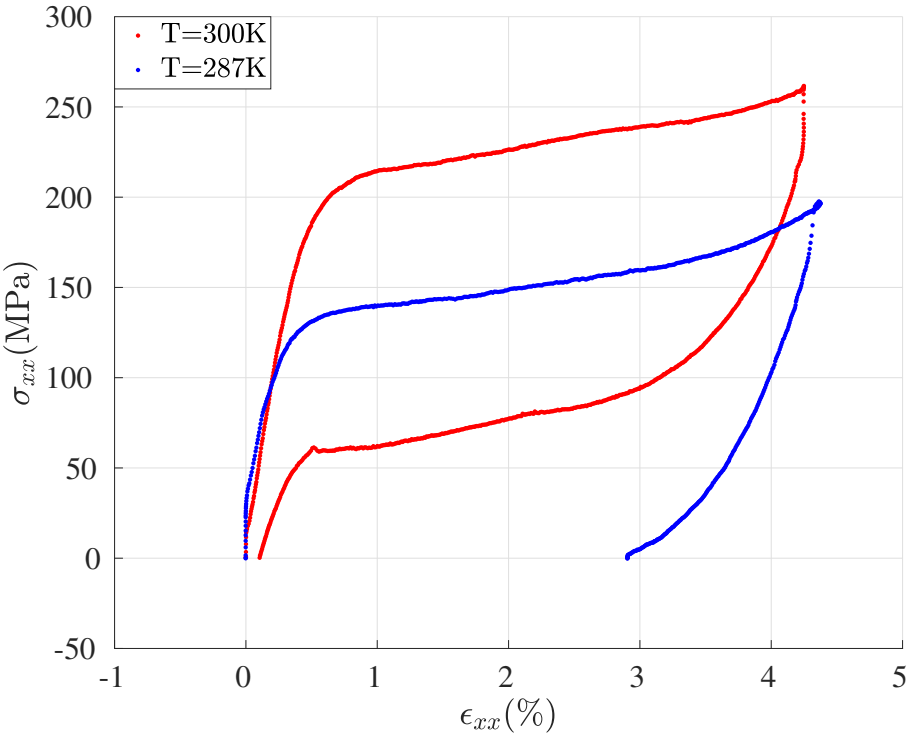

Figure 3.27: Axial stress/strain response of NiTi SMA at two different ambient temperatures: (red $T = 300K$, blue $T = 287K$)

At $\epsilon_{xx} = 2\%$, we observe a stress decrease of about $\Delta\sigma = 81.9\,\mathrm{MPa}$ for a temperature decrease of about $\Delta T = 13\,\mathrm{K}$. The ratio between these two values ($\frac{\partial\sigma}{\partial T} = 6.3\,\mathrm{MPa\,K^{-1}}$) defines the slope of A to M transition in the Clausius-Clapeyron Diagram.
In the model, indeed Equation 2.53 indicates an equiprobability of two phases {1,2} when they exhibit the same Gibbs free energy:

$$\begin{aligned} g_1 &= g_2 \\ h_1 - Ts_1 - \boldsymbol{\epsilon}_1^{tr} : \boldsymbol{\sigma} &= h_2 - Ts_2 - \boldsymbol{\epsilon}_2^{tr} : \boldsymbol{\sigma} \end{aligned} \tag{3.38}$$

This relationship defines a linear equation in the $(\boldsymbol{\sigma}, T)$ Clausius Clapeyron space. The slope of the curve is calculated as:

$$\boldsymbol{\gamma} = \frac{\partial\boldsymbol{\sigma}}{\partial T} = -\frac{\Delta s}{\Delta\boldsymbol{\epsilon}^{tr}} \tag{3.39}$$

Applied for the aforementioned uniaxial situation, the following estimation of γ gives:

$$\gamma \simeq 6.2(2)\,\mathrm{MPa\,K^{-1}}$$

This value is very close to the experimental observation ($6.3\,\mathrm{MPa\,K^{-1}}$).

Comparison with the multiscale stochastic model Numerical simulations of the PE behavior for different initial ambient temperatures have been carried out. Situations at $T = 300\,\mathrm{K}$ and $T = 287\,\mathrm{K}$ have been considered for the same textured polycrystal and the same moderate convection rate with environment k=0.05 J.m^{-3}.K^{-1}. The numerical simulations are presented in Figure 3.28, the axial stress-strain response at $T = 300\,\mathrm{K}$ and $T = 287\,\mathrm{K}$ are plotted in red and in blue respectively.
Several remarks can be made :

- the numerical prediction grants to provide a good estimation of the yield stress evolution:

$$\sigma_{M_s}^{\mathrm{exp}}(T = 300K) \simeq \sigma_{M_s}^{\mathrm{simu}}(T = 300K) \simeq 210\,\mathrm{MPa} \tag{3.40}$$
$$\sigma_{M_s}^{\mathrm{exp}}(T = 287K) \simeq \sigma_{M_s}^{\mathrm{simu}}(T = 287K) \simeq 150\,\mathrm{MPa} \tag{3.41}$$

- the numerical simulation tends to give a uniform hardening rate at the transformation plateau for both simulations, whereas the experimental hardening rates are slightly different;

- At $T = 300K$, the simulated backward transformation ends after $\sigma_{xx} \leq 50\,\mathrm{MPa}$. The backward transformation is also finished at this stress level but a slight

amount of residual strain is observed: $\epsilon_{xx}^{\text{res}} \leq 0.25\%$. At $T = 287K$, both simulated and experimental backward transformations are uncompleted; the residual strain levels are however different;

- All numerical predictions over-estimate the maximum strain value. This drawback has already been addressed in the previous section.

- This test underline the well-known strong sensitivity of the mechanical behavior to the temperature. The fact that the heterogeneity of the temperature field is not considered in the model leads of course to some observed discrepancies.

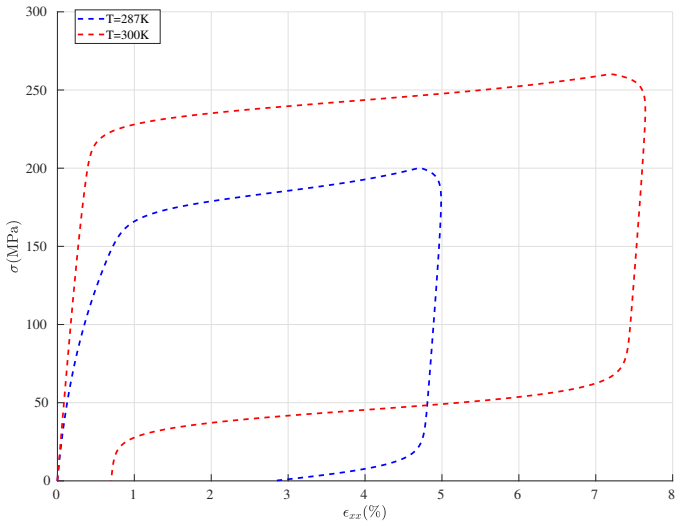

Figure 3.28: Simulation of textured polycrystal at two different temperatures with moderate convection

3.4.3 Strain rate effects

In order to have an initial estimation of the strain rate effect, a tensile loading with a much higher velocity has been applied to the 1D tensile strip at ambient temperature $T \simeq 300\,\text{K}$. The possibilities offered by *Miniastree* are however limited: a displacement controlled loading rate of $\dot{u}_x \simeq 0.05\text{mm}\,\text{s}^{-1}$ has been used (50 times higher than for the quasistatic tests), that remains a "low" strain rate ($\dot{\epsilon}_{xx} \simeq 0.005\text{s}^{-1}$). The axial displacement rate can be visualized in Figure 3.29. The engineering stress-strain curve is plotted in Figure 3.30. From this figure, several conclusions can be drawn :

- the yield stress $\sigma \simeq 230\,\text{MPa}$, which is a slightly higher value compared to quasi-static case.

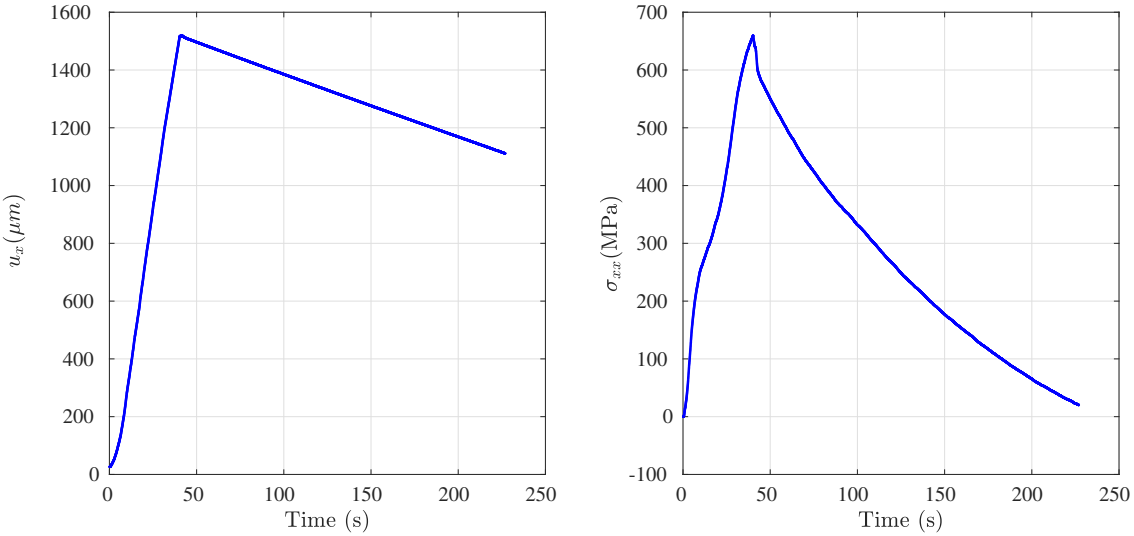

Figure 3.29: High-velocity displacement-controlled loading: (Left) external displacement applied as a function of time; (Right) engineering stress as a function of time

- the transformation plateau exhibits a significant 'higher' hardening rate compared to the quasi-static case. This is probably due to the rise of local temperature during the martensitic transformation.
- The end of the plateau is reached for a stress level of about $\sigma_{xx} \simeq 400\,\text{MPa}$. Afterwards, the stress-strain curve shows a martensitic elastic then plastic response, explaining probably the permanent strain observed at the end of the unloading.

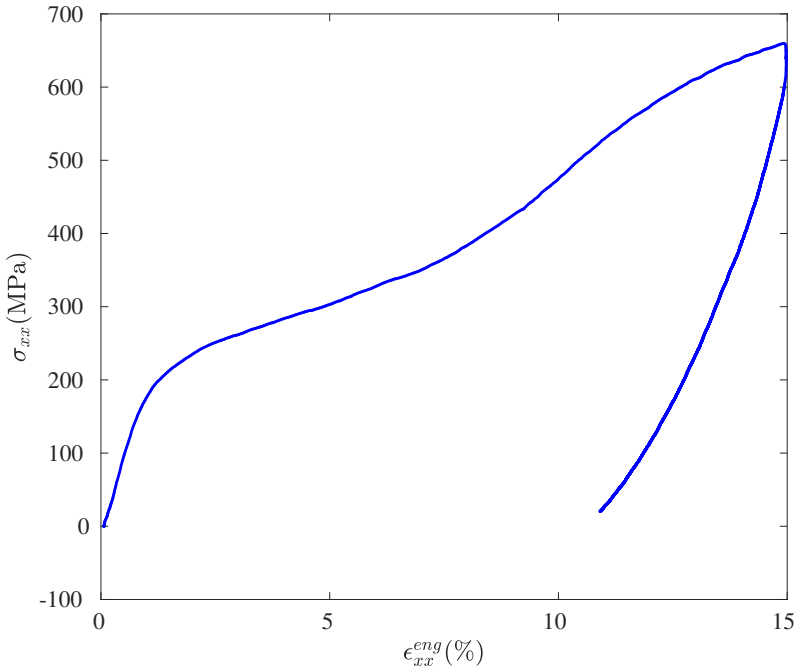

Figure 3.30: Engineering axial stress/strain curve of 1D Ni-Ti strip under "high" velocity loading

Kinematic field The sampling frequency of pictures is fixed at 10Hz, from $t = 0s$ to $t = 18.6\,\mathrm{s}$, leading to 186 images in total [5]. It covers an incomplete portion of stress-strain curve response of 1D strip under 'high' velocity tensile load. A first set of bands is formed at the right end of the 1D sample in Figure 3.32 ($t = 7\mathrm{s}$) while a secondary set of bands is nucleated at $t = 9\mathrm{s}$.

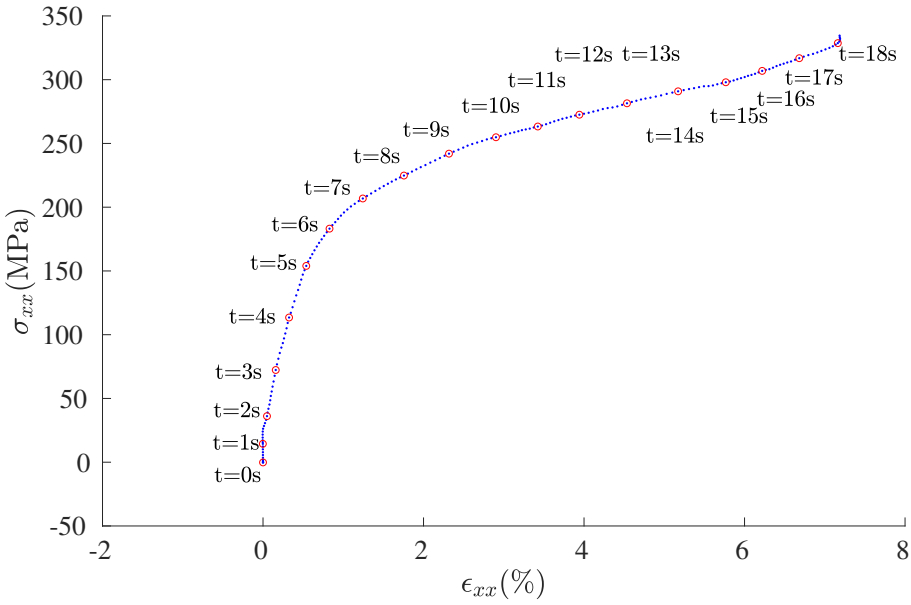

Figure 3.31: Axial stress/strain curve (red circles correspond to the strain fields reported in Figure 3.32)

Comparison with the multiscale stochastic model Experimental and numerical axial stress-strain curves are plotted in Figure 3.33. Several remarks need to be emphasized:

- the numerical prediction of the yield stress is slightly higher than the experimental one;
- the hardening rate during the transformation plateau are roughly in accordance;
- as for the previous tests, the experimental maximum axial strain value is lower than the numerical prediction;
- both numerical and experimental results indicate a similar value of martensite finish stress $\sigma = 400\,\mathrm{MPa}$;
- plasticity is observed at the end of the test. It is consequently nearly impossible to compare experimental data with the numerical prediction.

[5] This limitation is mainly due to the transfer velocity of USB ports.

Again, the probably major role of the true and unreachable thermal field of the NiTi strip during the test (especially for this high strain rate test) must be underlined, explaining for example the non-constant experimental hardening rate. This may explain the observed discrepancies too. This new set of results confirms the necessity to implement the constitutive model inside a structure calculation for adequate experiment/simulation comparisons.

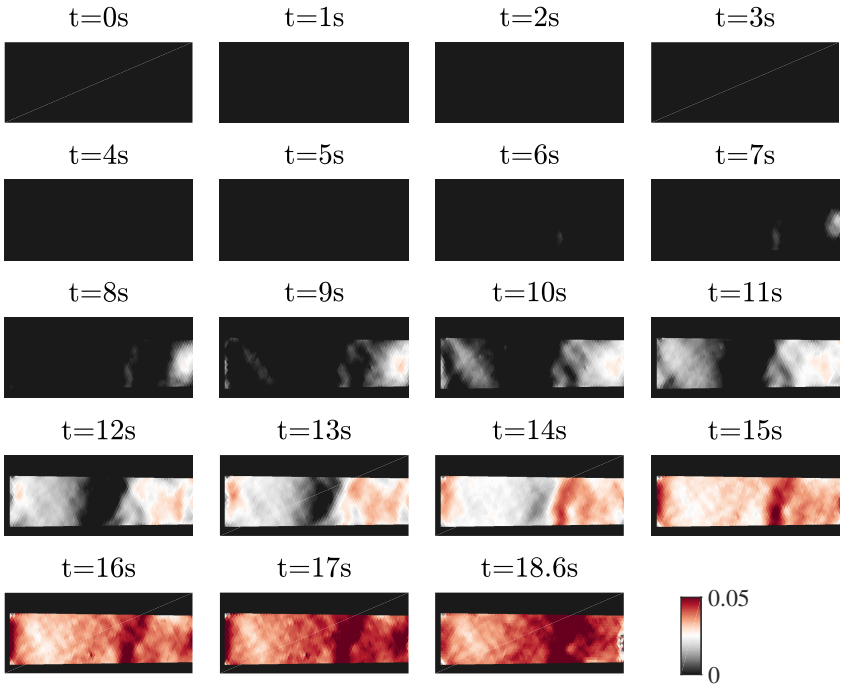

Figure 3.32: Equivalent strain field ϵ_{eq} as function of time

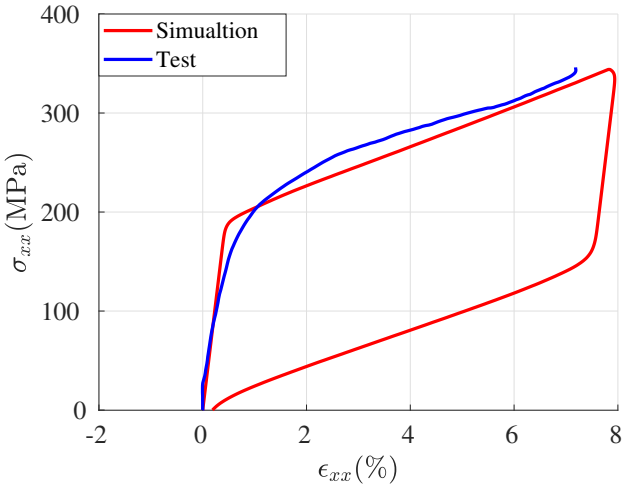

Figure 3.33: Axial stress/strain curve (the blue curve indicates the 1D tensile test and the red curve represents the 1D simulation)

3.5 Multiaxial proportional and non proportional loading

We present in this part different results of biaxial tests obtained using various displacement loading of the 2D specimen. We hope (had hoped) by these tests to obtain a RVE behavior to serve as validation points of the multiscale stochastic model.

3.5.1 Equi-Biaxial proportional test at $T = 298\,\mathrm{K}$

Prescribed loading and measured forces At $T = 298\,\mathrm{K}$, a proportional quasi-static displacement-controlled test is prescribed as follows:

$$u_x(t) = U_2(t) - U_4(t) = \frac{0.3t}{600}, \quad u_y(t) = U_3(t) - U_1(t) = \frac{0.3t}{600}, 0 \leq t \leq 1200\,\mathrm{s} \quad (3.42)$$

The axial forces $(F_x(t), F_y(t))$ are simultaneously collected by the force cells. Displacements and forces are reported in Figure 3.34. The test was stopped when a 2kN force was reached along the x axis. Going beyond may have damaged the actuators. Despite a proportional displacement on both axes, a significant drift of the force along the y-axis is observed after 841s of test. Given the final forces and the stress concentration matrix (Equation 3.31), an unbalanced biaxial stress state should be obtained in the center: $\{\sigma_{xx}, \sigma_{yy}\} \simeq \{250, 500\}$ MPa. The stress path is illustrated in Figure 3.35 where the theoretical transformation threshold (95% of remaining A phase) has been reported. The prescribed path should lead to a transformation of the medium.

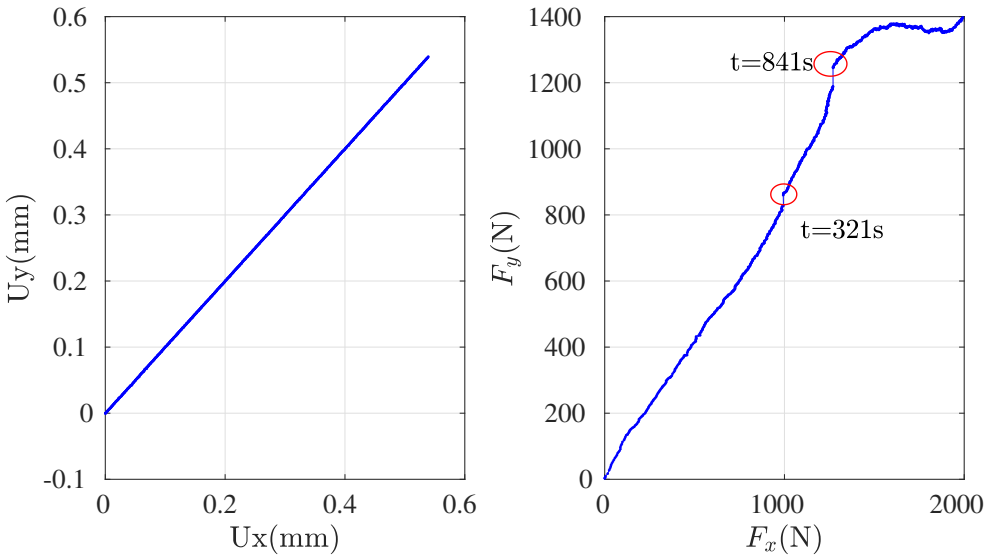

Figure 3.34: Equi-biaxial proportional test : (Left) prescribed displacement loading (Right) measured axial forces

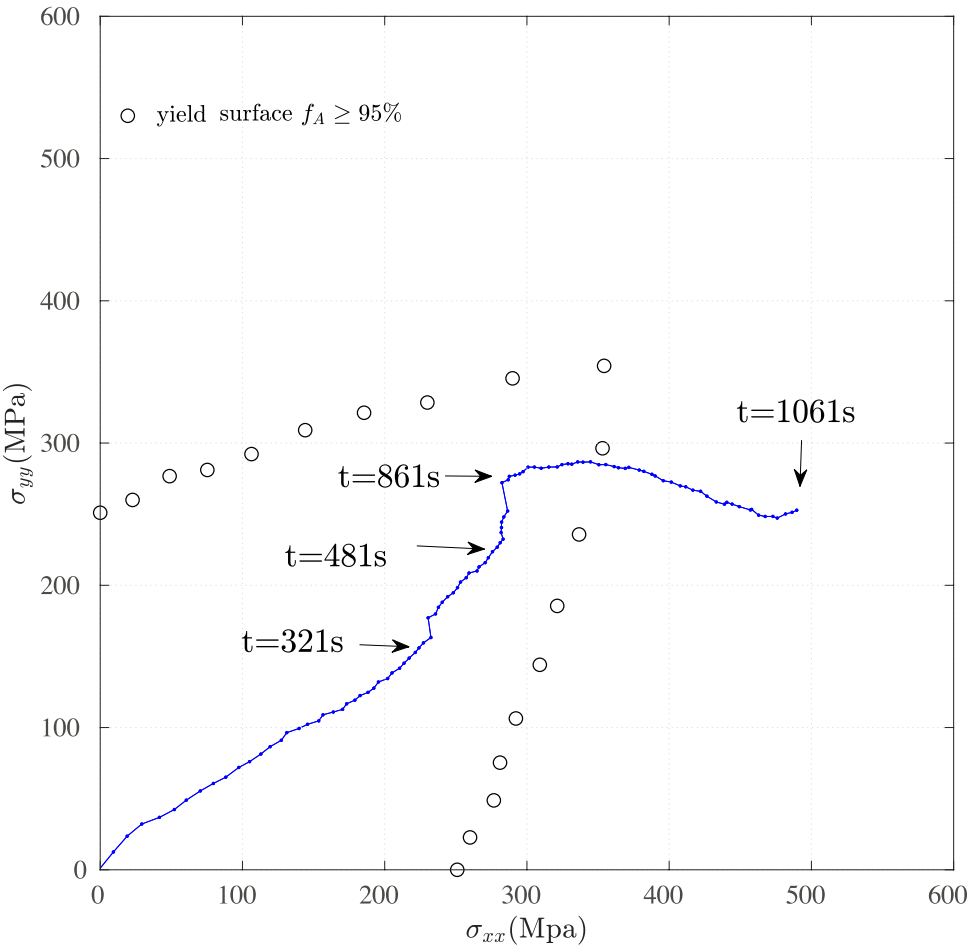

Figure 3.35: Visualization of stress path in the stress space.

Kinematic field

The two axial strain and equivalent strain field as function of time $\epsilon_{xx}(\mathbf{x}, t)$, $\epsilon_{yy}(\mathbf{x}, t)$, $\epsilon_{eq}(\mathbf{x}, t)$ are presented in Figure 3.36, Figure 3.37 and Figure 3.38.
These results show, on the one hand, that a localization appears about 850s after the beginning of the test, in connection with the drift of the force on the y axis. These results also show that deformations along the x-axis are generally larger than those observed along the y-axis. This result is consistent again with the drift of the force. We notice above all, by looking at the deformation along the x-axis (Figure 3.36), an unexpected local appearance of a deformation in the y-axis arms of the test piece (400s after the start of the test). This deformation explains the relaxation of force along the y axis. After $t \geq 851\,\mathrm{s}$, a real transformation begins to be massively observed in $\epsilon_{eq}(x, t)$, meaning probably that the yield stress has been bypassed.
The deformation levels observed in the center are however relatively low, and not much in accordance with what could be expected given the estimated stress levels. One can imagine that the premature localization in the arms leads to a global modification of the current stress actually acting in the center. Note also that we do not have access to what happens on the other side of the specimen.
These results are also worrying because they do not bode well for the rest of the tests if a localization persists to appear in the arms. One can also ask the question of the validity of the finite element calculations which has led to the initial dimension of the 2D specimen.

Comparison between experimental results and multiscale stochastic modeling

Despite the doubts raised by the results, we attempt a comparison between the experimental results and those from the multiscale stochastic model. The experimental equivalent strain is calculated over the blue circle plotted in Figure 3.39. The biaxial stress path extracted from the applied boundary forces reported in Figure 3.34b is introduced in the multiscale stochastic modeling. The strain tensor and the equivalent strain are obtained and compared directly to the experimental results in Figure 3.40.
The numerical simulation is consistent with the experimental data for the elastic regime and able to predict the same equivalent yield stress. No more consistency is observed afterwards: while the model predicts an equivalent deformation quickly reaching 6%, the measured equivalent strain stagnates. This probably means either that a large part of the applied force is used to compensate for the geometric non-linearities produced by the deformations of the arms, or that the terms of the passage matrix are highly over-estimated and that the stresses are actually much

lower than expected. Finally, it is also possible that some mechanisms not taken into account by the model are at work and that the strain hardening is much more intense during the biaxial loading. Obviously this test does not validate the modeling.

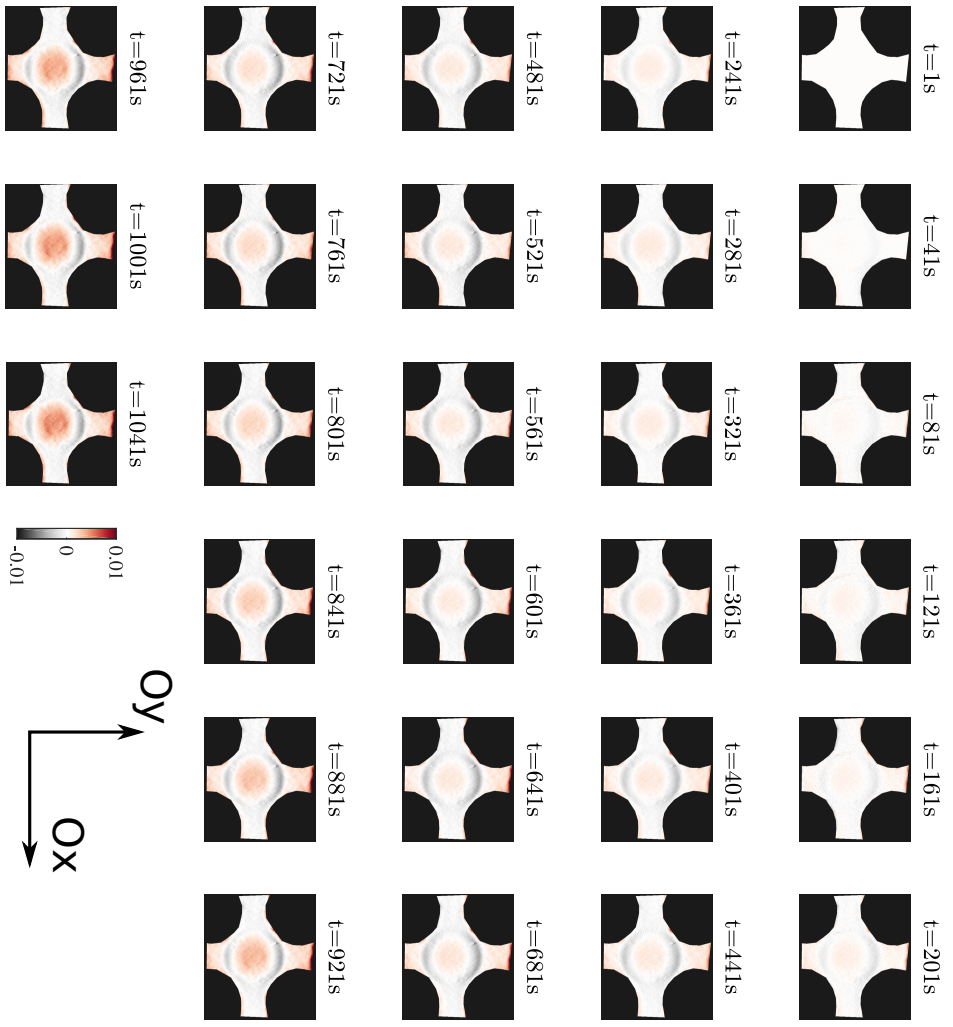

Figure 3.36: Axial strain field $\epsilon_{xx}(\mathbf{x}, t)$ as a function of time (axial strain $\epsilon_{xx}(\mathbf{x}, t)$ localizes at the upper and down branch region after $t \geq 321$s)

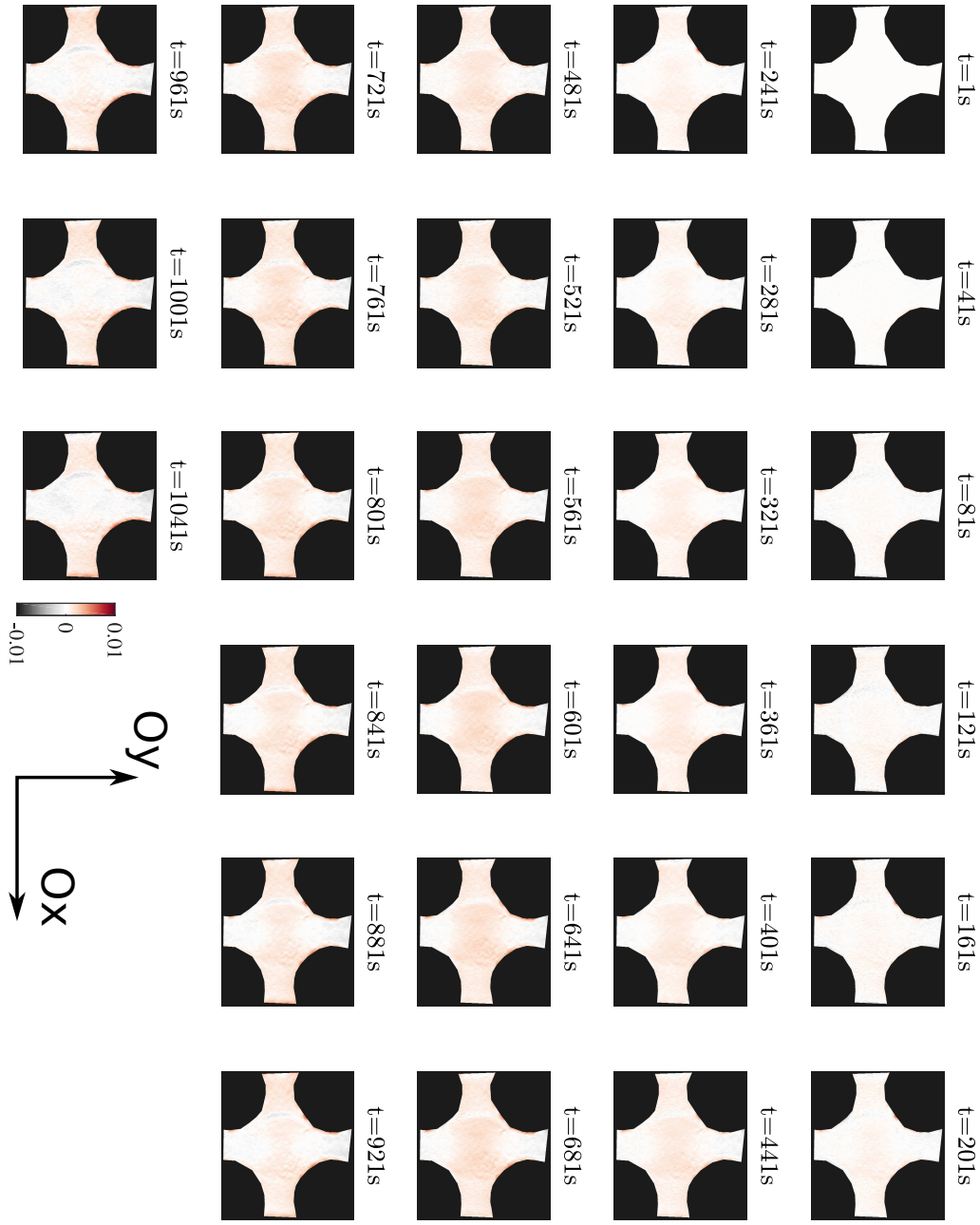

Figure 3.37: Axial strain field $\epsilon_{yy}(\mathbf{x}, t)$ as function of time

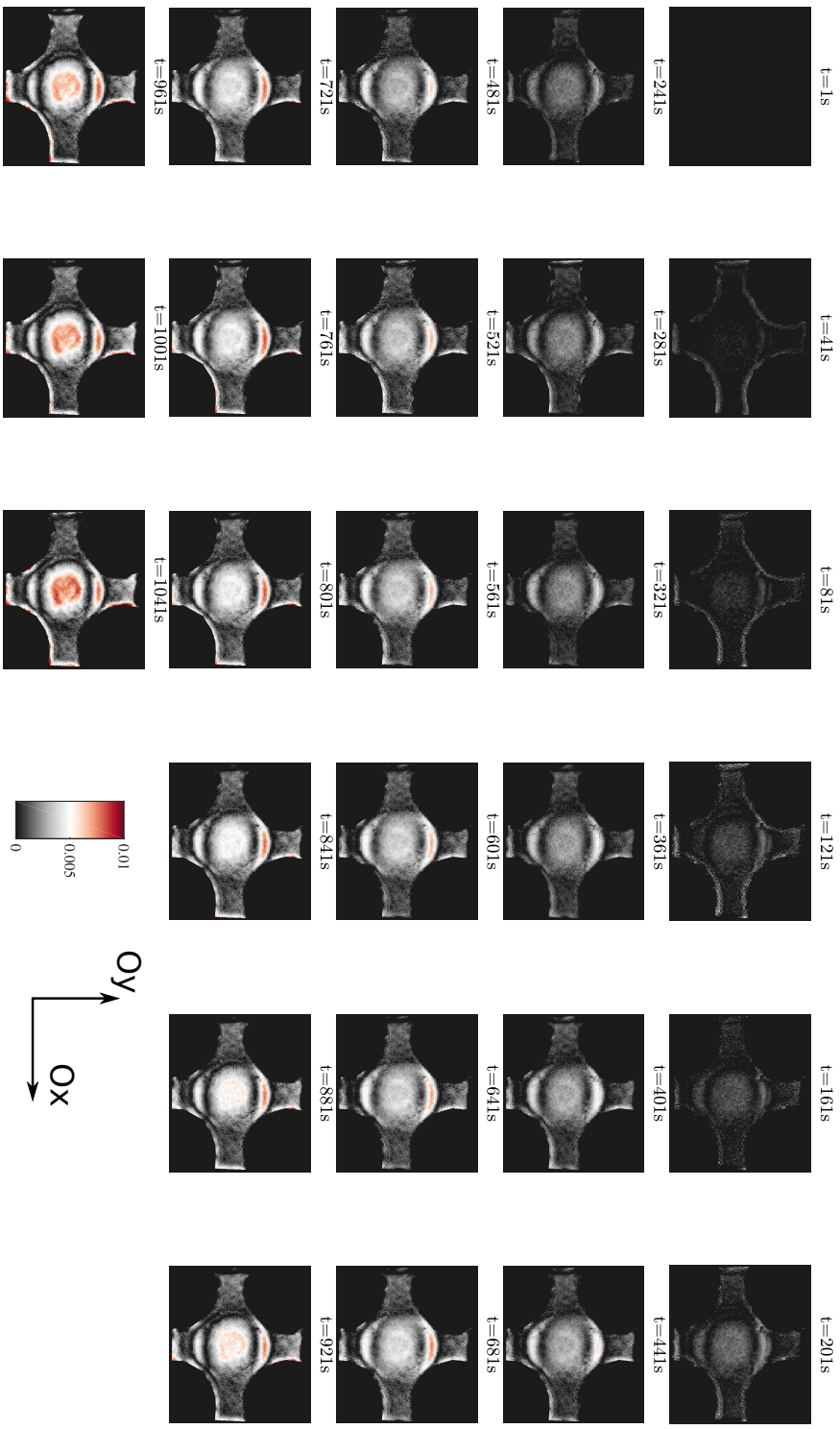

Figure 3.38: Equivalent strain field $\epsilon_{eq}(\mathbf{x}, t)$ as function of time ($\epsilon_{eq}(\mathbf{x}, t)$ localizes also at the upper and down branch region after $t \geq 321$s)

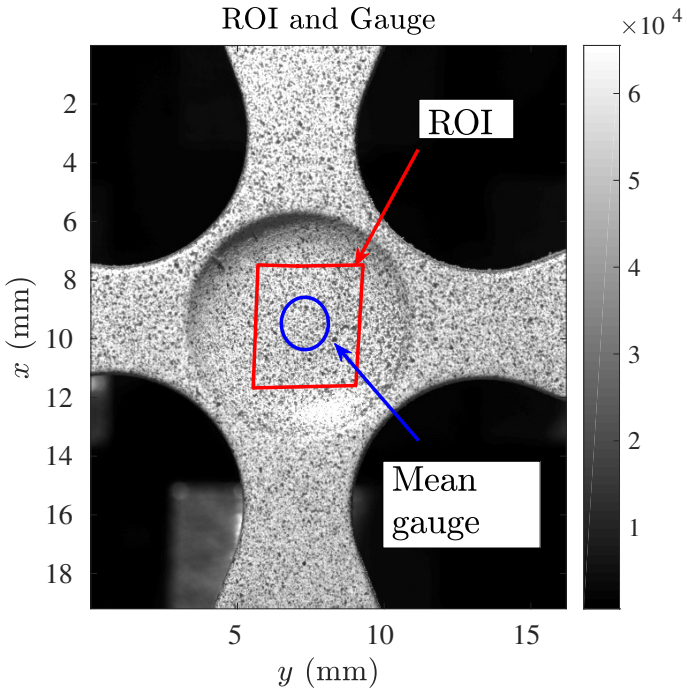

Figure 3.39: ROI (red rectangle) and gauge (blue circle)

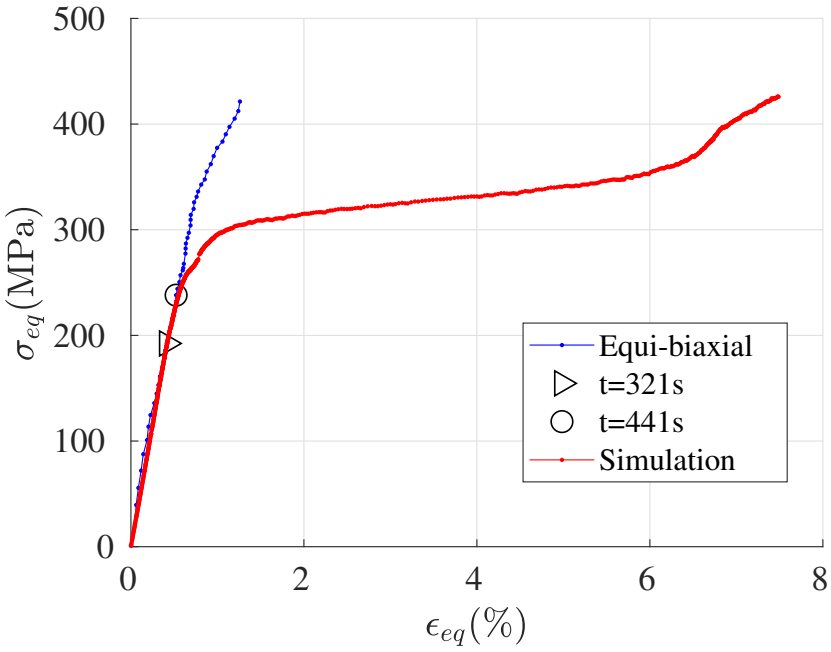

Figure 3.40: Comparison between the equi-biaxial experimental test (in blue) and numerical simulations (in red)

3.5.2 Non proportional test 1: L-shape test

The first non proportional loading that has been tested is a "L shape" test. It has been conducted at the room temperature $T = 298\,\mathrm{K}$.

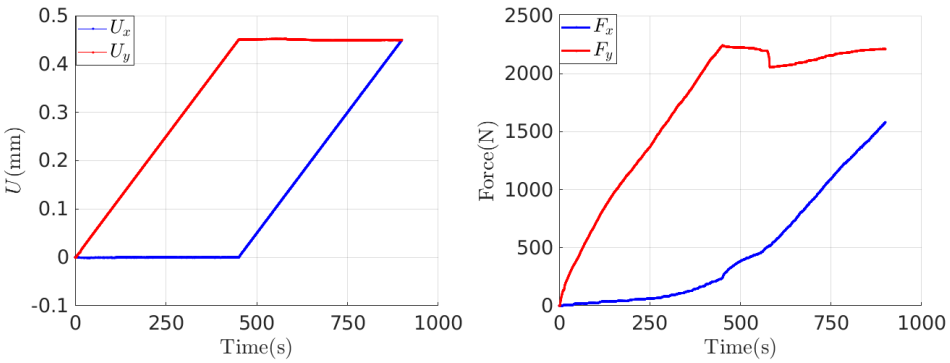

Figure 3.41: (Left) External displacement loading applied as function of time; (Right) measured axial force as function of time

Loading path

The loading path is illustrated in Figure 3.41 and detailed hereafter:

- In the first part of the loading path, a tensile displacement is applied along the y-axis up to $u_y = 0.5\,\mathrm{mm}$; the displacement along x-axis is held at zero.

$$u_y(t) = \frac{0.45t}{450} \text{ and } u_x(t) = 0, 0 \leq t \leq 450s \tag{3.43}$$

- In the second part of loading path, the displacement is held constant along the y axis, and a displacement along the x axis is applied, until a maximum amplitude of $u_x = 0.5\,\mathrm{mm}$

$$u_y(t) = 0.450 \text{ and } u_x(t) = \frac{0.45(t-450)}{450}, 450 \leq t \leq 900s \tag{3.44}$$

Temporal evolution of the strain field

Figure 3.42 shows the spatial-temporal evolution of equivalent strain field. Inside the center region, the following comments can be made:

- some localization bands appear in the center of the specimen between $t = 321\,\mathrm{s}$ and $t = 401\,\mathrm{s}$;
- the strain level reaches its maximum between $t = 441\,\mathrm{s}$ and $t = 481\,\mathrm{s}$. We observe two principal crossing bands, accompanied by multiple secondary nucleation bands.

- strain begins to decrease at the loading direction change of the loading path.
- at the end of the loading path ($t = 881\,\mathrm{s}$), some deformation remains: one of the two principal bands are still present.

For this test, even if no significant strain localization has been observed in the arms of the specimen, some deformation bands have reached the edges of the specimen. This result is not at all foreseen by the Abaqus elastic model, which can lead to an erroneous evaluation of the constants of the passage matrix.

Stress-strain response

Based on the measured axial forces and despite the doubts we can have concerning the validity of the matrix, the stress level at the center region has been nonetheless estimated by Equation 3.31. The L-shape non proportional loading path can be plotted in the stress space $(\sigma_{xx}, \sigma_{yy})$ as presented in Figure 3.43 (left). Figure 3.43 (right) shows the associated $(\epsilon_{xx}, \epsilon_{yy})$ deformation path, highlighting the points where the transformation threshold seems to be bypassed (black triangles) and the points when the localization has been observed at the edge of the sample (red dots).
From these results, it has been possible to plot the equivalent stress-strain curve in Figure 3.44(left) and the equivalent strain as function of time in Figure 3.44 (right). A first observation is that the equivalent stress-strain response behaves very differently compared to pseudoelasticity under uniaxial loading in several aspects::

- before reaching the transformation threshold, the ROI (blue circle in Figure 3.7) behaves as an elastic material.
- between $200 \leq t \leq 360\,\mathrm{s}$, the equivalent strain is nearly homogeneous with several scattered transformation in the central region. However, when $t \geq 200\mathrm{s}$, a significant strain localization appears in the left and right branch.
- After the onset of localization bands at $t = 360\,\mathrm{s}$, we observe a decrease of the tangent modulus. This looks like a beginning of PE transformation plateau.

Comparison test/simulation

As for the proportional test, we introduce the stress evolution extracted from the experimental data as the loading of the multiscale stochastic model of the NiTi sample, using room temperature $T = 300\mathrm{K}$ and with a chosen convection coefficient k= 0.05 $\mathrm{J.m^{-3}.K^{-1}}$ as thermal boundary conditions.
The equivalent stress-strain evolution for the numerical simulation and experimental results are compared in Figure 3.45. The corresponding biaxial deformation paths are plotted in Figure 3.46. Several comments can be drawn:

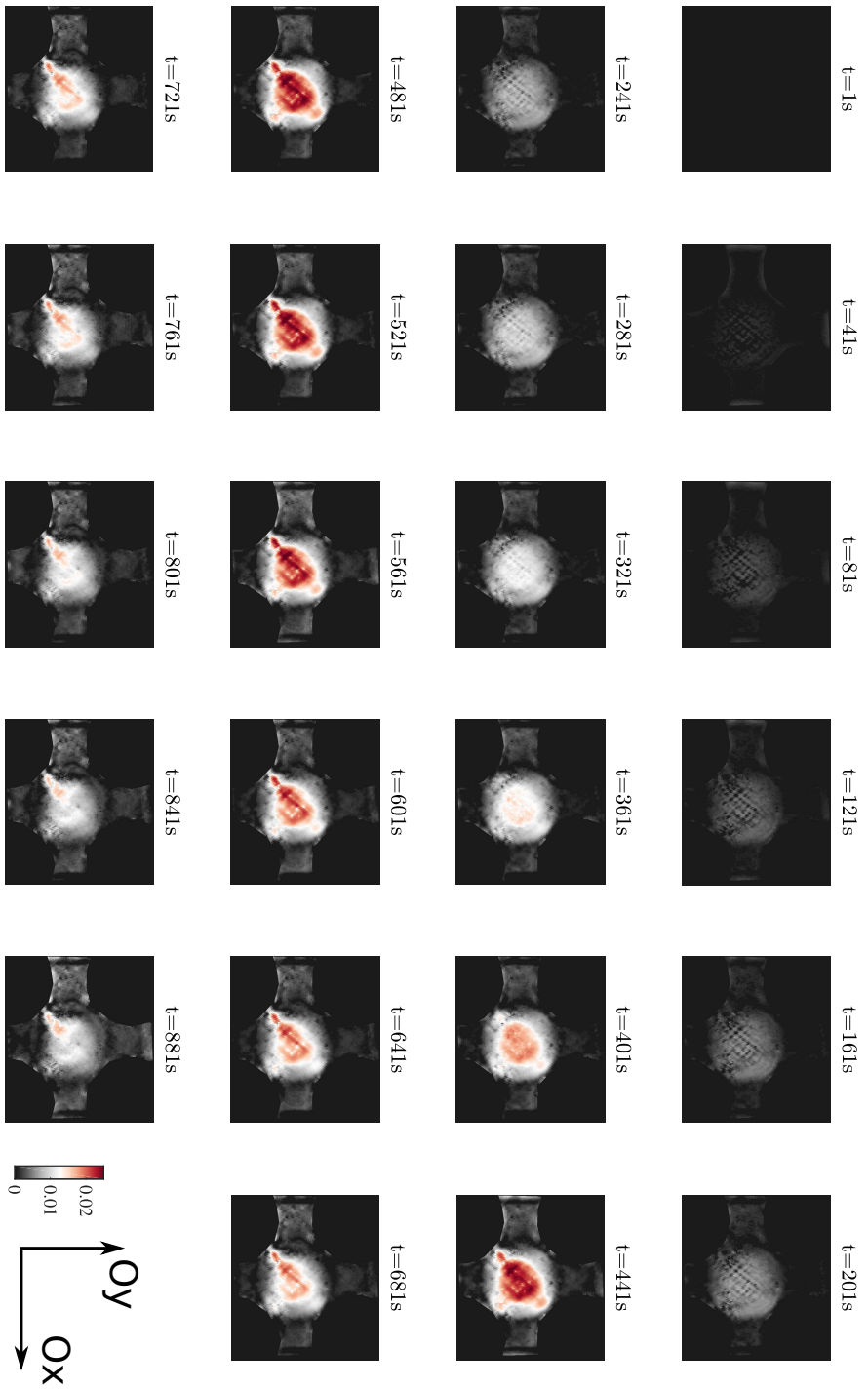

Figure 3.42: Equivalent strain field evolution for L shape test (undesired strain localization is observed at left/right branch)

- before reaching the yielding point, the numerical stress-strain evolution is in good agreement with the experimental data;
- as already observed, the numerical calculation strongly overestimates the strain level: the measured deformation is about ten times lower than the predicted one.

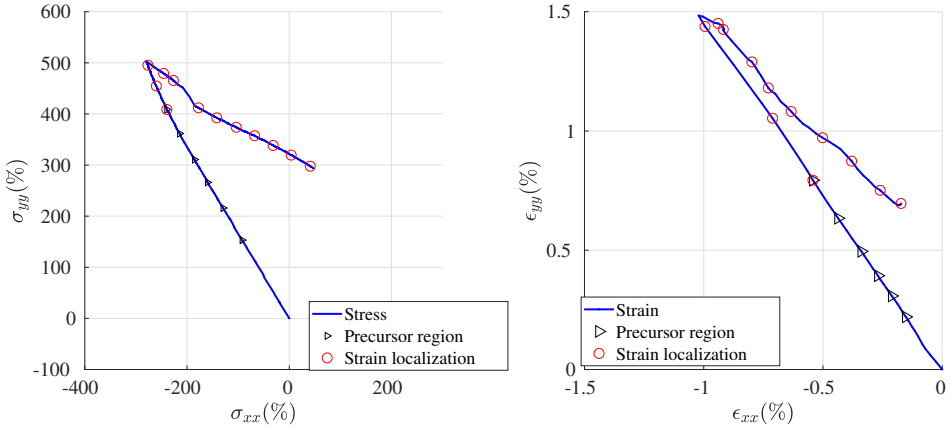

Figure 3.43: (Left) $(\sigma_{xx}, \sigma_{yy})$ stress estimation based on FE calculation; (Right) measured strain path in $(\overline{\epsilon}_{xx}, \overline{\epsilon}_{yy})$ (black triangles indicate points where the transformation threshold seems to be bypassed; red dots correspond to points after the localization at the edge of the sample).

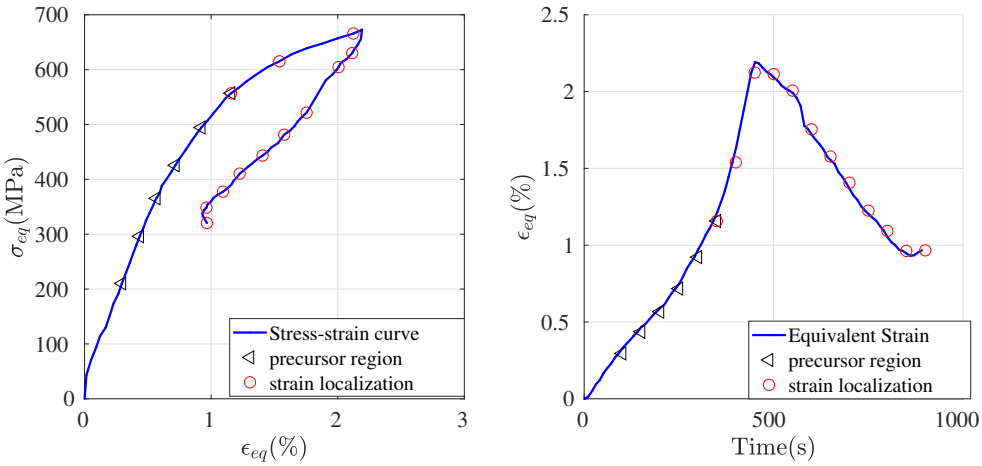

Figure 3.44: (Left): Equivalent stress-strain curve (black triangles indicate points where the transformation threshold seems to be bypassed; red dots correspond to points after the localization at the edge of the sample). (Right) equivalent strain as function of time

The reasons for these major differences seem to be the same as those mentioned above: a probable over-estimation of the terms of the passage matrix due to some geometric non-linearities not taken into account; a structural thermomechanical effect insufficiently corrected by the use of a simple exchange constant. The test, as for the proportional situation, does not allow a validation of the model.

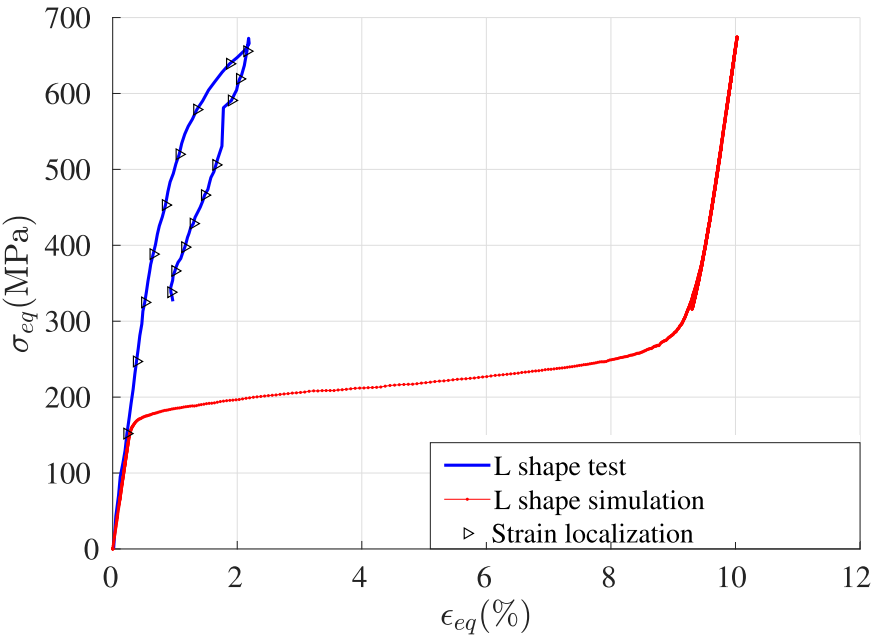

Figure 3.45: Experimental and modeled equivalent stress-strain curve during the first L shape loading (numerical prediction in red and experimental data in blue, black triangles indicate points where the transformation threshold seems to be by-passed)

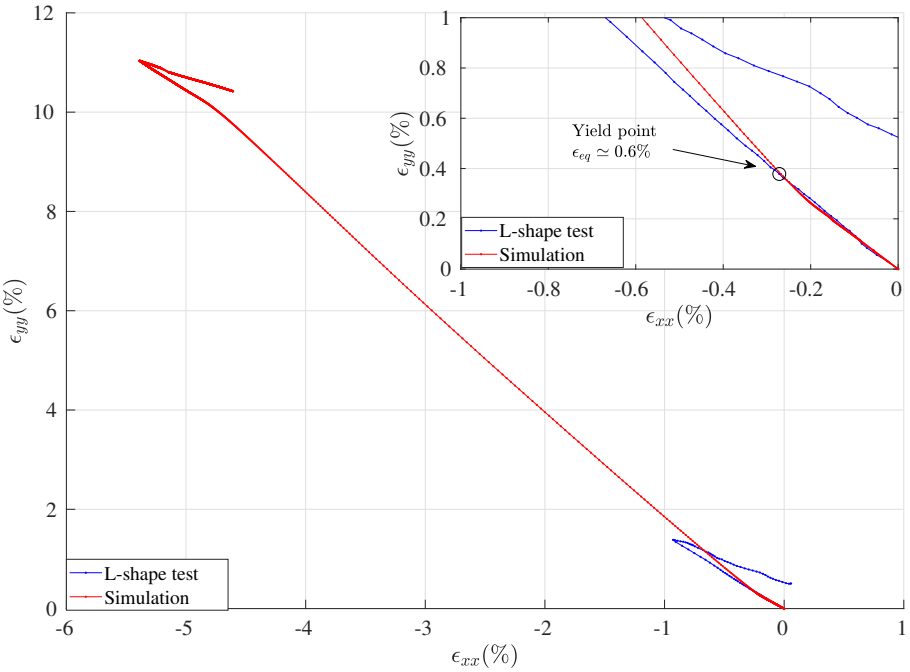

Figure 3.46: Comparison of strain evolution: Experimental data plotted in blue and numerical simulation plotted in red, yield point plotted in black

3.5.3 Non-proportional test 2: double-snail test

A "double snail" test has been conducted at $T = 287K$ (13K lower than the ambient temperature for the previous test) . According to the thermal impact over the tensile test results, we expect to observe a yield stress lower than for the L shape test.

Loading path The double snail test is corresponding to the following displacement controlled loading path applied to the 2D specimen (illustrated in Figure 3.47a and Figure 3.47b). The axial forces evolution during this loading path is reported in Figure 3.48.

Direct snail : an initial displacement controlled loading cycle is applied, following successively A-B-C-D-A in the displacement space (see Figure 3.47a).

Reverse snail : a 2nd loading is applied in the reverse direction, following successively A-D-C-B-A path in the displacement space;

Branch test A1 : From A to B then back to A (Axial displacement u_y varies whereas u_x is maintained at zero) .

Branch test A2 : From A to D then back to A (Axial displacement u_x varies whereas u_y is maintained at zero) .

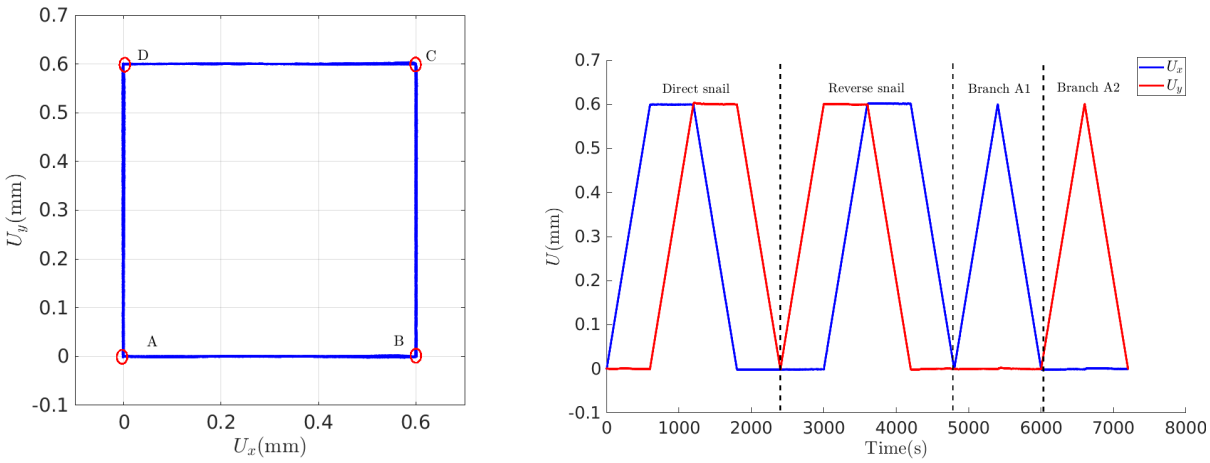

(a) Loading path in displacement plane (u_x, u_y)

(b) Applied axial displacement as function of time

Figure 3.47: The loading path and each stage: (a) displacement loading path; (b) axial displacement applied as a function of time

The equivalent strain field at different step times are reported in Figure 3.49 for the direct snail, in Figure 3.50 for the reverse snail, in Figure 3.51 and Figure 3.52 for the branch tests A1 and A2 respectively.
The following comments can be made:

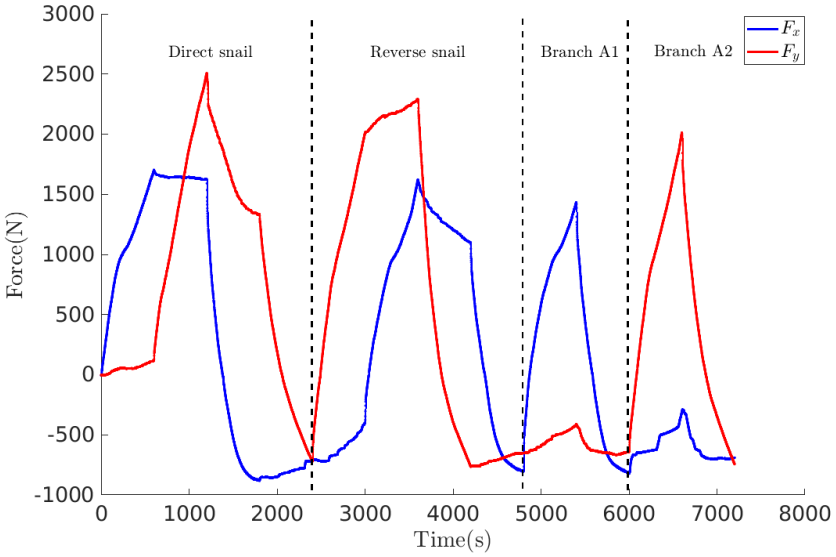

Figure 3.48: Measured axial forces along y-axis and x-axis.

- Direct snail test
  As we can see in Figure 3.49, when the initial displacement is applied from A to B, several minor localization bands nucleate ($t = 600$s). At $t = 1200$ s (mid point between point C and D in the displacements space), we begin to observe a strong nucleation and a propagation of some bands. The localization reaches its maximum at point D. Then, it decreases gradually towards its disappearance when point A is reached.

- Reverse snail test
  The reverse snail test triggers the localization phenomena rather quickly compared to the previous cycle. The localization begins at frame $t = 2400$ s between points A and D (Figure 3.47a). The localization decreases from points D to C (from $t = 3000$ s to $t = 3600$ s). From points C to B, we see that the average strain increases; however, no clear localization band has been observed at $t = 4200$ s corresponding to point B.

- Two branch tests along direction A1 and A2
  These two tests, even if symmetrical regarding to the expected equivalent strain, do not lead to the same force (as illustrated in Figure 3.48) or strain levels. The reached strain level is significantly higher for branch test A1, corresponding to the lower applied force. This result is symptomatic of the probable existence of an initial stress state or a consequence of stress-induced training.

In addition to the reasons mentioned above concerning the probable geometrical non-linearities on the one hand, and the existence of an initial stress state on the other hand, it is possible that a part of the martensite formed for example during

the branch test A1 is not completely retransformed into austenite at the beginning of the branch test A2, explaining that may explain the observed dissymmetry.

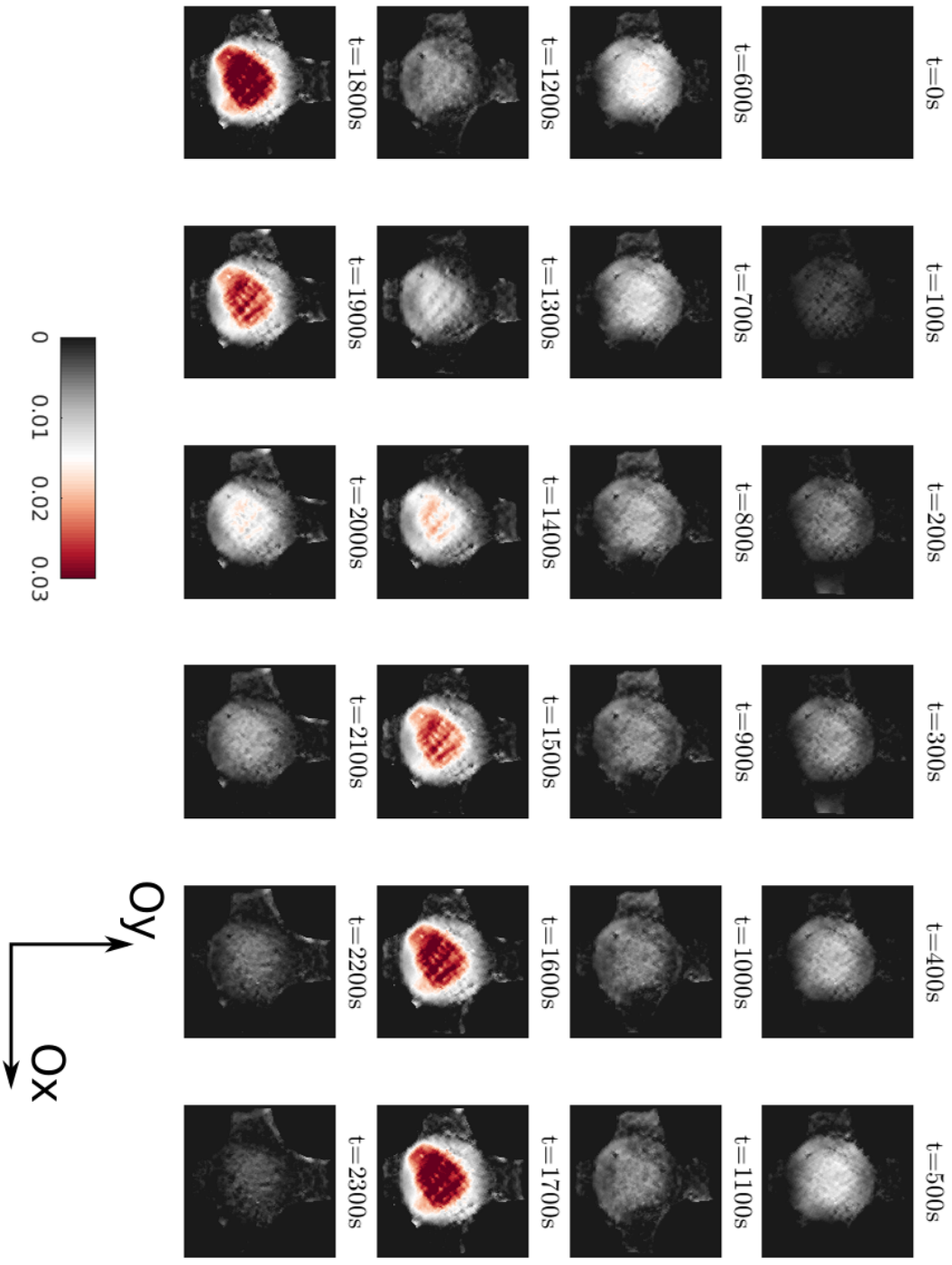

Figure 3.49: Equivalent strain field evolution $\epsilon_{\text{eq}}(x,t)$ during the direct snail (A-B-C-D-A)

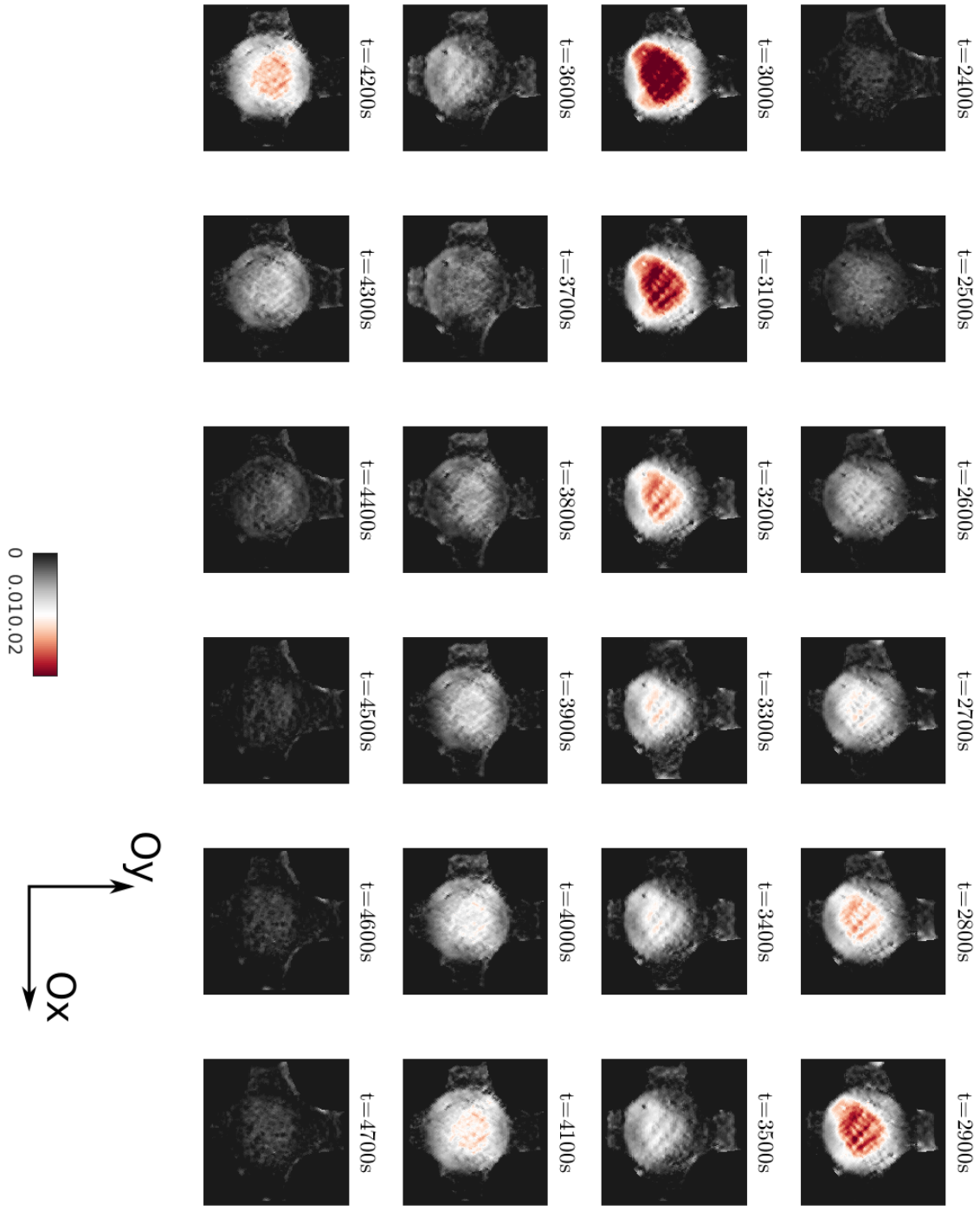

Figure 3.50: Equivalent strain field evolution $\epsilon_{\text{eq}}(x,t)$ during the reverse snail (A-D-C-B-A)

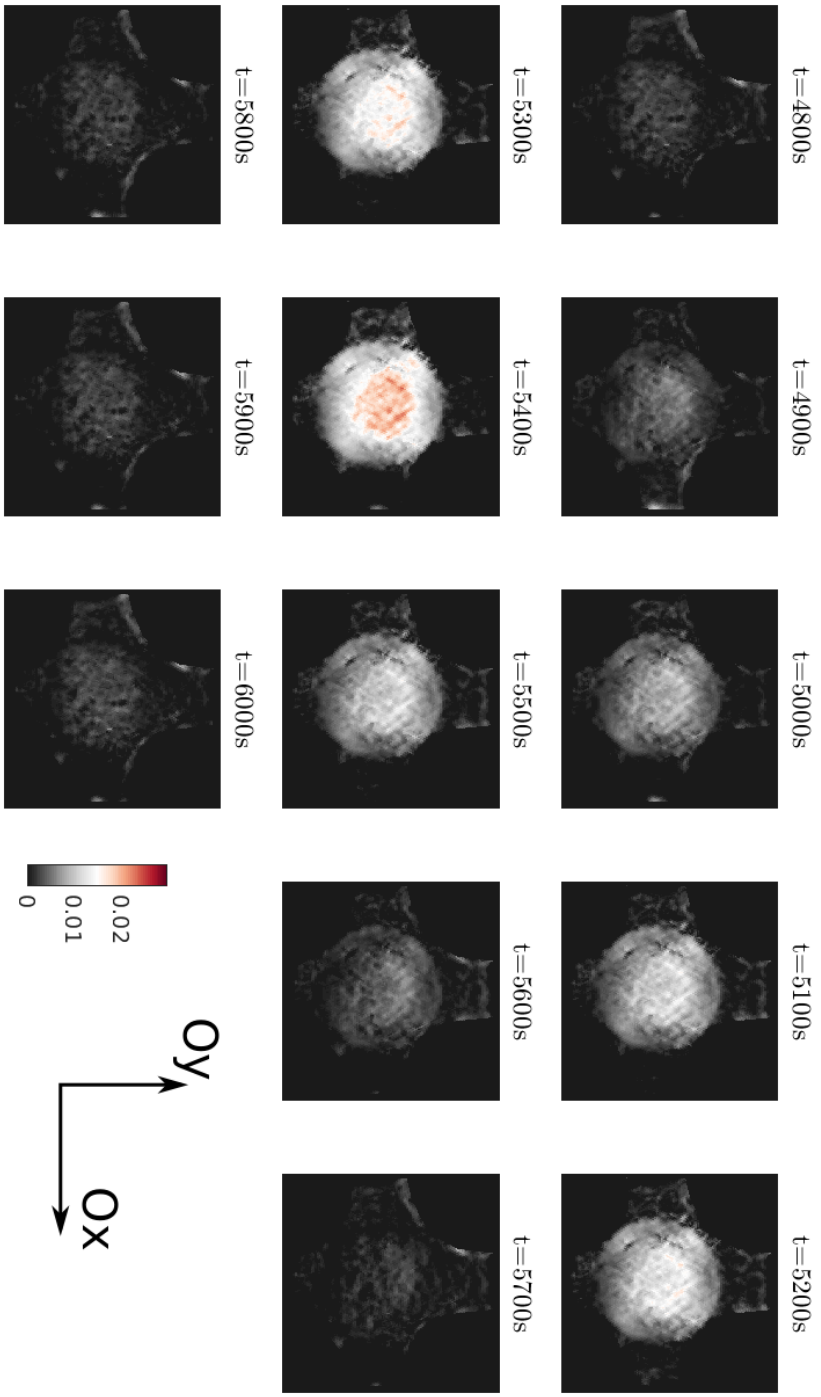

Figure 3.51: Equivalent Strain field evolution $\epsilon_{\text{eq}}(x,t)$ for the branch test along direction A1

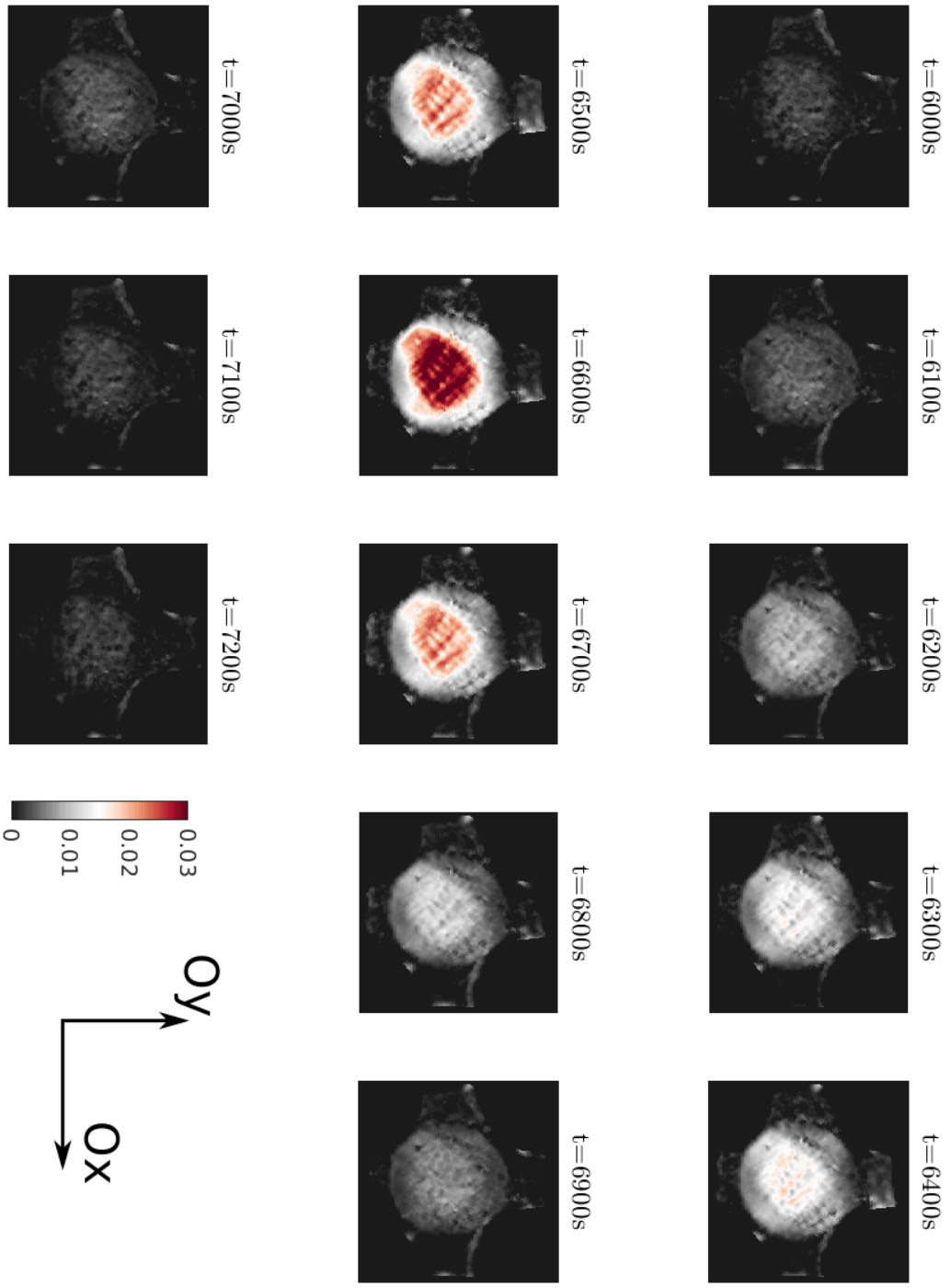

Figure 3.52: Equivalent Strain field evolution $\epsilon_{\text{eq}}(x,t)$ for the branch test along direction A2

Whatever the tests, it can be seen that the deformation levels observed are significantly lower than those observed during the uniaxial tests. The detection of transformation thresholds is therefore more difficult. Nevertheless, we can calculate the evolution of the central average equivalent strain as a function of time. This function is drawn in Figure 3.53. A deformation level threshold $\epsilon_{tr} = 0.6\%$ has been chosen as an indicator of a transformation start (a value consistent with the uniaxial tests); a 2% equivalent strain level seems to indicate the appearance of strong localizations. Levels beyond 0.6% have then been reported in red in Figure 3.54 along the stress path for each test. This representation makes it possible to visually determine the elastic domain. The results obtained seem consistent with this hypothesis.
From Figure 3.55 to Figure 3.58, it shows that the equivalent stress-strain responses associated with the direct snail, reverse snail, branch A1 and branch A2 tests. All lead to more or less complex mechanical hysteresis that it seems difficult to analyze without the help of a model.

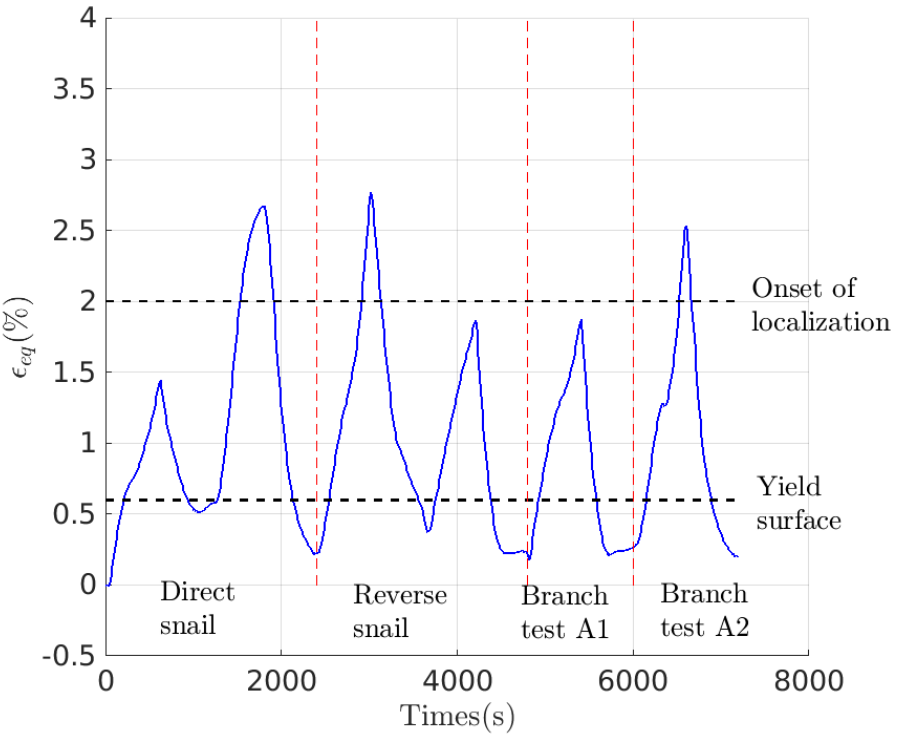

Figure 3.53: Equivalent strain evolution and estimation of thresholds for transformation (in black) and mean equivalent strain inside blue circle as presented in Figure 3.39.

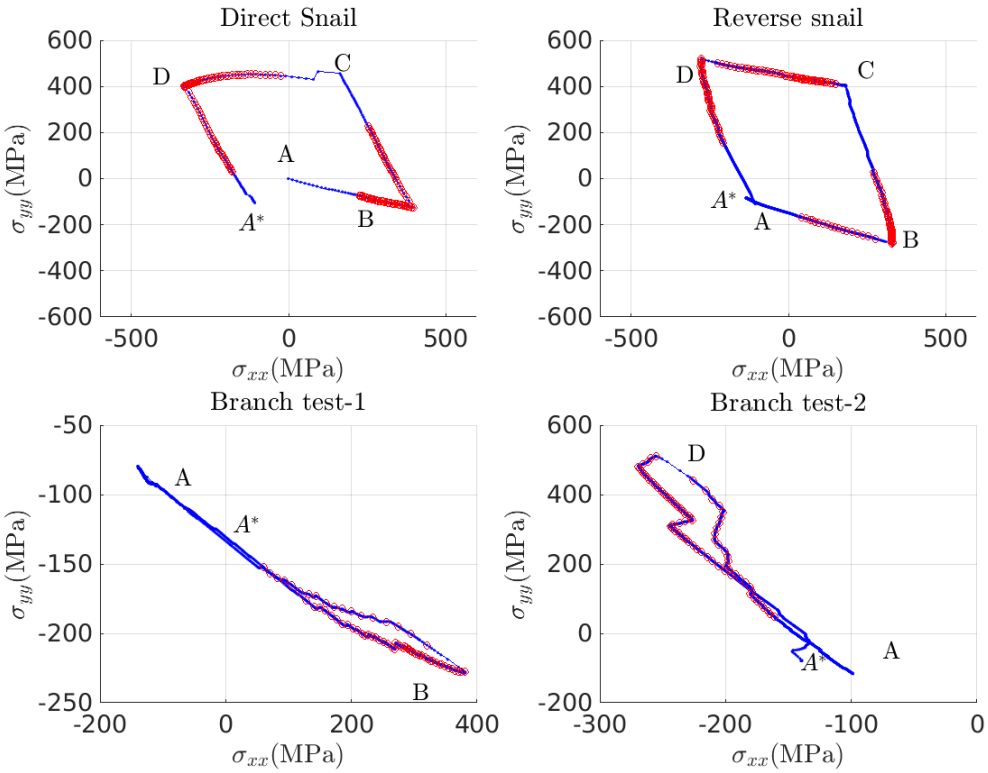

Figure 3.54: Loading path in stress space (Red dots represent states where the stress level bypass the chosen yield criteria): (Upper left): direct snail ($A \rightarrow B \rightarrow C \rightarrow D \rightarrow A^*$); (Upper right) reverse snail ($A \rightarrow D \rightarrow C \rightarrow B \rightarrow A^*$) ; (Bottom left) branch test A1 ($A \rightarrow B \rightarrow A^*$); branch test A2 ($A \rightarrow D \rightarrow A^*$)

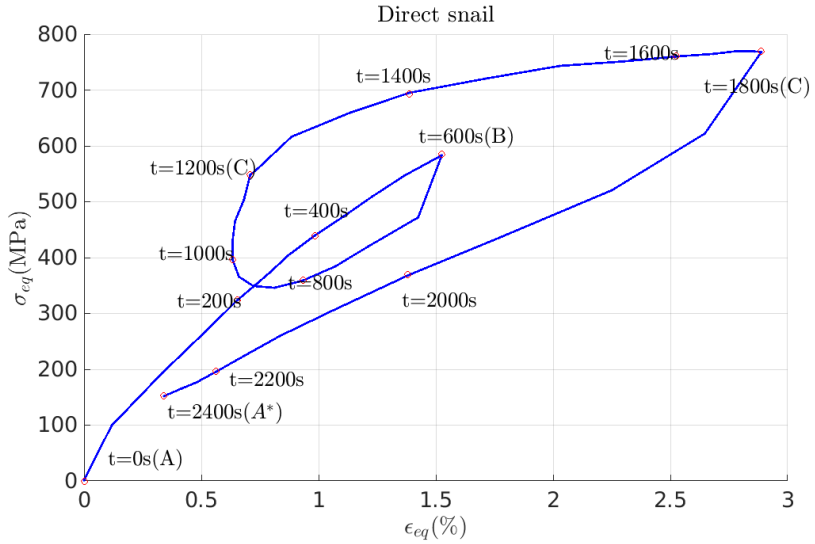

Figure 3.55: Equivalent stress/strain curve during the 'direct snail stage' (markers plotted in red correspond to Figure 3.49)

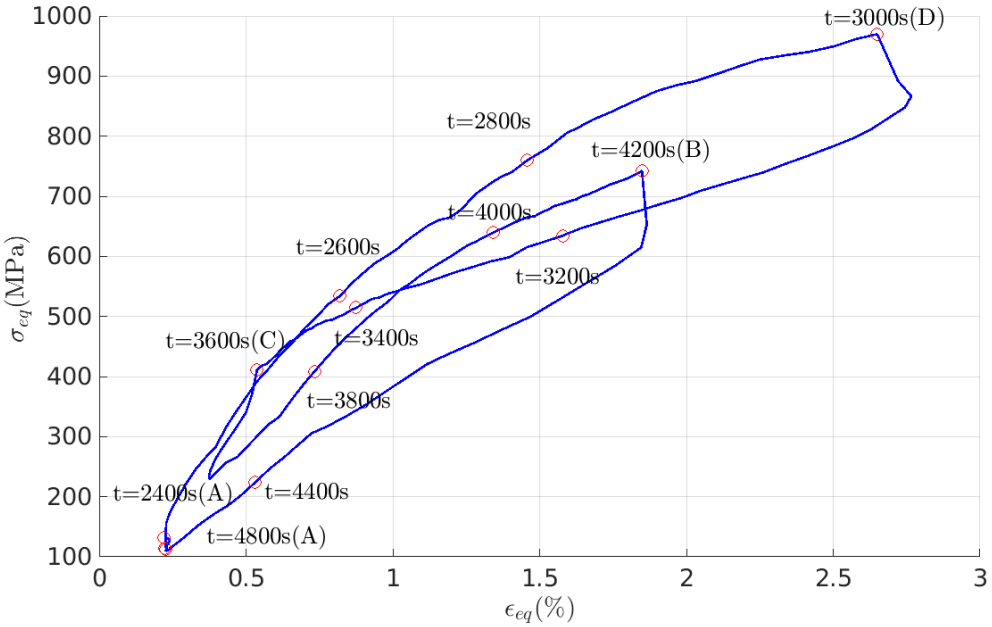

Figure 3.56: Equivalent stress/strain curve during the 'reverse snail stage' (markers plotted in red correspond to Figure 3.50)

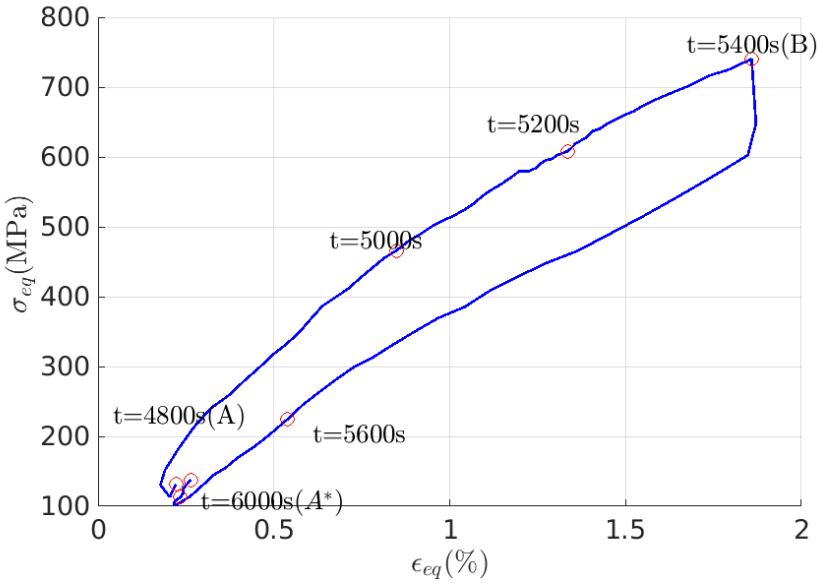

Figure 3.57: Equivalent stress/strain curve during the stage of 'Branch test A1' (markers plotted in black correspond to Figure 3.51)

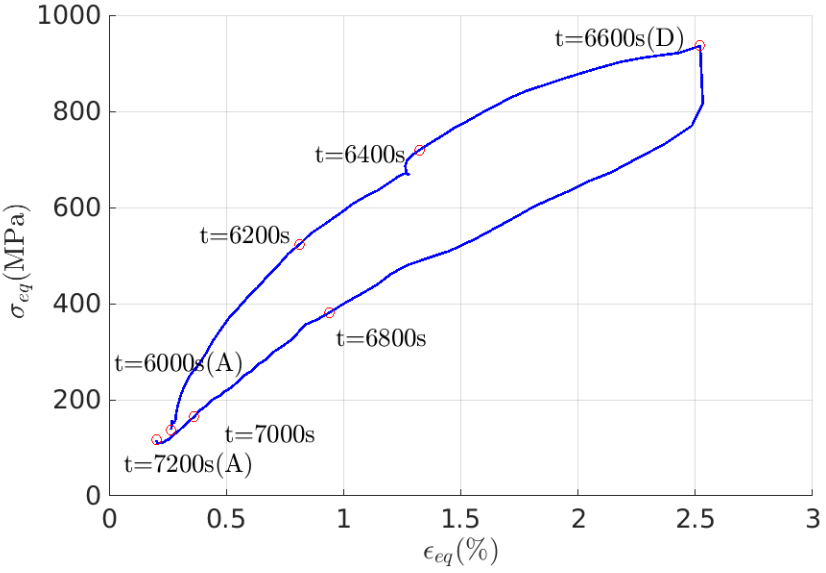

Figure 3.58: Equivalent stress/strain curve during the stage of 'Branch test A2' (markers plotted in black correspond to Figure 3.52)

Comparison Test/Simulation The experimental data are compared with the numerical simulations in Figure 3.59 and Figure 3.60 during the first direct snail $A \to B \to C \to D \to A$. As for the previous simulation, we introduce the stress evolution extracted from the experimental data as a loading of the multiscale stochastic model of the NiTi sample, using room temperature $T = 287$K and convection coefficient k=0.05 J.m^{-3}.K^{-1}. Similarly as previous multiaxial loading, the numerical simulation tends to give an accurate prediction of the yield stress. Since the room temperature during tensile test is $T = 287$K, the numerical yield stress is around $\sigma_{eq} \simeq 130\,$MPa. It corresponds to the point where the numerical simulation and experimental data begin to differ. The reasons that can be invoked to explain the observed discrepancies are the same as those already mentioned: geometric nonlinearities, poor estimation of the passage matrix, thermomechanical effects. A validation of the model can not be obtained via these tests.

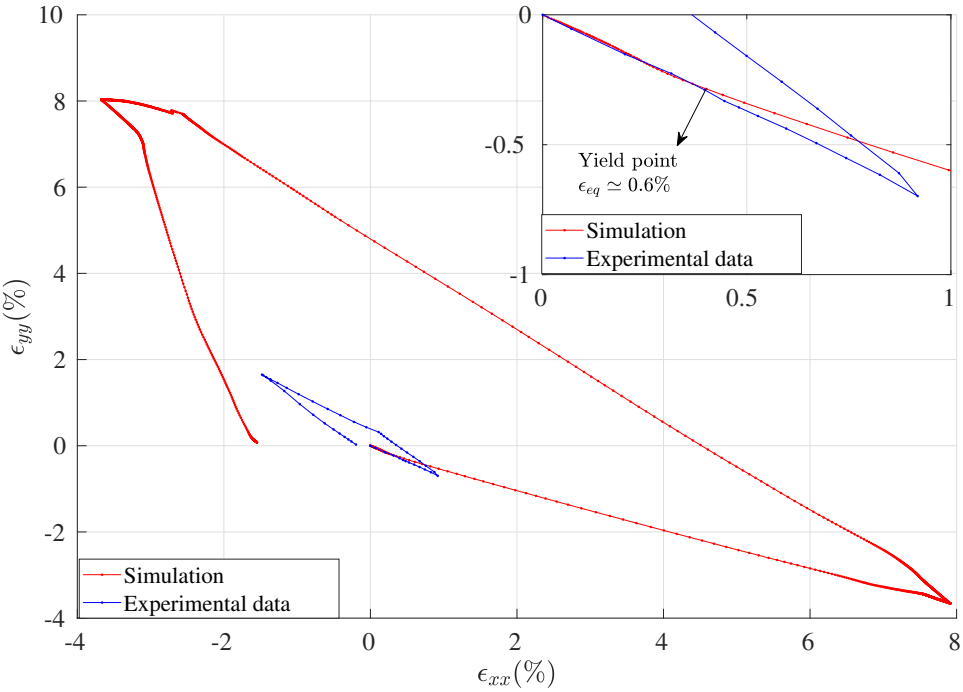

Figure 3.59: Axial strain evolution (simulation in red and experimental data in blue)

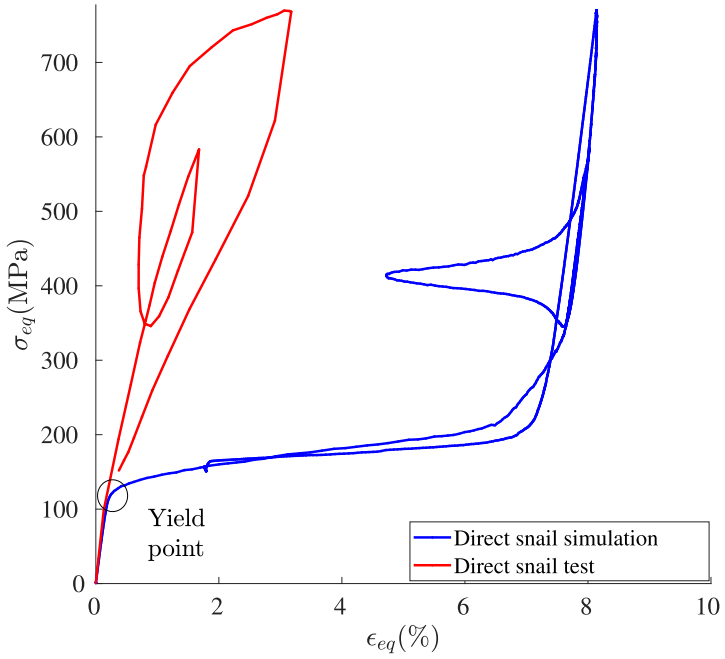

Figure 3.60: Equivalent stress/strain evolution during the first direct snail (simulation in red and experimental data in blue)

3.6 Conclusion

Objective The objective of this chapter was to obtain some full-field global and continuous observation of the kinematic fields under uniaxial and multiaxial loading by R-DIC techniques.

Regularization method The experimental challenge that consists to conduct mechanical tests inside an X-ray chamber (see next chapter) requires to employ tiny specimens. Moreover, the kinematic field of SMA is usually complex and heterogeneous due to the localization phenomenon. Combined with the extremely limited spatial size, solving the kinematic field is beyond the capacity of most commercial DIC codes. By employing a mechanical regularization, high frequency components of the displacement field are suppressed. Highly heterogeneous displacement and strain fields can then be deduced through an "educated" relaxation procedure.

Full field observation This technique has been applied to observe the localization phenomena of SMA subjected to uniaxial and multiaxial mechanical loadings under anisothermal conditions.

Collected database Strain and strain-rate field's evolution, the morphology of localization bands, and their occurrence under either uniaxial or multiaxial loading configurations, offer a rich database for any uniaxial or multiaxial model aiming at an experimental validation of a model.

Comparison with the multiscale stochastic model The multiscale model gives results that are globally consistent with the uniaxial tests for the different thresholds (forward, backward, hysteresis) for the two temperatures and the two velocities investigated. On the other hand, the model fails to reproduce the deformation levels observed. Over-simplified homogenization hypotheses can be critical in this regard. The inability of the model to reproduce the macroscopic transformation bands structure and the associated heterogeneous thermal field is probably at the origin of the main differences observed.
Similarly, the multiscale model is only able to simulate the main mechanical thresholds during the biaxial tests. In addition to the causes/effects similar to those identified for the uniaxial tests (formation of bands, thermomecanical heterogeneities), it is found that most of the biaxial tests are accompanied by a

premature deformation in the arms or at the edge of the specimen, whereas these deformations are not foreseen according to the initial calculations.

Improvements and strategy These tests show that, regarding to the study of the PE behavior of SMA in multiaxial situation, it is vain to seek to develop mechanically localized and homogeneous situations. The bands localization appears even at a very fine scale leading to numerous heterogeneities. On the other hand, the results highlight the need to have a truly efficient structure model. Such structure modeling is required for a complete exploitation of the uniaxial tests data too. An attempt of structure modeling consistent with the multiscale stochastic model was started in this thesis work. The main elements of this approach are reported in appendix B.
The knowledge of temperature and phases locally present would also be important, always in the perspective of validating a modeling approach, combined with a structure model. Inspiring from the work of [Maynadier et al., 2011], IR camera can also be used to collect the temperature field associated with the strain field (IRIC). On the other hand, a first attempt of phase field via X-ray diffraction has been proposed in the work of [Fall et al., 2016]. A novel multiview technique for the global observation of phase field (combination observation between DIC-XRD) is developed in chapter 4 for some uniaxial tensile testing.

Chapter 4

Phase field reconstruction via POD

Contents

4.1 Introduction

In the previous chapter, we have conducted an experimental campaign that consisted in carrying out uniaxial and multiaxial tests. These tests represent a data base of a very high spatial resolution kinematic information (regulation length being relaxed until $L_{elem} = 80\,\mu\text{m}$). The well known localization phenomenon has been confirmed both for the 1D and the 2D specimens.

This localization phenomenon remains difficult and challenging to explore because:

- Bands birth is associated with a local phase transformation accompanied by a latent heat emission or absorption. The local temperature evolution depends on both the fraction of phase nucleated and the heat exchange as function of time (conduction in the sample, convection with the environment).

- The Ni-Ti alloy used for these tests is able to develop a R-phase, intermediate between A and M phases, as observed in the DSC measurements. This R-phase (as martensite) is associated with a specific transformation strain that makes possible its nucleation during a mechanical loading. In the literature, the question of the apparition or not of the R-phase during the localization phenomenon remains an open issue. The answer to this question may have potential insight for a better understanding of the fatigue behavior of these material for example.

As a result, a multiview observation of thermal, phase and kinematic field during the localization phenomenon could be of great interest. The coupled measurement of both thermal and kinematic fields has been intensively studied by many authors (see the work of [Shaw and Kyriakides, 1995], [He and Sun, 2010] and [Maynadier, 2012]). However, few research concerns the simultaneous observation of phase field and kinematic field in SMA. This information may be accessible from a combined X-Ray Diffraction (XRD) [Lukas et al., 2002; Sittner et al., 2006] and Digital Images Correlation (DIC) [Bewerse et al., 2013; Hild et al., 2009; Maynadier et al., 2012]) as proposed in this chapter. It is however essential that XRD is performed *in situ* and that the XRD analyzed points are properly positioned in the DIC strain map.

One of the chalenges for the XRD analysis of NiTi SMA is that pure R phase diffraction profile can not be experimentally obtained. And last but not least, due to stress-induced variants selection (for both R and M phase), the presence of a strong crystallographic texture [Gall et al., 2001; Hasan et al., 2008] modifies the relative intensities between the diffraction peaks, making the quantification of phases with the classical (typically Rietveld) method very difficult.

To circumvent this difficulty, a variant of the Proper Orthogonal Decomposition (POD) (or Principal Component Analysis, PCA) technique [Matos et al., 2007] and [Obeidat and I. Al-Momani, 2011]) is introduced to identify the principal modes, over which the XRD spectra are decomposed. These modes are further interpreted as combinations of A, M and R phases. A robust quantification of the phase field is looked for .

It is noteworthy that a mere POD technique is not appropriate to reach this goal since physical constraints, such as the positivity of the diffraction pattern, are not included. The originality of the proposed methodology is that it accounts for these physical constraints. It allows a successful identification of both phases diffraction patterns and phases concentration at each analyzed point.

This chapter is organized as follows: in section 4.2, a general recall about X-ray diffraction and theory of powder diffraction is given; in section 4.3, the general experimental setup and the raw results of both DIC and XRD measurements are presented. Employing the Bragg's law, the diffraction peaks have been properly indexed, which justifies the co-presence of three principal phases at the transformation plateau; in section 4.4, the noise quantification is presented. The nearly uniform distribution of white Gaussian noise after Anscombe transformation helps us to choose properly the primal objective function to be optimized. The general associated algorithm is presented in section 4.5, where we illustrate how the POD allows the whole measured spectra to be presented with three principal modes , and how the implementation of the

physical constraints allows the identification of both the diffraction patterns and the phases fraction at each point. In section 4.7, the phase field and DIC strain maps are spatially correlated so that both kinematic and phase fractions can be compared at the same point.

4.2 Theory of powder diffraction

X-ray diffraction (XRD) technique is chosen to identify the phase field simultaneously with the kinematic field with minimum perturbations. Usually, XRD is a tool that helps to investigate the very local structure of matter (crystal or not). To understand the principle of XRD, it is worthy mentioning that diffraction is a scattering phenomenon in which a large number of atoms cooperates. Since the atoms are arranged periodically on a lattice, the scattered atoms may form destructive or constructive interferences, following the structure factor and the Bragg's law.

4.2.1 Bragg's law

Herein, two geometrical facts are worth mentioning:

1 The incident beam, the normal to the diffracting planes and the diffracted beam are always coplanar.

2 The angle between the diffracted beam and the transmitted beam is always $2\theta_{hkl}$ (with $\{hkl\}$ the Miller index of the diffraction plane), this angle is universally admitted as the *diffraction angle*, and in practice, X-ray emission at the diffraction angles is measured, stored and studied.

As previously stated, XRD occurs if and only if the wavelength of the X-ray source is of the same order of magnitude as the inter-planar distance. This requirement is usually named as **Bragg's law**:

$$\frac{n\lambda}{2d_{hkl}} = \sin(\theta_{hkl}) \tag{4.1}$$

where d_{hkl} denotes as the inter-planar spacing between two (hkl) planes and λ is the wavelength of X-ray radiation source.

4.2.2 Inter-planar spacing

One set of planes $\{hkl\}$ in a crystal lattice defines one inter-planar spacing. The exact relationship between the inter-planar spacing d_{hkl} and the lattice constants

$(a, b, c, \alpha, \beta, \gamma)$ depends on the crystal symmetry involved (Bravais network, see details in the work of [Cullity, 1957]). In Ni-Ti SMA, A, R, and M phases are associated with the following interplanar distances:

$$d_{hkl} = \frac{a}{\sqrt{h^2 + k^2 + l^2}} \rightarrow \text{A phase} \tag{4.2}$$

$$d_{hkl} = \frac{a\sqrt{1 - 3\cos^2(\alpha) + 2\cos^3(\alpha)}}{\sqrt{(h^2 + k^2 + l^2)\sin^2(\alpha) + 2(hk + kl + hl)(\cos^2(\alpha) - \cos(\alpha))}} \rightarrow \text{R phase} \tag{4.3}$$

$$d_{hkl} = \frac{\sin(\beta)}{\sqrt{\frac{h^2}{a^2} + \frac{k^2\sin^2(\beta)}{b^2} + \frac{l^2}{c^2} - \frac{2hl\cos(\beta)}{ac}}} \rightarrow \text{M phase} \tag{4.4}$$

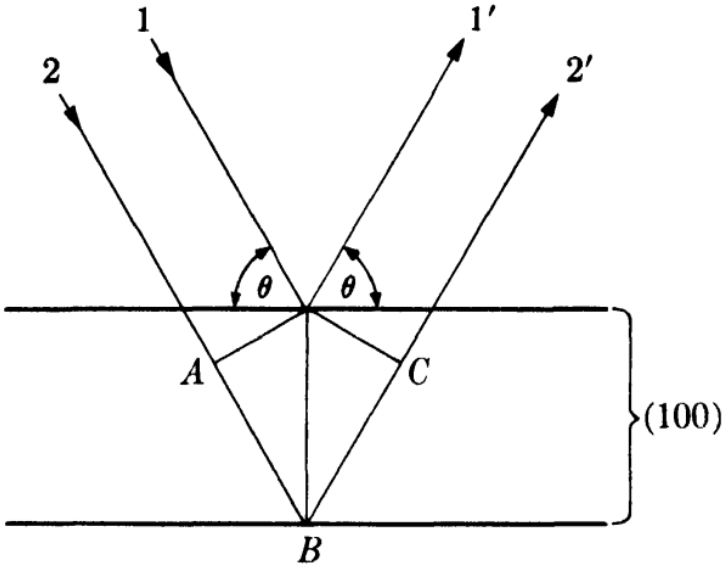

Figure 4.1: Schematic illustration of Bragg's law: for 2^{nd} order $\{100\}$ reflection [Cullity, 1957]

The most common way to apply Bragg's law experimentally, is to use a fixed X-ray radiation wavelength (for example wavelength associated with Cobalt k_α ray) and to measure the corresponding diffraction signals $D(2\theta)$. After calculation of the potential diffracting planes for all structures (calculation of structure factor F) and the associated angles, an indexation of the $\{hkl\}$ planes is made possible. A further identification of the phases ratio needs more information and assumptions.

4.2.3 Relative integrated intensities of diffraction profile

By neglecting the crystalline texture (crystal is considered to be as a 'powder'), the relative intensities of each diffraction line I_{hkl} associated with plane $\{hkl\}$ can

be expressed as follows:

$$I_{hkl} = |F^2| p \frac{1 + \cos^2 2\theta_{hkl}}{\sin^2 \theta_{hkl} \cos \theta_{hkl}} \tag{4.5}$$

where p the multiplication factor and θ_{hkl} the diffraction angle.
In Figure 4.2, the diffraction lines associated with M, R phase and A phases (considered as powders) are plotted. They are all different.

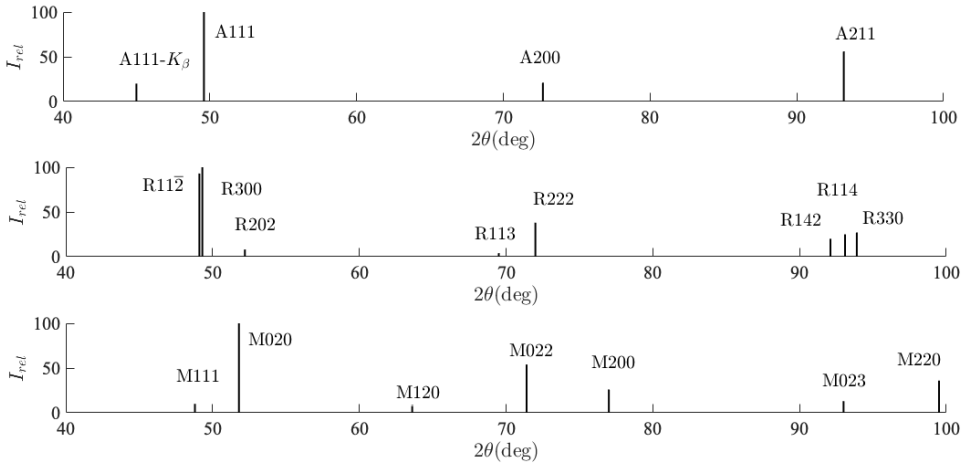

Figure 4.2: Theoretical diffraction patterns for A, M, and R phases

Therefore, in a NiTi alloy, at a 'local' analyzed point and assuming a homogeneous X-ray beam, the total diffractogram $D(2\theta)$ is assumed to be:

$$D(2\theta) = I_A(2\theta)C_A + I_M(2\theta)C_M + I_R(2\theta)C_R \tag{4.6}$$

where I_i is the relative intensity of A, M and R phase and C_i is the phase concentration (volume fraction).
Schematically, when a martensitic phase transformation occurs at the NiTi SMA transformation plateau, due to phase changes from A toward R phase then R-phase toward M, a variation of the local phases concentration should be observed. It would lead to a corresponding variation of the measured diffractogram :

$$\partial C_i \rightarrow \partial D(2\theta) \tag{4.7}$$

where ∂C_i indicates the variation for local phase concentration i and $\partial D(2\theta)$ indicates the variation of diffractogram. As a result, since the diffraction pattern between A, R phase and M phase is relatively easy to distinguish and is sensitive towards the changes of phase concentration, the phase transformation could be effectively captured by a XRD scan.

4.3 Combined XRD and DIC in situ measurements

4.3.1 Experimental setup

Our experimental setup is presented schematically in Figure 4.4: the X-ray wide angle diffractometer equipped with a conventional X-ray source (Cobalt k_α with a wavelength $\lambda = 1.79\,\text{Å}$ and a 1mm beam diameter) and a curved detector (Inel CPS-120) is used to measure the X-ray diffraction along the diffraction angle 2θ varying between $20° < 2\theta < 140°$. The X-ray generator is powered with a current $I = 40\,\text{mA}$ and a voltage $U = 30\,\text{kV}$. A Fe filter is also installed in front of the curved detector to suppress the contribution of Cobalt k_β radiation and reduce a part of the noise. The imperfection in Fe filter results in a double absorption at diffraction angles $62° \leq 2\theta < 65°$ as illustrated in Figure 4.7.
As shown in Figure 4.4, a parallelepipedic-shaped specimen of the Ni-Ti SMA (central zone of length $L = 10$ mm, width $l = 3$ mm and thickness $h = 0.3$ mm) is installed in the mechanical testing machine *mini-Astree* located in the XRD chamber. The specimen surface is speckled with white paints to provide enough contrast for Digital Image Correlation (DIC) analyses.

To prevent any perturbation between both setups, a prism is used to redirect the image of the specimen surface towards a visible-light camera. The prism obscures however the X-ray detector removing all detection for $2\theta \geq 100°$ as shown in Figure 4.3 and Figure 4.7.

A displacement-controlled 1D tensile test is carried out at ambient temperature $T = 300$ K with a loading command $\dot{u}_y = \pm 0.5$ µm.s^{-1} applied by actuators (corresponding to a longitudinal strain rate $\dot{\epsilon}_{yy} = 10^{-4}$ s^{-1}) and keeping the central point of the specimen motionless. The mechanical test is interrupted three times, during which the displacement is held constant (total stretching: $\Delta u_y = 0.3$ mm, 0.4 mm, 0.6 mm) along the first loading stage and a similar hold time is considered at unloading ($\Delta u_y = 0.3$ mm) to perform the XRD measurement along the length of the specimen. The corresponding stress / strain curve is reported in Figure 4.5. As illustrated in this figure, at each interruption before the launch of XRD scan, we observe a stress drop during the forward transformation plateau and a stress increase during the backward transformation plateau before the launch of each XRD scan. The reason of these drops is that during the hold time, the temperature of NiTi specimen gradually returns to the ambient temperature (cooling for forward transformation, heating for backward transformation), leading to a stress decrease or increase respectively.

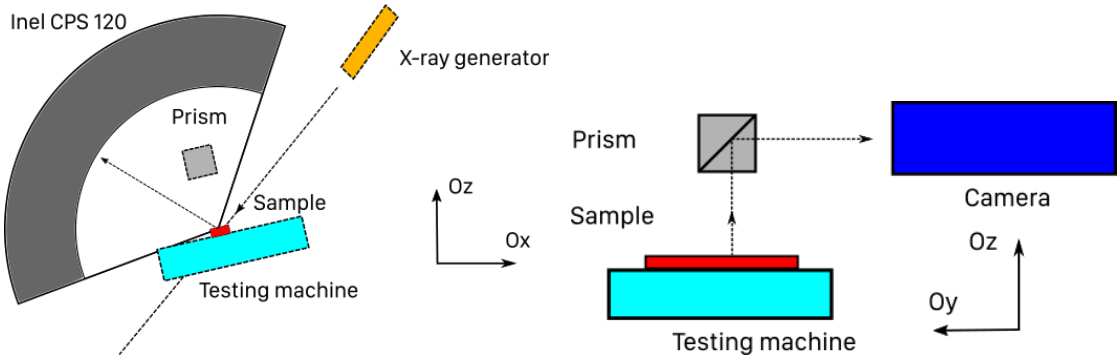

(a) XRD setup (b) DIC setup

Figure 4.3: Schematic of combined XRD-DIC setup.

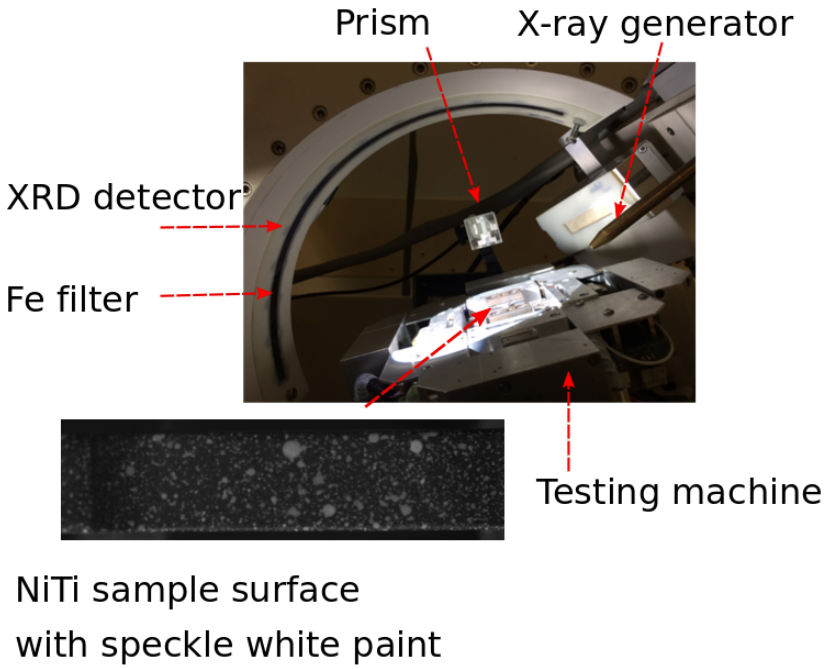

Figure 4.4: Experimental setup for combined XRD and DIC measurement.

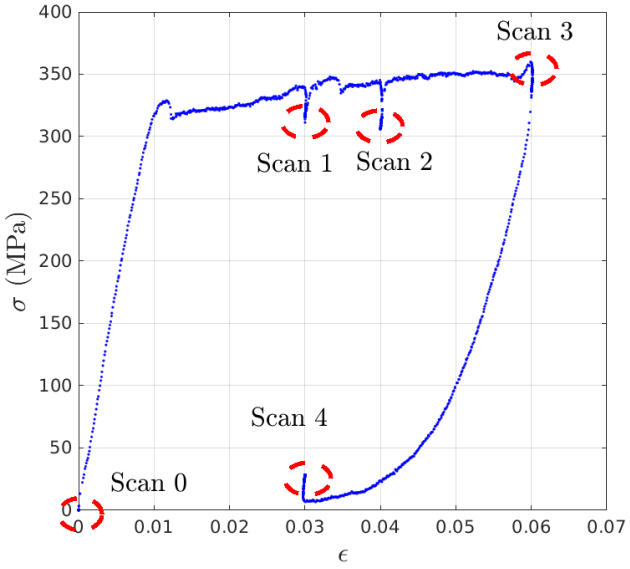

Figure 4.5: Stress/strain curve during combined XRD-DIC experiment: red circles indicate the steps where the XRD scans are recorded.

4.3.2 Experimental observations

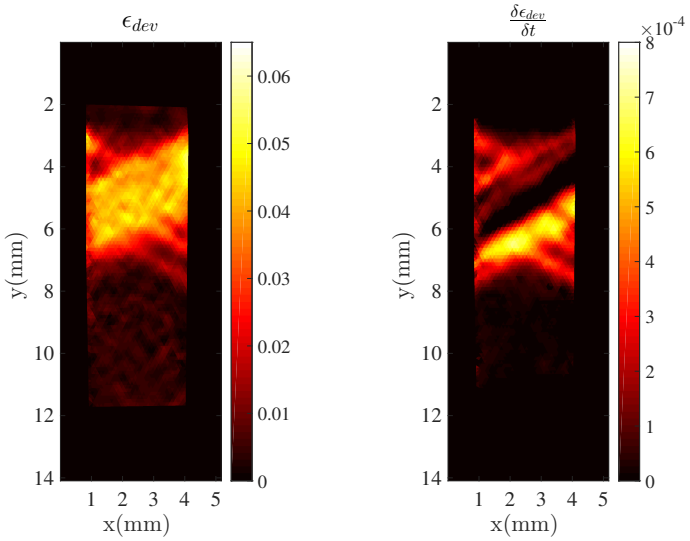

Figure 4.6: Strain ϵ_{dev} (left) and strain rate $\dot{\epsilon}_{\text{dev}}$ (right) fields during the first interruption stage.

DIC observations

Equivalent strain ϵ_{dev} and corresponding strain rate $\dot{\epsilon}_{\text{dev}}$ fields obtained just before the first XRD-scan are plotted in Figure 4.6 illustrating the strain localization in bands (point more extensively discussed in the previous chapter). The strain rate field indicates the location of the most recently formed bands (or the so-called transformation front), and shows both a broadening of the main band and the

nucleation of new bands whose orientations are at an opposite angle from the orientations of previous bands.

XRD observation

For each of the four interruptions, X-ray scans are carried out along the center line of the Ni-Ti specimen (corresponding to the spatial range -18 mm$\leq y \leq -5$ mm and -0.5 mm$\leq x \leq 0.5$ mm).

Masking In order to properly perform the phase indexation of the diffractograms, we mask both the regions impacted by the double absorption of the *Fe* filter and the presence of the *Prism*. We also exclude the contribution of Co k_β in the experimental X-ray diffractogram[1].
Figure 4.7 shows the different spectra obtained at different positions in the range -18 mm$\leq y \leq -5$ mm corresponding to the scan 1 in Figure 4.5. For the sake of readability, a vertical offset (100 counts) is added between each spectrum. The parts of signals shaded in gray within the range of corresponding diffraction angles varying from $[44°, 46°] \cup [62°65°] \cup [100°140°]$ correspond to the masked and k_β regions. They are discarded from the analysis throughout this chapter.

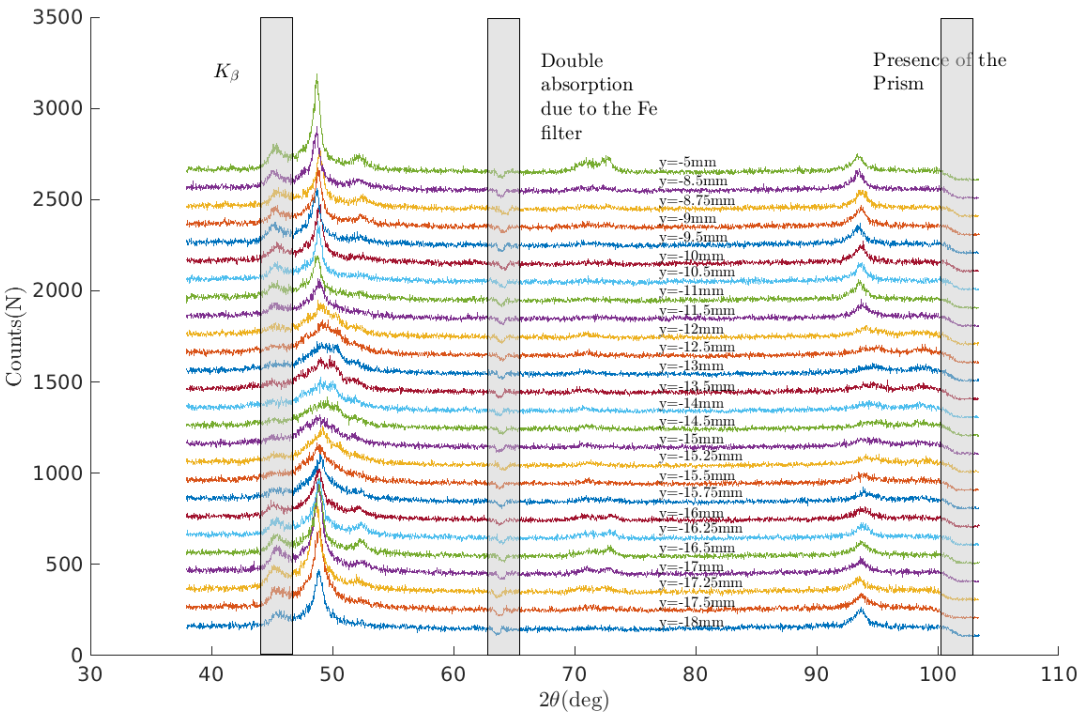

Figure 4.7: Ni-Ti XRD spectra along the scanning direction with an offset value of 100 counts for Y axis between each plot (at step 1 of XRD scan in Figure 4.5)

[1]Co k_β is imperfectly filtered by the Fe filter an leads to a significant {110} peak for austenite.

Background correction In addition to the sought diffraction peaks, a non-zero background signal is present in all spectra as a result of the diffuse scattering, and the unavoidable experimental imperfections [Cullity, 1957]. It is therefore necessary to estimate this background signal $D_{\text{background}}(2\theta, x)$ and to remove it from the raw spectra $D_{\text{raw}}(2\theta, x)$ prior to any further analysis.

$$D(2\theta, y) = D_{\text{raw}}(2\theta, y) - D_{\text{background}}(2\theta, y) \tag{4.8}$$

A fourth order polynomial function is chosen to account for the spectrum background. It should be such chosen that the resulting $D(2\theta, x)$ is always positive. Thus $D_{\text{background}}$ is computed from the minimization of the following cost function:

$$\mathcal{C} = \sum_{\theta} \alpha_1 H(D_{\text{background}}(2\theta, y) - D_{\text{raw}}(2\theta, y))^2 - \alpha_2 D_{\text{background}}(2\theta, y) \tag{4.9}$$

where H is the Heaviside function ($H(x) = 1$ if $x \geq 0$, and $H(x) = 0$ if $x < 0$), and α_1 and α_2 are two scalars. The first term promotes the positivity of $D(2\theta, x)$, while the second favors a high background so that it lines up to the minimum values of the spectrum. Only the ratio α_1/α_2 matters for the determination of the background and this ratio is chosen much larger than 1 (in our case, the ratio between α_1 and α_2 is about $\frac{\alpha_1}{\alpha_2} \simeq 10$). Figure 4.8 illustrates the result of this computation.

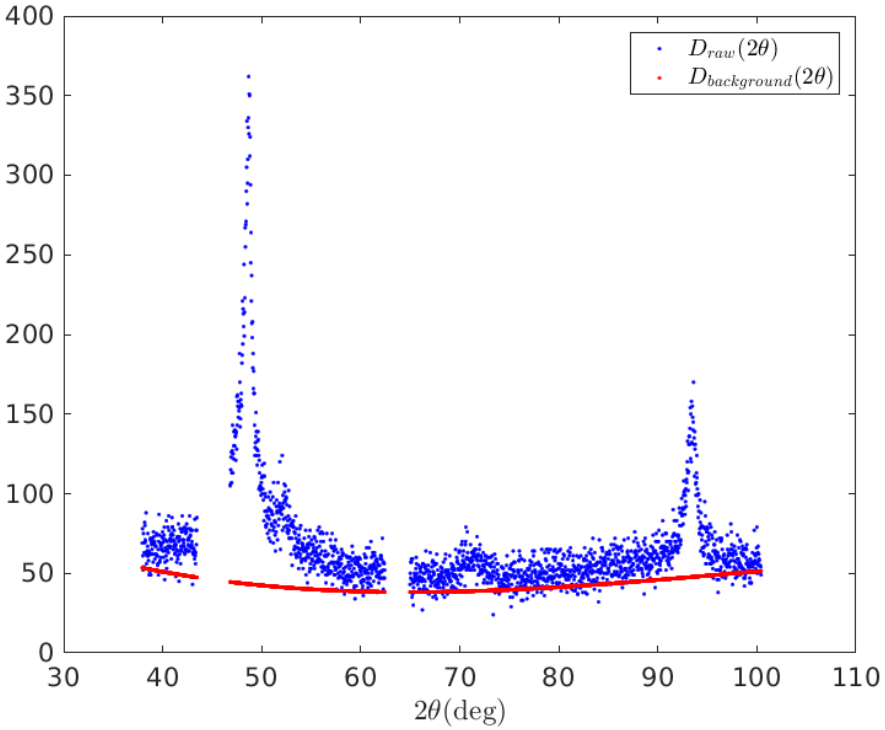

Figure 4.8: Background removal procedure (background plotted in red)

Initial qualitative comparison An initial qualitative comparison between the kinematic field and the XRD mapping along the center line is conducted. Results are plotted in Figure 4.9. Strain field has been shifted so that the XRD scans can be precisely located [2]. As observed in Figure 4.9, some significant differences are highlighted between the XRD scans in and out of the deformed regions of the specimen. For example, we observe a large shift/enlargement of the principal diffraction peak, in the range of $48° \leq 2\theta \leq 52°$ from scan a to scan g. Moreover, the typical double peak between $90° \leq 2\theta_b \leq 100°$ in scans c and d indicate without any doubt that the band region is composed mainly of pure martensite (this result is confirmed by some complementary diffraction profiles carried out at the end of stress-strain transformation plateau). Meanwhile the presence of a secondary peak at $2\theta = 51°$corresponding to R phase {202} crystal lattice diffraction plane and of the principal A phase {110} peak indicates the co-existence of A and R phase outside the localization region.

Qualitative Indexation by using the theory of diffraction
Let us consider three scans in Figure 4.9b: g (plotted in dark red), c (plotted in yellow), e (plotted in green). They have been plotted in Figure 4.10 and indexed

[2]Indeed, the control system of XRD scan does not fit with the DIC spatial coordinates. An offset is thus required to compare these two sets of data and put them in the same frame.

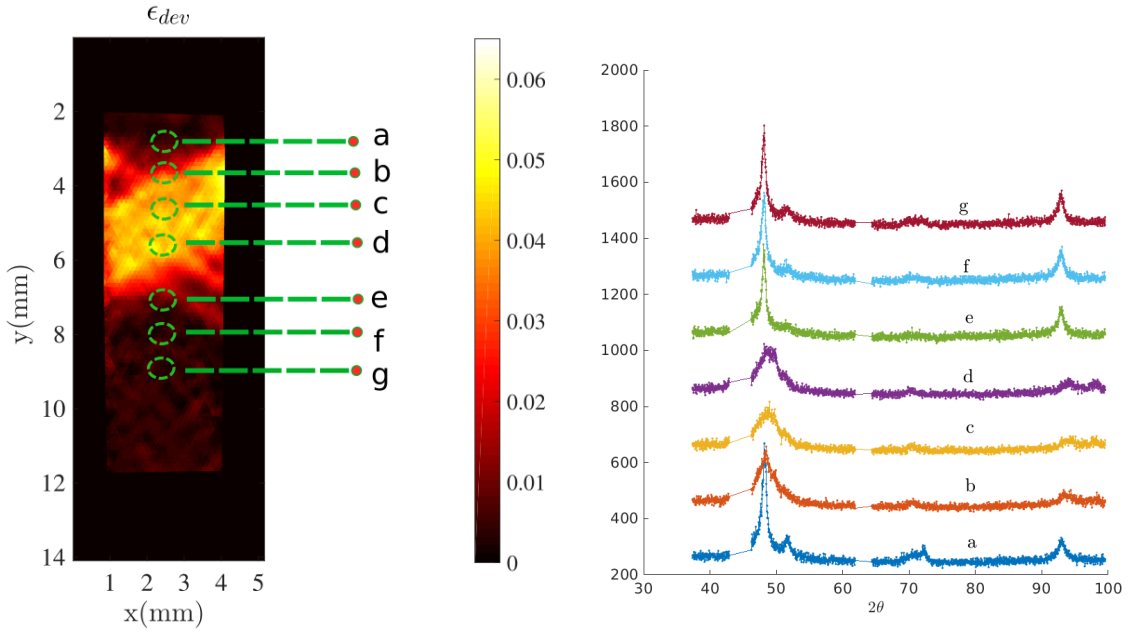

(a) several XRD scan spots repositioned in experienced strain field

(b) Several X-ray scans and their position over DIC strain map

Figure 4.9: Qualitative correspondance between DIC and XRD

using the theory of diffraction assuming an isotropic distribution of crystallites (powder) and a perfect Co k_α radiation. It can be easily observed that: spectrum g in blue indicates a mixture between A and R-phase; spectrum e in red shows a pure A phase composition; spectrum c in black shows a M phase dominant composition. This result proves the co-existence of the three phases during a 1D quasi-static loading at the phase transformation plateau.

We notice that A and R phases have a very similar experimental diffraction pattern in the range $40° \leq 2\theta \leq 100°$. This similarity renders the identification of each individual A/R/M phase very difficult using the classical Rietveld method in case of strong mixing. This question will be addressed in the next parts through a specific novel methodology designed to reduce the sensitivity to noise. However, in order to do so, it is first required to perform a thorough statistical characterization of the noise present in the spectra.

4.4 Noise analysis and Anscombe transformation

4.4.1 Static XRD measurement

For the purpose of uncertainty analysis, five static XRD measurements, $i = 1, ..., 5$, have been successively carried out over a Ni-Ti specimen, consisting of a mixture of A and R-phase at room temperature, with different acquisition times $(\Delta t)_i = [5, 10, 15, 25, 30]$ min (Figure 4.11). X-ray spectra, $D_i(2\theta)$, were collected at the same point. To get rid of the influence of the first measurement over the

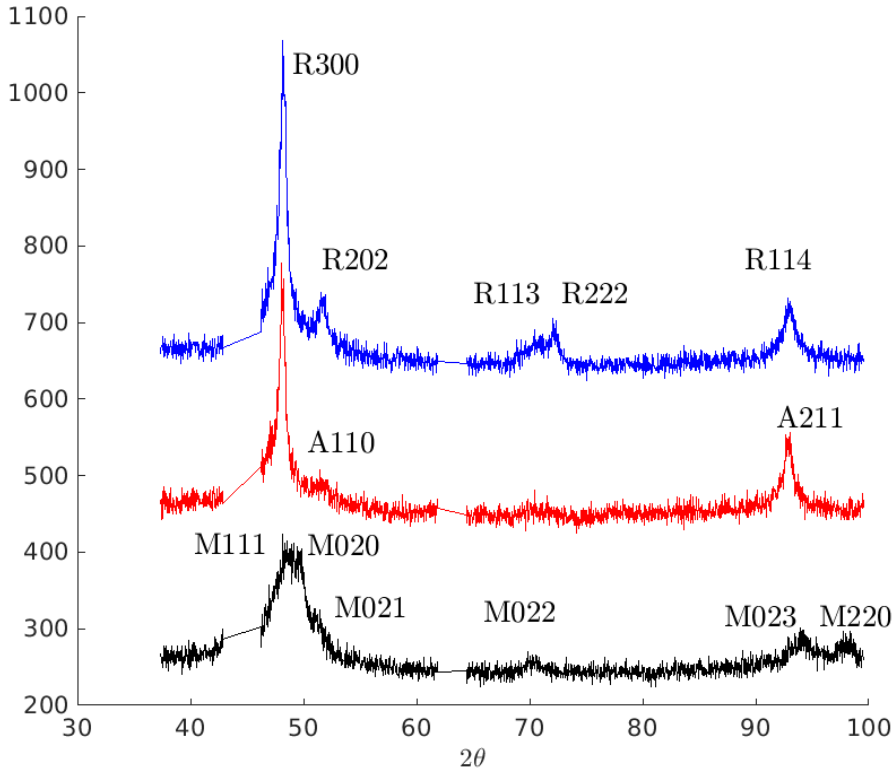

Figure 4.10: Three diffraction scans of Ni-Ti SMA extracted from Figure 4.9 and indexed using the diffraction theory, showing: mixture of A and R-phase (g - in blue), pure A phase (point e - in red), and pure M (c in black) - representation using a vertical offset of 200 counts between each spectrum.

others, the nominal difference between each XRD measurement, $\widehat{D}_n(2\theta)$ (given by Equation 4.10) is also plotted.

$$\widehat{D}_n(2\theta) = \frac{D_{n+1}(2\theta, n) - D_n(2\theta, n)}{t_{n+1} - t_n} \tag{4.10}$$

In absence of noise, the different diffractograms are expected to differ only by a scale factor proportional to their acquisition time.

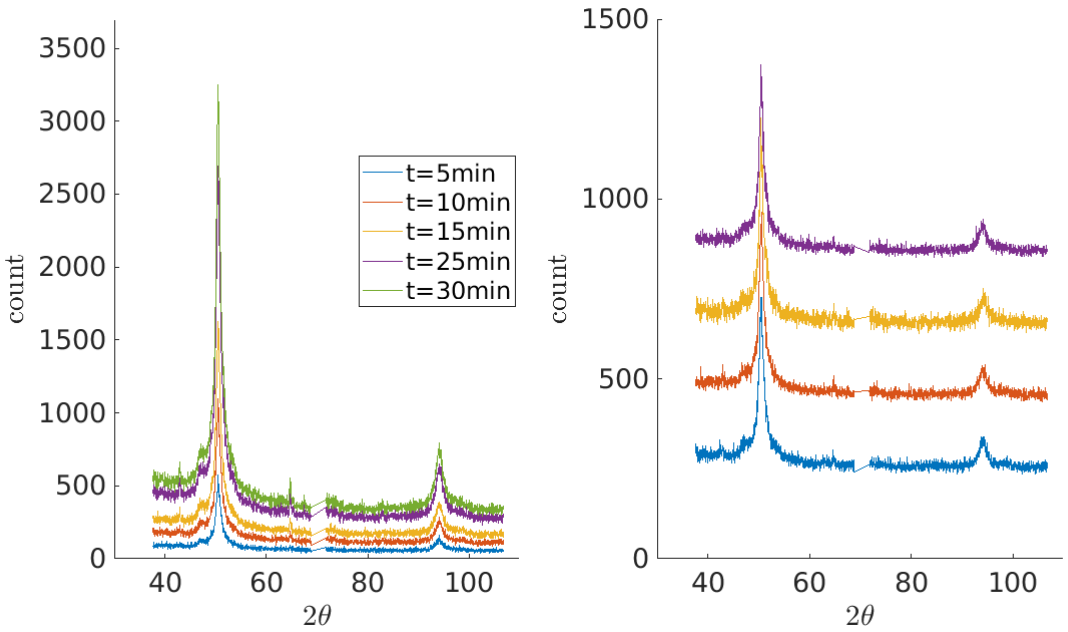

Figure 4.11: Static XRD spectra for a Ni-Ti specimen acquired for different acquisition times. (Left) Raw diffractogram $D_i(2\theta)$ plotted using a vertical offset of 100 counts between each spectrum; (Right) Nominal difference between each spectrum $\widehat{D_i}(2\theta)$ using a vertical offset of 50 counts between each spectrum.

Thus the diffractograms can be written as a composition of physical information $U(2\theta)$ and noise $\eta_i(2\theta)$:

$$\widehat{D_i}(2\theta) = (\Delta t)_i U(2\theta) + \eta_i(2\theta) \tag{4.11}$$

This expression gives access to the noise and hence its statistical properties, once $U(2\theta)$ has been determined. An easy way to validate the above assumption, and simultaneously to correct uncertainties in the acquisition time $(\Delta t)_i$ and finally to estimate $\eta_i(2\theta)$ is to employ a Principal Component Analysis (PCA) also called Proper Orthogonal Decomposition (POD). PCA/POD allows a decomposition of $\widehat{D_i}$ into a sum of products of separated modes depending on i and on θ. By retaining only one mode, Equation 4.11 is obtained, where the mode is $U(2\theta)$ itself. Truncation after one mode accounts for almost the entire signal $\widehat{D}$, as the residual is of order 10^{-3} of the original signal. The amplitude of the first mode

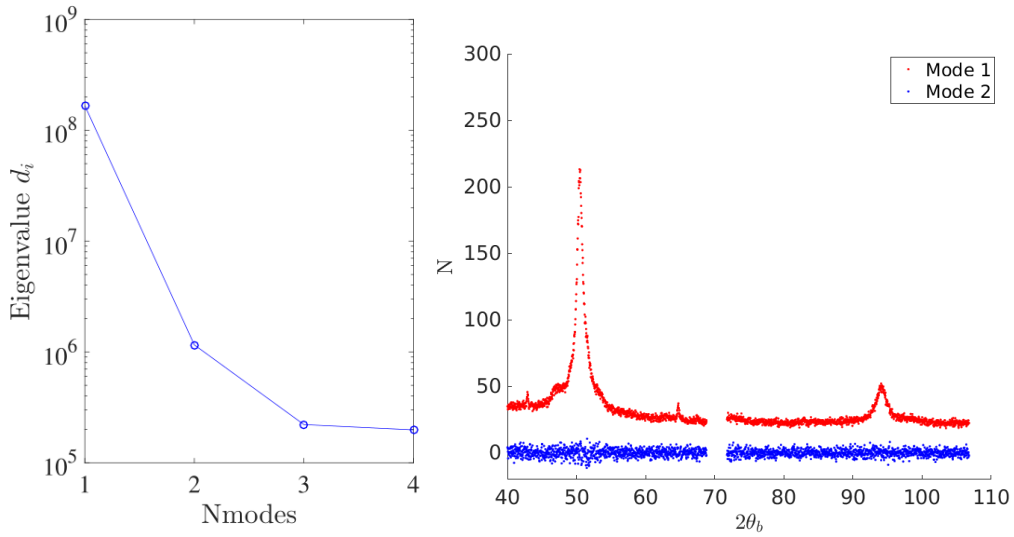

(a) (b)

Figure 4.12: POD analysis over $\widehat{D}$: (Left) eigenvalue of each POD mode; (Right) first two POD angular modes.

$U(2\theta)$ is indeed linear with the acquisition time $(\Delta t)_i$ as expected. This procedure thus provides a direct determination of the noise term $\eta_i(2\theta)$.

In the case where the acquisition is limited by the X-ray photon noise, $\eta_i(2\theta)$ is expected to be a Poisson noise. In particular its variance is expected to vary in proportion of the signal $(\Delta t)_i U(2\theta)$. It is convenient to introduce the re-scaled noise:

$$\hat{\eta}_i(2\theta) = \frac{\eta_i(2\theta)}{\sqrt{(\Delta t)_i U(2\theta)}} \tag{4.12}$$

This re-scaled noise is expected to have a variance independent of both $(\Delta t)_i$ and θ, a property that is illustrated in Figure 4.13.

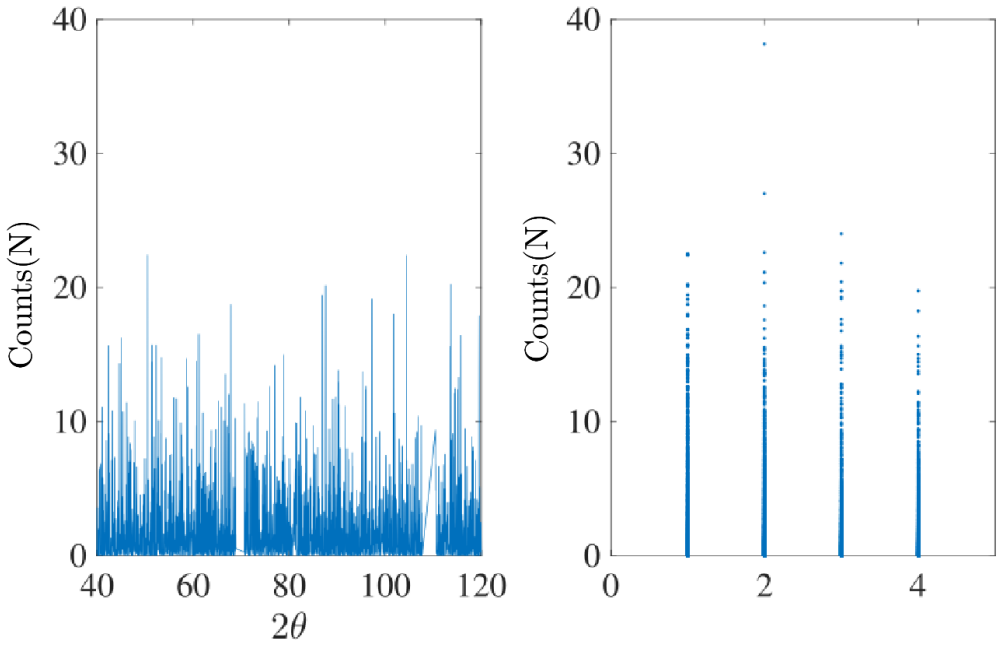

Figure 4.13: angle/time independency of the variance of $\hat{\eta}_i(2\theta)$

4.4.2 Anscombe transformation

A signal that contains a Poisson noise is disturbed by a stationary Gaussian noise of uniform variance after Anscombe transformation [Anscombe, 1948]. In the present case, the Anscombe transformation simply consists in taking the square root of the signal

$$\widetilde{D}_i(2\theta) = \sqrt{D_i(2\theta)} \tag{4.13}$$

The same POD/PCA routine as in the previous section is applied for the new diffraction signal $\widetilde{D}_i(2\theta)$ after Anscombe transformation. The noise matrix $\widetilde{\eta}_i(2\theta)$ after the truncation of the first mode of $\widetilde{D}_i(2\theta)$ can be constructed as follows :

$$\widetilde{D}_i(2\theta) = (\Delta t)_i \widetilde{U}(2\theta) + \widetilde{\eta}_i(2\theta) \tag{4.14}$$

The non-correlation between the noise and signal is then appreciated in Figure 4.14. We also observe that the amplitude of the noise tends to stabilize when the XRD acquisition time is higher than 10 minutes. The presence of a stationary Gaussian noise of uniform variance in time and angle allows the variance of noise matrix to be replaced by a fixed constant.

$$\langle \widetilde{\eta}_i^T(2\theta)\widetilde{\eta}_i(2\theta)\rangle = k \tag{4.15}$$

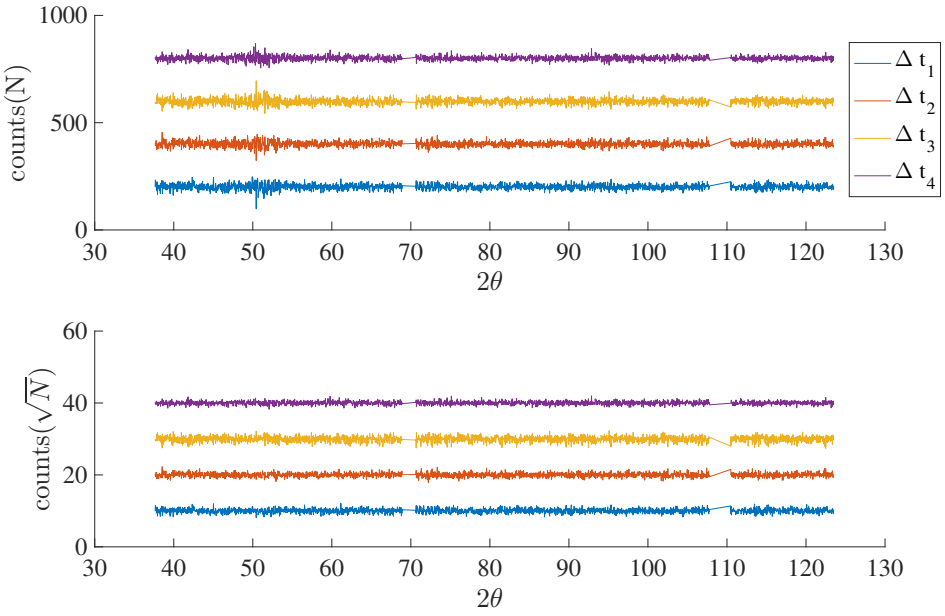

Figure 4.14: (Up) Poisson noise distribution $\eta_i(2\theta)$- representation using a vertical offset of 200 counts between each spectrum; (down) uniform distribution of the noise matrix $\widetilde{\eta}_i(2\theta)$ after Anscombe transformation - representation using a vertical offset of 10 counts between each spectrum.

4.5 Determination of the phases volume fraction

After background correction and masking, each scan $D(2\theta, y)$ is supposed to be composed of the three principal phases of the Ni-Ti alloy: A, M and R-phase. For their proper identification of phases, it is possible to prepare the specimen to obtain pure A and M phases with either a load-free state above Austenite finish temperature (A), or under stress load after a full transformation (M). However, this is not the case for R-phase, since it is generated only at the intermediate stages, and never uniformly. Thus the determination of the pure R-phase spectrum is an additional challenge. It is addressed in this section.

4.5.1 Phases volume fraction and diffractogram

Let first assume that any diffractogram, obtained at a given spatial coordinate $D(2\theta, y)$, is equal to the sum of the contribution of each pure i phase spectrum $S_i(2\theta)$[3] weighted by its volume fraction $C_i(y)$ (i index represents the different phases : A/M/ R-phase) :

$$D(2\theta, y) = \sum_{j=1}^{j=3} C_i(y) S_i(2\theta), \tag{4.16}$$

[3]Spectrum $S_i(2\theta)$ is a *true* spectrum. It corresponds to the $I_i(2\theta)$ spectrum (see subsection 4.2.3) in an ideal situation: isotropic, no residual stress, no metallurgical defect.

The volume fractions are subjected to obvious constraints: they must be all positive and their sum must be equal to 1:

$$\begin{aligned} &C_i(y) \geq 0 \\ &\sum_{i=1}^{i=3} C_i(y) = 1 \ . \end{aligned} \tag{4.17}$$

The assumption of linear contribution is strong. It implies that there exists a unique experimental diffraction profile for each individual phase, meaning that the variant selection is uniform and remains unchanged across the specimen upon the mechanical loading, This is of course not true for the case of reorientation for example: indeed a rotation of a pure phase may change the relative weight of some diffraction peaks. This phenomenon is however limited to the multiaxial non-proportional loading or under high heterogeneous stress [Yu et al., 2015] [Song et al., 2014]. The hypothesis that the orientation of each phase remains unchanged at each spatial coordinate, keeping the associated diffraction profile for each phase during XRD scan unchanged, is acceptable. It will be retained for the identification procedure.

As previously mentioned, pure A and M phases can be obtained experimentally under specific thermomechanical conditions. However, to measure $C_i(y)$ from Equation 4.16, the spectrum of pure R-phase is needed. A POD-based methodology is proposed to identify it.

4.5.2 POD analysis

The linear superposition of modes, in Equation 4.16, suggests to carry out a POD analysis. The latter assumes that the entire set of spectra, denoted $D(2\theta, y)$, can be decomposed as a linear combination of N principal modes

$$D(2\theta, y) = \sum_{j=1}^{j=N} d_j u_j(2\theta) v_j(y) \tag{4.18}$$

where $u_j(2\theta)$, for $j = 1, ..., N$ are the angular modes, and $v_j(y)$ are the spatially resolved corresponding amplitudes.

In a standard POD analysis, it is customary to normalize u_j and v_j, (say $\sum_x v_j(y)^2 = 1$ and $\sum_\theta u_j(2\theta)^2 = 1$), so that an amplitude d_j is needed, that corresponds to the eigenvalue of mode j in the singular value decomposition. In other words, d_j qualifies the contribution of each mode j to the entire database. By plotting the evolution of d_j ranked in decreasing order (see Figure 4.15a), it is observed that at least three modes are needed to represent the entire signal

$D(2\theta, y)$ (the ratio between the third and the first mode eigenvalues is lower than 1%).

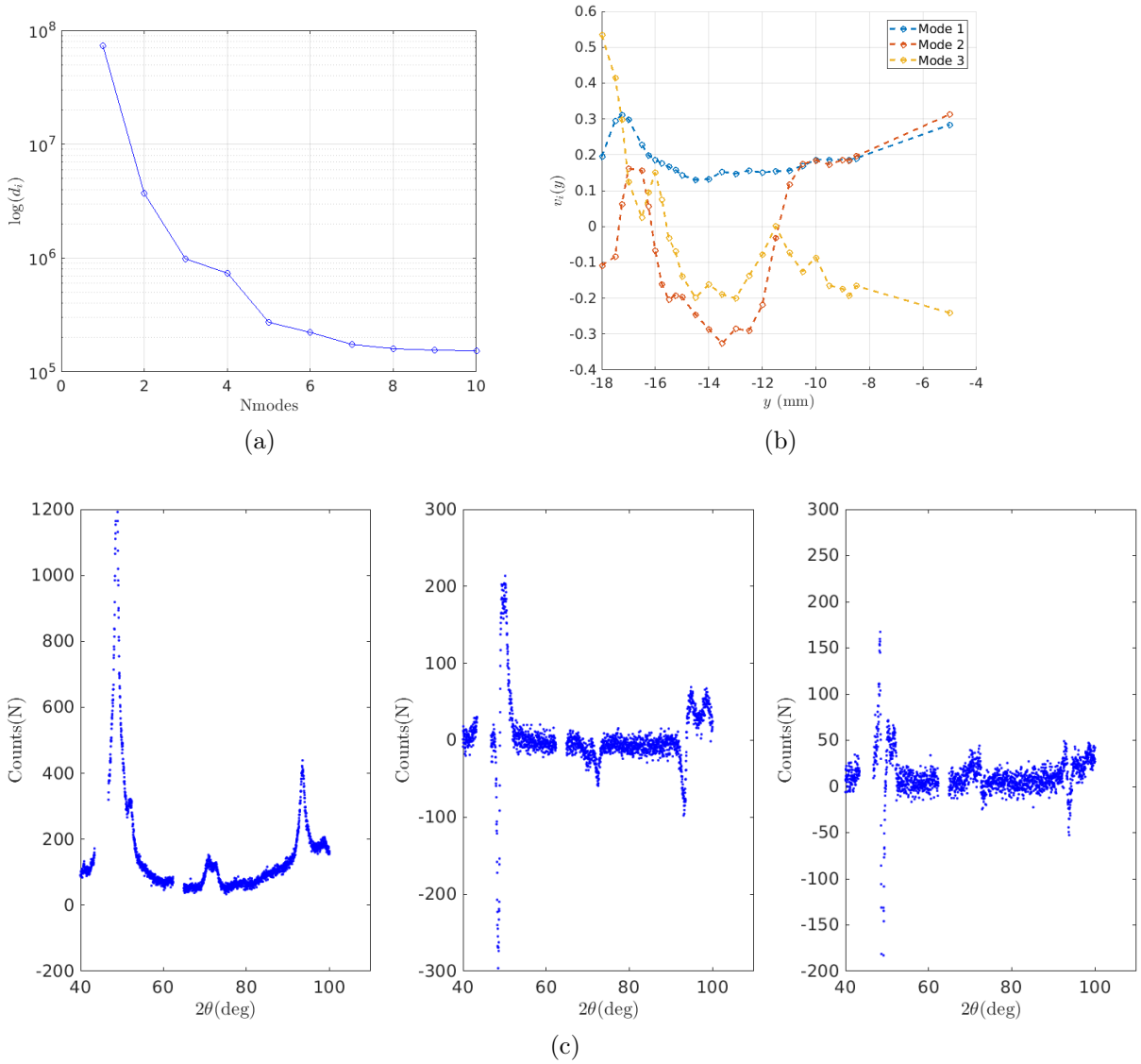

Figure 4.15: POD analysis: (a) eigenvalues d_i as a function of mode number; (b) spatial amplitude of the first three POD modes ranked with the highest eigenvalue; (c) first three POD angular modes $u_j(2\theta)$ ranked with the highest eigenvalue d_i

As shown in Figure 4.15c, the first angular mode $u_1(2\theta)$ captures the mean diffraction spectrum, which is consistent with the fact that the spatial amplitude $v_1(y)$ is almost constant. The following two modes i={2, 3} (see Figure 4.15c), could be further interpreted as the modulation related to the presence of A, M and R phase.

4.5.3 Initial reconstruction of R-phase spectrum $S_R(2\theta)$

Although the first three POD modes generate the subspace that embeds all spectra, the spatial shape functions $v_j(y)$ do not directly provide the three volume fractions $C_i(y)$, because the spectra of pure phases are not completely known. It is proposed to use the property that only the three phases of NiTi SMA (A, R and M) are present and hence Equation 4.16 and Equation 4.17 should be fulfilled. Austenite $S_A(2\theta)$ and Martensite $S_M(2\theta)$ phase spectra can be achieved experimentally. Thus, these two spectra can be fully expressed in the subspace generated from the first three POD modes $u_j(2\theta)$, ranked with the highest eigenvalues.

$$S_A(2\theta) = \sum_{j=1}^{j=3} a_{A,j} u_j(2\theta) \tag{4.19}$$

$$S_M(2\theta) = \sum_{k=1}^{k=3} a_{M,k} u_k(2\theta) \tag{4.20}$$

Then, the *direction* of pure R-phase spectrum can be deduced from the available data:

$$a_{R,l} = \varepsilon_{jkl} a_{A,j} a_{M,k} \tag{4.21}$$

$$S_R^*(2\theta) = \sum_{l=1}^{l=3} a_{R,l} u_l(2\theta) \tag{4.22}$$

where ε_{jkl} is the Levi-Civita symbol (see details in section A.3), so that the above equations hold for pure R-phase spectrum.

Figure 4.17 shows the reconstruction of the R-phase spectrum $S_R(2\theta)$. All peaks have been indexed according to the powder diffraction theory . Finally the theoretical values (see Figure 4.2) and the experimental data of Figure 4.17 show a good agreement.

It needs to be emphasized that the POD approach provides an initial estimation of the R-phase spectrum in the POD subspace. However its amplitude can not be directly provided through the POD reconstruction (see Equation 4.22). This difficulty can be circumvented by enforcing the physical constraints expressed by Equation 4.17.

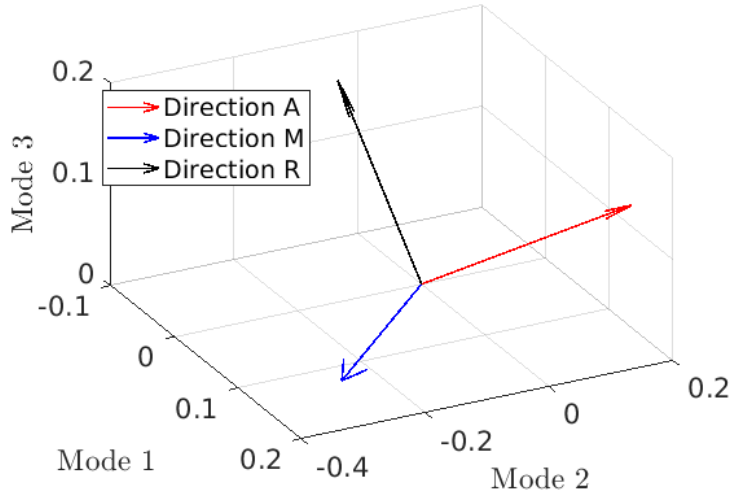

Figure 4.16: Initial estimation of R-phase *direction* in POD subspace

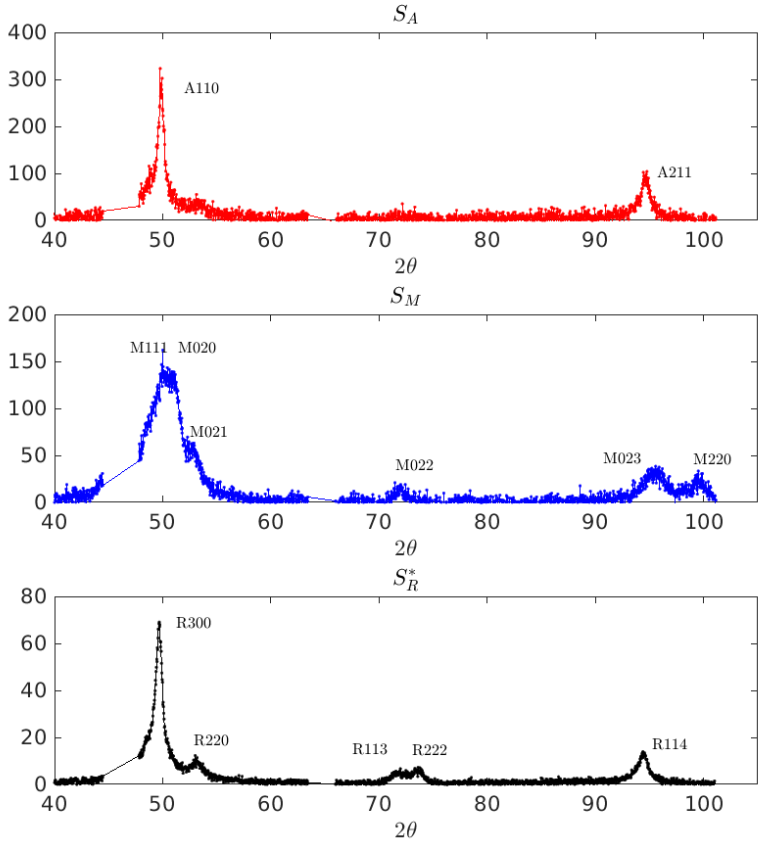

Figure 4.17: Initial estimation of experimental spectrum for pure A, M and R-phase

4.5.4 Determination of R-phase spectrum amplitude

Over-determined linear system

Recall that each diffractogram $D(2\theta, y)$ can be seen as a linear combination between the spatial concentrations of each phase $C_i(y), i = A, R, M$ and their

experimental spectrum $S_A(2\theta)$, $S_M(2\theta)$ and $S_R(2\theta)$, that respects Equation 4.16 and Equation 4.17.

The initial estimation of R phase spectrum $S_R^*(2\theta)$ has been provided. Its amplitude γ is however still missing to correspond to a *real* experimental R-phase diffraction pattern:

$$S_R(2\theta) = \gamma S_R^*(2\theta) \tag{4.23}$$

Nonetheless, the over-determined system can be solved using a least square method:

$$D(2\theta, y) = S_A(2\theta)C_A(y) + S_M(2\theta)C_M(y) + S_R^*(2\theta)C_R^*(y), \forall y \tag{4.24}$$

Meanwhile, it is noteworthy that in literature, X-ray diffraction is frequently a reported to have Poisson type of uncertainty. We propose therefore to minimize the ad-hoc primary objective and less noise sensitive function as follows:

$$\mathbf{C} = [C_A(y); C_M(y); C_R^*(y)], \ \forall y$$
$$\mathbf{S} = [S_A(y); S_M(y); S_R^*(y)], \ \forall y$$
$$\mathbf{f}(\mathbf{C}) = ||\frac{\mathbf{D} - \mathbf{CS}}{\sqrt{\mathbf{D}}}||^2 = \sum_{2\theta} \frac{(D(2\theta, y) - S_A(2\theta)C_A(y) - S_M(2\theta)C_M(y) - S_R^*(2\theta)C_R^*(y))^2}{D(2\theta, y)}$$

An optimum of $\mathbf{C}$ is the solution which minimizes the primary objective function:

$$\frac{\partial \mathbf{f}(\mathbf{C})}{\partial \mathbf{C}} = 0 \rightarrow \mathbf{C} = \arg\min \mathbf{f}(\mathbf{C}) \tag{4.25}$$

The final constraint to be implemented concerns the concentration of each phase that must fulfill the following admissibility:

$$\begin{aligned} 1 \geq & C_A(y), C_M(y) \geq 0, \ \forall y \\ & C_R^*(y) \geq 0, \ \forall y \end{aligned} \tag{4.26}$$

Expressing these physical constraints in a compact matrix of the form $\mathbf{EC} \leq \mathbf{F}$, such constraints can be implemented as Lagrange Multipliers in the linear system. Consequently, the dual objective function can be expressed as:

$$\mathbf{g}(\mathbf{C}, \lambda) = \mathbf{f}(\mathbf{C}) + \sum \lambda(\mathbf{EC} - \mathbf{F}) = f(\mathbf{C}) + \sum_m \lambda_m(E_m C_m - F_m) \tag{4.27}$$

The optimum solution respecting both physical admissibility and Equation 4.24 is the solution that minimizes the dual objective function $\mathbf{g}(\mathbf{C}, \lambda)$

$$(\mathbf{C}, \lambda) = \arg\min \mathbf{g}(\mathbf{C}, \lambda) \rightarrow \frac{\partial \mathbf{g}}{\partial \mathbf{C}} = \mathbf{0} \text{ and } \frac{\partial \mathbf{g}}{\partial \lambda} = \mathbf{0} \tag{4.28}$$

POD analysis

By solving the over-determined linear system with enforced physical admissibility, the initial phase concentration $\mathbf{C} = [C_A(y); C_M(y); C_R^*(y)]$ at each analyzed point can be obtained. We can then remove the spectral contribution of A and M from the diffraction matrix $D(2\theta, y)$. The remaining signals (at each space step y) are denoted as $R(2\theta, y)$:

$$R(2\theta, y) = D(2\theta, y) - C_A(y)S_A(2\theta) - C_M(y)S_M(2\theta) \tag{4.29}$$

The remaining signals are plotted in Figure 4.18. This figure shows a mixture between the R-phase signal and the error due to the resolution of the linear system. By assuming that the error of the linear system is mostly independent to the R-phase diffraction profile, the covariance between the error of linear system $\eta(2\theta)$ and the initial reconstructed R-phase spectrum $S_R^*(2\theta)$ should be much lower than the auto-covariance of the R-phase diffraction profile:

$$0 \simeq cov(\eta(2\theta), S_R^*(2\theta)) \ll cov(S_R^*(2\theta), S_R^*(2\theta)) \tag{4.30}$$

Therefore, for the purpose of regularization (excluding all possible errors of the linear system), we propose to evaluate the covariance between $R(2\theta, y)$ and $S_R^*(2\theta)$ at all spatial coordinates to select the reliable analyzed data points.

$$h(y) = cov(R(2\theta, y), S_R^*(2\theta)) \tag{4.31}$$

It the case shown in Figure 4.18, all analyzed points, where $h(y) \geq 1500, \forall y$ are selected. Data points with a lower covariance value than the criterion are excluded from the following POD analysis. The modal analysis is then applied over $R(2\theta, y)$:

$$R(2\theta, y) = \sum d_i U_i(2\theta) V_i(y) \tag{4.32}$$

As shown in Figure 4.19, plotting the eigenvalue of each POD modes in decreasing order, the weight of the first mode is dominant in terms of eigenvalue (the amplitude of the second mode is nearly hundred times smaller than the first mode). With the assumption that R-phase has a unique diffraction pattern, we assume that the first mode does correspond to the R-phase diffraction pattern and

we discard the other modes.

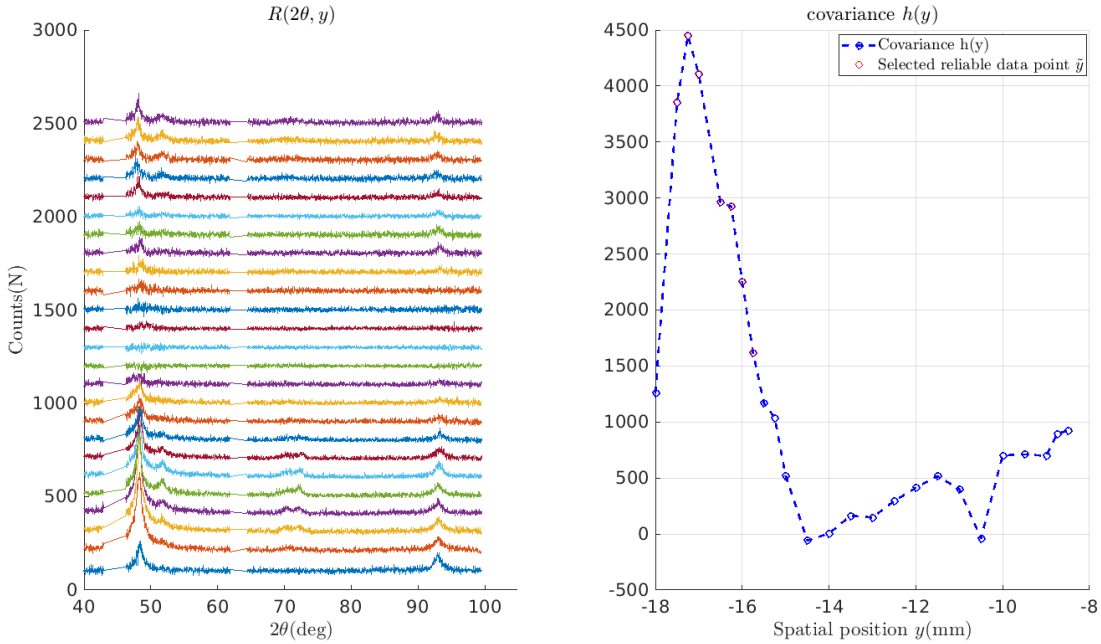

Figure 4.18: (Left) Remaining signals $R(2\theta, y)$ after removal of A and M contribution; (right) Evaluation of the covariance $h(y)$ to select the reliable analyzed points $\tilde{y}$ (selected data point plotted in red).

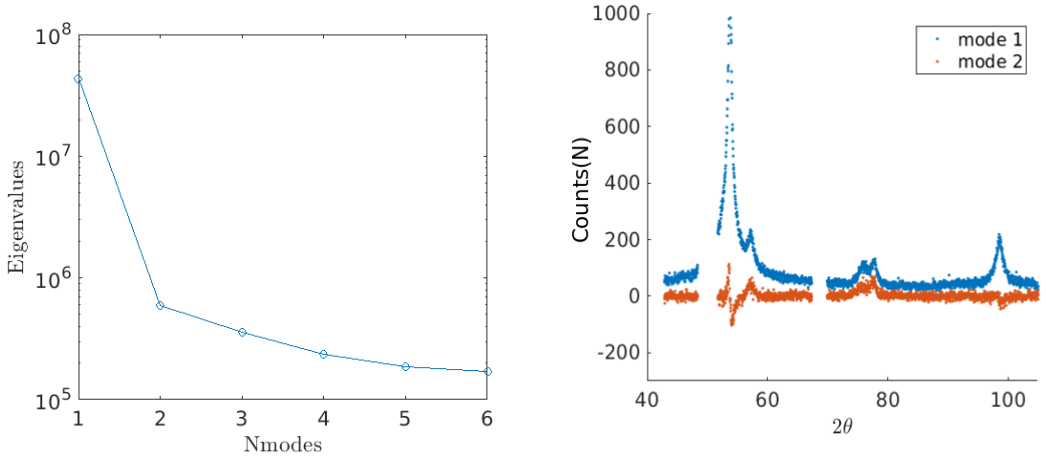

(a) Eigenvalue

(b) First two angular modes

Figure 4.19: POD modal analysis of the remaining signals $R(2\theta)$.

At all spatial points respecting the regularized criterion, the matrix of remaining signals $R(2\theta, y)$ after this POD truncation could be also expressed as R-phase diffraction profile multiplied by its spatial concentration:

$$R(2\theta, y) \simeq d_1 U_1(2\theta) V_1(y) = C_R(y) S_R(2\theta), \ \forall y \tag{4.33}$$

To respect the physical admissibility, the sum of concentration should be equal to 1, at all spatial coordinates y, leading to:

$$C_A(y) + C_M(y) + C_R(y) = 1, \ \forall y \tag{4.34}$$

Combining Equation 4.33 and Equation 4.34, the experimental amplitude γ of the R-phase spectrum, $S_R(2\theta)$ can be calculated by solving the following over-determined linear system at all spatial positions:

$$(1 - C_A(y) - C_M(y))S_R(2\theta) = d_1 U_1(2\theta)V_1(y), \forall y \tag{4.35}$$

Since that the experimental spectrum of R-phase is restored, we can use the following linear system to further improve the consistency of the phase concentrations $\mathbf{C}$:

$$\begin{aligned}
&\mathbf{C} = [C_A(y); C_R(y); C_M(y)];\\
&\mathbf{S} = [S_A(2\theta), S_R(2\theta), S_M(2\theta)];\\
&\mathbf{EC} \leq \mathbf{F}\\
&\mathbf{g}(\mathbf{C}, \lambda) = \sum(|\frac{\mathbf{D} - \mathbf{CS}}{\sqrt{\mathbf{D}}}|^2) + \max(\mathbf{0}, \lambda)(\mathbf{EC} - \mathbf{F})\\
&(\mathbf{C}, \lambda) = \arg\min \mathbf{g}(\mathbf{C}, \lambda)
\end{aligned} \tag{4.36}$$

The obtained phase field is plotted in Figure 4.20, after the reconstruction of R-phase spectrum via POD. The phase field respects in most cases the applied physical constraints and vanishes the corresponding residual field $\rho(2\theta, y)$:

$$\rho(2\theta, y) = \frac{||D(2\theta, y) - \sum_{i=1}^{i=3} C_i(y)S_i(2\theta)||^2}{D(2\theta, y)} \tag{4.37}$$

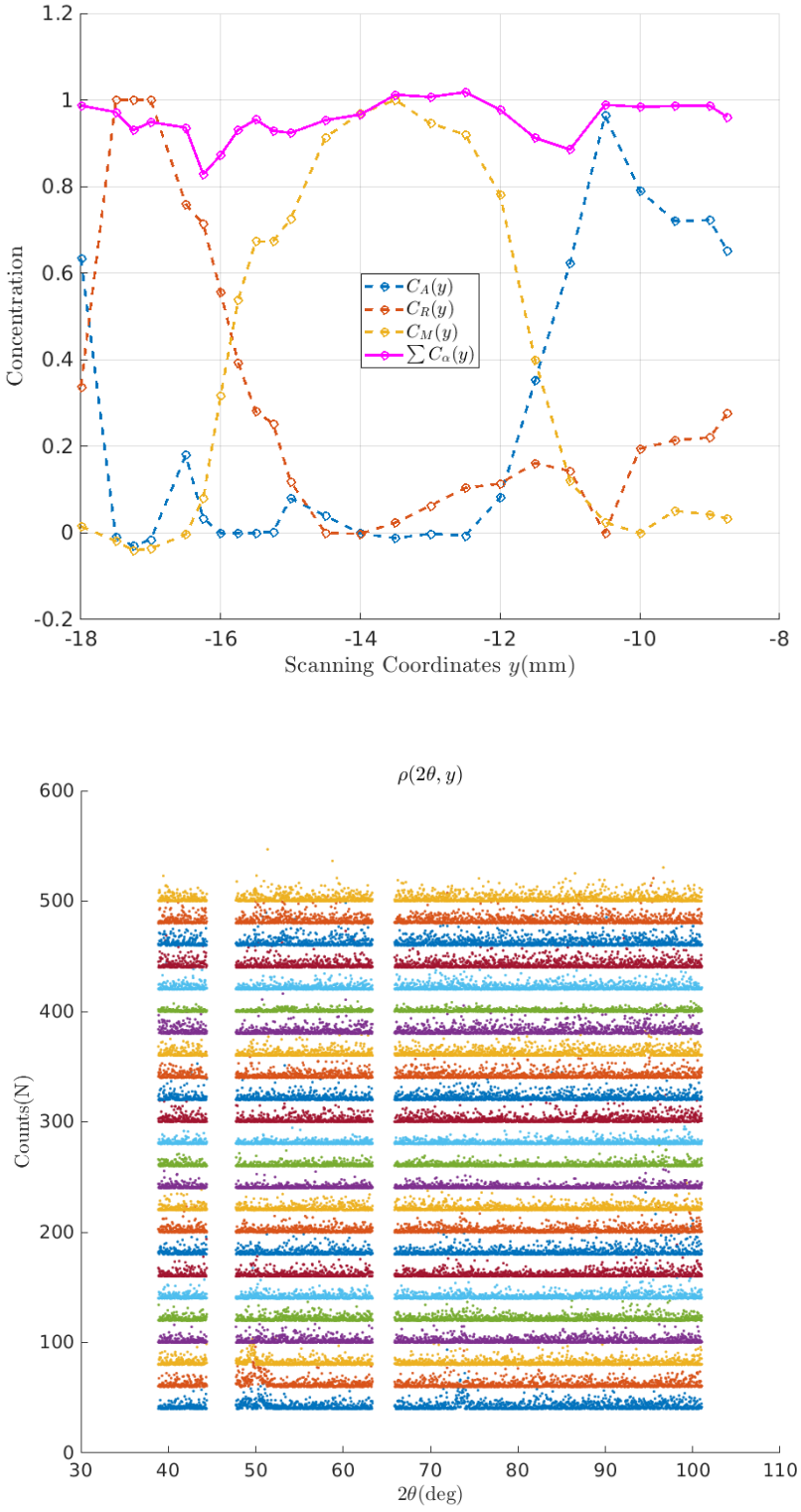

Figure 4.20: (a) Phase concentration with three experimental spectra; (b) residual field $\rho(2\theta, y)$ - representation using an offset value of 25 counts.

Several comments and remarks can be drawn considering for the Figure 4.20 :

- Phase presence : Compared to previous qualitative phase indexation, we see

that the M phase saturates at $C_M \simeq 100\%$ in the central region among all the scan coordinates, whereas A and R phase concentrate at the two boundaries (corresponding to the out of band zone).

- Interface : The interfaces between different phases are very smooth. It must be recalled that the incident X-ray beam has a non negligible radius (0.5mm). Hence, the above reconstructed phase map is the result of a convolution between the true phase field and beam size.

- Residual : As we see in Figure 4.20, the residual field $\rho(2\theta, y)$ has been mostly vanished in all scan coordinates y. However, for several spatial points, the sum of concentration $\sum C_\alpha$ is inferior/superior compared to 1. These imperfections demonstrate that the constructed three phase diffraction profile is not sufficient enough to represent all the diffraction data and to satisfy the physical constraints. The high level of residual at the bottom of Figure 4.20b leads to the same conclusion.

4.5.5 Influence of stress-induced texture and necessity of further modal enrichment

Looking back to the POD illustrated in Figure 4.19b (extracted from scan 1 during the tensile test), we observe that the secondary POD mode holds a very small portion of the remaining signals. The first POD mode is considered to be the diffraction pattern of the pure R-phase. But the shape of the second angular mode seems to correspond to a split of two R-phase diffraction peaks at very close angle (R11$\overline{2}$ and R300) and to an undulation between their relative weights at different analyzed points.
The third XRD scan has been carried out after the end of the transformation plateau (see Figure 4.5). We selected eight XRD scans conducted inside the transformation band. They have been repositioned in the strain map as illustrated in Figure 4.21a.
The same POD analysis routine has been conducted over the eight XRD scans located inside the transformation band (that should correspond to pure M). The associated first three POD spatial modes ranked with the highest eigenvalues (Figure 4.22) are reported in Figure 4.23. This result shows that two modes at least are necessary to take into account the whole diffractograms. The second POD angular mode can be also interpreted as some undulations of relative weight between {111} and {200} M peaks at each analyzed point:

- the 1rst angular mode represents the average diffraction spectrum of M phase, which is represented in the diffraction matrix $D(2\theta, y)$ by a nearly constant

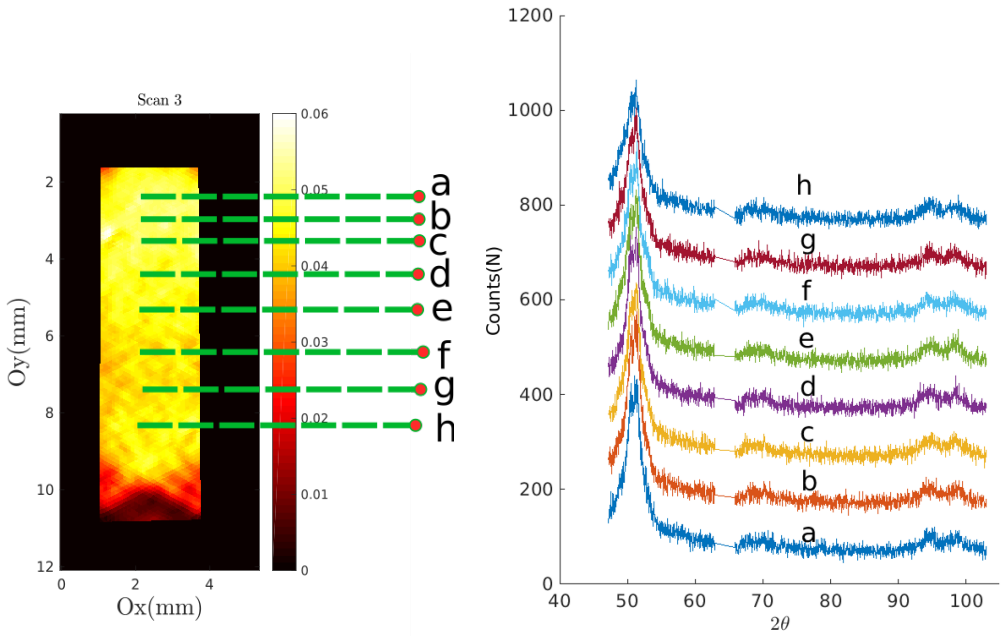

(a) (b)

Figure 4.21: Several XRD scan positions reported in the equivalent strain map. Measurement carried out during the stage 3 of the tensile test: (a) strain field with position of XRD scans; (b) diffractograms at the different positions - representation using an offset value of 100 counts.

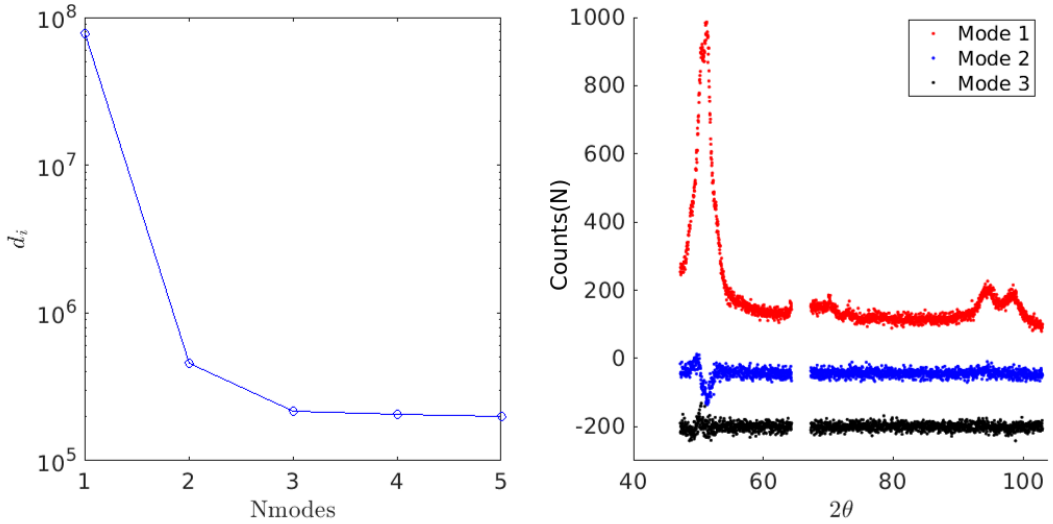

Figure 4.22: (Left) POD modes ranked with their eigenvalues in decreasing order; (right) first three angular POD modes exhibiting the highest eigenvalues.

spatial amplitude. On the contrary, the second POD angular shape function represents the variation in relative weight between diffraction peaks {111} and {200} of M phase. The diffraction signal of the third angular mode is non-significant: it may be associated with the measurement noise that justifies the POD truncation at this level.

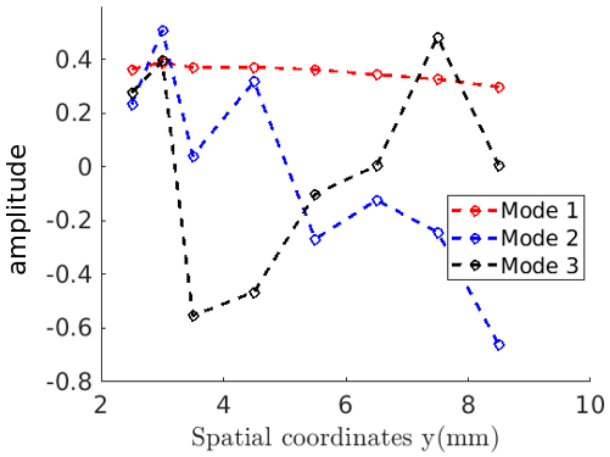

Figure 4.23: First three POD spatial modes ranked with the highest eigenvalues, extracted from diffraction matrix $D(2\theta, y)$ during scan 3.

- the spatial amplitude of the second POD mode (plotted in blue) is highly undulated at each analyzed point. This spatial undulation reflects that the relative weight between {111} and {200} diffraction peaks is highly heterogeneous, suggesting that martensitic variants orientation is also heterogeneously distributed along the axis of the strip.

During the tensile test, a stress-induced martensitic transformation occurs. Indeed, some variants are favored compared to others according to the local stress state and the boundary conditions. Consequently the relative weight between the different {hkl} diffraction peaks can be influenced by some potential heterogeneous variant selection.
The undulations observed for both M and R-phase are some indicators of this spatial heterogeneity. They also indicate a stress heterogeneity, since the external stress is the key driving force for martensite variant selection.
The non-unicity of the diffraction pattern for each phase is an undesirable consequence of this variant selection. It makes the identification of the volume fraction of each of the phases more difficult. The deployment of a model-enriched procedure as introduced in section 4.6 is required. Indeed, the diffraction spectra can be better represented with an enriched base of diffraction patterns, leading to a strong decrease of the residual field $\rho(2\theta, y)$.

4.6 POD Modal enrichment

Austenite phase of equiatomic NiTi SMA has a B2 structure. The material used for experiments exhibits a transverse isotropic texture. The relative weight of different A phase peaks observed from XRD measurement results from this texture.

It is supposed in the following that the texture of remaining A phase does not change significantly during its transformation into R and/or M phase. We suppose that only R and M phases are concerned by stress-induced texture associated with *macroscopic* variant selection that may change the relative weight of the different peaks. Herein we take the model enrichment of M phase spectrum as the example. This procedure can be also applied to the enrichment of R phase spectrum.

4.6.1 Martensite profile's enrichment

It must be recalled that for the first XRD scan, the phase field $\mathbf{C} = [C_A(y); C_R(y); C_M(y)]$ is initially solved with a relatively poor spectrum profile $\mathbf{S}$ containing only one single diffraction profile for A, R and M phase, with respect to the physical constraints reported in Equation 4.36.
The enrichment of the M phase diffraction profile requires first to remove the contribution of diffraction signals related to A and R phase from the global spectrum. The remaining signals after this removal are denoted as $R(2\theta, y)$. A POD analysis is next performed over $R(2\theta, y)$ at all reliable analyzed points. Figure 4.24 (left) shows the amplitude of the modes. The signals associated with the three first modes are presented in Figure 4.24 (right). Even if the second mode is much lower than the first mode, it contains informations that differ from the noise (especially at $2\theta \approx 49°$ and $2\theta \approx 94°$). On the contrary the third mode seems less significant. Thus in the following, these two first modes will be considered as two martensite profiles. They are considered as sufficient to take into account the whole diffraction profile for the M phase during the mechanical test. The two POD

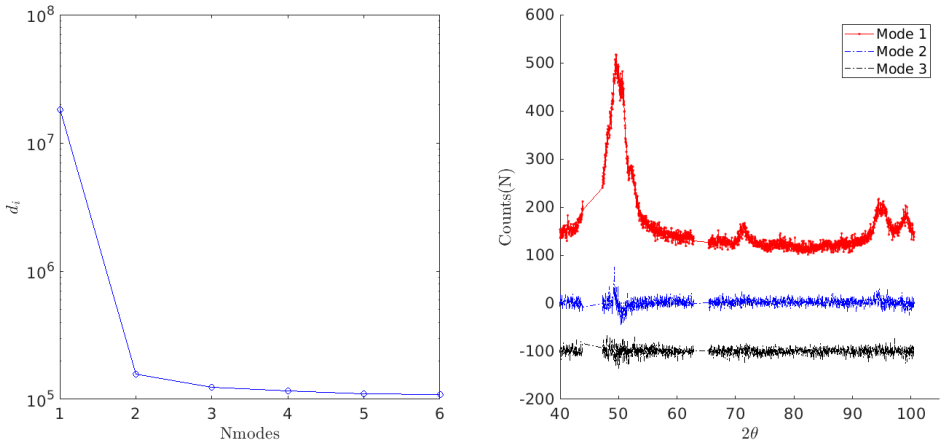

Figure 4.24: POD analysis of remaining signals after removal the contribution of A and R phase: (left) eigenvalues of POD modes (right) POD angular modes ranked with highest eigenvalues (3 modes represented) - representation using a vertical shift of 100 counts.

modes do not directly represent the true spectra. It is however possible to build

two admissible martensite diffraction patterns respecting the following equations:

$$
\begin{aligned}
&R(2\theta, y) \simeq \sum_{k}^{2} U_k(2\theta) V_k(y) = \sum_{j}^{2} C_{M_j}(y) S_{M_j}(2\theta) \\
&S_{M_j}(y) = \sum_{k}^{2} \kappa_k^j U_k(2\theta) \\
&C_{M_1}(y) + C_{M_2}(y) = 1 - C_A(y) - C_R(y) \\
&C_{M_j}(y) \geq 0, \ \forall y
\end{aligned}
\tag{4.38}
$$

The solution of this over-determined linear system is not unique. Among all of them, we propose to use the following set of admissible solutions for the martensite diffraction profiles $(S_{M_1}(2\theta), S_{M_2}(2\theta))$ plotted in Figure 4.25. This set is interesting because it seems leading to a formal separation between dominant {111} or dominant {020} diffraction patterns.

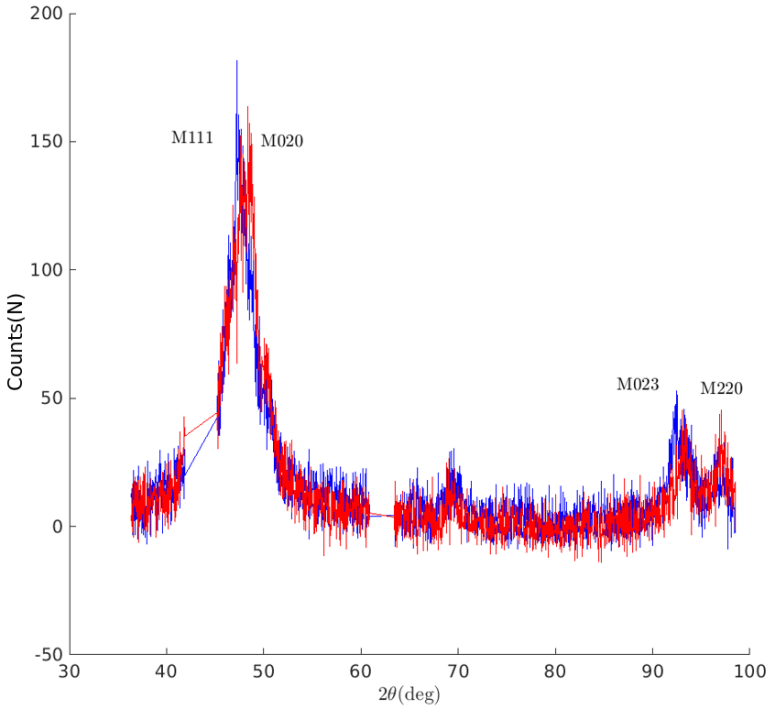

Figure 4.25: Enriched profile of martensite diffraction: illustration of diffraction patterns $S_{m_1}(2\theta)$ and $S_{m_2}(2\theta)$

The global set of diffraction patterns is now composed of four terms:

$$
\widehat{\mathbf{S}} = [S_A(2\theta), S_R(2\theta), S_{M_1}(2\theta), S_{M_2}(2\theta)] \tag{4.39}
$$

The concentration of each phase (M_1 and M_2 are considered as two distinct

phases) can be solved respecting the following constraints:

$$\begin{aligned} &\widehat{\mathbf{C}} = [C_A(y); C_R(y); C_{M_1}(y); C_{M_2}(y)] \\ &0 \leq C_i(y) \leq 1, i = A, R, M_1, M_2 \\ &\sum C_i(y) = 1 \end{aligned} \tag{4.40}$$

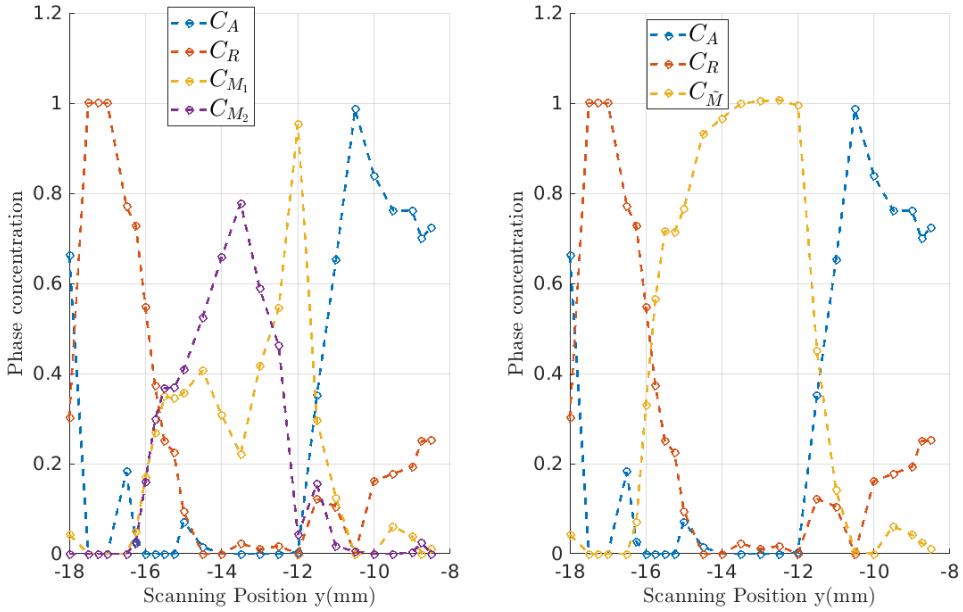

Figure 4.26: Phase field reconstruction using four experimental diffraction patterns: (a) concentration of each diffraction pattern including M_1 and M_2; (b) concentration of each phase considering that $C_{\tilde{M}} = C_{M_1} + C_{M_2}$

Concentrations are plotted in Figure 4.26. The phase distribution is obviously not fundamentally changed: we find the interfaces between A, R and M phases where they were observed during the first reconstruction. The presence of two M phases, however, gives an additional degree of freedom. It is remarkable to see that the fractions of M_1 and M_2 do not follow the same variations especially at the right interface. This spatial heterogeneity in phase concentration indicates an heterogeneous distribution of martensite variants inside the localization bands, close to the interfaces. This is the sign of a highly heterogeneous stress distribution, although the mechanical test remains a *simple* tensile test.
As presented in Figure 4.27, the additional martensite diffraction profile is closer to the diffraction pattern detected inside the band at the interface. Hence, the variation of martensite concentration near the interface has been significantly improved with this additional degree of freedom.

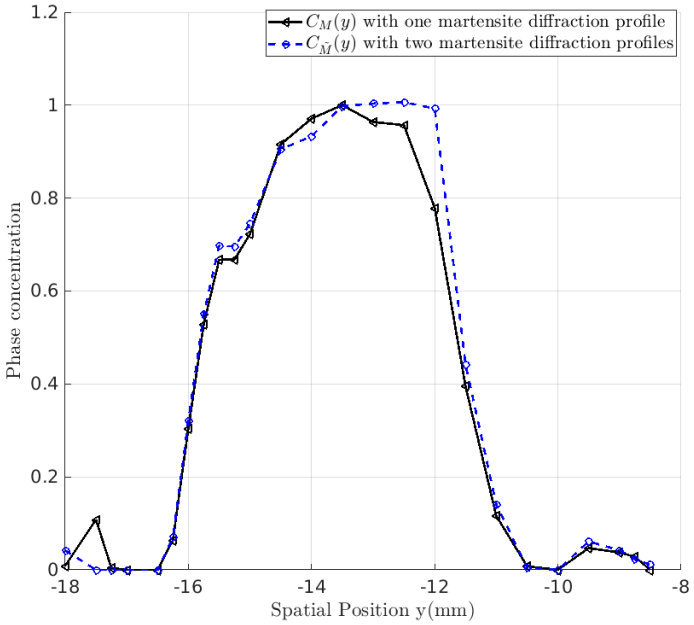

Figure 4.27: Comparison between two diffraction profiles: ($C_M(y)$ - black) M concentration calculated from one M diffraction pattern; ($C_{\tilde{M}}$ - blue) M concentration calculated from two diffraction martensite patterns (C_{M_1}, C_{M_2})

4.6.2 R phase profile's enrichment

The same enrichment procedure is applied to the R-phase:

1. Remove M and A phase diffraction contributions to obtain the remaining signals $R(2\theta, y)$;

2. Perform POD analysis, based on the criteria of eigenvalue and angular POD modes, reconstruct the physical admissible diffraction pattern of the R phase;

3. Re-evaluate the linear system with the enriched spectrum $\widehat{\mathbf{S}}$.

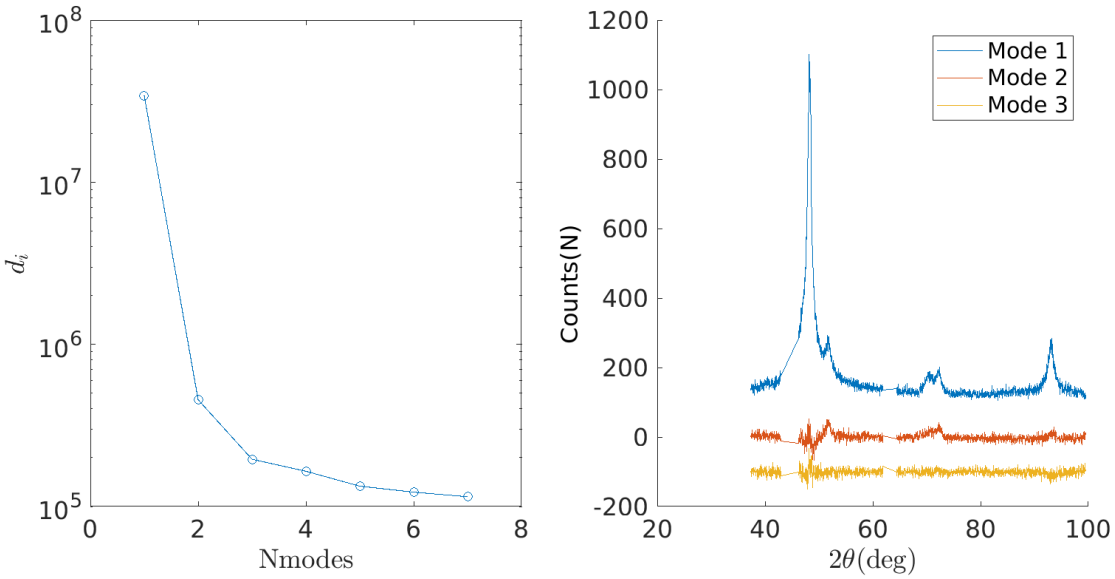

Figure 4.28: Step 1 - POD analysis: (left) eigenvalue of each POD mode; (right) first three angular modes exhibiting the highest eigenvalues.

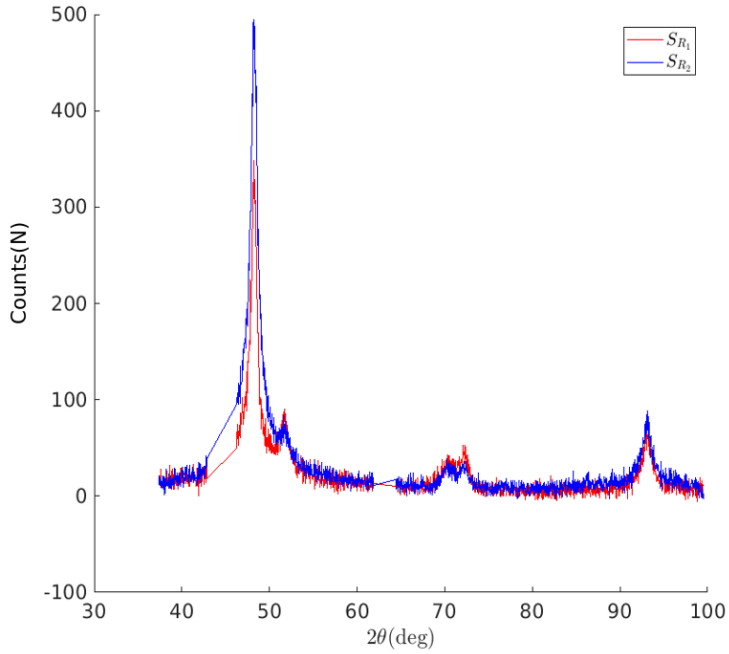

Figure 4.29: Two different R phase patterns representing stress-induced texture: S_{R_1} (in red) and S_{R_2} (in blue)

Figure 4.28 shows the result of the POD analysis. The two first modes are used to generate two diffraction patterns S_{R_1} and S_{R_2} for the R phase. These patterns are plotted in Figure 4.29. The procedure leads to an interesting separation between dominant {300} or dominant {222} diffraction patterns. These two patterns are present in the R-phase signal. The separation in two modes is probably the sign of a spatial-dependent variant selection.

Figure 4.30 shows the concentration profile obtained after this new POD

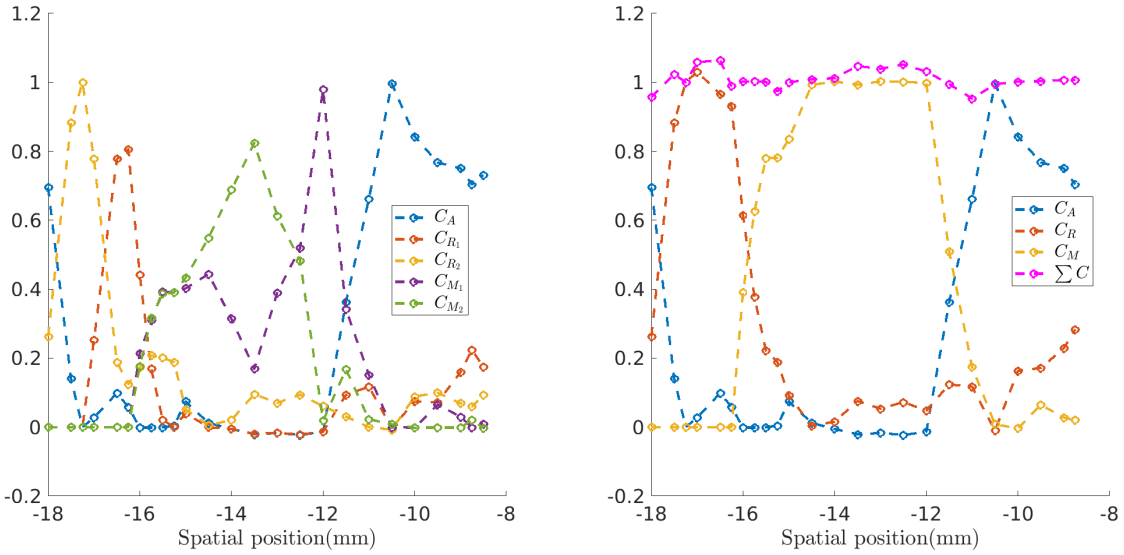

Figure 4.30: Phase concentration: (left) concentration associated with each diffraction pattern; (right) reconstructed concentration of each phase.

enrichment. The left hand figure shows the concentration associated with the five diffraction patterns. The right hand figure shows the associated reconstructed distribution of A, R and M phases. The following comments can be made:

1. As already commented, M phase is concentrated in the central region. The concentration of two M patterns strongly differ at some points indicating different variants selections inside the same band, especially located at the boundary of the band.

2. R-phase is concentrated at the left hand interface between band and matrix. As for M phase, strong differences of the two R-phase concentrations indicate different variants selections. A spatial separation in two R-phase variants is clearly located at the left interface.

3. The sum of the concentrations plotted in the right figure is nearly always close to 1, and all concentrations are positive. The two principal physical constraints are fulfilled.

The fluctuations of R_1/R_2 and M_1/M_2 are probably the result of a search for accommodation of transformation strains and compatibility with the applied loading.

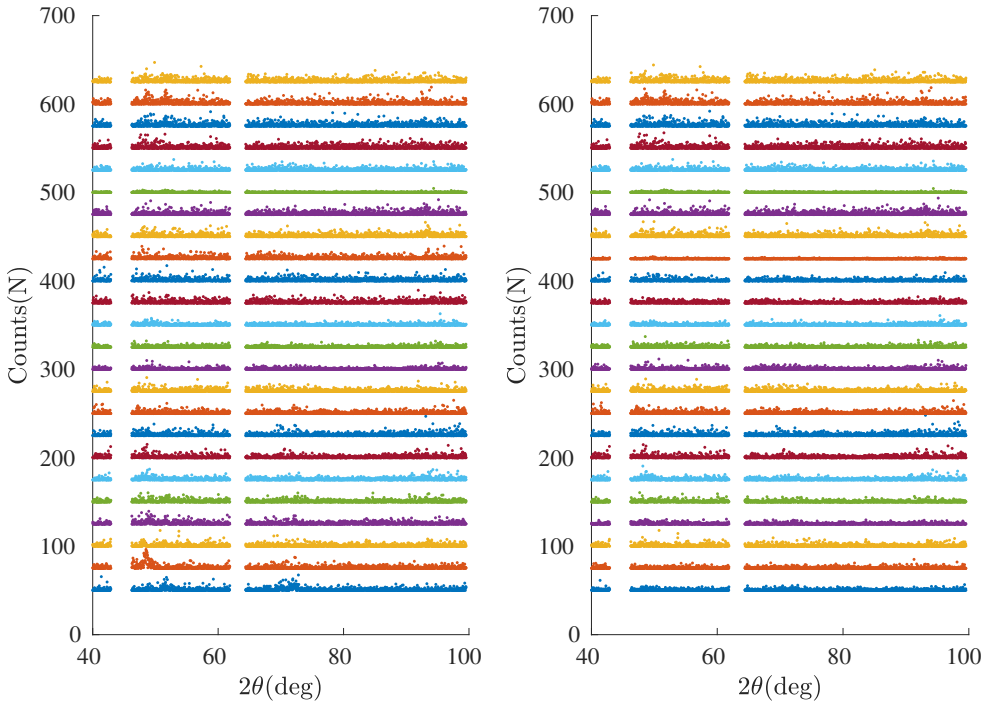

Figure 4.31: Residual field $\rho(2\theta, y)$ - representation using an offset value of 25 counts between each plot: (left) residual field after using three diffraction patterns; (right) residual field after using five diffraction patterns

The residual of the linear system obtained with the initial decomposition in three patterns is plotted in the left part Figure 4.31. It is clear that a large part of this residual is the consequence of the non-unicity of R phase/Martensite diffraction pattern: Hence by enriching the profile progressively, ending up with the five diffraction patterns in the data base, the residual of the linear system has been significantly reduced, as stated in the of Figure 4.31.

4.7 Comparison between kinematic and phase field

The intrinsic transformation strain of the M phase has a much higher amplitude than those of the R-phase. It can thus be supposed that, by variant-selection, this phase leads to the highest contribution to the macroscopic deformation of a sample under mechanical loading. After positioning both XRD and equivalent deformation in the same reference frame, it is possible to compare the evolution of the M concentration and the equivalent transformation strain measured by DIC. This comparison is performed for the 5 XRD scans carried out during the tensile test.

4.7.1 Numerical convolution over strain field

Obviously the spatial resolution of the XRD and the DIC results are strongly different. It must be recalled that experimental XRD is using a X-ray beam with a radius of $r = 0.5\,\text{mm}$. Moreover the incident angle of the X-ray beam is of about 40° from the vertical axis and *Mini-astree* machine is also tilted by an angle of about 13.5° from the vertical to increase the diffraction angle range. The X-ray scan direction is on the other hand conducted along the specimen whose axis is perpendicular to the X-ray beam (Figure 4.32). Hence the effective surface of XRD spot is an ellipse, whose long/short (a, b) axes are calculated by the following equation:

$$b = 0.5\,\text{mm} \text{ and } a = \frac{b}{\sin 27^\circ} \tag{4.41}$$

We decided to use this area as a virtual gauge to get an *average* equivalent strain field at the appropriate (deteriorated) spatial resolution, able to be compared to the phase field.

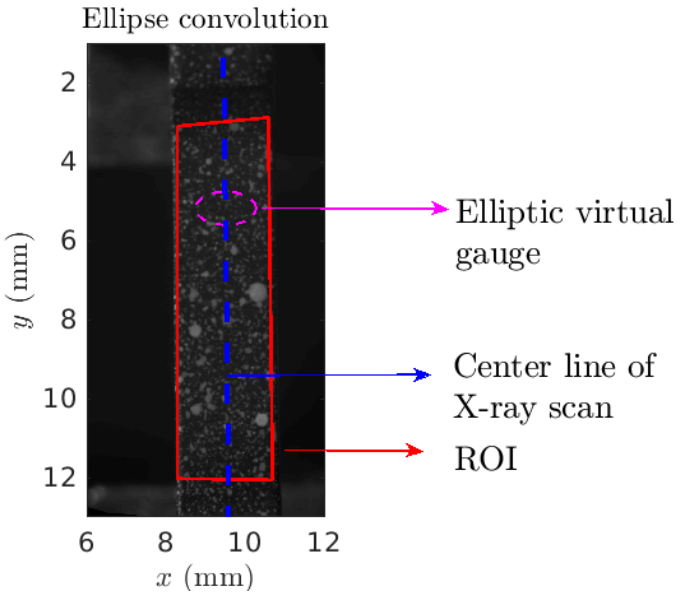

Figure 4.32: Illustration of the elliptic diffraction area used for the calculation of the average strain field.

4.7.2 Stage 0 : undeformed state

Since the initial image is taken at the reference state before the mechanical loading, the equivalent strain is obviously null everywhere. Based on the initial X-ray Diffraction scan Figure 4.33, the quantitative phase concentrations have been nevertheless calculated. The profiles of phases concentration of phases are plotted in Figure 4.34. No M phase is detected as awaited. We observe however a

slight concentration of R phase all along the sample despite an initial austenitization of the sample. This R phase may have been created during the installation of the specimen inside the machine. Indeed the installation procedure requires the use of a 100N pre-loading, gradually put to 0N before the tensile text. This R phase may also reveal some initial distribution of structural defects.

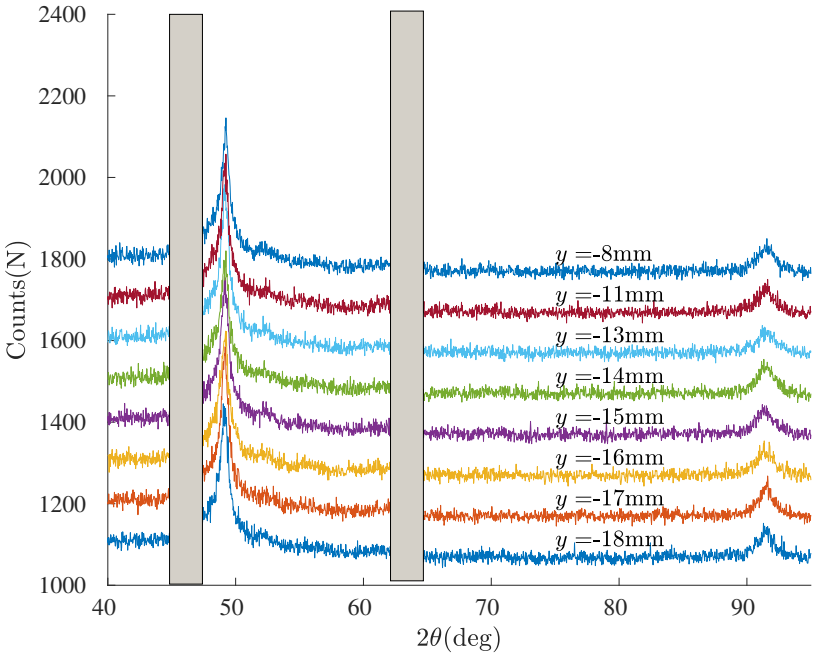

Figure 4.33: X-ray scan at stress free state

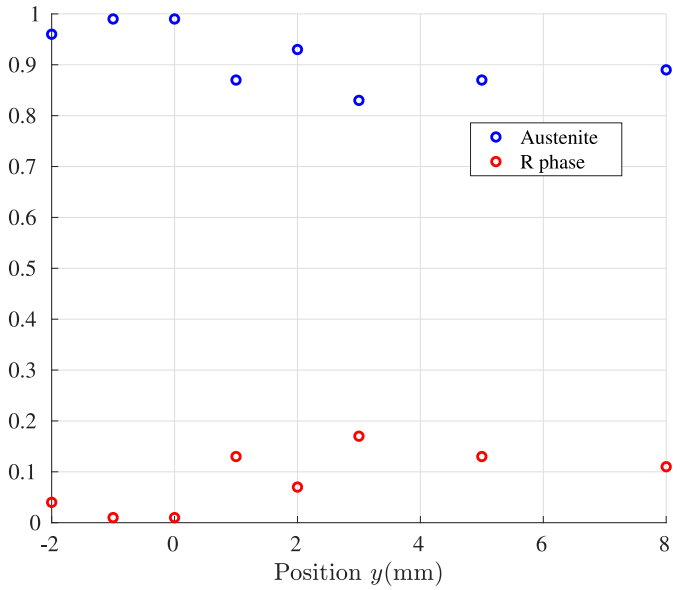

Figure 4.34: Phase concentration as function of y at stress free state

4.7.3 Stage 1: 1st interruption at $u_y = 0.3\,\mathrm{mm}$

Equivalent strain field and XRD scans for this stage have already been presented in subsection 4.3.2. They are now gathered in Figure 4.35. We observe that the bands region coincides with the phase concentration of martensite. The width of M phase and deformation bands are in good agreement. R phase and Austenite are dominant in the left and right of the figure, in accordance with a small deformation level. R phase saturates at the interface where the broadening along $-\mathbf{e}_y$ direction is stopped.

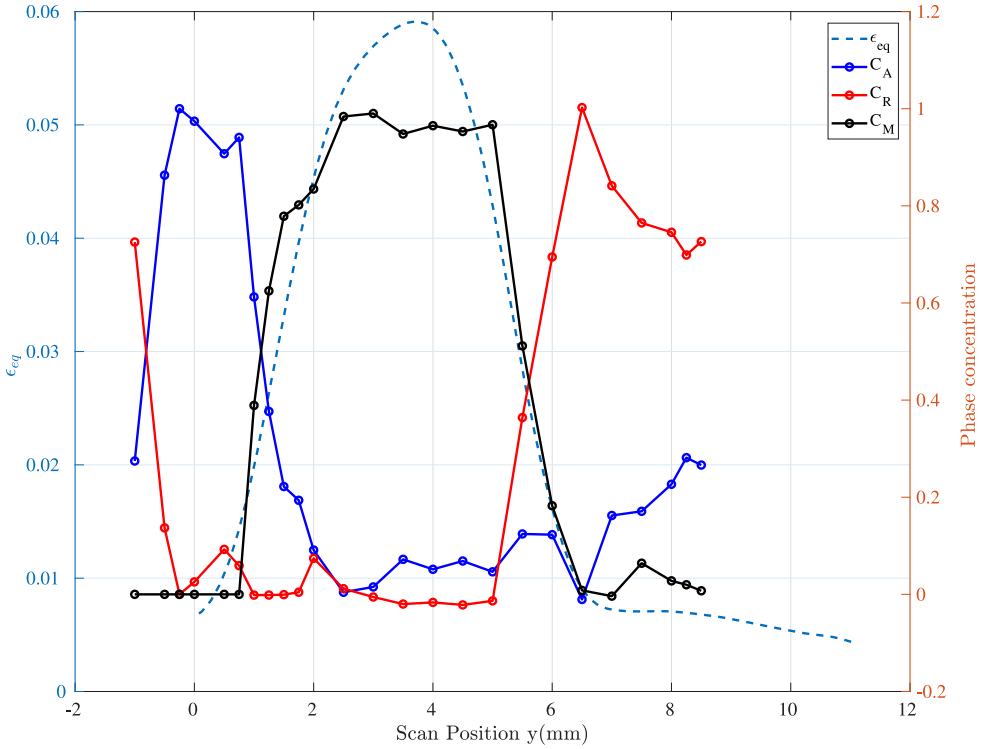

Figure 4.35: Comparison between the phase field and the equivalent strain in the same deformed configuration : A plotted in Red; M plotted in Black; R phase plotted in Blue; Equivalent strain plotted in Cyan.

4.7.4 Stage 2: 2nd interruption at $u_y = 0.4\,\text{mm}$

Figure 4.36 shows the phase fields obtained at the second stage. The coexistence of A/R/M can be both qualitatively and quantitatively verified. Results are close to those obtained at the first stage.

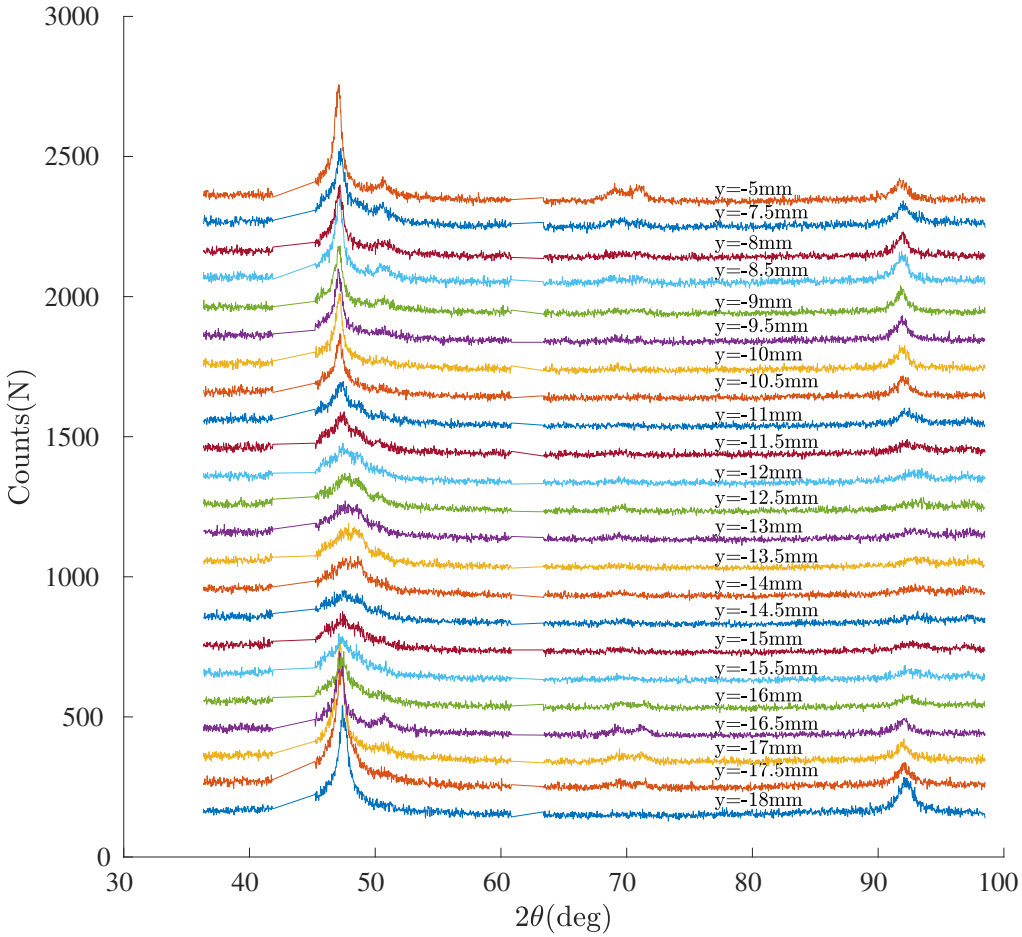

Figure 4.36: Ni-Ti XRD spectra along the scanning direction with an offset value of 100 counts for y axis between each plot (at step 2 of XRD scan in Figure 4.5)

M-phase and equivalent strain fields are presented in Figure 4.38. We observe a global broadening of the transformed/deformed areas, compared to the results obtained at the first stage (Figure 4.37). We observe furthermore a second transformation front stopped along the $-\mathbf{e}_y$ direction.

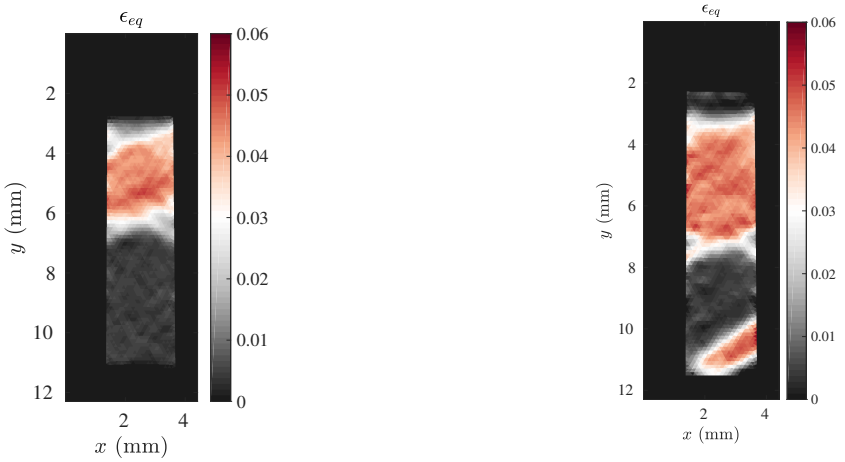

(a) Strain ϵ_{eq} at the first stage

(b) Strain ϵ_{eq} at the second stage

Figure 4.37: Comparison of the equivalent strain field at the first and second interruption

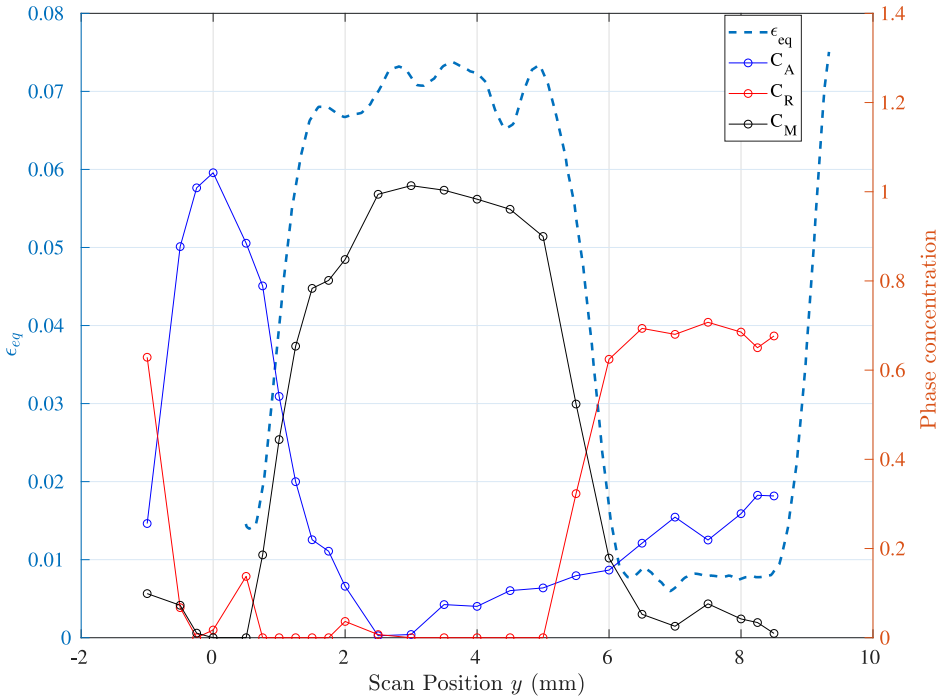

Figure 4.38: Comparison between phase and equivalent strain fields: A plotted in Red; M plotted in black; R plotted in Blue; equivalent deformation plotted in Cyan.

4.7.5 Stage 3 : fully transformed

At the third stage, all X-ray diffraction spectra indicate a dominant concentration of M phase This result is consistent with the kinematic field shown in Figure 4.21a where the deformed region covers nearly the whole XRD observation window.

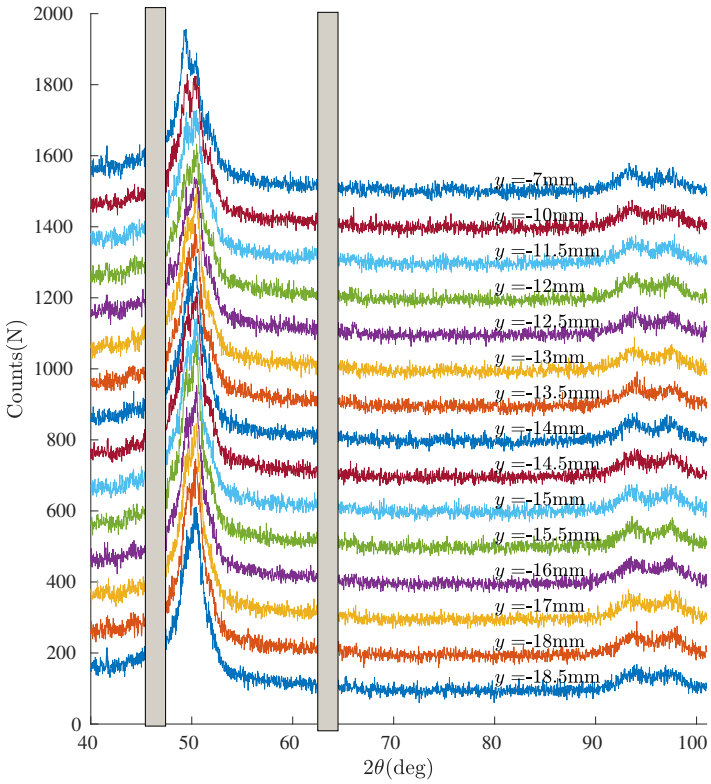

Figure 4.39: Ni-Ti XRD spectra along the scanning direction with an offset value of 100 counts for Y axis between each plot (at step 3 of XRD scan in Figure 4.5)

4.7.6 Stage 4: 4th interruption at $u_y = 0.3\,\mathrm{mm}$

At the fourth interruption, the XRD scan shows an heterogeneous distribution as for phase concentration as presented in Figure 4.40 and Figure 4.41.
Unfortunately, at this stage, the fixation of *prism* has been perturbed and the spatial position reference has been lost, leading to an undesired displacement of images. Thus the phase concentration experienced at this stage remains much **more qualitative** compared to stages $0, 1, 2, 3$.
Nevertheless, there is again an interesting concordance between the level of equivalent deformation and its fluctuations, with the martensitic phase profile and concentration. In particular, on the right, a decrease of deformation appears to be correlated with a return to the R phase.

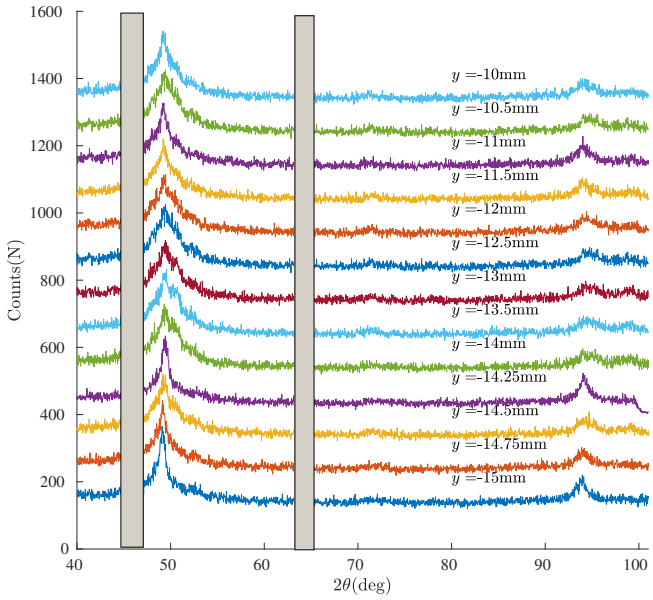

Figure 4.40: Ni-Ti XRD spectra along the scanning direction with an offset value of 100 counts for Y axis between each plot (at step 4 of XRD scan in Figure 4.5)

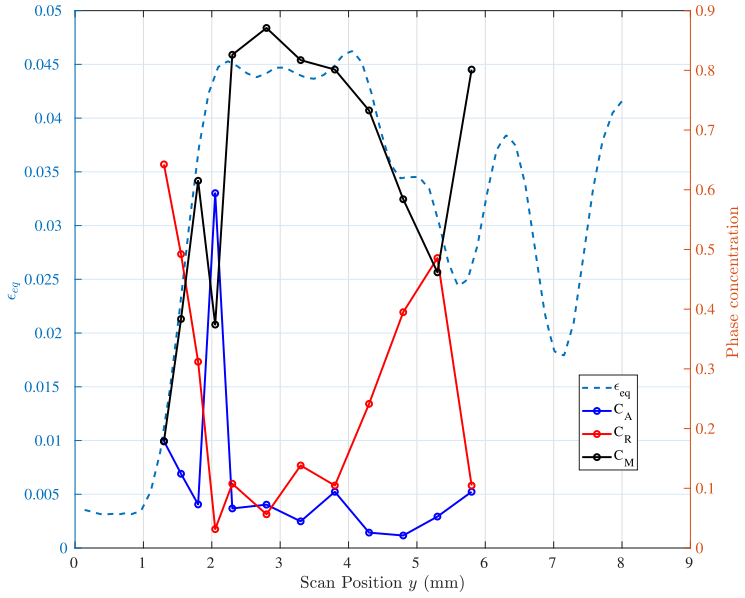

Figure 4.41: Comparison between phase field and equivalent strain in the same deformed configuration: A plotted in Red; M plotted in black; R phase plotted in Blue; equivalent strain plotted in Cyan.

Figure 4.42 shows the evolution of the M phase concentration deduced from the POD approach as a function of the equivalent deformation, for all the experimental points got from all stages. There is an interesting three parts correlation between these two indicators, highlighting a 1% equivalent strain threshold and a saturation at an equivalent strain of about 5%. The largest deviations correspond to probable enormous spatial shifts between fields. The 1% equivalent strain threshold is probably related to the R-phase contribution.

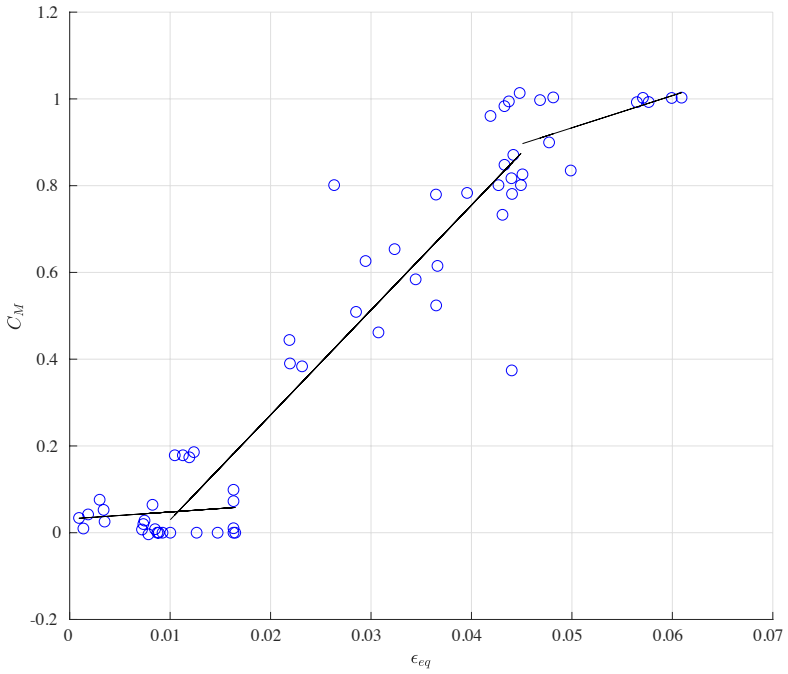

Figure 4.42: Concentration of M deduced from the POD procedure as function of the average equivalent strain at the same point.

4.8 Comparison between multiscale stochastic model and experimental results.

The multiscale stochastic model is a RVE model that allows the calculation of the phases volume fraction during a tensile test. The only way to make a comparison between the results of this model and the realized phase measurements is to use the average value of the phase fields over the observation window.
We define hereafter the average operation used to calculate the experimental average volume fraction f_α^e of an α phase:

$$f_\alpha^e = \frac{1}{N_d} \sum_{y}^{N_d} C_\alpha(y), \ \forall \alpha \tag{4.42}$$

where N_d defines the number of XRD scans. The experimental loading path is applied to the multiscale model and phases are extracted at each stage. Experimental and modeled results are plotted in the Figure 4.43. The modeling results differ from the experimental results, except for the scan 3 where a full martensite situation is obtained. Several conclusions can be drawn:

- The numerical model globally over-estimates the production of M-phase during the loading and over-estimates its removal during the unloading. Even after a long relaxation time (relevant to remove some accumulated heat), the homogenized RVE prediction does not match with the average response of 1D strip under simple tensile loading.

- The R phase amount, on the contrary is strongly under-estimated by the modeling. Indeed R-phase has been mainly observed as an intermediate phase between M and A phase in order to play an important accommodation role. This kind of contribution makes sense only when geometrical parameters are involved in the mechanical equilibrium.

This result once again highlights the need to use the model as a constitutive law in a structure model. We can see very well at this stage our inability to reproduce even the average fields given the structure effects. These effect seems to be impossible to reduce, even for a test as simple as a tensile test.

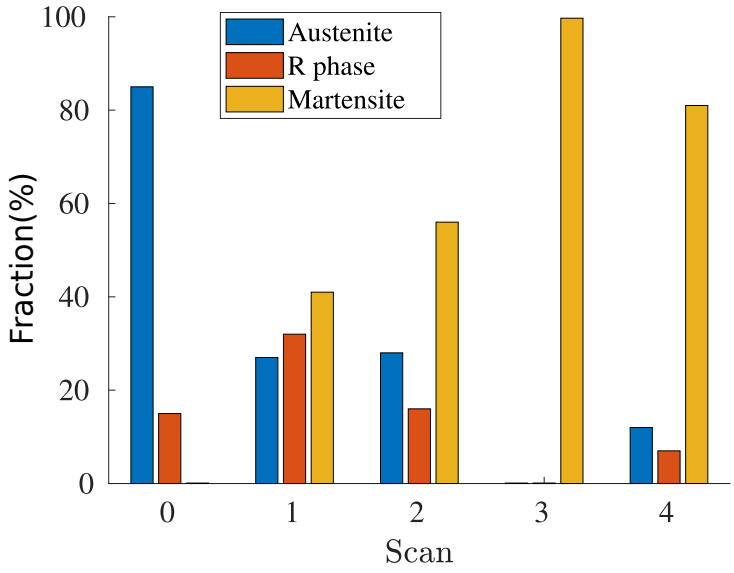

(a) Experimental average phase concentration for each XRD scan

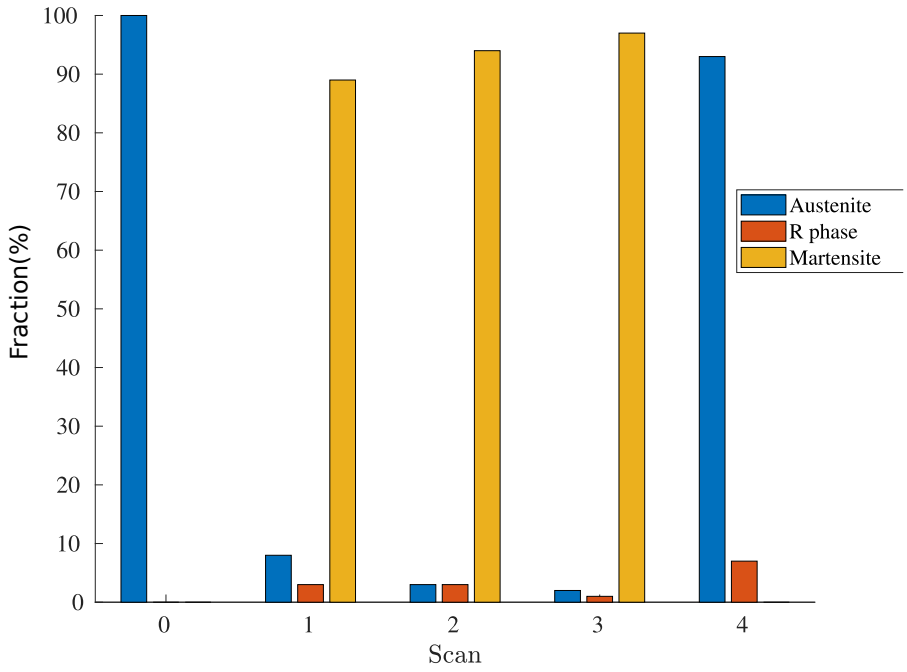

(b) Predicted phase concentration for each XRD scan

Figure 4.43: Comparison in terms of phase concentration for each XRD scan

4.9 A qualitative explanation for variant-selection heterogeneity

A potential explanation is given here to explain the observed spatial heterogeneity of the variant selection. Two sets of symmetrical bands are usually formed during

a 1D tensile test to ensure the stress equilibrium, as shown in Figure 4.6 and illustrated in Figure 4.44. Since the strain jump direction is different for these two sets of bands (bands A and B), the stress jump differs as well. Consequently, the two sets of bands are experiencing different stress states, leading to some differences in the variant selection process. The recorded strain rate evolution Figure 3.19 (previous chapter) showed on the other hand that bands do not propagate continuously and simultaneously. It is consequently possible to observe one dominant set or the other at the interface depending on the propagation state. A more accurate (by improving the spatial resolution of X-ray beam) XRD could help do visualize the diffraction pattern separately in regions A and B.

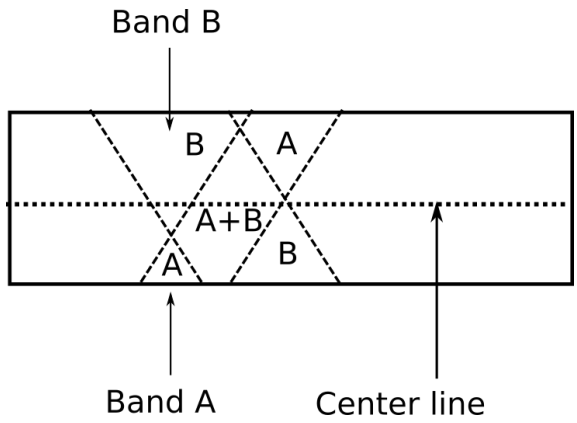

Figure 4.44: Schematic explanation for variant selection heterogeneity

4.10 Conclusion

Interest of the multiview set-up Due to heterogeneity in stress/strain/thermal/phase field, the mere knowledge of kinematic field and Dirichlet force boundary conditions are not enough to understand properly how a localization phenomenon occurs during a 1D tensile test. A multiview setup is of great interest to locally determine a relationship between the different phases and strain. It has been proven that this information is accessible by a combination of XRD and DIC:

- DIC provides a continuous global observation of displacement, strain and strain-rate fields during the tensile loading test.
- XRD allows a local evaluation of phase composition at the same time and position

Indeed to relate both characterization, it is essential that XRD is performed *in situ* and that the analyzed points are positioned in the same (for instance reference) configuration.

Co-existence of A, R and M phases It can be concluded from this work that A, R and M phases coexist during a tensile test.

POD-based phase field reconstruction To circumvent the impossibility to obtain an experimental pure R-phase diffraction profile, a positive POD (PCA) based phase field reconstruction algorithm has been proposed. After background correction, three POD modes obtained from all measured spectra can be selected to take into account all the diffraction data. With the a-priori knowledge of A and M diffraction pattern, the direction and amplitude of R phase can be deduced from an iterative correction in the POD space.

Quantitative comparison between kinematic field and phase field After comparing the kinematic field and the phase field at each analyzed point, we state that martensite is nearly saturated inside the strain bands, and austenite is overwhelmingly dominant outside the bands. R-phase is meanwhile observed at some interfaces between a band and a non-transformed area. The multiscale stochastic modeling, as a modeling for a representative volume element, is unable to simulate the average phase concentration evolution during the tensile test of a NiTi strip. The R-phase, playing a significant role of macroscopic accommodation between M and A phase, is strongly underestimated by the modeling. These results highlight the requirement of a structure model for a better fitting between experimental and modeling results.

Heterogeneous variant-selection and stress distribution At the end of the transformation plateau, the undulation of some {hkl} diffraction peaks of M and R phase seems to be correlated to a non-uniform variant-selection along the specimen axis, indicating that the stress distribution is highly heterogeneous along the 1D strip.

POD diffraction profile enrichment The enrichment of the experimental diffraction patterns in order to take account of the stress-induced texture during the PE stress-strain behavior (involving both M and R phases) can also be achieved by a progressive POD reconstruction.

Chapter 5

General conclusion and future works

As a conclusion, a summary of the main original works detailed in this manuscript is presented. They concern the field of shape memory alloys and their properties.

This work was first the opportunity to propose **a multiscale stochastic model able to simulate the hysteretic behavior of SMA at variant/single crystal/polycrystal scale**. We have chosen to build this multiscale model based on the experimental DSC scan of the investigated SMA :

- The thermal hysteresis observed during the thermal loading without applied stress indicates that a germination energy is necessary to induce any phase transformation. Otherwise, the thermal response during the DSC analysis of the SMA would have been symmetrical for heating and cooling.

- The characteristic relaxation time observed during a temperature plateau carried out at any time during the peak of transformation during a DSC scan demonstrates that the phase transformation can not be explained by a thermodynamic equilibrium alone. Part of the hysteresis of transformation is therefore transient.

This multiscale model is formulated based on these two experimental observations:

- The first point is that a certain amount of additional potential is needed to induce a significant phase transformation in SMA. This slight shift can be seen as the energy required to nucleate a new phase inside a former phase. The delay can be measured and correctly identified by DSC scanning. The intrinsic time (relaxation time) can also be measured through a thermal DSC cycle. This provides an additional information on the magnitude of the energy barrier to be exceeded. These two energetic terms implemented are the main elements driving the hysteretic response of the model.

- The second key point is that when a multi-phase SMA is out of equilibrium, the Clausius-Duhem inequality can help us to determine the direction of phase transformation by comparing the thermodynamic forces with the experimentally identified thresholds. The major drawback of many models based on this approach is that this inequality relation can not provide any kinetic information on the phase transformation, nor on the time-increment of each phase volume fraction. This is the main reason why a stochastic formulation was chosen during this thesis. By describing the Gibbs free energy density of each variant, the master equation governing the phase transformation can be correctly expressed, allowing us to evaluate the competition between each type of phase transformation at a given mechanical loading, and calculating the temporal variation of each volume fraction. In the meantime, to avoid high calculation costs, a kinetic Monte-Carlo method ensures a robust response of the SMA system.

- With only two additional parameters (germination energy and relaxation time) compared to the anhysteretic model, this multiscale stochastic model provides an almost complete and robust prediction of the pseudoelastic behavior of SMA (the approach can be extended, of course to other materials than NiTi), the memory effect (one-way or two-way), taking into account the thermomechanical coupling integrating naturally the multiaxial loadings. Different scales can also be considered: single variant, multi-phase crystal or polycrystal.

In a second time, for the purpose of experimental validation, **a detailed experimental campaign** has been carried out throughout this thesis: **Uniaxial tensile and multiaxial proportional and non proportional loadings have been tested over several 1D and 2D specimens**. In order to get an appropriate estimation of the strain field, PGD-RT3 DIC code developed at LMT including a mechanical regularization protocol has been used. The mechanical regularization allows a sharp decrease of the high frequency components of the displacement field by enforcing the mechanical admissibility. Consequently, the DIC analysis grants us to access the kinematic displacement field with a extremely high spatial resolution and to reduce the uncertainties compared to any other commercial code. As a result, the stress-strain curve, the occurrence and evolution of strain localization, the pattern and the morphology of the localization bands under uniaxial and multiaxial loading have been properly collected. This experimental campaign offers an extremely rich data base both in space and time, and offers a great opportunity for the validation of the multiscale model. Experimental results have been compared with numerical simulations. Results are consistent in uniaxial condition and allow an appropriate description of the yield

surface in multiaxial condition. It was not however possible to compare results above the threshold due to structural effects. The multiaxial experimental campaign highlights the difficulty of setting up a true multiaxial loading without structural effect.

However, since the model is a RVE model, and although the mean values are consistent, it is unable to simulate the observed evolution of the localization bands even for a *simple* uniaxial test. A question arises concerning the consistence between experimental and simulation concerning the phases involved during a PE cycle. A **new multiview multi-instrumental full-field observation device combining XRD and DIC** was developed during this thesis to answer this question. The objective is to add a quantitative measurement of phase field to be compared with the strain field. Qualitatively, the coexistence between A, M and R phases has been observed during the transformation plateau of a 1D tensile test performed at the room temperature.

To circumvent the challenge of obtaining the experimental pure R phase diffraction profile, **a positive POD(PCA) based phase field reconstruction algorithm has been proposed**. After background subtraction, three POD modes obtained from all measured spectra can be selected to build all diffraction data. With the a-priori knowledge of A and M patterns, the direction and amplitude of R phase pattern has been deduced after an iterative correction. Spatial undulations of spectra have been related to some anisotropic selection of diffraction planes associated with some potential heterogeneous stress distribution at the near band/matrix interface regions. Enrichment of the POD modes allows the identification of these pattern fluctuations and the improvement of the phases fraction calculation. This work finally justifies the requirement of a numerical model to perform the coupled calculation of phase, stress and thermal fields all together. A first attempt of numerical modeling is presented in appendix B.

Several future prospects are listed bellow. They concern both experimental and numerical aspects:

For the experimental part:

- Adding a high spatial resolution IR camera into the current multiview setup would allow us to express both the phase concentration and the local temperature at the same point of the strain map. It would grant us a much better understanding of the relationship between the localization phenomenon and the macroscopic thermo-mechanical coupling/competition at the macroscopic scale. However, between the security issues due to X-ray and the over-crowding problem of multiview setup inside small size chamber, a compromise solution would have to be find in order to properly set up the

additional IR camera.

- Carry out the same kind of in-situ multiview test inside a X-ray synchrotron would allow to reach a much higher spatial resolution of phase field with a large window and with a strongly reduced acquisition time per loading point. This technique would be really interesting if we imagine to design a dedicated biaxial machine and biaxial samples, the beam going through the sample. The evolution of the phase field in case of proportional and non-proportional loading could be compared.

For the numerical part:

- In order to have a more realistic description of SMA microstructure, the twinning interdiction between some Martensite variants needs to be implemented inside the current stochastic model. Indeed, uniform germination energies are used in the present model to represent the overall germination cost during the phase transformation. As a consequence, a local standard unit may transform into a specific M variant and its neighbors can transform in other M variants that may be incompatible with the first variant set. This potential incompatibility and the associated energy is not taken into account. A potential layer could be so added to the current stochastic model. The computational cost (in term of storage and time) of such an implementation would be probably prohibitive.

- The extension of the RVE model towards a macroscopic model would be of great interest of course: allowing the estimation of localization, and instabilities via the computation of the full thermo-mechanical problem. The use of an interface operator and of the for a 1D isothermal problem is an interesting prospective. Its extension to a 2D modeling and an anisothermal situations would be necessary.

Appendix A

Details of the stochastic multiscale model

Contents

A.1 Inversion Monte-Carlo Method to implement Monte-Carlo step

The description of KMC in subsection 2.3.4 is nearly complete, except for how we randomly generate transformation variables (τ, μ) at each step (this pair of variable is usually called 'Monte-Carlo step'). In this paper, we adopt the direct method (Inversion Monte-Carlo Method [Reiher, 1966]) to implement the Monte-Carlo step. Another numerical implementation approach (called as 'first transformation method') exists. Both methods have been demonstrated to be exact and rigorous [Daniel, 1976]). When the system exceeds three transformation types, the direct method is more efficient (for the case of Ni-Ti polycrystal, we have 272 different transformation types between variants).
The 'inversion Monte-Carlo method' provides a stochastic application to generate random variables according to prescribed density probability functions, or by using random numbers generated in the unit interval [0,1] (RNG application is available in softwares such as Matlab and C++).

In this appendix, we detail this well known technique for both the continuous variable applied for the case of $p_1(\tau) \rightarrow \tau$ and discrete variable applied for the case of $p_2(\mu|\tau) \rightarrow \mu$.

We seek to generate a random variable y according to the one-variable density

function $p(y)$. By definition, the probability that y is generated inside the interval $[y', y' + dy]$ is $p(y')dy$. Based on it, we can build a parent probability function F:

$$F(y) = \int_0^y p(y')dy' \tag{A.1}$$

Trivially, $F(y_0)$ measures the probability that variable $y \leq y_0$ (this function is defined as probability distribution function). It must be noticed that with the normality of $p(y)$, F is built to have this type of property and its monotony is ensured:

$$F(y = 0) = 0 \text{ and } F(y = \infty) = 1 \tag{A.2}$$

$$p(y) \geq 0 \tag{A.3}$$

The basic philosophy of 'inversion method' is that in order to generate a variable y based on $p(y)$, it is easy to select a random number (RN) r belonging to the unit interval $[0, 1]$ and then take for y a value that satisfies:

$$y = F^{-1}(r) \tag{A.4}$$

Where F^{-1} is the inverse function of F (the existence of F^{-1} is guaranteed by Equation A.2 and Equation A.3).

Thus considering probability $p_1(\tau)$, the parent function $F_1(\tau)$ can be written as:

$$F_1(\tau) = 1 - \exp(-\zeta\tau) \tag{A.5}$$

$$\tau = \frac{1}{\zeta}\log(\frac{1}{r}) \tag{A.6}$$

With r uniformly distributed in the unit interval $[0, 1]$

In the discrete case, the procedure is even more trivial. We calculate:

$$F_2(\mu) = \sum_{\mu} p_2(\mu|\tau) \tag{A.7}$$

$$F_2(\mu - 1) \leq r \leq F_2(\mu) \tag{A.8}$$

A.2 Convergence of KMC algorithm - influence of independent selections

When a complex thermo-mechanical loading is applied, the crystal system may encounter a scenario where several variants exhibit the same Gibbs free energy density at current time, meaning that the activation of these transformation types are equiprobable.
Unfortunately, KMC randomly choose one of the specific transformation types and moves forward. Convergence to solution is not guaranteed. Other KMC tests are necessary. Indeed, all the results are probably different but have the same tendency. In stochastic theory, the stochastic average eventually converges towards the macroscopic average when enough independent tests based on probability functions are

performed.
Figure A.1 illustrates this progressive convergence for DSC simulation with an increasing number of numerical tests.

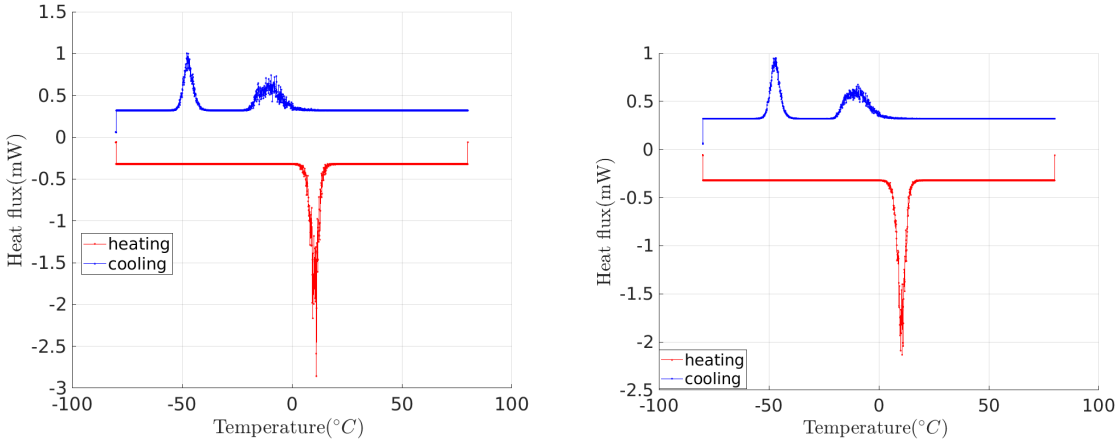

(a) 50 tests

(b) 150 tests

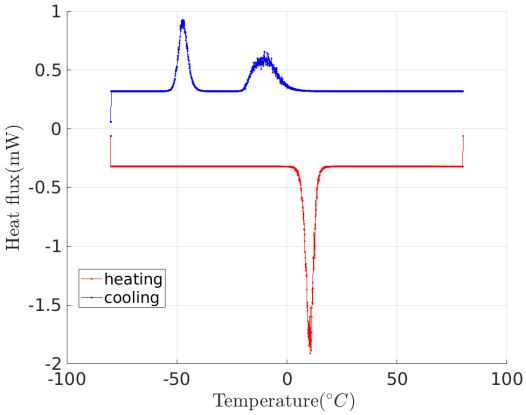

(c) 300 tests

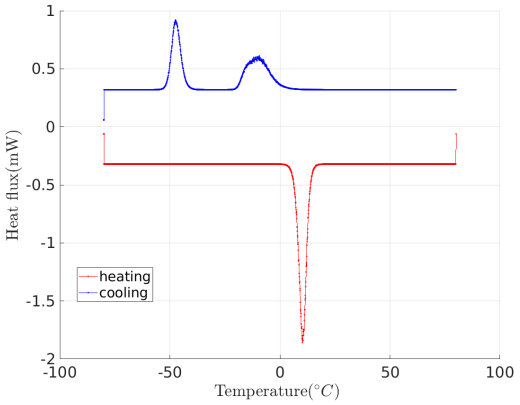

(d) 3000 tests

Figure A.1: Relation between convergence and number of independent tests

A.3 Levi-Civita symbol and cross product vector/tensor

The Levi-Civita symbol ϵ_{ijk} is a third-rank pseudo-tensor and is defined as follows:

$$\begin{aligned} \epsilon_{ijk} &= 0, \textit{if two labels are the same} \\ &= 1, \textit{if } ijk \textit{ are an even permutation of } 1,2,3 \\ &= -1, \textit{if } ijk \textit{ are an odd permutation of } 1,2,3 \end{aligned} \tag{A.9}$$

Hence the Levi-Civita symbol is anti-symmetric on each pair of index.

The interest to use the symbol of Levi-Civita tensor is the compact expression of the determinant

$$det(A) = \begin{bmatrix} a_{11} & a_{12} & a_{13} \\ a_{21} & a_{22} & a_{23} \\ a_{31} & a_{32} & a_{33} \end{bmatrix} = \sum_i \sum_j \sum_k \epsilon_{ijk} a_{1i} a_{2j} a_{3k} = \epsilon_{ijk} a_{1i} a_{2j} a_{3k} \tag{A.10}$$

Note that the compact Einstein notation where the summation over the spatial directions is dropped. This notation is used throughout this PhD thesis.
The Levi-Civita symbol can be expressed itself as a determinant, or as the mixed product of the unit vectors (direct cartesian coordinates) $(\hat{\mathbf{e}}_\mathbf{1}, \hat{\mathbf{e}}_\mathbf{2}, \hat{\mathbf{e}}_\mathbf{3})$:

$$\epsilon_{ijk} = det(\hat{\mathbf{e}}_\mathbf{1}, \hat{\mathbf{e}}_\mathbf{2}, \hat{\mathbf{e}}_\mathbf{3}) = \hat{\mathbf{e}}_\mathbf{1}\dot{(}\hat{\mathbf{e}}_\mathbf{2} \times \hat{\mathbf{e}}_\mathbf{3}) \tag{A.11}$$

We can define the simple cross product by analogy :

$$\mathbf{a} \times \mathbf{b} = det(\begin{bmatrix} \hat{\mathbf{e}}_\mathbf{1} & \hat{\mathbf{e}}_\mathbf{2} & \hat{\mathbf{e}}_\mathbf{3} \\ a_1 & a_2 & a_3 \\ b_1 & b_2 & b_3 \end{bmatrix}) = \epsilon_{ijk}\hat{\mathbf{e}}_\mathbf{i} a_j b_k \tag{A.12}$$

We obtain for each coordinate :

$$(\mathbf{a} \times \mathbf{b})_i = \epsilon_{ijk} a_j b_k \tag{A.13}$$

A.4 Sub-gradient projection algorithm

We consider the problem of minimizing a quadratic convex function over the noisy linear constraints:

$$\text{minimize } \ (\frac{1}{2})x^T(A^TA)x - (A^Tb)x \tag{A.14}$$

$$\text{subject to } C^Tx - d^T \leq 0 \tag{A.15}$$

In order to promote maximum the positivity of $\gamma = b - Ax$, the augmented Lagrangian is ad-hoc modified:

$$L(x, \lambda) = (\frac{1}{2})|Ax - b|^2 + \lambda(C^Tx - d) + (\frac{1}{2})|\frac{w}{\sigma}(Ax - b)|^2 \tag{A.16}$$

$$w = \sqrt{10} \text{ if } Ax - b > 0 \tag{A.17}$$

$$w = 1 \text{ if } Ax - b <= 0 \tag{A.18}$$

where σ is the standard deviation of uncertainty associated to the signal b.

Consequently, the projected sub-gradient algorithm for the dual Lagrangian can be expressed as:

$$\frac{\partial L}{\partial x} = 0 \rightarrow x^n = (A^TA + (\frac{w}{\sigma}A)^T(\frac{w}{\sigma}A))\backslash(A^Tb + \frac{w^2}{\sigma^2}A^Tb - \lambda^n c^T) \tag{A.19}$$

Finding the nearest feasible point inside the unit box

$$x^n = \min(\max(x^n, 0), 1) \tag{A.20}$$

$$\frac{\partial L}{\partial \lambda} = 0 \rightarrow \lambda^{n+1} = \max(0, \lambda^n + \alpha(C^Tx - d)) \tag{A.21}$$

Appendix B

An attempt of macroscopic modeling

The stochastic multiscale model presented in chapter 2 is able to simulate the PE behavior of a RVE. 1D and 2D experiments showed, during the pseudoelastic cycle, that the deformation propagates heterogeneously in the material through bands that concentrate most of the transformation strain. Such a band structure can only be simulated by introducing the constitutive law into a structure model. We propose in this part to give the first elements of such a simulation.

We propose especially to introduce the intrinsic interface as a *constitutive* property rather than a geometrical variation inside a finite element modeling (see the work of [Hill, 1983]). This constitutive property allows a link between the strain jump and the stress jump across the interface between the band and the matrix, defining a residual stress of the interface.

For simplicity consideration, a homogeneous stress hypothesis is retained for the RVE modeling and numerical applications will be provided for a single crystal only, in isothermal condition.

A finite difference scheme has been used for the numerical applications.

B.1 Constitutive property of intrinsic interface

We consider two adjacent elements that develop two transformation strain tensors $\boldsymbol{\epsilon}_1$ and $\boldsymbol{\epsilon}_2$. The interaction energy, assuming an elastic accommodation can be seen as:

$$g_{int} = (\boldsymbol{\epsilon}_1 - \boldsymbol{\epsilon}_2) : \mathbb{C} : (\boldsymbol{\epsilon}_1 - \boldsymbol{\epsilon}_2) - \xi \tag{B.1}$$

$$\xi \leq |\mathbb{C}^{\frac{1}{2}}(\boldsymbol{\epsilon}_1 - \boldsymbol{\epsilon}_2)|^2 \tag{B.2}$$

where $\mathbb{C}$ is the fourth rank tensor for elastic moduli.

The minimum interaction energy between two elements is achieved if and only if the following kinematic compatibility relationship is respected [Hill, 1983]:

$$[\boldsymbol{\epsilon}] = \boldsymbol{\epsilon}_1 - \boldsymbol{\epsilon}_2 \propto (\mathbf{b} \otimes \mathbf{n} + \mathbf{n} \otimes \mathbf{b}) \tag{B.3}$$

where $\mathbf{n}$ is the surface (normal) vector of interface and $\mathbf{b}$ is the displacement vector across the interface.

As we can see in Equation B.1, the interaction energy is always positive:

$$g_{int} \geq 0 \tag{B.4}$$

g_{int} is zero if $\boldsymbol{\epsilon}_1$ and $\boldsymbol{\epsilon}_2$ are compatible. If the compatibility relationship is not respected, the strain jump gives rise to residual stress .

Perfect bonding condition

We assume first a perfect phase interface between band and matrix (recall Figure 1.24, which justify the choice to deploy single crystal for the simulation). The displacement and the interfacial stress across the interface must be continuous, as a result, we have:

$$[\mathbf{u}] \cdot \mathbf{n} = u_n(\gamma^+) - u_n(\gamma^-) = 0 \tag{B.5}$$

and

$$[\boldsymbol{\sigma}] \cdot \mathbf{n} = \sigma_n(\gamma^+) - \sigma_n(\gamma^-) = 0 \tag{B.6}$$

$\mathbf{n}$ indicates the unit vector, normal to the interface from γ^- side to the γ^+ side.

Interfacial operator

Following the work of [Siredey et al., 1999], we assume that the stress fluctuates weakly inside the element and jumps only at the interface. Relationship between strain and stress jump may be evaluated using an interface operator. The jump of the average transformation strain across the interface is considered as the source of incompatibilities.

Let us assume that inside the shear band, the starred variables $(\boldsymbol{\sigma}^*, \boldsymbol{\epsilon}^*)$ are linked constitutively by :

$$\boldsymbol{\sigma}^* = \mathbb{C}(\boldsymbol{\epsilon}^* - \boldsymbol{\eta}) \tag{B.7}$$

where $\boldsymbol{\sigma}^*$ is the Cauchy stress, $\boldsymbol{\epsilon}^*$ is the infinitesimal strain. $\boldsymbol{\eta}$ is the free strain (associated with the martensitic phase transformation in our case).

For an elastic and isotropic medium (assuming that A, M and R phases share the same stiffness), the interfacial jump can be calculated by:

$$\begin{aligned}
&\boldsymbol{\epsilon} - \boldsymbol{\epsilon}^* = (\mathbb{A} : \mathbb{C}) : \boldsymbol{\eta},\ \boldsymbol{\sigma} - \boldsymbol{\sigma}^* = \mathbb{Q}\boldsymbol{\eta} \\
&2\mu A_{ijkl} = E_{ijkl} - \frac{\lambda}{\lambda + 2\mu} n_i n_j n_k n_l \\
&\frac{1}{2\mu} Q_{ijkl} = F_{ijkl} + \frac{\lambda}{\lambda + 2\mu} (\delta_{ij} - n_i n_j)(\delta_{kl} - n_k n_l)
\end{aligned} \tag{B.8}$$

where n_i indicates an intrinsic axes, λ and μ are Lamé coefficients, $\mathbb{Q}$ is the interfacial operator and $\mathbb{A}$ is the deformation concentration 4th rank tensor, function of $\mathbb{C}$.

E_{ijkl} and F_{ijkl} are expressed as follow:

$$E_{ijkl} = \frac{1}{2}(\delta_{ik} n_j n_l - \delta_{jk} n_i n_l + \delta_{il} n_j n_k + \delta_{jl} n_i n_k) - n_i n_j n_k n_l \tag{B.9}$$

$$F_{ijkl} = \frac{1}{2}(\delta_{ij} - n_i n_j)(\delta_{kl} - n_k n_l) + \frac{1}{2}(\delta_{jk} - n_j n_k)(\delta_{il} - n_i n_l) \tag{B.10}$$

Consequently the stress jump can be estimated as follow:

$$[\boldsymbol{\sigma}] = -\mathbb{Q}[\boldsymbol{\epsilon}] \tag{B.11}$$

where $[\boldsymbol{\sigma}]$ is the stress jump across the interface, $[\boldsymbol{\epsilon}]$ is the incompatible strain jump across the interface.

If the martensitic phase transformation follows the macroscopic shear localization mechanism, the discontinuity in the stress gradient can be constitutively deduced from an incompatible deformation tensor and the Hill interfacial operator.

In addition, these stress jumps can be considered as quasi-static low waves in a spatially continuous elastic medium. Due to their quasi-static nature, we can consider the residual stress applied to the boundaries as an additional stress term modifying the free energy densities of each element concerned, without disturbing the macroscopic equilibrium.

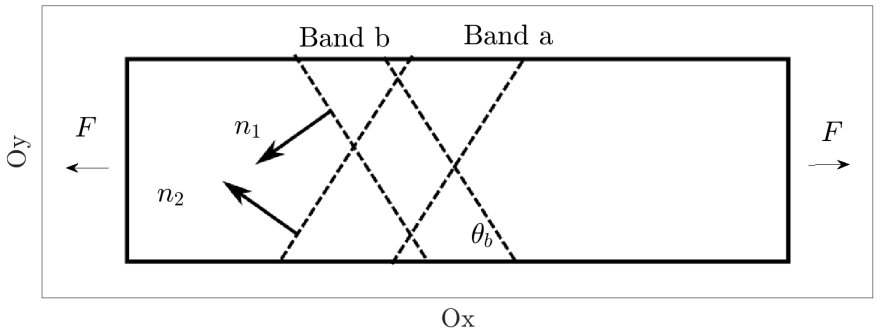

Figure B.1: Schematic illustration of kinematic displacement field due to localization instability for 1D strip subjected to a 1D tensile loading: two sets of bands are created, forming a symmetrical angle of θ_b with respect to the transverse direction of the strip.

B.2 Residual stress and mismatch in transformation strain

On one hand, the macroscopic stress is supposed homogeneously distributed for each elements except for the elements subjected to the structural defect.
On the other hand, as already mentioned, any incompatible interface develop a residual stress to overcome the kinematic incompatibility or to mismatch the transformation strain. Consequently, the residual stress applied at any incompatible interface seeks to minimize the experienced incompatibility by mismatching two different strain tensors by a reorientation mechanism.

In a schematic way, we may consider the example of two elements where element 1 is martensitic and element 2 is a mixture between A and R phase, the residual stress at the interface can be plotted as in Figure B.2.

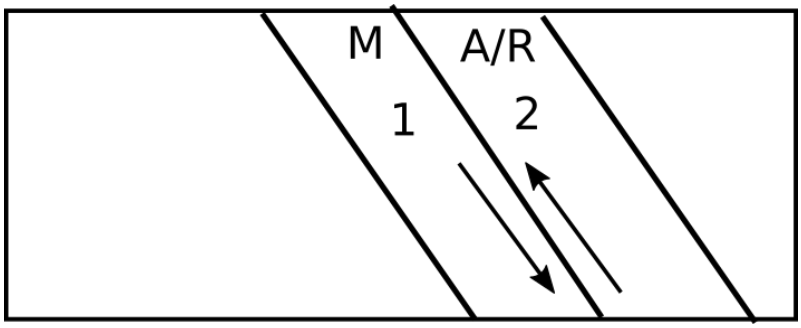

Figure B.2: Schematic illustration of the role of residual stress. Arrows represent the shear at the interface.

$$[\boldsymbol{\epsilon}]_{12} = (\mathbb{A} : \mathbb{C})^{-1}(\boldsymbol{\epsilon}_1 - \boldsymbol{\epsilon}_2) \tag{B.12}$$

$$[\boldsymbol{\sigma}]_{12} = -\mathbb{Q}[\boldsymbol{\epsilon}]_{12} \tag{B.13}$$

$$\boldsymbol{\sigma}_2 = \boldsymbol{\sigma} + [\boldsymbol{\sigma}]_{12} \text{ an } \boldsymbol{\sigma}_1 = \boldsymbol{\sigma} - [\boldsymbol{\sigma}]_{12} \tag{B.14}$$

where $\boldsymbol{\epsilon}_\alpha$ $\alpha = 1, 2$ is the strain tensor of element 1 and 2, $\boldsymbol{\sigma}$ is the macroscopic stress.

The residual stress applied to the element 1 seeks to reorient the martensite variants so that the deformations are in agreement between the element 1 and the element 2. At the same time, the residual stress applied to the element 2 seeks to induce a martensitic transformation in this element, which explains the propagation of the localization to the adjacent elements.
With the appearance of new variants and potential reorientations, the residual stress is reduced. Hill showed on the other hand that the band is oriented at $\theta = 54°$of the tensile axis in case of plane stress situation.

B.3 1D macroscopic model

We restrict the simulation to a uniaxial structure (the length $l_0 = 10\,\mathrm{mm}$) in isothermal situation ($T = 293\,\mathrm{K}$). Under tensile loading, the plane stress condition is achieved. The left-hand boundary is clamped. A stress-controlled loading is applied at the right-hand side boundary, with the stress rate $\dot{\sigma} = 1\,\mathrm{MPa\,s^{-1}}$. The material investigated is the Ni-Ti SMA whose constants have been detailed in chapter 1. It is 95% austenitic at $T = 293K$ (about 5% of R-phase). Only the single crystal case has been investigated to reduce the computation time and to facilitate the interpretation of results. The tensile axis is a $\langle 111 \rangle$ direction.
The specimen is meshed using $n_e = 200$ elements with a spatial resolution $\partial l = 50\,\mu\mathrm{m}$. The stochastic sampling time is fixed at $\partial t = 0.5\,\mathrm{s}$.
A structural defect has been introduced in one element (randomly chosen), corresponding to a fictitious 20% section reduction. This defect point is the source of localization.

B.3.1 1D Macroscopic model flowchart

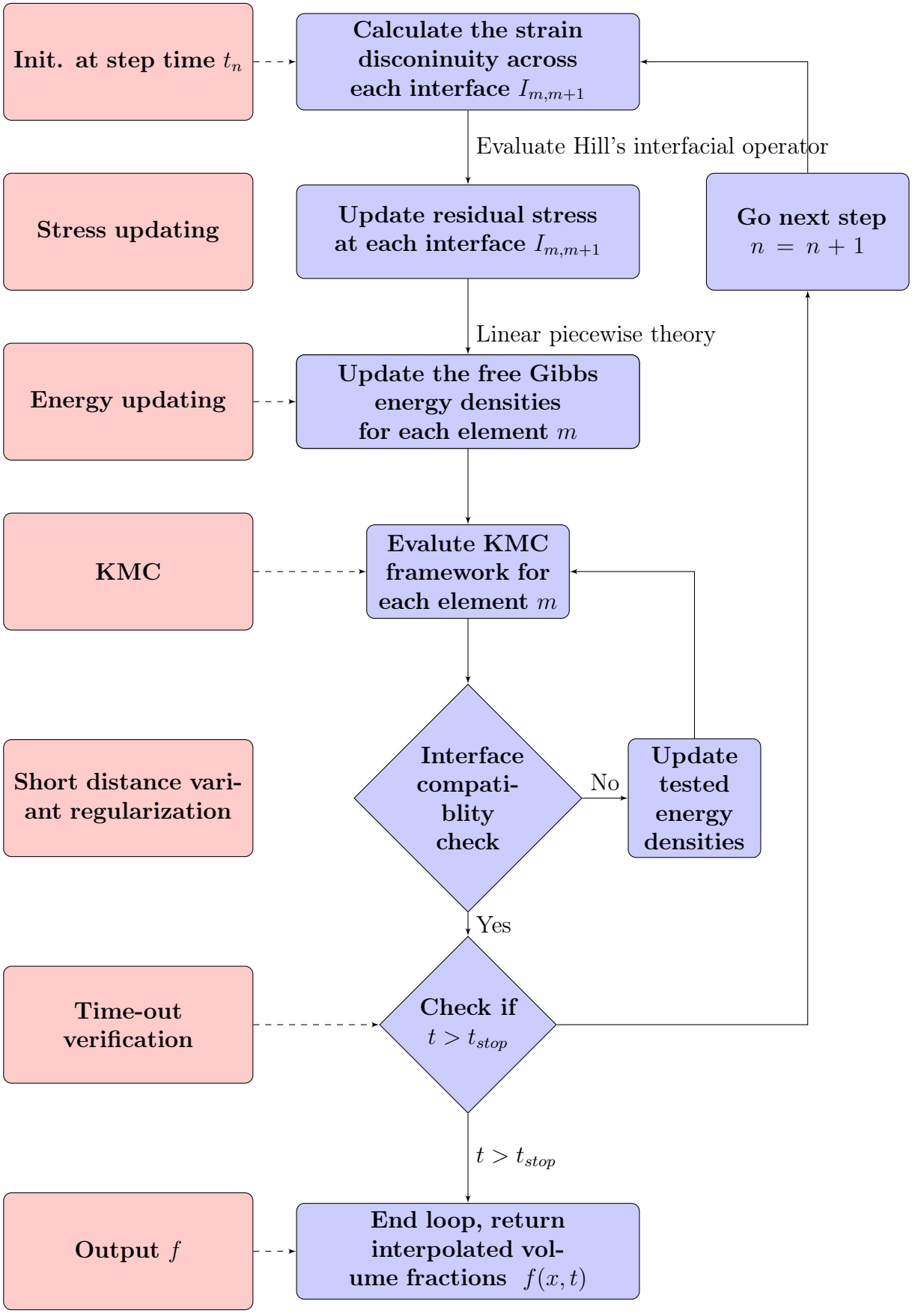

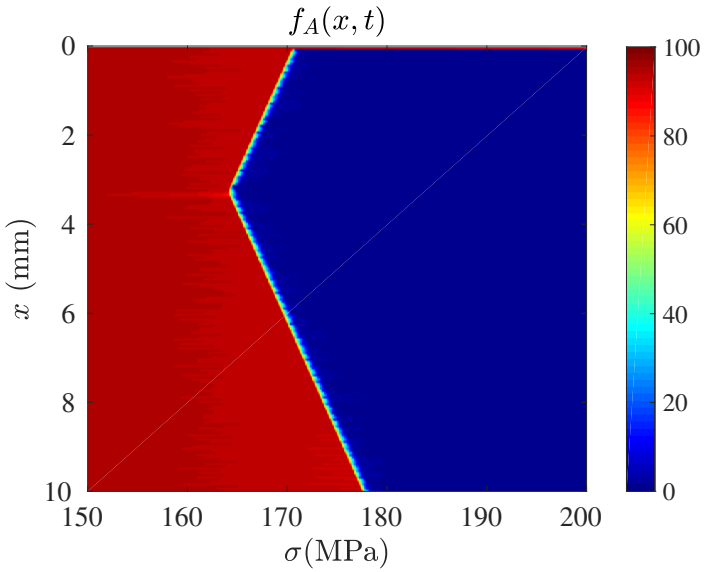

Figure B.3: Austenite volume fraction as function of applied stress

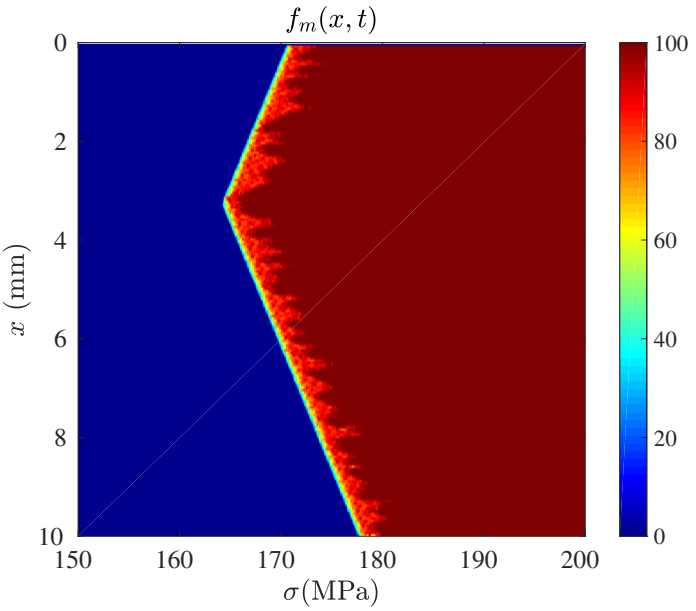

Figure B.4: Martensite volume fraction as function of applied stress

Simulations As we can see in Figure B.3, Figure B.4 and Figure B.5, the structural defect is located at $x = 3.2\,\text{mm}$. It induces the onset of localization at $\sigma = 152\,\text{MPa}$. Under isothermal configuration, the residual stress serves as the main driving force to propagate the transformation front. Hence the transformation front propagates in the two directions ($-O_x$ and O_x). As observed in chapter 4, R phase is present between M variants and the parent austenitic phase during all the transformation plateau. At $\sigma = 220\,\text{MPa}$, the external stress is above σ_{M_f} and A and R phase have completely disappeared.By plotting the external stress as function

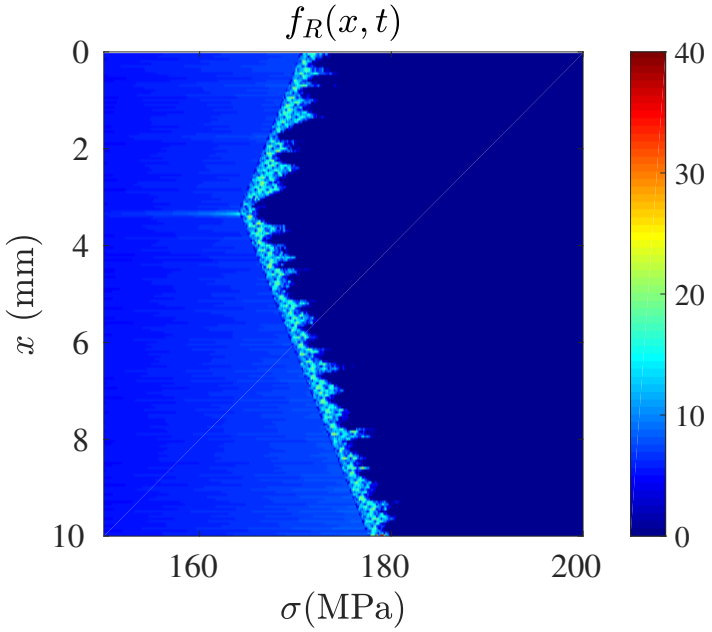

Figure B.5: R phase volume fraction as function of applied stress

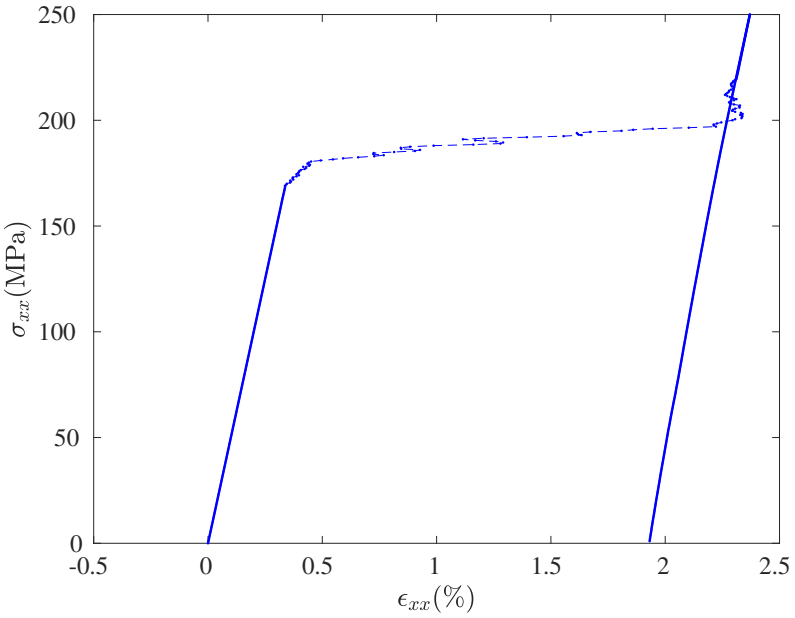

Figure B.6: Engineering stress/strain curve

of engineering strain along O_x ($\Delta l/l_0$) in Figure B.6, we observe that the deformation is lower than the expected deformation for a tensile loading along a $\langle 111 \rangle$ axis using the stochastic multiscale model for one element.

Indeed, during the 1D simulation, a mesoscopic selection of variants is made due to the interface operator. To illustrate that point, we decided to plot the spatial variation of the two following mesoscopic variants:

$$f_A(x) = f_2(x) + f_3(x) + f_7(x) + f_9(x) \tag{B.15}$$

$$f_B(x) = f_4(x) + f_5(x) + f_{11}(x) + f_{12}(x) \tag{B.16}$$

$f_A(x)$ and $f_B(x)$ can be considered as two different detwinning patterns.

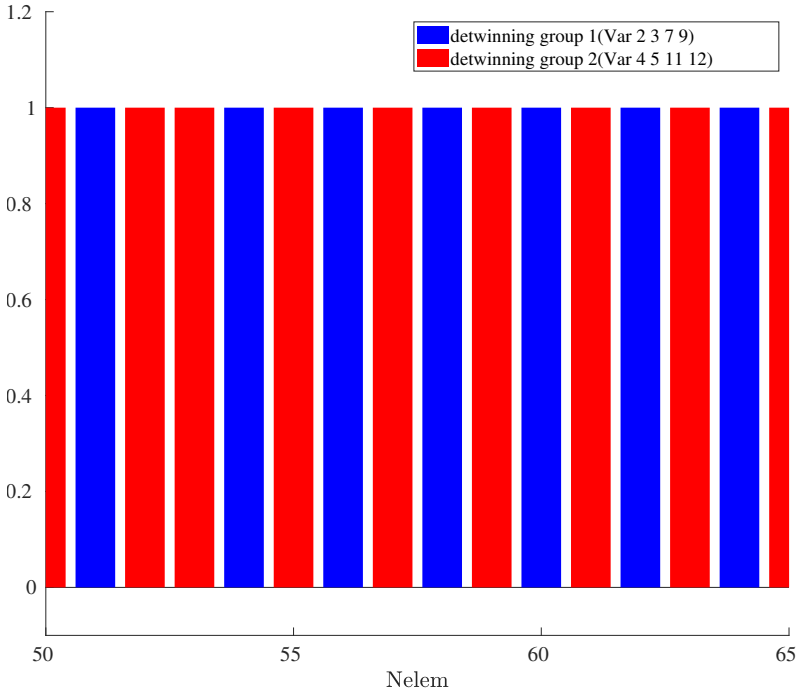

Figure B.7: Detwinning pattern formed once fully transformed

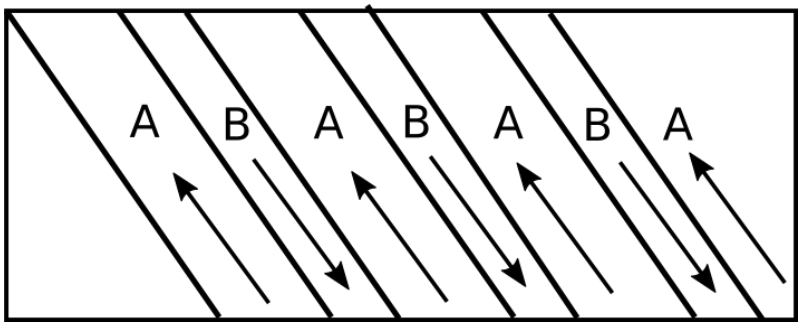

Figure B.8: Schematic illustration: strain tensor and distorted cohabit plane during 1D tensile loading (Region type A: slipped and dilated; Region type B: slipped and compressed)

As we can see, with residual stress as the main driving force to propagate transformation front, two set of detwinning patterns (group A in blue and B red) are formed successively and nearly periodically. Indeed the 8 martensite variants activated during tensile load are separated in two spatial groups. The cross twinning structure is formed. Consequently, the transformation strain average value at macroscopic scale is reduced compared to the case of one single crystal experiencing a uniaxial stress without the interfacial term. In this theoretical situation, only one group is created during the loading.

In terms of axial strain, the value predicted by the current macroscopic model is nearly the half the value reported in the experimental test in [Gall et al., 2001](Localization instability is not considered, hence only one set of localization bands is produced in numerical simulation.)

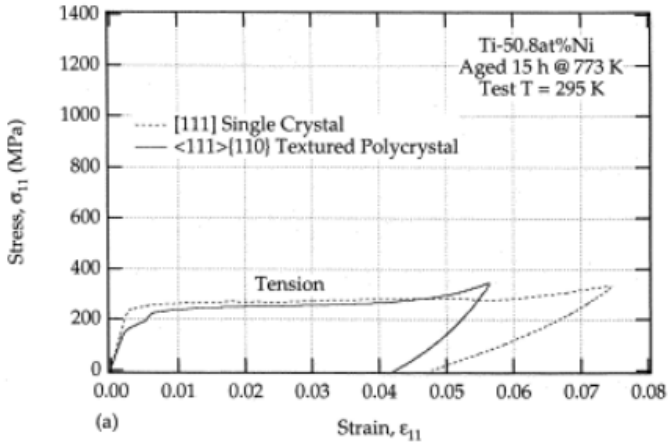

Figure B.9: PE experimental response of a NiTi single crystal loaded along $\langle 111 \rangle$ direction

Bibliography

F. J. Anscombe. The transformation of poisson, binomial and negative-binomial data. *Biometrika*, 35(3-4):246–254, 1948. doi: 10.1093/biomet/35.3-4.246. URL http://dx.doi.org/10.1093/biomet/35.3-4.246.

R. Araya, M. Marivil, C. Mir, O. Moroni, and A. Sepulveda. Temperature and grain size effects on the behavior of cualbe sma wires under cyclic loading. *Materials Science and Engineering: A*, 496(1):209 – 213, 2008. ISSN 0921-5093. doi: https://doi.org/10.1016/j.msea.2008.05.030. URL http://www.sciencedirect.com/science/article/pii/S0921509308005716.

F. Auricchio and J. Lubliner. A uniaxial model for shape-memory alloys. *International Journal of Solids and Structures*, 34(27):3601 – 3618, 1997. ISSN 0020-7683. doi: https://doi.org/10.1016/S0020-7683(96)00232-6. URL http://www.sciencedirect.com/science/article/pii/S0020768396002326.

M. Berny, T. Archer, A. Mavel, P. Beauchêne, S. Roux, and F. Hild. On the analysis of heat haze effects with spacetime dic. *Optics and Lasers in Engineering*, 111:135 – 153, 2018. ISSN 0143-8166. doi: https://doi.org/10.1016/j.optlaseng.2018.06.004. URL http://www.sciencedirect.com/science/article/pii/S0143816618301118.

M. Bertin. *Mechanical and fatigue properties of bellows determined with Integrated DIC and IR Thermography*. Theses, Université Paris-Saclay, September 2016. URL https://tel.archives-ouvertes.fr/tel-01370444.

C. Bewerse, K. R. Gall, G. J. McFarland, P.P Zhu, and L.C. Brinson. Local and global strains and strain ratios in shape memory alloys using digital image correlation. *Materials Science and Engineering: A*, 568:134 – 142, 2013. ISSN 0921-5093. doi: https://doi.org/10.1016/j.msea.2013.01.030. URL http://www.sciencedirect.com/science/article/pii/S0921509313000713.

K. Bhattacharya. Phase boundary propagation in a heterogeneous body. *Proceedings: Mathematical, Physical and Engineering Sciences*, pages 757–766, 1999.

K. Bhattacharya et al. *Microstructure of martensite: why it forms and how it gives rise to the shape-memory effect*, volume 2. Oxford University Press, 2003.

A.B. Bortz, M.H. Kalos, and J.L. Lebowitz. A new algorithm for monte carlo simulation of ising spin systems. *Journal of Computational Physics*, 17(1):10 – 18, 1975. ISSN 0021-9991. doi: https://doi.org/10.1016/0021-9991(75)90060-1. URL http://www.sciencedirect.com/science/article/pii/0021999175900601.

C. Bouvet, S. Calloch, and C. Lexcellent. A phenomenological model for pseudoelasticity of shape memory alloys under multiaxial proportional and nonproportional loadings. *European Journal of Mechanics - A/Solids*, 23(1):37 – 61, 2004. ISSN 0997-7538. doi: https://doi.org/10.1016/j.euromechsol.2003.09.005. URL http://www.sciencedirect.com/science/article/pii/S0997753803001104.

J.G. Boyd and D.C. Lagoudas. A thermodynamical constitutive model for shape memory materials. part i. the monolithic shape memory alloy. *International Journal of Plasticity*, 12(6):805 – 842, 1996. ISSN 0749-6419. doi: https://doi.org/10.1016/S0749-6419(96)00030-7. URL http://www.sciencedirect.com/science/article/pii/S0749641996000307.

W. J. Buehler, J. V. Gilfrich, and R. C. Wiley. Effect of Low-Temperature Phase Changes on the Mechanical Properties of Alloys near Composition TiNi. *Journal of Applied Physics*, 34:1475–1477, May 1963. doi: 10.1063/1.1729603.

J. Cederstrom. Relationship between shape memory material properties and applications. *The Journal de Physique IV*, 5(C2):C2–335, 1995.

X.Y. Chang, K. Lavernhe-Taillard, and O. Hubert. Observation of martensite phase transformation in shape memory alloys using a combined xrd-dic technique. August 2018. URL https://hal.archives-ouvertes.fr/hal-01889571.

X.Y. Chang, K. Lavernhe-Taillard, and O. Hubert. Stochastic multiscale modeling of the thermomechanical behavior of polycrystalline shape memory alloys. *Mechanics of Materials*, 144:103361, 2020. ISSN 0167-6636. doi: https://doi.org/10.1016/j.mechmat.2020.103361. URL http://www.sciencedirect.com/science/article/pii/S0167663619308567.

Y. Chemisky, G. Chatzigeorgiou, P. Kumar, and D. C. Lagoudas. A constitutive model for cyclic actuation of high-temperature shape memory alloys. *Mechanics of Materials*, 68:120 – 136, 2014. ISSN 0167-6636. doi: https://doi.org/10.1016/j.mechmat.2013.07.020. URL http://www.sciencedirect.com/science/article/pii/S0167663613001518.

L. Chevalier, S. Calloch, F. Hild, and Y. Marco. Digital image correlation used to analyze the multiaxial behavior of rubber-like materials. *European Journal of Mechanics - A/Solids*, 20, 12 2005. doi: 10.1016/S0997-7538(00)01135-9.

C. Chu and R. D. James. Analysis of microstructures in cu-14.0%al-3.9%ni by energy minimization. *J. Phys. IV France*, 05:C8–143–C8–149, 1995. doi: 10.1051/jp4:1995817. URL https://doi.org/10.1051/jp4:1995817.

B.D. Cullity. Elements of x-ray diffraction. *American Journal of Physics*, 25(6):394–395, 1957.

L. Daniel, O. Hubert, N. Buiron, and R. Billardon. Reversible magneto-elastic behavior: A multiscale approach. *Journal of the Mechanics and Physics of Solids*, 56(3):1018 – 1042, 2008. ISSN 0022-5096. doi: https://doi.org/10.1016/j.jmps.2007.06.003. URL http://www.sciencedirect.com/science/article/pii/S0022509607001263.

T. G. Daniel. A general method for numerically simulating the stochastic time evolution of coupled chemical reactions. *Journal of Computational Physics*, 22(4):403 – 434, 1976. ISSN 0021-9991. doi: https://doi.org/10.1016/0021-9991(76)90041-3. URL http://www.sciencedirect.com/science/article/pii/0021999176900413.

D. Depriester, A. Maynadier, K. Lavernhe-Taillard, and O. Hubert. Thermomechanical modelling of a niti sma sample submitted to displacement-controlled tensile test. *International Journal of Solids and Structures*, 51(10):1901 – 1922, 2014. ISSN 0020-7683. doi: https://doi.org/10.1016/j.ijsolstr.2014.01.027. URL http://www.sciencedirect.com/science/article/pii/S0020768314000377.

T. Duerig, A. Pelton, and D. Stöckel. An overview of nitinol medical applications. *Materials Science and Engineering: A*, 273:149–160, 1999.

M. D. Fall. *Mesure et modélisation multiéchelle du comportement thermo-magnéto-mécanique des alliages à mémoire de forme*. PhD thesis, 2017. URL http://www.theses.fr/2017SACLN013. Theses, Paris Saclay 2017.

M. D. Fall, O. Hubert, F. Mazaleyrat, K. Lavernhe-Taillard, and A. Pasko. A multiscale modeling of magnetic shape memory alloys: Application to nimnga single crystal. *IEEE Transactions on Magnetics*, 52(5):1–4, May 2016. ISSN 0018-9464. doi: 10.1109/TMAG.2016.2514705.

Y. Furuya. Design and material evaluation of shape memory composites. *Journal of intelligent material systems and structures*, 7(3):321–330, 1996.

K. Gall, H. Sehitoglu, R. Anderson, I. Karaman, Y. I. Chumlyakov, and I. V. Kireeva. On the mechanical behavior of single crystal niti shape memory alloys and related polycrystalline phenomenon. *Materials Science and Engineering: A*, 317(1):85 – 92, 2001. ISSN 0921-5093. doi: https://doi.org/10.1016/S0921-5093(01)01183-2. URL http://www.sciencedirect.com/science/article/pii/S0921509301011832.

M. Hasan, W.W. Schmahl, K. Hackl, R. Heinen, J. Frenzel, S. Gollerthan, G. Eggeler, M. Wagner, J. Khalil-Allafi, and A. Baruj. Hard x-ray studies of stress-induced phase transformations of superelastic niti shape memory alloys under uniaxial load. *Materials Science and Engineering: A*, 481-482:414 – 419, 2008. ISSN 0921-5093. doi: https://doi.org/10.1016/j.msea.2007.02.156. URL http://www.sciencedirect.com/science/article/pii/S0921509307012531. Proceedings of the 7th European Symposium on Martensitic Transformations, ESOMAT 2006.

A. Hautcoeur and A. Eberhardt. Eyeglass frame with very high recoverable deformability, June 17 1997. US Patent 5,640,217.

Y.J. He and Q.P. Sun. Rate-dependent domain spacing in a stretched niti strip. *International Journal of Solids and Structures*, 47(20):2775 – 2783, 2010. ISSN 0020-7683. doi: https://doi.org/10.1016/j.ijsolstr.2010.06.006. URL http://www.sciencedirect.com/science/article/pii/S0020768310002192.

Y.J. He and Q.P. Sun. On non-monotonic rate dependence of stress hysteresis of superelastic shape memory alloy bars. *International Journal of Solids and Structures*, 48(11):1688 – 1695, 2011. ISSN 0020-7683. doi: https://doi.org/10.1016/j.ijsolstr.2011.02.017. URL http://www.sciencedirect.com/science/article/pii/S002076831100076X.

G. Helbert, L. Dieng, S.A. Chirani, L. Saint-Sulpice, T. Lecompte, S. Calloch, and P. Pilvin. Investigation of niti based damper effects in bridge cables vibration response: Damping capacity and stiffness changes. *Engineering Structures*, 165:184 – 197, 2018. ISSN 0141-0296. doi: https://doi.org/10.1016/j.engstruct.2018.02.087. URL http://www.sciencedirect.com/science/article/pii/S014102961731903X.

F. Hild, S. Roux, R. Gras, N. Guerrero, and M. E. Marante. Displacement measurement technique for beam kinematics. *Optics and Lasers in Engineering*, 47(3):495 – 503, 2009. ISSN 0143-8166. doi: https://doi.org/10.1016/j.optlaseng.2008.03.006. URL http://www.sciencedirect.com/science/article/pii/S0143816608000432. Optical Measurements.

R. Hill. Interfacial operators in the mechanics of composite media. *Journal of the Mechanics and Physics of Solids*, 31(4):347 – 357, 1983. ISSN 0022-5096. doi: https://doi.org/10.1016/0022-5096(83)90004-2. URL http://www.sciencedirect.com/science/article/pii/0022509683900042.

D. E. Hodgson, W.H. Ming, and R. J. Biermann. Shape memory alloys. *ASM International, Metals Handbook, Tenth Edition.*, 2:897–902, 1990.

H. Huang, B. Durand, Q.P. Sun, and H. Zhao. An experimental study of niti alloy under shear loading over a large range of strain rates. *International Journal of Impact Engineering*, 108:402 – 413, 2017. ISSN 0734-743X. doi: https://doi.org/10.1016/j.ijimpeng.2017.03.007. URL http://www.sciencedirect.com/science/article/pii/S0734743X16309381. In Honour of the Editor-in-Chief, Professor Magnus Langseth, on his 65th Birthday.

W Huang. On the selection of shape memory alloys for actuators. *Materials & design*, 23(1):11–19, 2002.

W. Huang and W. Toh. Training two-way shape memory alloy by reheat treatment. *Journal of Materials Science Letters*, 19(17):1549–1550, Sep 2000. ISSN 1573-4811. doi: 10.1023/A:1006721022185. URL https://doi.org/10.1023/A:1006721022185.

J.V. Humbeeck. Non-medical applications of shape memory alloys. *Materials Science and Engineering: A*, 273:134–148, 1999.

J.M. Jani, M. Leary, A. Subic, and M.A. Gibson. A review of shape memory alloy research, applications and opportunities. *Materials Design (1980-2015)*, 56:1078 – 1113, 2014. ISSN 0261-3069. doi: https://doi.org/10.1016/j.matdes.2013.11.084. URL http://www.sciencedirect.com/science/article/pii/S0261306913011345.

M. Kohl. *Shape memory microactuators*. Springer Science & Business Media, 2013.

D. C. Lagoudas, Yves Chemisky, George Chatzigeorgiou, and Fodil Meraghni. Modeling of coupled phase transformation and reorientation in shape memory alloys under non-proportional thermomechanical loading. *International Journal of Plasticity*, 82:192 – 224, 2016. ISSN 0749-6419. doi: https://doi.org/10.1016/j.ijplas.2016.03.005. URL http://www.sciencedirect.com/science/article/pii/S0749641916300353.

D.C. Lagoudas, P.B. Entchev, P. Peter, E. Patoor, L.C. Brinson, and X.J. G. Shape memory alloys, part ii: Modeling of polycrystals. *Mechanics of Materials*, 38(5-6): 430–462, 5 2006. ISSN 0167-6636. doi: 10.1016/j.mechmat.2005.08.003.

K. Lavernhe-Taillard. *Etude du comportement thermomécanique des Alliages à Mémoire de Forme sous sollicitations multiaxiales complexes*. PhD thesis, Ecole normale supérieure de Cachan-ENS Cachan, 2006.

K. Lavernhe-Taillard, S. Calloch, S. Arbab-Chirani, and C. Lexcellent. Multiaxial shape memory effect and superelasticity. *Strain*, 45(1):77–84, 2009. doi: 10.1111/j.1475-1305.2008.00528.x. URL https://onlinelibrary.wiley.com/doi/abs/10.1111/j.1475-1305.2008.00528.x.

J. Lemaitre, J-L. Chaboche, and P. Germain. *Mécanique des matériaux solides*, volume 2. Dunod Paris, 1985.

C. Lexcellent and P. Blanc. Phase transformation yield surface determination for some shape memory alloys. *Acta Materialia*, 52(8):2317 – 2324, 2004. ISSN 1359-6454. doi: https://doi.org/10.1016/j.actamat.2004.01.022. URL http://www.sciencedirect.com/science/article/pii/S1359645404000473.

C. Lexcellent, A. Vivet, C. Bouvet, S. Calloch, and P. Blanc. Experimental and numerical determinations of the initial surface of phase transformation under biaxial loading in some polycrystalline shape-memory alloys. *Journal of the Mechanics and Physics of Solids*, 50(12):2717 – 2735, 2002. ISSN 0022-5096. doi: https://doi.org/10.1016/S0022-5096(02)00007-8. URL http://www.sciencedirect.com/science/article/pii/S0022509602000078.

C. Lexcellent, M.L. Boubakar, C. Bouvet, and S. Calloch. About modelling the shape memory alloy behaviour based on the phase transformation surface identification under proportional loading and anisothermal conditions. *International Journal of Solids and Structures*, 43(3):613 – 626, 2006. ISSN 0020-7683. doi: https://doi.org/10.1016/j.ijsolstr.2005.07.004. URL http://www.sciencedirect.com/science/article/pii/S0020768305004361.

C. Liang and C. A. Rogers. One-dimensional thermomechanical constitutive relations for shape memory materials. *Journal of Intelligent Material Systems and Structures*, 8(4):285–302, 1997. doi: 10.1177/1045389X9700800402. URL https://doi.org/10.1177/1045389X9700800402.

Y.N. Liu, Y. Liu, and J. V. Humbeeck. Two-way shape memory effect developed by martensite deformation in niti. *Acta Materialia*, 47(1):199 – 209, 1998. ISSN 1359-6454. doi: https://doi.org/10.1016/S1359-6454(98)00325-5. URL http://www.sciencedirect.com/science/article/pii/S1359645498003255.

P. Lukas, P. Sittner, D. Lugovoy, D. Neov, and M. Ceretti. In situ neutron diffraction studies of the r-phase transformation in the niti shape memory alloy. *Applied Physics A*, 74(1):s1121–s1123, Dec 2002. ISSN 1432-0630. doi: 10.1007/s003390101201. URL https://doi.org/10.1007/s003390101201.

J. Ma, I. Karaman, and R. D. Noebe. High temperature shape memory alloys. *International Materials Reviews*, 55(5):257–315, 2010. doi: 10.1179/095066010X12646898728363. URL https://doi.org/10.1179/095066010X12646898728363.

R. S. Matos, M. J. Xavier, L. S. Barreto, N. B. Costa, and I. F. Gimenez. Principal component analysis of x-ray diffraction patterns to yield morphological classification of brucite particles. *Analytical Chemistry*, 79(5):2091–2095, 2007. doi: 10.1021/ac061991n. URL https://doi.org/10.1021/ac061991n. PMID: 17326603.

A. Maynadier. *Thermomechanical coupling in shape memory alloys : thermal and kinematic full field measurements and multi-scale modeling*. Theses, Ecole normale supérieure de Cachan - ENS Cachan, November 2012. URL https://tel.archives-ouvertes.fr/tel-01044998.

A. Maynadier, D. Depriester, K. Lavernhe-Taillard, and O. Hubert. Thermomechanical description of phase transformation in ni-ti shape memory alloy. *Procedia Engineering*, 10:2208 – 2213, 2011. ISSN 1877-7058. doi: https://doi.org/10.1016/j.proeng.2011.04.365. URL http://www.sciencedirect.com/science/article/pii/S1877705811005534. 11th International Conference on the Mechanical Behavior of Materials (ICM11).

A. Maynadier, M. Poncelet, K. Lavernhe-Taillard, and S. Roux. One-shot measurement of thermal and kinematic fields: infrared image correlation (iric). *Experimental Mechanics*, 52(3):241–255, 2012.

N.B. Morgan. Medical shape memory alloy applications in the market and its products. *Materials Science and Engineering: A*, 378(1-2):16–23, 2004.

S. M. Obeidat and et a.l. I. Al-Momani. Combination of icp-oes, xrf and xrd techniques for analysis of several dental ceramics and their identification using chemometrics. *Spectroscopy*, 26:141–149, 2011. doi: 10.3233/SPE-2011-0521.

K. Otsuka and X. Ren. Physical metallurgy of tini-based shape memory alloys. *Progress in Materials Science*, 50(5):511 – 678, 2005. ISSN 0079-6425. doi: https://doi.org/10.1016/j.pmatsci.2004.10.001. URL http://www.sciencedirect.com/science/article/pii/S0079642504000647.

K. Otsuka and C. M. Wayman. *Shape memory materials*. Cambridge university press, 1999.

J.R. Patel and M. Cohen. Criterion for the action of applied stress in the martensitic transformation. *Acta Metallurgica*, 1(5):531 – 538, 1953. ISSN 0001-6160. doi: https://doi.org/10.1016/0001-6160(53)90083-2. URL http://www.sciencedirect.com/science/article/pii/0001616053900832.

E. Patoor, A. Eberhardt, and M. Berveiller. Micromechanical modelling of superelasticity in shape memory alloys. *J. Phys. IV France*, 06:C1–277–C1–292, 1996. doi: 10.1051/jp4:1996127. URL https://doi.org/10.1051/jp4:1996127.

E. Patoor, D. C. Lagoudas, P. B. Entchev, L. C. Brinson, and X.J. Gao. Shape memory alloys, part i: General properties and modeling of single crystals. *Mechanics of Materials*, 38(5):391 – 429, 2006. ISSN 0167-6636. doi: https://doi.org/10.1016/j.mechmat.2005.05.027. URL http://www.sciencedirect.com/science/article/pii/S0167663605001195. Shape Memory Alloys.

R. Plietsch and K. Ehrlich. Strength differential effect in pseudoelastic niti shape memory alloys. *Acta Materialia*, 45(6):2417 – 2424, 1997. ISSN 1359-6454. doi: https://doi.org/10.1016/S1359-6454(96)00354-0. URL http://www.sciencedirect.com/science/article/pii/S1359645496003540.

I. Ponikarova, N. Resnina, S. Belyaev, and E. Iaparova. Influence of maximum thermal cycle temperature on the two-way shape memory effect in tini alloy. *Materials Today: Proceedings*, 4(3, Part B):4737 – 4742, 2017. ISSN 2214-7853. doi: https://doi.org/10.1016/j.matpr.2017.04.062. URL http://www.sciencedirect.com/science/article/pii/S2214785317306387.

W. Reiher. Hammersley, j. m., d. c. handscomb: Monte carlo methods. methuen & co., london, and john wiley & sons, new york, 1964. vii + 178 s., preis: 25 s. *Biometrische Zeitschrift*, 8(3):209–209, 1966. doi: 10.1002/bimj.19660080314. URL https://onlinelibrary.wiley.com/doi/abs/10.1002/bimj.19660080314.

L. Saint-Sulpice, S. A. Chirani, and S. Calloch. A 3d super-elastic model for shape memory alloys taking into account progressive strain under cyclic loadings. *Mechanics of Materials*, 41(1):12 – 26, 2009. ISSN 0167-6636. doi: https://doi.org/10.1016/j.mechmat.2008.07.004. URL http://www.sciencedirect.com/science/article/pii/S0167663608001051.

T.A. Schroeder and C.M. Wayman. The two-way shape memory effect and other training phenomena in cu-zn single crystals. *Scripta Metallurgica*, 11(3):225 – 230, 1977. ISSN 0036-9748. doi: https://doi.org/10.1016/0036-9748(77)90058-8. URL http://www.sciencedirect.com/science/article/pii/0036974877900588.

J.A. Shaw and S. Kyriakides. Thermomechanical aspects of niti. *Journal of the Mechanics and Physics of Solids*, 43(8):1243 – 1281, 1995. ISSN 0022-5096. doi: https://doi.org/10.1016/0022-5096(95)00024-D. URL http://www.sciencedirect.com/science/article/pii/002250969500024D.

J.A. Shaw and S. Kyriakides. On the nucleation and propagation of phase transformation fronts in a niti alloy. *Acta Materialia*, 45(2):683 – 700, 1997. ISSN

1359-6454. doi: https://doi.org/10.1016/S1359-6454(96)00189-9. URL http://www.sciencedirect.com/science/article/pii/S1359645496001899.

N. Siredey, E. Patoor, M. Berveiller, and A. Eberhardt. Constitutive equations for polycrystalline thermoelastic shape memory alloys.: Part i. intragranular interactions and behavior of the grain. *International Journal of Solids and Structures*, 36(28):4289 – 4315, 1999. ISSN 0020-7683. doi: https://doi.org/10.1016/S0020-7683(98)00196-6. URL http://www.sciencedirect.com/science/article/pii/S0020768398001966.

P. Sittner, M. Landa, P. Lukas, and V. Novak. R-phase transformation phenomena in thermomechanically loaded niti polycrystals. *Mechanics of Materials*, 38(5):475 – 492, 2006. ISSN 0167-6636. doi: https://doi.org/10.1016/j.mechmat.2005.05.025. URL http://www.sciencedirect.com/science/article/pii/S0167663605001225. Shape Memory Alloys.

Y. Soejima, S. Motomura, M. Mitsuhara, T. Inamura, and M. Nishida. In situ scanning electron microscopy study of the thermoelastic martensitic transformation in ti-ni shape memory alloy. *Acta Materialia*, 103:352 – 360, 2016. ISSN 1359-6454. doi: https://doi.org/10.1016/j.actamat.2015.10.017. URL http://www.sciencedirect.com/science/article/pii/S1359645415300136.

D. Song, G.Z. Kang, Q.H. Kan, C. Yu, and C.Z. Zhang. Non-proportional multiaxial transformation ratchetting of super-elastic niti shape memory alloy: Experimental observations. *Mechanics of Materials*, 70:94 – 105, 2014. ISSN 0167-6636. doi: https://doi.org/10.1016/j.mechmat.2013.12.003. URL http://www.sciencedirect.com/science/article/pii/S0167663613002548.

M. Sreekumar, T. Nagarajan, M. Singaperumal, M. Zoppi, and R. Molfino. Critical review of current trends in shape memory alloy actuators for intelligent robots. *Industrial Robot: An International Journal*, 34(4):285–294, 2007.

D. Stoeckel. Shape memory actuators for automotive applications. *Materials & Design*, 11(6):302–307, 1990.

L. Sun, W. M. Huang, Z. Ding, Y. Zhao, C. C. Wang, H. Purnawali, and C. Tang. Stimulus-responsive shape memory materials: a review. *Materials & Design*, 33:577–640, 2012.

Q.P. Sun and Y.J. He. A multiscale continuum model of the grain-size dependence of the stress hysteresis in shape memory alloy polycrystals. *International Journal of Solids and Structures*, 45(13):3868 – 3896, 2008. ISSN 0020-7683. doi: https://doi.org/10.1016/j.ijsolstr.2007.12.008. URL http://www.sciencedirect.com/science/article/pii/S0020768307005100. Special Issue Honoring K.C. Hwang.

P. Thamburaja, H. Pan, and F.S. Chau. Martensitic reorientation and shape-memory effect in initially textured polycrystalline tini sheet. *Acta Materialia*, 53(14):3821 – 3831, 2005. ISSN 1359-6454. doi: https://doi.org/10.1016/j.actamat.2005.03.054. URL http://www.sciencedirect.com/science/article/pii/S1359645405002557.

Z. Tomicevic, F. Hild, and S. Roux. Mechanics-aided digital image correlation. *The Journal of Strain Analysis for Engineering Design*, 48:330–343, 07 2013. doi: 10.1177/0309324713482457.

C. Yu, G. Kang, D. Song, and Q. Kan. Effect of martensite reorientation and reorientation-induced plasticity on multiaxial transformation ratchetting of superelastic niti shape memory alloy: New consideration in constitutive model. *International Journal of Plasticity*, 67:69 – 101, 2015. ISSN 0749-6419. doi: https://doi.org/10.1016/j.ijplas.2014.10.001. URL http://www.sciencedirect.com/science/article/pii/S0749641914001958.

X.H. Zhang, P. Feng, Y.J. He, T.X. Yu, and Q.P. Sun. Experimental study on rate dependence of macroscopic domain and stress hysteresis in niti shape memory alloy strips. *International Journal of Mechanical Sciences*, 52(12):1660 – 1670, 2010. ISSN 0020-7403. doi: https://doi.org/10.1016/j.ijmecsci.2010.08.007. URL http://www.sciencedirect.com/science/article/pii/S0020740310002110.

X.Y. Zhang and Huseyin Sehitoglu. Crystallography of the b2 - r - b19 phase transformations in niti. *Materials Science and Engineering: A*, 374(1):292 – 302, 2004. ISSN 0921-5093. doi: https://doi.org/10.1016/j.msea.2004.03.013. URL http://www.sciencedirect.com/science/article/pii/S0921509304002758.

L. Zheng, Y.J. He, and Z. Moumni. Effects of lüders-like bands on niti fatigue behaviors. *International Journal of Solids and Structures*, 83:28 – 44, 2016. ISSN 0020-7683. doi: https://doi.org/10.1016/j.ijsolstr.2015.12.021. URL http://www.sciencedirect.com/science/article/pii/S0020768315005211.

R.B. Zider and J.F. Krumme. Eyeglass frame including shape-memory elements, 1988. US Patent 4,772,112.

université PARIS-SACLAY

ÉCOLE DOCTORALE
Sciences mécaniques et énergétiques, matériaux et géosciences (SMEMAG)

Titre: Mesure et modélisation multiéchelle du comportement thermomécanique des alliages à mémoire de forme sous chargement mécanique multiaxial

Mots clés: Alliages à Mémoire de Forme, Modélisation multi-échelle, Modélisation stochastique, Corrélation d'Images Numeriques (CIN), Diffraction des Rayons-X (DRX), Chargement multiaxial

Résumé: Depuis leur découverte, les alliages à mémoire de forme (AMF) ont connu un développement croissant de leurs applications industrielles (par example implants médicaux, aérospatial) en relation avec leurs propriétés mécaniques remarquables (effet mémoire et pseudo-élasticité). La transformation martensitique est au coeur de ces propriétés, ce type de transformation pouvant être induit par un chargement thermique, un chargement mécanique, ou un chargement thermomécanique couplé (les alliages à mémoire de forme magnétiques font figure d'exception puisque pour ces alliages, le chargement magnétique est une troisième source de transformation ; ils ne seront pas traités dans ce mémoire). Un des obstacles majeurs à une utilisation beaucoup plus générale de ces matériaux est un manque de modèle de comportement robuste. Il s'agit en effet de restituer un comportement non-linéaire généralement dissipatif dans un cadre thermomécanique multiaxial. Les approches multi-échelles, utilisant un jeu de variables internes et de potentiels écrits à une échelle appropriée, peuvent permettre de relever ce défi, avec bien entendu une mise en place d'outils de localisation et d'homogénéisation appropriés. Le modèle développé pendant ce travail de thèse, par une approche stochastique du calcul des fractions de variantes du milieu (l'approche peut s'appliquer à n'importe quel AMF), permet une généralisation du modèle multi-échelle réversible développé dans la thèse d'A. Maynadier (2012) à un cadre irréversible. Une campagne d'essais expérimentaux a été réalisée en parallèle du développement du modèle, permettant d'en identifier les paramètres intrinsèques et de le valider via un certain nombre de simulations numériques. Le matériau retenu est un NiTi équiatomique traité pour être pseudo-élastique. Dans ce cadre, un banc d'essais in-situ et une procédure d'identification totalement novatrice ont été développés : le banc d'essais permet de combiner les mesures du champ cinématique par corrélation d'images numériques (CIN) à celle des champs de phases par diffraction des rayons X (DRX), le tout au cours d'un essai de traction uniaxial, puis lors d'essais multiaxiaux proportionnels et non proportionnels. Le champ cinématique permet d'avoir une description continue du phénomène de localisation en bandes de transformation; la mise en place d'une procédure de décomposition en modes propres spatio-angulaires (POD) a permis une identification robuste des champs de phases cohérente avec le champ cinématique, et mettent en évidence des phénomènes d'interface et de sélection de variantes jusqu'ici jamais reportés dans la littérature. Cette comparaison multi-champs permet d'avoir une meilleure compréhension du phénomène de localisation en bandes et suggère une piste potentielle de développement d'un modèle de structure pertinent.

Title: Measurement and multiscale modeling of the thermomechanical behavior of shape memory alloys subjected to multiaxial mechanical loading

Keywords: Shape Memory Alloys, Multiscale modeling, Stochastic modeling, Digital Images Correlation (DIC), X-Ray Diffraction (XRD), Multiaxial loading

Abstract: Since their discovery, shape memory alloys (SMA) have experienced an increasing development of their industrial applications (e.g. medical implants, aerospace) in relation to their remarkable mechanical properties (memory effect and pseudo-elasticity). The martensitic transformation is at the heart of these properties, this type of transformation being able to be induced by a thermal loading, a mechanical loading, or a coupled thermo-mechanical loading (magnetic shape memory alloys are exceptions since for these alloys, the magnetic loading is a third source of transformation: they will not be treated in this work). One of the major obstacles to a much more general use of these materials is a lack of robust constitutive model. Indeed, the behavior that is expected is a non-linear and generally dissipative behavior in a thermo-mechanical multiaxial framework. Multiscale approaches, using a set of internal variables and potentials written at an appropriate scale, can meet this challenge, with, of course, the implementation of appropriate localization and homogenization procedures. The model developed in this thesis, with a stochastic approach for the computation of the variants volume fractions (this approach can be applied to any SMA), allows a generalization of the reversible multi-scale model developed in the PhD of A. Maynadier (2012) to an irreversible framework. An experimental test campaign was carried out in parallel to the development of the model, making it possible to identify its intrinsic parameters and to validate it via a large number of numerical simulations. The material retained is a pseudo-elastic equi-atomic NiTi. In this context, an in-situ test bench and a completely innovative identification procedure have been developed: the test bench makes it possible to combine a kinematic field measurements by digital image correlation (DIC) with a phase field measurement by X-ray diffraction (XRD) simultaneously, during a uniaxial tensile test first, then during proportional and non-proportional multiaxial tests. The kinematic field allows a continuous description of the localization phenomenon in transformation bands to be obtained; the implementation of a spatio-angular proper order decomposition (POD) method allows a robust identification of the phase fields coherent with the kinematic field, and highlights interfaces and variant selection phenomena until now never reported in the literature. This multi-field comparison provides a better understanding of the band localization phenomenon and suggests a potential track for developing a relevant structure model.

Université Paris-Saclay
Espace Technologique / Immeuble Discovery
Route de l'Orme aux Merisiers RD 128 / 91190 Saint-Aubin, France